Protection of Direct-Current Systems

by

Khaled Saleh

A thesis
presented to the University of Waterloo
in fulfillment of the
thesis requirement for the degree of
Doctor of Philosophy
in
Electrical and Computer Engineering

Waterloo, Ontario, Canada, 2017

Examining Committee Membership

The following served on the Examining Committee for this thesis. The decision of the Examining Committee is by majority vote.

External Examiner	ATHANASIOS P. MELIOPOULOS Professor
Supervisor	EHAB F. EL-SAADANY Professor
Internal Member	CLAUDIO A. CANIZARES Professor
Internal Member	MAGDY SALAMA Professor
Internal-external Member	GIOVANNI CASCANTE Professor

I hereby declare that I am the sole author of this thesis. This is a true copy of the thesis, including any required final revisions, as accepted by my examiners.

I understand that my thesis may be made electronically available to the public.

Abstract

The overwhelming advancement in power electronics converters throughout the past few decades is leading to an increasing interest in the integration of Direct-Current (DC) systems to the existing AC ones on the generation, Low Voltage DC (LVDC), Medium Voltage DC (MVDC), and High Voltage DC (HVDC) levels. The utilization of DC systems offer many benefits over their AC counterparts such as the significant reduction in power losses and costs as well as the minimization of reactive current component. Nevertheless, DC systems still face many challenges among which protection is the most salient.

This dissertation investigates and addresses the protection challenges posed by DC faults' behaviour in five DC systems. On the generation level, it explores the nature of various faults and partial shading conditions in utility-scale Photovoltaic (PV) arrays. The unique PV modules' voltage behaviour during faults and partial shading conditions is scrutinized to identify distinctive characteristics. These voltage features are utilized to propose a new time-domain voltage-based protection scheme. The proposed scheme's underlying concepts are analytically proved for generic PV modules, validated using detailed time-domain model of PV panels, and verified experimentally using polycrystalline-silicon panels.

On the LVDC level, the dissertation examines the behaviour of low- and high-resistance faults. The analysis are founded upon a detailed time-domain simulation of a meshed LVDC microgrid. The failure of conventional protection methods in the presence of even small amounts of fault resistance are demonstrated. An effective method is proposed to detect such faults by using the resonance frequency generated from passive oscillators installed on the line terminals.

The protection of MVDC microgrids is a major challenge as very high fault current magnitudes are attained within a couple of milliseconds. This dissertation reveals unique fault-launched Travelling wave (TW) waveform and polarity properties. These properties are exploited to propose an adequate time-domain TW-based protection scheme that detects, classifies, and locates DC faults in a timely manner.

The impediments to reliable protection of hybrid AC/DC microgrids are twofold: (i) the very low AC fault current magnitudes in the AC-side due to the current control capability

of inverter-based Distributed Generation (DG)s, and (ii) the very high DC fault current magnitudes attained within few milliseconds in the DC-side due to the uncontrollable discharge of the converters' DC link capacitors. A unified discriminant function TW-based protection scheme is proposed for hybrid AC/DC microgrids to detect, classify, and locate both AC and DC faults.

DC faults in HVDC grids can cause severe damage to the converter stations and large loss of infeed within few milliseconds. Ensuring selectivity and sensitivity of the protection system within a short time window is a major challenge. This dissertation analyze the frequency spectra of the TWs initiated by faults on HVDC grids. Using the spectral content and polarity of the current TWs, a novel frequency-domain TW-based scheme is proposed to detect and locate faults within the required timeframe.

Acknowledgements

Foremost, I would like to express my sincere gratitude to my Ph.D. advisor, Dr. Ehab El-Saadany, for his valuable guidance, scholarly inputs, and consistent encouragement throughout my doctoral studies. Despite his busy schedule, he has always made himself available to clarify my doubts. During the past three years, I always came out from meetings with Dr. El-Saadany more inspired, motivated, and confident about my abilities. For that, and all his support since the day I met him during my undergraduate studies, I sincerely thank Dr. El-Saadany.

I am honoured that this dissertation has been examined by Dr. Athanasios P. Meliopoulos, Dr. Claudio Canizares, Dr. Magdy Salama, and Dr. Giovanni Cascante. I owe respect and thanks to them for their time and insight.

I always say that my doctoral studies went smoothly due to my collaboration with Dr. Ali Hooshyar. He is everything one could look for in a good mentor. Dr. Hooshyar is always reachable, even during holidays, to answer my never-ending questions and guide me through the contradicting ideas/conclusions that I had. I will always be grateful to Dr. Hooshyar for his support and kindness.

I have consistently been on the receiving end of my M.Sc. advisor's kind attention. I am truly grateful to Dr. Hatem Zeineldin for his valuable contribution and feedback to the research work presented in this dissertation.

I owe a lot to my parents, who encouraged and helped me at every stage of my personal and academic life, and longed to see this achievement come true. I always fall short of words when it comes to describing their support. Yet, I am sure that I would not have achieved anything without them. I am also thankful to my sisters, Alaa, Heba and Mira, for their support and love. Special thanks go to my sister, soon-to-be Dr. Alaa, for being a great host in Montreal and a sightseeing companion for the past year.

Last but not least, I would like to extend my gratitude to my friends in Canada who made my life more enjoyable. Thanks to Abdelhalim for being a great neighbour, travel mate, and cooking/food partner. Thanks to Assem for all the video gaming nights and endless debates about random topics. Also, thanks to Nahid, Dima, and Mohammed for organizing all the fun activities in Montreal, which often involve being soaked.

to
Mum & Dad,
Alaa, Heba, & Mira

Table of Contents

List of Tables

List of Figures

List of Abbreviations

ADC	Analog-to-Digital.
CB	Circuit Breaker.
CTI	Coordination Time Interval.
DC	Direct-Current.
DF	Discriminant Functions.
DG	Distributed Generation.
DWT	Discrete Wavelet Transform.
EPRI	Electric Power Research Institute.
EU	European Union.
FDF	Forward Discriminant Function.
FFT	Fast Fourier Transformer.
FSR	Frequency Spectrum Ratio.
HVDC	High Voltage DC.
IEA	International Energy Agency.
IED	Intelligent Electronic Device.
IGBT	Insulated Gate Bipolar Transistor.

IRENA	International Renewable Energy Agency.
LCC	Line Commutated Converter.
LL	Line-to-Line.
LLG	Line-to-Line-to-Ground.
LVDC	Low Voltage DC.
MMC	Modular Multilevel Converter.
MPPT	Maximum Power Point Tracker.
MVDC	Medium Voltage DC.
NPG	Negative-Pole-to-Ground.
OC	Open-Circuit.
OHL	Overhead Line.
OT	Operation Time.
PG	Pole-to-Ground.
PP	Pole-to-Pole.
PPG	Positive-Pole-to-Ground.
PV	Photovoltaic.
RDF	Reverse Discriminant Function.
SG	String-to-Ground.
SLG	Single-Line-to-Ground.
SNR	Signal-to-Noise Ratio.
SS	String-to-String.

STC Standard Test Condition.

TW Travelling wave.

UGC Underground Cable.

VSC Voltage-Sourced Converter.

WGN White Gaussian Noise.

List of Symbols

A_f	Normalized area of D_f.
C_R	Relay capacitor.
C_p	PV cell leakage capacitor.
C_x	Capacitance per unit length of line/cable.
C_{conv}	DC/DC converter capacitor.
C_{dc}	DC link capacitor.
D	Duty cycle.
$D1$	Detail 1 signal decomposition level.
$D1_{pu}$	Detail 1 pickup voltage.
D_f	Forward discriminant function.
D_r	Reverse discriminant function.
$D_t\delta_m^1$	First derivative of δ_m^1.
$D_t\delta_m^2$	First derivative of δ_m^2.
$D_t^2\delta_m^1$	Second derivative of δ_m^1.
$D_t^2\delta_m^2$	Second derivative of δ_m^2.
D_{bp}	Bypass diode.
D_{pv}	PV diode.
F_d	Passive elements resonance frequency.
F_n	Natural frequency.
F_s	Sampling frequency.
$F_{n'',m''}$	Fault node with the lower pre-fault voltage.
$F_{n',m'}$	Fault node with the higher pre-fault voltage.

$F_{n,m}$	Fault node at the n-th row and m-th string.
G	Irradiance seen by a shaded PV module.
G^S	Shade irradiance.
G^{pr}	Pre-shade irradiance.
G^{ref}	Irradiance level at the STC.
Gx	Conductance per unit length of cable's dielectric.
H	Height of cumulus clouds.
H_{meas}	Height at which wind speed is measured.
I_R	Current passing through the relay.
I_0	PV module saturation current.
I_{Lr}	Relay inductor current.
I_{bp}	Current through the PV bypass diode.
I_{conv}	Converter current output.
$I_{f_{Rx}}$	Fault current seen by relay x.
$I_{fault_{Rx}}$	Total current seen by relay x during fault condition.
I_f	Fault current.
$I_{load_{Rx}}$	Load current seen by relay x during pre-fault condition.
I_{mp}	PV module maximum power current.
I_m^L	Current of an illuminated PV module in a partially shaded string.
I_m^S	Current of a shaded PV module.
I_{ph}	Photocurrent of an illuminated PV module.
I_{ph}^S	Photocurrent of a shaded PV module.
I_{pu}	Pickup current.
I_{sc}	PV module short-circuit current.
L	Signal decomposition level.

L_R	Relay inductor.
L_c	Cable inductor.
L_x	Inductance per unit length of line/cable.
L_{conv}	DC/DC converter inductor.
M	Number of PV strings in an array.
N	Number of PV modules in a string.
N_d	Number of bypass diodes per module.
N_m^L	Number of illuminated modules in string m.
N_m^S	Number of shaded modules in string m.
N_m^f	Number of modules below the fault node in string m.
N_s	Number of series PV cells per module.
$PV_{n,m}$	PV module at the n-th row and m-th string.
R_c	Cable resistance.
R_p	PV module shunt resistance.
R_s	PV module series resistance.
R_x	Resistance per unit length of line/cable.
R_f	Fault resistance.
U_T	PV thermal voltage.
V_R	Voltage across C_R.
V_{SW}	Switch voltage.
V_c	DC link capacitor voltage.
V_d	Diode forward-bias voltage drop.
V_{mp}	PV module maximum power voltage.
$V_{n,m}$	Voltage across $PV_{n,m}$.
$V_{n,m}^L$	Voltage across an illuminated $PV_{n,m}$.
$V_{n,m}^S$	Voltage across a shaded $PV_{n,m}$.
V_{oc}	PV module open-circuit voltage.

V_{pv}	PV array voltage.
W_F	Time-domain window size.
Z_c	Line/cable's characteristic impedance.
$\Delta V_{n,m}$	Absolute change in $V_{n,m}$ magnitude from pre-disturbance V_{mp} to disturbance value.
Δt	Duration of a disturbance.
Ψ	Threshold for i_{hp}.
α	Attenuation constant for line/cable.
α_D	Attenuation due to dielectric loss.
α_G	Attenuation due to conductivity of dielectric loss.
α_R	Attenuation due to radiation loss.
α_S	Attenuation due to skin-effect loss.
α_{dp}	Damping factor.
β	Phase constant.
χ	Distance travelled by the TW from the fault to the measurement location.
δ_m^1	Difference of the normalized V_{pv} and $V_{1,m}$.
δ_m^2	Difference of the normalized V_{pv} and $V_{N,m}$.
ϵ_r	Relative dielectric constant.
γ	Propagation constant.
λ	Wind velocity power law equation constant.
μ	Conductor's permeability.
ω	Angular frequency.
ω_0	AC fundamental radian frequency.
ω_d	Damped radian frequency.
ω_n	Natural radian frequency.
σ	Conductor's conductivity.

τ	Time constant of i_{TW}.
ζ	Relay reach setting threshold.
ζ_a	Relay reach setting threshold.
c	Speed of light.
dbM	Daubechies mother wavelet of order M.
f	Frequency component of a TW.
$i_{TW,N}$	Normalized current TW.
i_{TW}	Current travelling wave.
i_{hp}	High-pass filtered i_{TW}.
i_i	Incident current travelling wave.
i_r	Reflected current travelling wave.
n	Ideality factor.
r_m^S	Ratio of N_m^S to N_m^L modules in string m.
t_1	Time at which a disturbance begins.
t_2	Time at which a disturbance voltage reaches steady-state value.
t_{g1}	Time at which shade starts covering a module.
t_{g2}	Time at which shade fully covers a module.
tf_i	Fault detection time of relay i.
v	Propagation velocity.
v_{TW}	Voltage travelling wave.
v_c	Cloud velocity.
$v_{w,meas}$	Measured wind velocity.
$\tan(\delta)$	Dielectric dissipation factor.

Chapter 1

Introduction

1.1 Description of the Problem

Today's aging power system infrastructure have led to several grid outages and blackouts throughout the last 30 years [1],[2]. Thus, the existing power system infrastructure requires major update in the near future [3],[4]. The high penetration of power electronics devices due to the changes of the generation and load nature, has lead to the increased popularity of DC grids. The utilization of DC rather than AC grids can result in significant reduction of power losses and cost savings. For instance, a PV-based DG can directly supply DC powered loads eliminating the DC/AC converter. According to [5], on the generation side, the elimination of DC/AC converters can result in a reduction of the converters' energy losses which typically range from 7% to 15%. Furthermore, on the load side, a large number of AC/DC adapters are utilized, each with transformers that introduce considerable losses during stand-by mode. According to the International Energy Agency (IEA), the total domestic consumption of electronic equipment in stand-by mode has been estimated to be more than 36 TWh/year [6]. DC grids at the distribution level will eliminate of large number of 230V AC/DC adapters, leading to significant reduction in losses and cost savings [6]. However, regardless of all the aforementioned benefits and due to the predominant existence of AC generation, loads, transmission, and distribution networks, it is highly likely that future grid will feature hybrid AC/DC networks, at all levels. The illustration

of new power grids in Figure 1.1 shows that the grid has four interconnected DC systems, one at each power level.

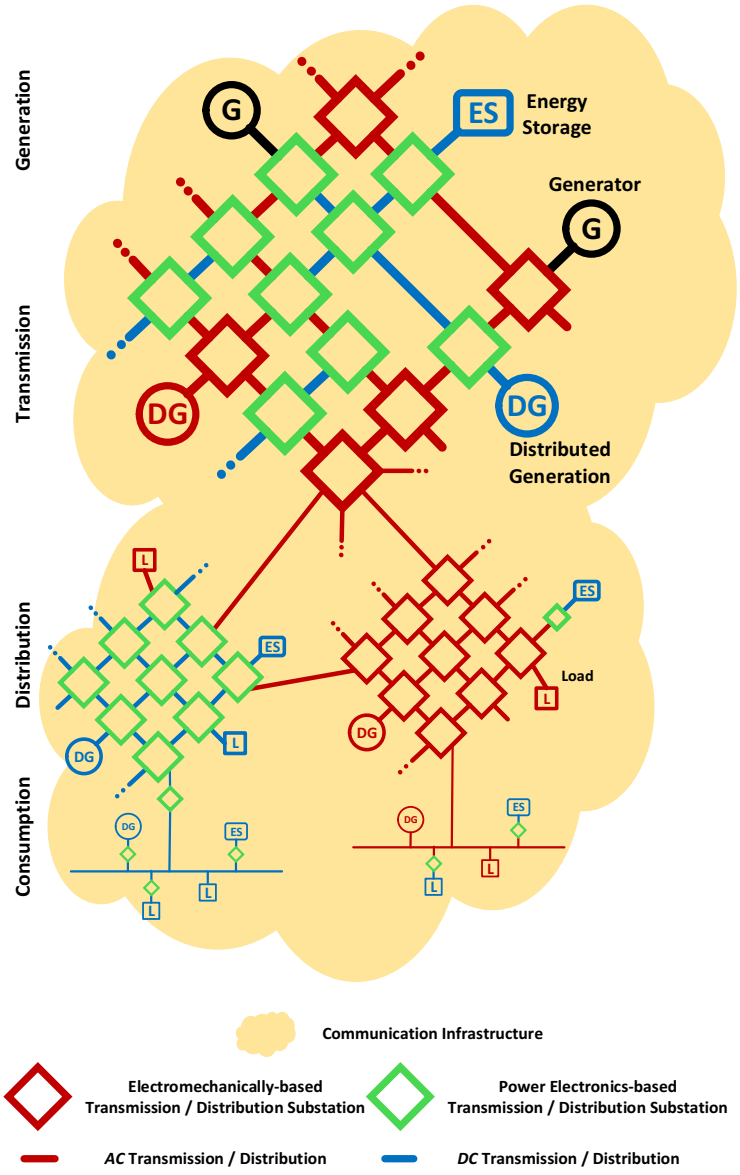

Figure 1.1: Illustration of new power grids.

On the generation level, solar PV-based DG has become the most popular DC DG.

According to the International Renewable Energy Agency (IRENA), the global PV capacity soared from 40 GW in 2010 to 219 GW in 2015, when it accounted for approximately 20% of all newly installed power generation capacity. Moreover, solar PV will account for as much as 7% of global power generation by 2030—a sixfold increase from today [7]. A utility-scale PV array typically consists of a large number of modules that occupy a huge surface area, which makes it a full-scale DC system. Depending on the size of the PV arrays, they are connected to larger DC systems on the consumption, distribution, and transmission levels using DC/DC converters.

On the consumption level, the existing LVDC networks are fairly small and their respective applications are limited [8]. For instance, such DC systems are utilized in power plants and substations for auxiliary installations. Additionally, applications including electric traction systems, aircraft power systems, and electric ships employ LVDC networks due to the wide usage of DC motors and the enhanced controllability of DC [8], [9]. Lately, LVDC microgrids have been utilized for powering different sized data centers as they are considered to include energy-saving technologies [5]. Recently, a study conducted by the Electric Power Research Institute (EPRI) revealed that the usage of 380V LVDC microgrids to supply small and medium sized data centers will result in up to 15% improvement in the electrical efficiency and 36% lower lifetime cost [10]. Furthermore, ABB has announced that 10% reduction in capital costs with respect to an AC network was achieved for the 1MW 380V DC network that is built in 2012 to supply a medium sized data centre [10]. LVDC microgrids can be islanded or interconnected to larger DC systems on the distribution level using DC/DC converters.

On the distribution level, MVDC microgrids have been used in electric ships such as the U.S Navy, and mine sites [11]–[13]. Such DC systems feature a multi-terminal architecture, which offers an improved reliability, downsized capacity, ease of maintenance, and power exchange and trading [14]. Moreover, as shown in Figure 1.1, MVDC microgrids can be part of a hybrid AC/DC microgrid configuration with an interlinking converter. Similar to LVDC, MVDC microgrids can be islanded or interconnected to smaller and larger DC systems.

On the transmission level, DC has been utilized as a cost-effective solution for delivering power over long distances with better power flow controllability through HVDC

transmission system. The mature HVDC technology is the thyristor-based converter stations type, the so-called Line Commutated Converter (LCC). LCC-based HVDC is rated upto 8000MW. This is currently the dominating technology that is utilized as a point to point link between two AC systems. Nevertheless, two exceptions exist where HVDC system has more than two points of connection and is commonly referred to as HVDC grids. The first one is the Sardinia-Corsica-Italy (SACOI) interconnection [15], while the second one is the Hydro-Quebec-New England interconnection [16]. Both projects started as point-to-point and then were extended to multi-terminal schemes with unidirectional power flow, and hence not truly meshed networks. Moreover, LCC-based HVDC faces many limitations, including voltage instability, large voltage flicker, harmonic instability, in addition to the large footprint of its converter stations [14]. Alternatively, the emerging Voltage-Sourced Converter (VSC)-based HVDC technology offers significant advantages over its LCC counterpart at a lower power rating (reaching up to 1000MW). These include but are not limited to, low cost and footprint for converter stations, use of lighter and stronger cables, and reliable operation. Besides, VSC-based HVDC technology allows bidirectional flow of power without altering the DC voltage polarity, which makes it suitable for the development of meshed DC grid. Such features make VSC-based HVDC attractive for offshore transmission [14]. The rated capacity of VSC-based HVDC is limited by the available individual switches (i.e., Insulated Gate Bipolar Transistor (IGBT)) voltage and current ratings (up to 5 kV, 2 kA), as well as the subsea polymeric cables voltage ratings that can reach up to 320 kV [14]. In 2013, a 500MW VSC-based HVDC link has been commissioned between Ireland and Wales [17]. Besides, two VSC-based HVDC corridors each rated at 1000 MW between France and Spain have been commissioned in 2014 under the INELFE project [14]. These are just a few examples of the existing VSC-based HVDCs. On the other hand, China has developed a five-terminal HVDC grid in 2015 [18]. The total HVDC installed capacity worldwide is over 100 GWs with an additional 200 GWs being planned in China [14]. HVDC is interconnected to smaller DC systems as shown in Figure 1.1.

DC faults pose a major challenge for the aforementioned DC systems as these faults can remain undetected, cause severe damage to the systems' equipment, or result in a huge loss of infeed. Accordingly, the catastrophic failures and permanent power losses caused

by DC faults have made protection of DC systems an avenue of research over the last few years. The following describes the protection challenges faced by each DC system.

1.1.1 Protection of Utility-Scale PV Arrays

PV arrays are prone to numerous failures such as arc, Open-Circuit (OC), String-to-Ground (SG), and String-to-String (SS) faults. Some of these failures cause problems such as fire hazards, others may cause either permanent or temporary power loss [19].

The existing fuse and residual current detector-based PV array protection methods either lack the required sensitivity for different fault conditions, or can be affected by the leakage current of a PV array [20]–[24]. Faults can remain undetected by the existing schemes under various conditions, such as low-irradiance, high-resistance fault, or small fault location mismatch [24], [25]. In addition to the permanent power loss introduced by an undetected faults, any subsequent fault can result in high fault current magnitude that causes severe damage to the PV array [21], [26]. Moreover, the existing methods trip the whole PV array during SG faults, and thus are not selective for the majority of PV arrays due to their central inverter topology.

Energy yield and power loss model-based detection [27], statistical analysis [28], pattern recognition [29], and heuristic supervised [30] and semi-supervised [31] machine learning methods have been proposed. However, most methods either require training a classifier, which makes the method system-dependent, or result in accuracy levels that depend on the quality of gathered meteorological data and PV model precision. Yet, the above methods' main shortcoming is their sensitivity to partial shading [28], [32]. Although partial shading conditions cause power losses, they do not result in any damage, provided that bypass diodes are installed, and are cleared while the PV array is online [19]. Hence, the PV array should not be tripped under partial shading to avoid unnecessary outage time. In [33], a probabilistic method that differentiates between faults and partial shading conditions based on the PV operating voltage and ambient temperature is proposed for small scale one-string PV systems. Yet, the method is not capable of distinguishing between faults and partial shading conditions for large scale PV systems with more than one string and fails

in scenarios where both faults and partial shading conditions result in the same operating voltage.

Fault location is another challenge for PV protection, because most existing techniques use thermal or infrared imaging [34], which is manual and time consuming. An artificial intelligence based approach has also been proposed [35], which performs better for the system used in the training stage.

1.1.2 Protection of LVDC Microgrids

DC faults on LVDC microgrids occur on the systems' poles. Faults are either Pole-to-Pole (PP) or Pole-to-Ground (PG). PP faults are uncommon but possible if poles are laid side by side in the same trench [14]. PG faults can be either Positive-Pole-to-Ground (PPG) or Negative-Pole-to-Ground (NPG). PG faults are more frequent but less severe than PP faults. Both of these fault types can consist of up to three stages: two sequential natural response stages (capacitor discharge and diode freewheeling) and one forced response stage (grid injection) [36]. The occurrence of all or some of the stages depends on the converter station and cable parameters, as well as on the fault type, location, and resistance [8],[14],[36]–[38]. It is extensively reported that the signature of DC fault currents is their very high rate of change and magnitude with the peak usually attained within 2 ms [8],[14],[36]–[43].

Research conducted on LVDC microgrids suggests fault detection approaches that are based on the overcurrent/undervoltage [8], [43], rate of change in current/voltage [37], or differential [38], [41], [42]. However, the highest fault resistance considered in these studies is 0.5 Ω, and no study has been conducted to detect non-bolted faults in LVDC microgrids (for the voltage range 75V–1.5kV [8]).

1.1.3 Protection of MVDC Microgrids

As mentioned in Section 1.1.2, the signature of DC fault currents is their very high magnitude with the peak usually attained within a couple of milliseconds after the onset of a

fault. Such large currents can damage the IGBT switches of a VSC. Thus, the IGBTs are blocked quickly after the current grows above a threshold determined by the IGBTs' thermal inertia. When the IGBTs are blocked, the controllability over the VSC can potentially be lost [44]. As a result, if a selective protection system does not isolate the faulty section of the grid within the couple of milliseconds after the fault inception, the VSCs in the neighbourhood of the fault will be lost, and the integrity of the entire MVDC microgrid will be put in jeopardy. Therefore, a fast and selective protective relaying scheme is crucial to realize fault-resilient MVDC microgrids.

Conventional protection schemes that are based on overcurrent/undervoltage [8], [45], rate of change in current/voltage [37], or differential scheme [38], [46], either lack the required sensitivity for detecting high-resistance faults, or are vulnerable to communication delay and failure. Moreover, none of the above methods meet the speed requirement for an MVDC microgrid as their Operation Time (OT) can reach up to 5 ms [46]. In [47], a directional current-based protection scheme that detects faults in 100 μs is proposed. However, apart from this method's vulnerability to communication failures, the utilization of high-bandwidth fiber optic communication is not economically justifiable for microgrids.

1.1.4 Protection of Hybrid AC/DC Microgrids

In addition to the DC-side protection challenges mentioned in Section 1.1.3, fault signals on the AC-side can be radically different depending on the microgrid connection mode, i.e., grid-connected and islanded modes. In addition, AC faults signals are affected by the type of distributed generations (DGs) connected, i.e., synchronous-based and inverter-based DGs. Accordingly, conventional protection, such as the ones based on directional overcurrent relays often fail in detection, fault direction identification, and coordination [48]. Therefore, a sensitive and grid configuration independent protective relaying scheme is crucial to realize a fault-resilient AC-side.

During AC faults, the interlinking VSC limits the fault contribution from the DC-side, and hence DC-side equipment are not endangered by overcurrents. Moreover, during DC faults, fault contribution from the AC-side begins after the interlinking VSC's IGBTs are blocked, which can be avoided by the implementation of a fast and selective DC-side

protection scheme [14]. Accordingly, AC- and DC-side faults do not adversely affect the other side. Nevertheless, a unified protection scheme is necessary to address the challenges posed by the diverse fault properties of both sides and meet their respective protection requirements.

1.1.5 Protection of HVDC Grids

An HVDC grid's half-bridge Modular Multilevel Converter (MMC) is vulnerable to the very high fault current magnitude attained within a couple of milliseconds after the fault inception. Thus, the IGBTs are blocked quickly and the diodes act as an uncontrolled rectifier, which maintains the flow of the fault current to the DC line [49]. As in MVDC microgrids [Section 1.1.3], if a selective protection system does not isolate the faulty section of the grid within the couple of milliseconds after the onset of a fault, controllability over the MMCs in the neighbourhood of the fault will be lost, and the integrity of the entire DC grid will be put in jeopardy. Therefore, a fast and selective protective relaying scheme is crucial to realize fault-resilient DC grids.

In [50], a protection scheme based on tripping the AC side of all of the converters is proposed. Not only does de-energizing the entire DC grid cause a huge loss of infeed that might result in large excursions in the frequency of the surrounding AC systems, but also the slow action of the AC breakers can potentially damage MMCs and DC lines. Fault detection methods on the DC side using overcurrent/undervoltage and the rate of change in current/voltage have been proposed, but they lack the required sensitivity for detecting high-resistance faults [14]. The schemes that are based on the addition of line reactors to limit the DC fault current [51], or measure the rate of change of voltage [52], or analyze the inductor's transient voltage [49] have a negative impact on the stability of the DC grid [53], [54]. Communication-based schemes, such as current differential protection [55] and harmonic current protection [56], are vulnerable to communication delays and failures.

TW-based protection schemes satisfy the high-speed requirement by detecting and locating the faults close to the speed of light on both AC and HVDC transmission lines [57]–[64]. In [57], an approach based on the reflection properties of the voltage TW has been proposed. The sensitivity and selectivity of this approach is impacted by system and

fault conditions. Polarity comparison [58], discriminant function [59], and superimposed component trajectory [60] TW-based schemes can detect the direction of the fault, but require communication to determine the faulted zone. In [61], a differential TW-based scheme that operates based on the summation of the first arriving TW at both line terminals has been proposed. However, this scheme requires GPS time synchronization and is as well vulnerable to communication delays and failures. Distance protection based on the arrival times of the TWs also has been proposed for fault detection and location [62]–[64]. This scheme can be implemented using single- or two-terminal measurements. The single-terminal method utilizes the arrival times of the first two fault-initiated TWs. However, detection of the second TW can be difficult due to its attenuated magnitude, confusion with another TW reflection, and the very small time difference between the two successive TWs for close-in faults [65]. On the other hand, the two-terminal method utilizes only the arrival time of the first TW at each terminal, but it can suffer from communication delays and failures. Furthermore, both single- and two-terminal methods can be subject to inaccuracies in determining the exact arrival times of the TWs, which cause significant errors in fault location for long lines and also make these methods inapplicable to short distribution lines [64], [66].

1.2 Research Objectives

The scope of this dissertation is a multi-dimensional protective relating study. Figure 1.2, illustrates a flowchart of the dissertation scope. This dissertation investigates the aforementioned five DC systems under three main categories namely 1) DC generation, 2) DC grids, and 3) Hybrid Systems. For each system, either a time- or frequency-domain based scheme is proposed. Each scheme is developed based on voltage, current, or both signals.

As a protective relaying study, the outcome of this research work is intended to assist relay manufacturers in developing relays that operate successfully in the aforementioned five DC systems. On this basis, the dissertation has been driven by two main objectives:

1. Investigating the effect of the exclusive DC fault behaviour on each of the above-

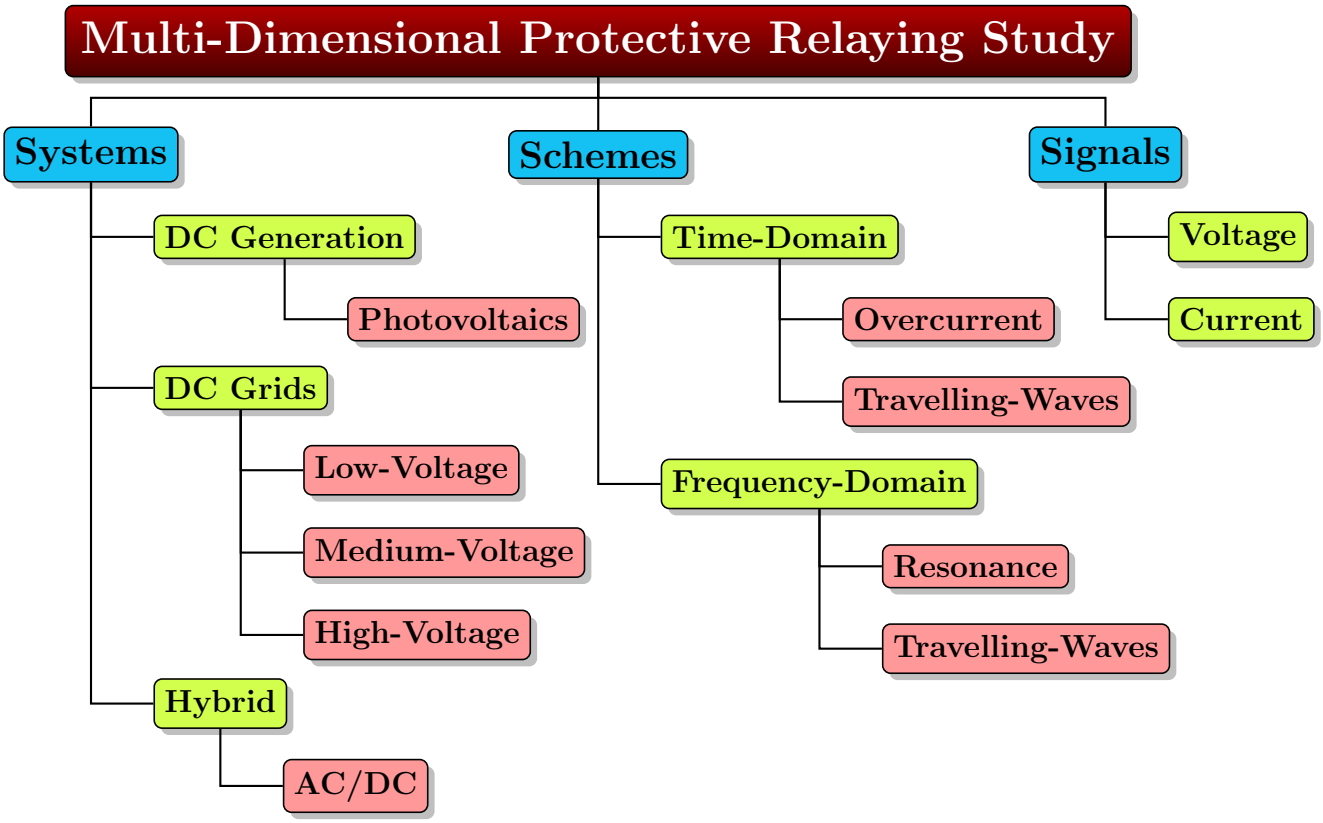

Figure 1.2: Illustration of the dissertation scope.

mentioned DC systems. The objective is to identify unique properties of fault signals that can be used to devise a new relaying algorithm. The analyses are founded upon time-domain simulation of detailed practical models of the five DC systems. In utility-scale PV arrays, the impacts of DC faults and partial shading conditions on the voltage signals are scrutinized. In LVDC microgrids, the effect of low- and high-resistance DC faults on the transient voltage and current magnitudes is examined. In MVDC microgrids, the waveshape and polarity of the DC fault-launched TWs are studied. Finally, in HVDC grids, the frequency spectra of the DC fault-launched TWs are inspected.

2. Designing an adequate protection scheme for each DC system with the following features:

- Speed: fulfill the speed requirement for the protection of DC systems by acting before the fault damages equipment or could no longer be interrupted by the circuit breakers.
- Selectivity: operate only under fault conditions and only isolate the faulted section. In PV arrays, the scheme should isolate only the faulted strings. In DC grids, the scheme should isolate only the faulted pole within the faulted line.
- Sensitivity: detect all DC faults including high-resistance faults.
- Reliability: be reliable by having a backup system in case of the failure of the primary protection system.
- Robustness: be able to discriminate between faults and other operations such as set-point changes.
- Communication-independence: operates entirely based on local measurements with no form communication between protective devices.
- Accuracy: identify the exact location of the fault within the faulted segment.
- Generality: be independent of the DC systems' models and configurations.

1.3 Dissertation Outline

This dissertation is divided into five main chapters, each concentrating on one of the five DC systems. The individual chapters are organized as follows.

Chapter 2 reveals the characteristics of PV module voltage within an array under normal, fault, and partial shading conditions. Identified properties, such as the magnitude and waveshape of voltage signals are used to propose a voltage-based protection scheme that detects, classifies, and locates SG, SS, and OC faults in utility-scale PV arrays. Some salient features of this method include its capability to distinguish between fault and partial shading conditions, and its independence from meteorological data.

Chapter 3 demonstrates that low- and high-resistance DC faults on LVDC microgrids results in very low fault currents, and thus conventional protection approaches fail to detect

such faults. A hybrid passive-overcurrent relay is proposed to overcome this problem. The proposed relay consists of one current and one voltage transducer as well as two passive elements; an inductor and a capacitor. For bolted and very low-resistance faults, the relay uses a simple overcurrent function to detect the resultant high fault current magnitudes within 2 ms. On the other hand, for relatively high-resistance faults, a real-time Discrete Wavelet Transform (DWT) is used to detect the voltage transients generated by the relay passive elements in less than 5 ms.

Chapter 4 begins by explaining the waveshape and polarity properties of the first locally measured TW after the inception of a fault. By utilizing these properties instead of the TWs' arrival time, a time-domain TW-based method to detect, classify, and locate different DC fault types in MVDC microgrids is proposed. Therefore, the proposed method is faster than the existing techniques, and also requires no form of communication. As a result, it can effectively operate as both primary and backup protection.

Chapter 5 proposes a unified discriminant function TW-based method to detect, classify, and locate different ac and DC fault types in hybrid AC/DC microgrids. The proposed method uses the waveshape and polarity properties of the first locally measured TW that are discussed in Chapter 4.

Chapter 6 shows how the frequency content of the first locally measured TW after the inception of a fault changes with respect to the location of the DC fault. A frequency-domain TW-based approach to detect, classify, and locate different DC fault types in HVDC grids is proposed. The method's applicability to different HVDC configurations and line types is also discussed.

Chapter 7 concludes the dissertation, highlights its contributions, and suggests topics for future research.

Chapter 2

Voltage-Based Protection Scheme for Utility-Scale PV Arrays

As mentioned in Chapter 1, permanent power loss and major catastrophic failures are among the potential consequences of undetected faults within PV arrays. This chapter proposes a voltage-based protection scheme that detects, classifies, and locates SG, SS, and OC faults in utility-scale PV arrays. The protection scheme operates based on the magnitude and wave-shape properties of voltage signals. Some salient features of this method include its capability to distinguish between fault and partial shading conditions, and its independence from meteorological data. The performance of the proposed approach is assessed on two utility-scale grounded PV arrays under various conditions. Moreover, the proposed method is tested on an experimental setup of a small grid-connected ungrounded PV array. Simulation and experimental results verify the scheme's accuracy, high speed, and scalability.

2.1 PV Array Model

Figure 2.1 displays the layout of a PV array with a central inverter topology simulated using PSCAD/EMTDC. This $N \times M$ array is composed of M parallel strings, each with N

identical series 235 W BP3 PV modules [67]. A 10×10, 23.5 kW, 300 V PV array is used as a testbed for this study. Another PV array testbed, with a different size, is studied in section 2.5.4. $PV_{n,m}$ denotes the PV module at the n-th row and m-th string. The main parameters of the PV module under the Standard Test Condition (STC) [1000 W/m^2 irradiance, 25^{o}C temperature, 1.5 air mass] are the open-circuit voltage V_{oc}=37.2 V, maximum power voltage V_{mp}= 29.8 V, short-circuit current I_{sc}= 8.48 A, and maximum power current I_{mp}= 7.89 A. The number of series cells per module is N_s=60. Each module has three bypass Schottky diodes (N_d=3) with 0.4 V voltage drop (V_d=0.4 V) [68]. The conductors are sized so that the voltage drop is within 2% under the STC [69]. The implemented Maximum Power Point Tracker (MPPT) uses the perturb and observe method [70].

The fault location in an array is described by:

1. Fault node: Denoted by $F_{n,m}$ in Figure 2.1. SS faults have two nodes, denoted as $F_{n',m'}$-$F_{n'',m''}$, where $F_{n',m'}$ designates the node with the higher pre-fault voltage.

2. Location mismatch: The percentage of PV modules either between $F_{n,m}$ and the ground for SG faults, or between $F_{n',m'}$ and $F_{n'',m''}$ for SS faults, with respect to the total number of string modules [24].

Figure 2.1 illustrates the three fault types investigated in this study. The following bolted faults are discussed throughout this chapter:

1. $Flt1$: SG fault at $F_{3,1}$ with 70% location mismatch.

2. $Flt2$: SG fault at $F_{9,1}$ with 10% location mismatch.

3. $Flt3$: SS fault at $F_{8,2}$-$F_{9,3}$ with 10% location mismatch.

4. $Flt4$: SS fault at $F_{1,2}$-$F_{2,3}$ with 10% location mismatch.

5. $Flt5$: SS fault at $F_{5,2}$-$F_{6,3}$ with 10% location mismatch.

6. $Flt6$: SS fault at $F_{4,2}$-$F_{8,3}$ with 40% location mismatch.

7. $Flt7$: OC fault at $F_{5,1}$.

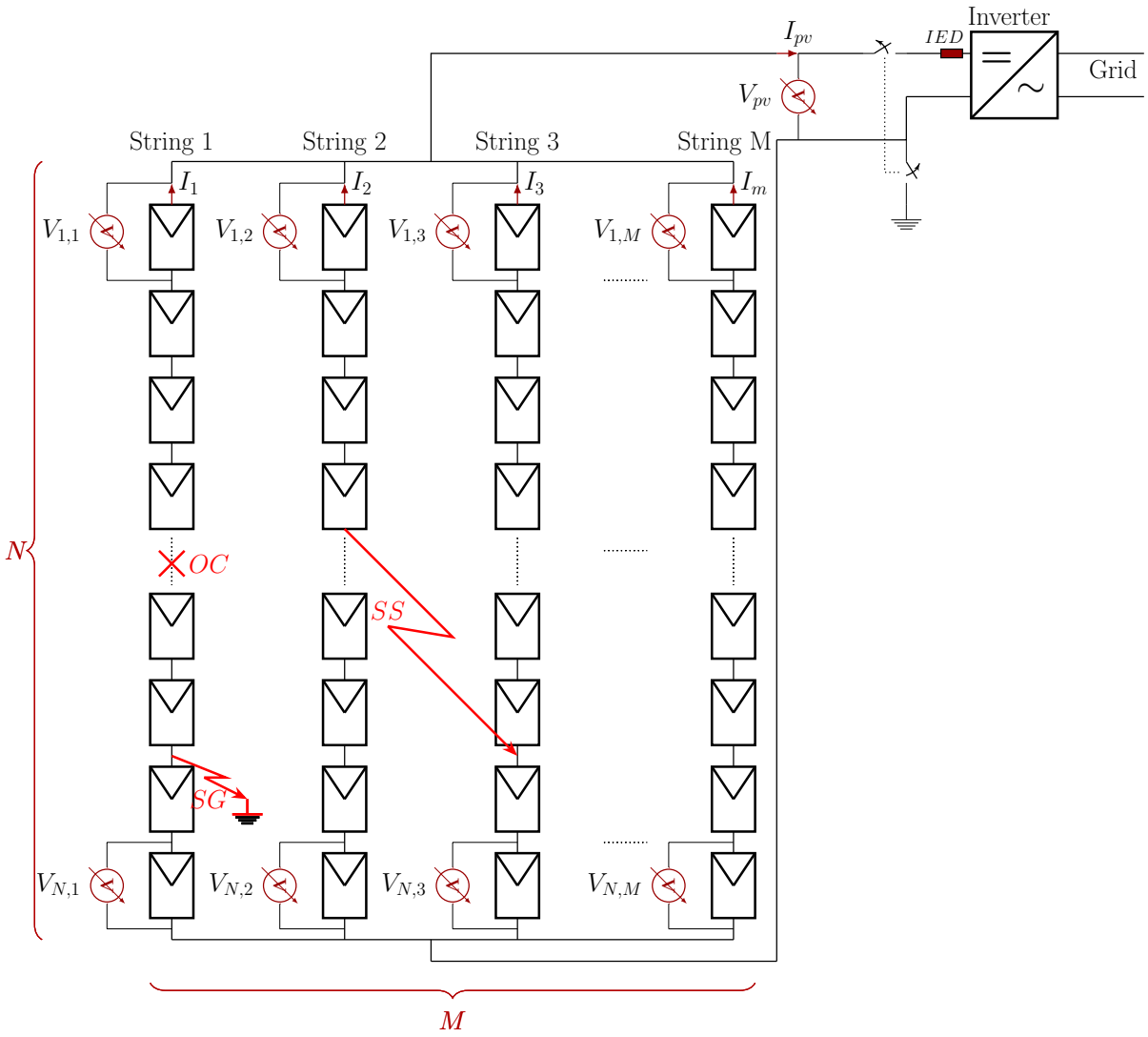

Figure 2.1: Layout of the PV array under study.

2.2 PV Array Voltages During Faults

This section presents the characteristics of PV module voltage within an array under normal, fault, and partial shading conditions. It is assumed, at this stage, that all of the PV modules in a string are subjected to the same irradiance level. Therefore, the total

voltage of a PV array, denoted by V_{pv} in Figure 2.1, is distributed uniformly among the modules of a string during fault-free conditions. As a result, V_{pv} can be expressed as the product of the voltage across the last PV module ($V_{n,m}$) and the number of modules in a string. This linear relation is shown by (2.1) for the arbitrary m-th string.

$$V_{pv} = V_{N,m}N \tag{2.1}$$

As an example, Figure 2.2a shows that V_{pv} is ten times larger than $V_{10,1}$ for the test array under the fault-free interval before t=50 ms. During a fault, however, the voltage is not uniformly distributed among the modules, and so (2.1) no longer holds true. For instance, the V_{pv} and $V_{10,m}$ curves in Figure 2.2a, 2.2b, and 2.2c after t=50 ms show that $Flt1$, $Flt6$ and $Flt7$ are all signified by a violation of (2.1). Meanwhile, (2.1) can also be violated when the modules of a PV string receive different levels of irradiance as in the case of partial shading. For instance, the voltages of (2.1) are shown in Figure 2.2d for a non-fault condition in which a moving cloud shades $PV_{10,1}$ after t=50 ms. While $V_{10,1}$ significantly drops, V_{pv} remains almost unaffected. In other words, violation of (2.1) indicates the presence of either a fault or a partial shading condition.

It is worth mentioning that MPPT does not affect the above-discussed features for the voltage because:

- The time taken by MPPT to change the PV voltage is significantly longer than the time span of faults. According to [70], the MPPT perturbs the PV voltage every 30 ms. Yet, the combined time frame of faults and the filter used by the proposed method does not exceed 10 ms.
- The adaptive voltage perturbation size applied by MPPT in every 30 ms ranges from 0.5% to 2% of the open circuit voltage of PV array [71], which is substantially smaller than the voltage changes during faults.
- A centralized MPPT perturbs the voltage of the entire array. Therefore, the effect of MPPT on the voltages of individual PV modules—which is later used by the proposed method—is negligible.

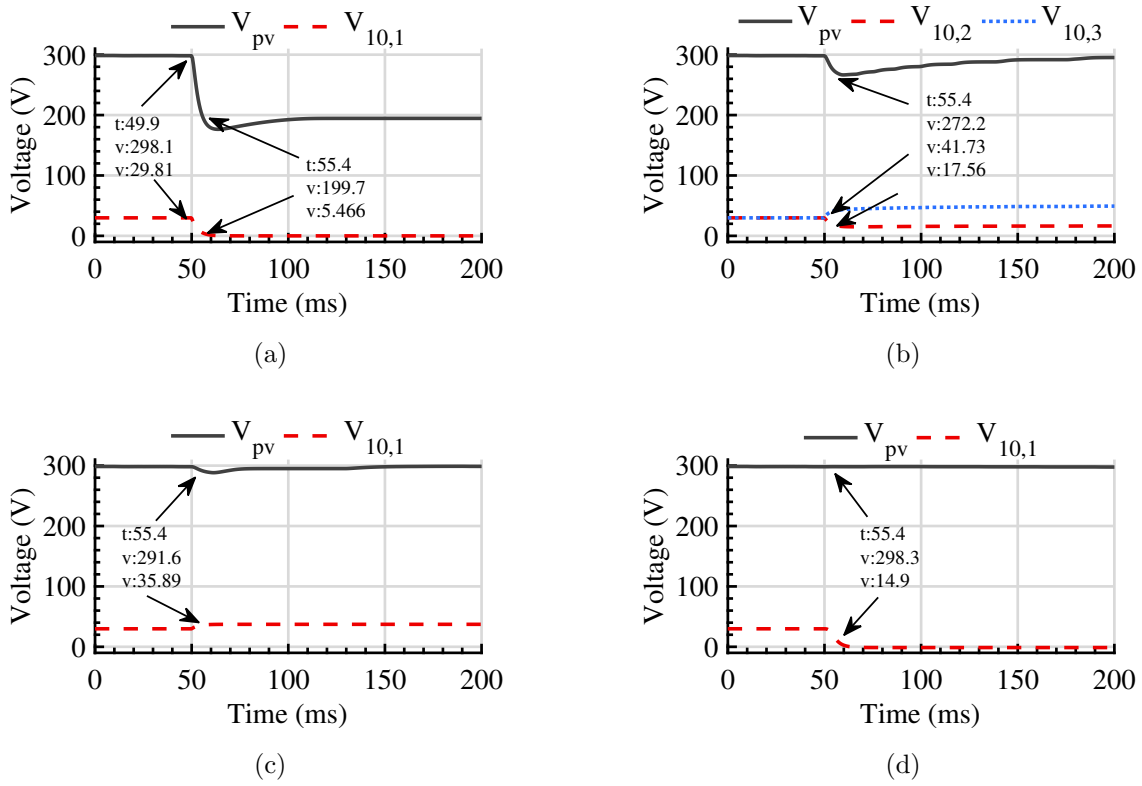

Figure 2.2: V_{pv} and $V_{10,m}$ (m=1, 2 and 3) under a) $Flt1$, b) $Flt6$, c) $Flt7$, and d) shading of $PV_{10,1}$.

The above issues can be discerned from Figure 2.2. For example, Figure 2.2b displays that the fault-induced drop of V_{pv} takes only 5.4 ms, but the recovery of V_{pv} by the MPPT takes about 150 ms. Moreover, the MPPT has negligible effect on the voltages of the faulted PV modules, $V_{10,2}$ and $V_{10,3}$, in strings 2 and 3, respectively.

To further support the above explanation, Figure 2.3 shows V_{pv}, $V_{1,1}$, and $V_{10,1}$ waveforms under $Flt2$ in the PV array with MPPT algorithm enabled and disabled. It can be seen that the MPPT algorithm has no effect on the exponential change in all of the voltage waveforms during the first 10 ms of the fault inception. After 10 ms, the MPPT starts recovering V_{pv}, yet it has negligible effect on the shape of $V_{1,1}$ and no effect on the shape of $V_{10,1}$. Therefore, the wave-shape features later used by the proposed method are

independent of the MPPT.

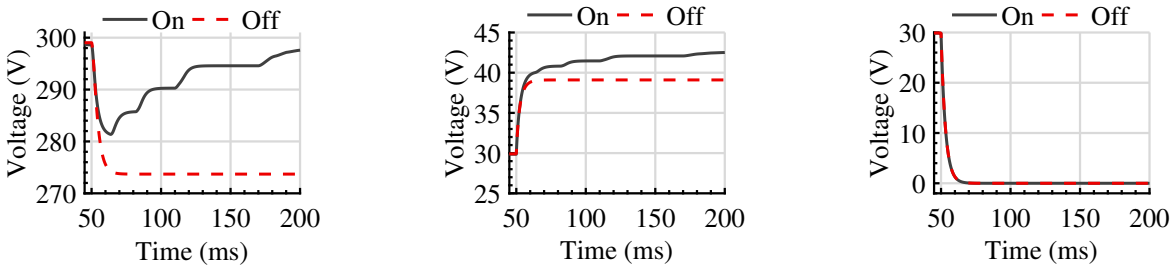

Figure 2.3: Voltage waveforms under *Flt*2 in the PV array with MPPT algorithm enabled and disabled: a) V_{pv} b) $V_{1,1}$, and c) $V_{10,1}$.

This section and the next section reveal some waveshape features of PV array voltages during fault and partial shading conditions. These features will later be used to discriminate between these two conditions.

2.2.1 SG Faults

As can be seen from Figure 2.4a, the occurrence of SG fault splits the faulted string into two regions: 1) the N_m^f modules below the fault node, and 2) the $N-N_m^f$ modules above the fault node. KVL for the fault loop indicates that the PV modules in the N_m^f region are operating at a voltage different from those in the $N-N_m^f$ region. Moreover, for any SG fault node within a string m, $PV_{1,m}$ is always in the $N-N_m^f$ region, whereas $PV_{N,m}$ is always in the N_m^f region. Thus, to capture the voltage response of the PV modules in each region under any fault location, two transducers per string are used to measure the voltages across $PV_{1,m}$ ($V_{1,m}$) and $PV_{N,m}$ ($V_{N,m}$) as shown in Figure 2.1. Consequently, based on KVL for the fault loop, V_{pv} during an SG fault can be expressed as:

$$V_{pv} = V_{1,m}(N - N_m^f) + V_{N,m}N_m^f \tag{2.2}$$

Figure 2.5 shows that (2.2) holds true under SG faults for different fault locations and fault resistances, R_f. For instance, Figure 2.5a–1 shows V_{pv}= 184.6 V under bolted *Flt*1,

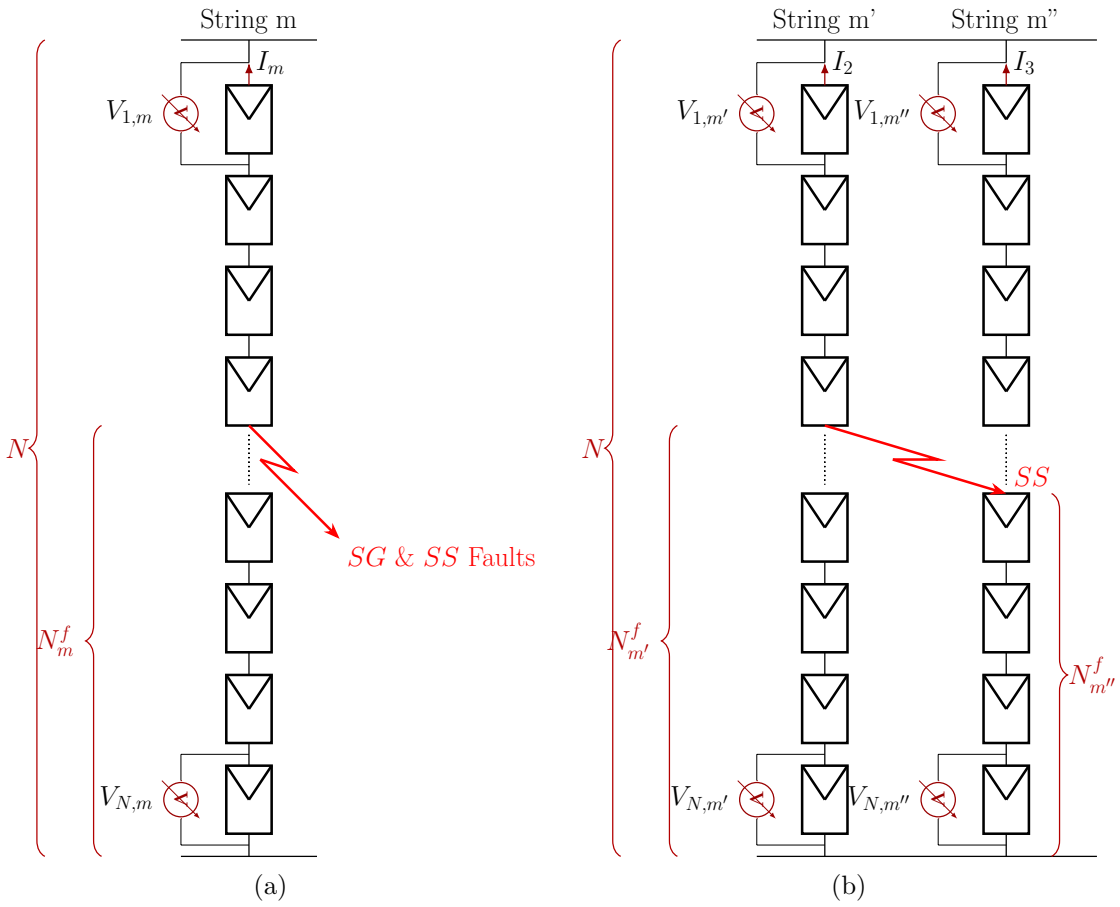

Figure 2.4: Illustrations of SG and SS faults a) intra-string and b) inter-string relationships.

which is equal to $V_{1,1}$=61.53 V times $N - N_1^f$=3 plus $V_{10,1}$=0 V times N_1^f=7, as shown in Figure 2.5a–2. Figure 2.5 also indicates that $V_{N,m}$ reduces during an SG fault. The exact reduced value can be obtained through KVL and is given by (2.3).

$$V_{N,m} = \frac{I_f R_f}{N_m^f} \tag{2.3}$$

where I_f is the fault current passing through R_f. For (2.2) to be satisfied, $V_{1,m}$ undergoes a corresponding increase with respect to the pre-fault value V_{mp}.

The absolute change in $V_{n,m}$ magnitude from pre-fault V_{mp} to the value during SG faults

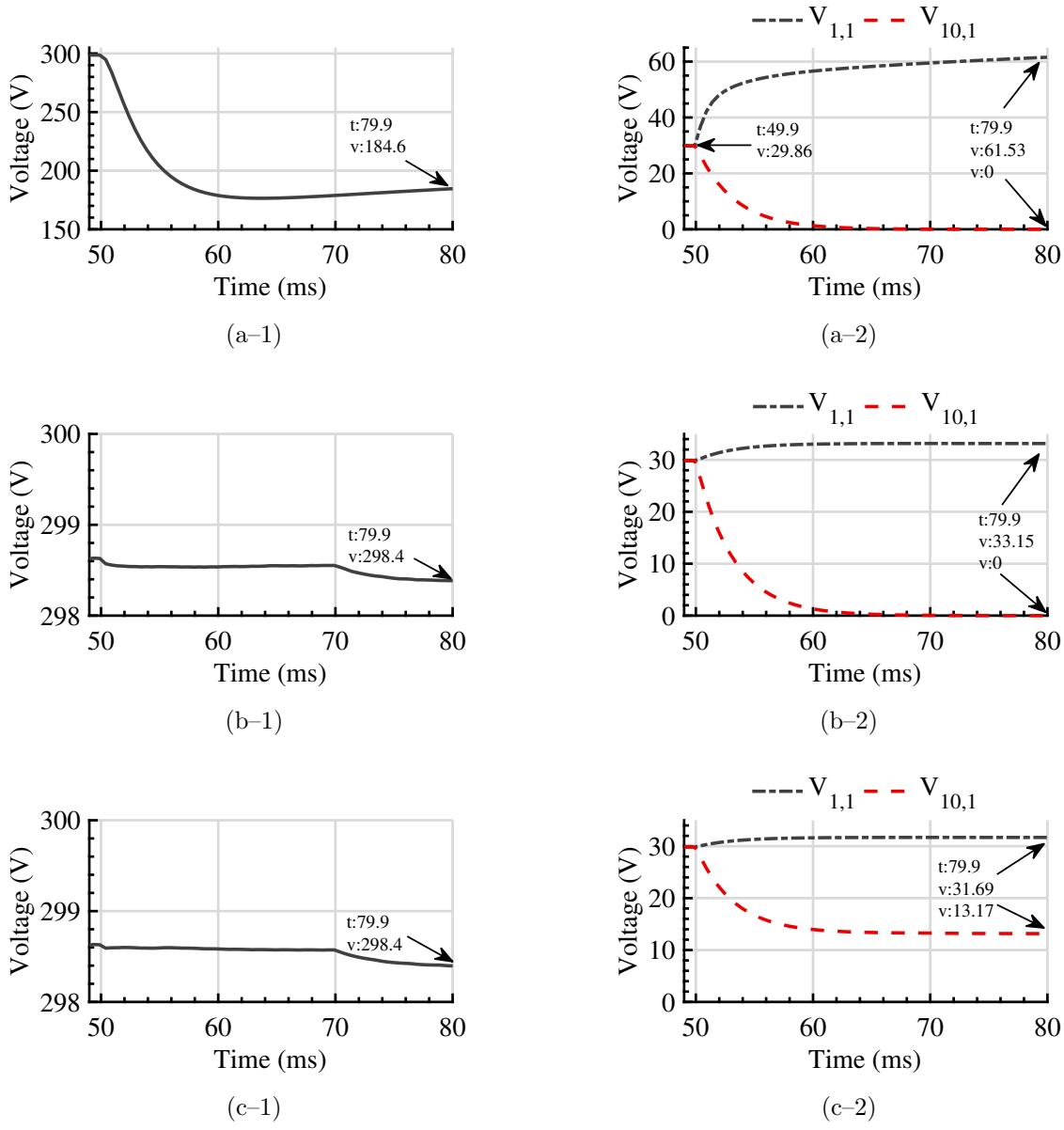

Figure 2.5: V_{pv}, $V_{1,1}$, and $V_{10,1}$ under a) bolted $Flt1$, b) bolted $Flt2$, and c) $Flt2$ with R_f=10 Ω.

is denoted by $\Delta V_{n,m}$. $\Delta V_{1,m}$ and $\Delta V_{N,m}$ depend on the location mismatch and the fault resistance. The higher the location mismatch is, the larger $\Delta V_{1,m}$ and $\Delta V_{N,m}$ become. For example, $\Delta V_{1,1}$ of the bolted $Flt1$ and $Flt2$—with 70% and 10% location mismatches—is 31.67 V and 3.29 V in Figures 2.5a–2 and 2.5b–2, respectively. Yet, $\Delta V_{10,1}$ for both faults is 29.86 V because R_f=0 Ω resulting in $V_{10,1}$=0 V (refer to (2.3)). In addition, for the same location mismatch, the higher R_f is, the smaller $\Delta V_{1,m}$ and $\Delta V_{N,m}$ become. For example, $\Delta V_{1,1}$ and $\Delta V_{10,1}$ of $Flt2$ with R_f=10 Ω are 1.83 V and 16.69 V in Figure 2.5c–2, respectively, which are much lower values than those attained under bolted $Flt2$ in Figure 2.5b–2.

Figure 2.5 also shows that $V_{1,1}$ and $V_{10,1}$ waveshapes change in an exponential fashion during Δt. In this chapter, Δt is the disturbance transient period, which is the interval between the beginning of a disturbance at t_1 and the time after which the voltage reaches steady-state value at t_2. The obtained exponential curves are consistent with the fact that a PV cell's dynamic model consists of a small leakage capacitor (C_p) in parallel with the shunt resistor (R_p). Thus, an SG fault results in a first order natural transient response [72]. Yet, if the PV dynamic model is not considered, an SG fault results in a step change in the voltage, which causes an exponential shape for the change in voltage after applying a first-order low-pass filter. Therefore, $V_{1,m}$ and $V_{N,m}$ waveforms during Δt are exponential.

2.2.2 SS Faults

Like SG faults, SS faults split each of the two faulted strings into two linear regions (Figure 2.4a). Thus, Figure 2.6 shows that (2.2) holds true for each of the faulted strings under SS faults at various fault locations and with different fault resistances. In addition, an inter-string relationship between the faulted strings exists as illustrated in Figure 2.4b. For a bolted SS fault, the voltages at $F_{n',m'}$ and $F_{n'',m''}$, denoted by $V_{n',m'}$ and $V_{n'',m''}$, are equal during the fault. Therefore, the inter-string relation between the voltages in the $N - N^f_{m'}$ and the $N - N^f_{m''}$ regions ($V_{1,m'}$ and $V_{1,m''}$) of the faulted strings m' and m'' is represented by (2.4). Similarly, the inter-string relationship between the voltages in the $N^f_{m'}$ and the

$N^f_{m''}$ regions ($V_{N,m'}$ and $V_{N,m''}$) is expressed in (2.5).

$$V_{1,m'}(N - N^f_{m'}) = V_{1,m''}(N - N^f_{m''}) \tag{2.4}$$

$$V_{N,m'}N^f_{m'} = V_{N,m''}N^f_{m''} \tag{2.5}$$

Since $V_{n',m'}$ exceeds $V_{n'',m''}$ before the fault (Section 2.1), $N^f_{m'}$ is larger than $N^f_{m''}$. Therefore, $V_{N,m'}$ is a fraction of $V_{N,m''}$ during the fault. For (2.5) to hold, $V_{N,m'}$ undergoes a reduction, while $V_{N,m''}$ experiences an increase. Similarly, for (2.4) to hold, $V_{1,m'}$ undergoes

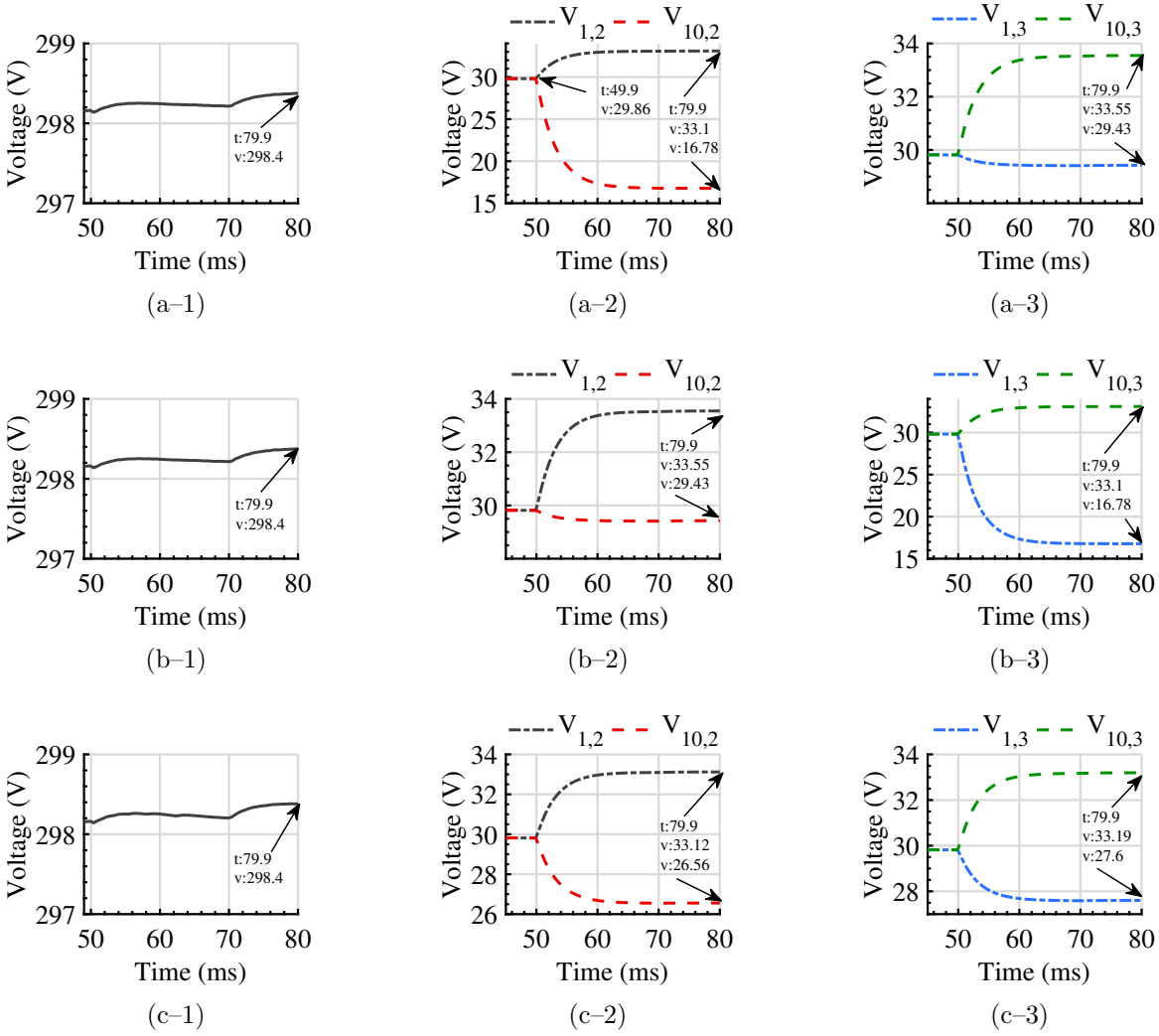

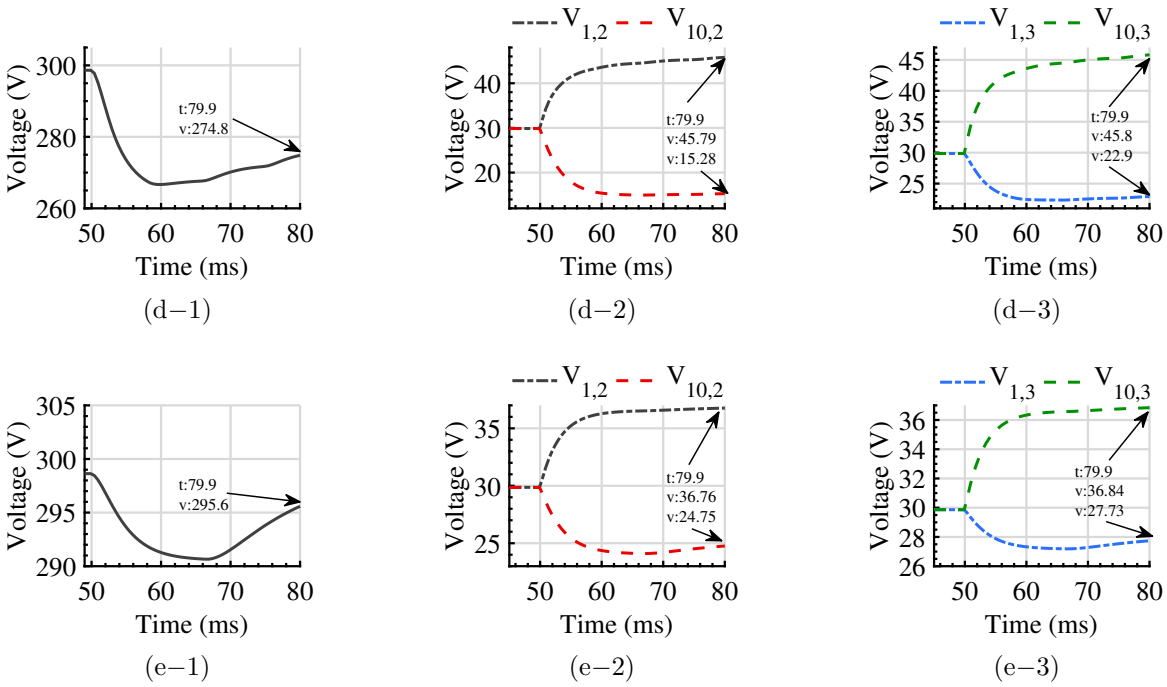

Figure 2.6: V_{pv}, $V_{1,m}$, and $V_{10,m}$ (m=1 and 2) under bolted a) $Flt3$, b) $Flt4$, c) $Flt5$, d) $Flt6$, and e) $Flt6$ with R_f=10 Ω.

an increase, while $V_{1,m''}$ experiences a reduction. Take, for instance, bolted $Flt6$ in Figure 2.6d with $N^f_{m'} = N^f_2 = 6$ and $N^f_{m''} = N^f_3 = 2$. $V_{10,2}$ reduces to 15.28 V (Figure 2.6d−2), which is one-third (i.e., $\frac{N_3}{N_2} = \frac{2}{6}$) of $V_{10,3}$=45.8 V (Figure 2.6d−3). Similarly, because $N - N^f_2 = 4$ and $N - N^f_3 = 8$, $V_{1,2}$ increases to 45.79 V (Figure 2.6d−2), which is twice (i.e., $\frac{N-N_3}{N-N_2} = \frac{8}{4}$) $V_{1,3}$=22.9 V (Figure 2.6d−3).

$\Delta V_{1,m'}$ and $\Delta V_{N,m'}$ as well as $\Delta V_{1,m''}$ and $\Delta V_{N,m''}$ depend on the fault location, location mismatch, and fault resistance. For the same location mismatch, fault locations closer to $PV_{N,m'}$ and $PV_{N,m''}$ result in higher $\frac{N^f_{m''}}{N^f_{m'}}$, and thus, have a more profound impact on $V_{N,m'}$ and $V_{N,m''}$. For example, $Flt3$ and $Flt4$ have the same 10% fault location mismatch, but $\frac{N^f_{m''}}{N^f_{m'}}$ is equal to 1/2 and 8/9, respectively. As a result, in contrast to the 13.08 V reduction of $V_{10,2}$ and 3.64 V increase of $V_{10,3}$ during $Flt3$ (Figures 2.6a–2 and 2.6a–3), $\Delta V_{10,2}$ and $\Delta V_{10,3}$ are only 0.43 V and 3.24 V for $Flt4$ (Figures 2.6b–2 and 2.6b–3). This smaller $\Delta V_{10,2}$

and $\Delta V_{10,3}$ arise from the longer distance between $Flt4$ and the bottom of the string where $V_{10,2}$ and $V_{10,3}$ are measured. Meanwhile, $Flt4$ makes a greater impact on the voltages in its vicinity, that is, the top of the string. Thus, $\Delta V_{1,2}$=3.69 V and $\Delta V_{1,3}$=13.08 V for $Flt4$ (Figures 2.6b–2 and 2.6b–3), which are significantly larger than the 0.43 V and 3.24 V variation of $V_{10,2}$ and $V_{10,3}$.

Accordingly, mid-string faults become the farthest faults from the measurement locations causing the lowest variation in the measured voltages, particularly if the location mismatch of the fault is small. An example of such fault is $Flt5$ in Figure 2.6c. For string 2, $\Delta V_{1,2}$ and $\Delta V_{10,2}$ are 3.26 V and 3.3 V, respectively. For string 3, $\Delta V_{1,3}$ and $\Delta V_{10,3}$ are 2.26 V and 3.33 V, respectively. These values are 10% plus variations with respect to the pre-fault voltage and so are readily detectable.

Moreover, the higher the location mismatch is, the larger the absolute change in all of the measured voltages becomes. For example, $\Delta V_{10,2}$ of faults $Flt3$ and $Flt6$—with 10% and 40% location mismatches—is 13.08 V and 14.58 V in Figures 2.6a–2 and 2.6d−2, respectively. In addition, with the same fault location and location mismatch, the higher the R_f is, the smaller the absolute change in all of the measured voltages becomes. For example, $\Delta V_{1,2}$ and $\Delta V_{10,2}$ of $Flt6$ with R_f=10 Ω are 6.9 V and 5.11 V in Figure 2.6e−2, respectively, lower than the values attained under bolted $Flt6$ in Figure 2.6d−2. A similar conclusion is drawn from the string 3 measurements under those two faults in Figures 2.6d−2 and 2.6e−2.

Finally, like SG fault, an SS fault loop includes R_p and C_p, resulting in a first-order natural transient response. Thus Figure 2.6 shows that for SS faults at various fault locations and with different fault resistances, $V_{1,2}$, $V_{10,2}$, $V_{1,3}$, and $V_{10,3}$ waveforms during Δt are exponential.

2.2.3 OC Faults

OC faults make the current in a faulted string equal to zero, causing all of the modules in this string to operate at V_{oc}. Figure 2.7 shows $V_{1,1}$ and $V_{10,1}$ under $Flt7$, which are equal to 37.22 V. Moreover, like other fault types, OC faults result in a first-order natural transient response, and thus $V_{1,1}$ and $V_{10,1}$ waveforms during Δt are exponential.

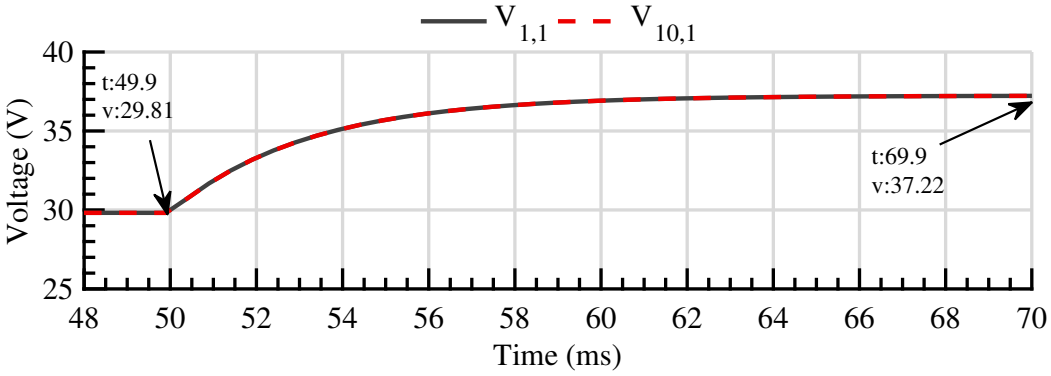

Figure 2.7: $V_{1,1}$ and $V_{10,1}$ under $Flt7$.

2.3 PV Array Voltages During Partial Shading

Partial shading divides the modules within a string to N_m^S shaded and N_m^L illuminated modules. Figure 2.8 shows the DC equivalent model of a module within a string during partial shading, which is analyzed to determine the effect of different partial shading conditions on the shaded and illuminated modules' voltages denoted by $V_{n,m}^S$ and $V_{n,m}^L$, respectively. Basically, the model of the module being shaded consists of a single diode (D_{pv}) connected in parallel with a photocurrent generated source I_{ph}^S, in addition to the parasitic parallel (R_p) and series (R_s) resistances. The module is equipped with an equivalent bypass diode (D_{bp}), which consists of N_d series diodes. The remaining illuminated PV modules in the partially shaded string are modelled by a constant current source producing, I_m^L, which can be expressed as a function of the voltage across an illuminated PV module [73]:

$$I_m^L = I_{ph} - I_0 \left[exp\left(\frac{\frac{V_{n,m}^L}{N_s} + I_m^L R_s}{nU_T} \right) - 1 \right] - \left[\frac{\frac{V_{n,m}^L}{N_s} + I_m^L R_s}{R_p} \right] \tag{2.6}$$

where I_{ph} is the photocurrent generated by an illuminated module receiving an unshaded irradiance, I_0 is the module saturation of dark current, U_T is the thermal voltage, and n is the ideality factor. Similarly, the current produced by the PV module being shaded (I_m^S)

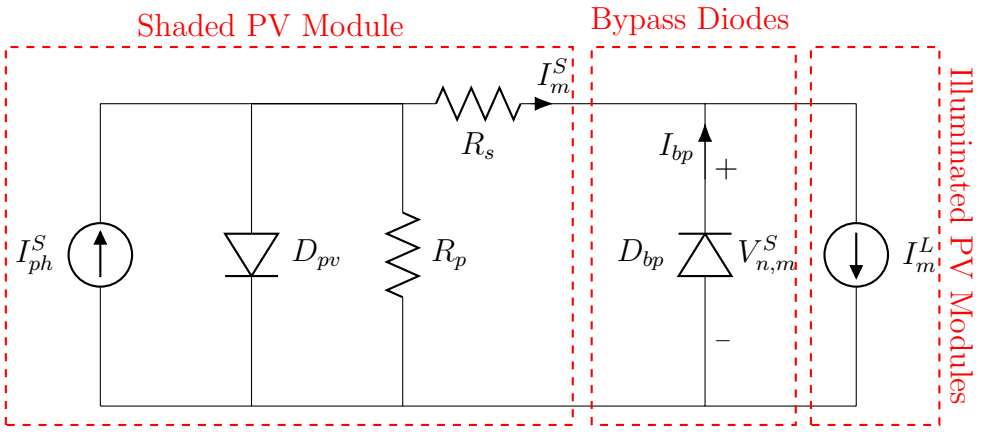

Figure 2.8: Equivalent model of a PV module during partial shading.

is given by:

$$I_m^S = I_{ph}^S - I_0 \left[exp\left(\frac{\frac{V_{n,m}^S}{N_s} + I_m^S R_s}{nU_T} \right) - 1 \right] - \left[\frac{\frac{V_{n,m}^S}{N_s} + I_m^S R_s}{R_p} \right] \tag{2.7}$$

I_{ph}^S is directly proportional to the irradiance seen by the module being shaded (G), as shown in (2.8) [73].

$$I_{ph}^S(t) = I_{sc} \frac{G(t)}{G^{ref}} \tag{2.8}$$

where G^{ref} is the irradiance level at the STC. G is a function of time, and its variation rate is proportional to cloud speed (v_c) [74]. Accordingly, as shade covers a PV module, G drops from the pre-shade irradiance (G^{pr}) at t_{g1} to the shade irradiance (G^S) received by that module at t_{g2} (2.9).

$$G(t) = \begin{cases} G^{pr} & t < t_{g1} \\ \frac{(G^S - G^{pr})v_c}{d} t & t_{g1} \leq t < t_{g2} \\ G^S & t \geq t_{g2} \end{cases} \tag{2.9}$$

where d is the PV module dimension covered by shade.

From Figure 2.8, the current through D_{bp} (I_{bp}) is expressed as:

$$I_{bp} = I_m^L - I_m^S = I_0 \left[exp\left(\frac{-V_{n,m}^S}{nU_T} \right) - 1 \right] \tag{2.10}$$

From (2.7) and (2.10), $V_{n,m}^S$ is given by:

$$V_{n,m}^S(t) = \overbrace{nU_T N_s \ln \left(\frac{I_{ph}^S(t) - I_m^S - \frac{\frac{V_{n,m}^S}{N_s} + I_m^S R_s}{R_p}}{I_0} + 1 \right)}^{Ln_1} \underbrace{-nU_T \ln \left(\frac{I_{bp}}{I_0} + 1 \right)}_{Ln_2} \tag{2.11}$$

$V_{n,m}^S$ in (2.11) consists of two logarithmic terms denoted as Ln_1 and Ln_2, respectively. By analyzing Figure 2.8, the response of $V_{n,m}^S$ during Δt is divided into the following stages:

1. **PV Forward-bias operation:** At the beginning of the shading, t_1, I_{ph}^S is greater than I_m^S, and I_m^S is equal to I_m^L [75]. Applying KCL at the nodes before and after R_s shows that D_{pv} is forward-biased and D_{bp} is reverse-biased. Thus, I_{bp} of (2.10) is zero, and Ln_2 is zero. As I_{ph}^S in (2.8) drops with the drop in G of (2.9), $V_{n,m}^S$, governed only by Ln_1, drops logarithmically from the pre-shade V_{mp} until the inflection point is reached.

2. **Inflection point:** At this point, I_{ph}^S reaches I_m^S, where I_m^S is still equal to I_m^L. Applying KCL at the nodes before and after R_s shows that both D_{pv} and D_{bp} are reverse-biased. Accordingly, at the inflection point $V_{n,m}^S$=0 V because both Ln_1 and Ln_2 are zeros.

3. **PV Reverse-bias operation:** From the previous stage, I_{ph}^S is equal to I_m^S, but I_{ph}^S can no longer match the string current I_m^L [75], and thus I_m^S is less than I_m^L. Accordingly, D_{pv} remains reverse-biased, whereas D_{bp} becomes forward-biased. Therefore, I_{bp} becomes equal to I_m^L. Governed only by Ln_2, $V_{n,m}^S$ drops further from 0 V until it saturates at the total voltage drop across the the bypass diodes, that is, $-N_d V_d$.

From the above analysis of (2.11), $V^S_{n,m}$ features a sigmoid-like "S" shaped curve during Δt. On the other hand, $V^L_{n,m}$ can be given by [75]:

$$V^L_{n,m}(t) = \frac{V_{pv}}{N^L_m} - V^S_{n,m}(t) r^S_m \tag{2.12}$$

where r^S_m is the ratio of N^S_m to N^L_m modules in string m. From (2.12), $V^L_{n,m}$ is a function of $V^S_{n,m}$, and accordingly features a sigmoid-like curve during Δt.

The steepness of the sigmoidal curve is governed by the coefficient I^S_{ph}(t) in Ln_1, which is ultimately affected by v_c, G^{pr}, and G^S of (2.9). Moreover, for partial shading scenarios with high r^S_m, $V^L_{n,m}$ increases in (2.12), causing a significant decrease of I^L_m in (2.6). Thus, I^S_{ph} remains greater than I^L_m, and consequently the shaded PV modules remain forward-biased throughout the shade period [75]. The logarithmic drop governed by Ln_1 saturates when G reaches G^S in (2.9), and thus $V^S_{n,m}$ in such cases features a sigmoidal response.

The following four shading scenarios are presented to verify the above analysis:

1. *Shd*1: $PV_{10,1}$ is fully shaded (i.e., G^S=0 W/m^2 and r^S_1=1/9) at the highest v_c=51.3 m/s [Appendix A] and the illuminated modules are operating at the STC (i.e., G^{pr}=1000 W/m^2).

2. *Shd*2: $PV_{10,1}$ is fully shaded at typical v_c=15 m/s [76] and the illuminated modules are operating at the STC.

3. *Shd*3: $PV_{7,1}$ to $PV_{10,1}$ are fully shaded (i.e., r^S_1=4/6) at v_c=51.3 m/s and the illuminated modules are operating at the STC.

4. *Shd*4: $PV_{10,1}$ is 50% shaded at v_c=51.3 m/s and the illuminated modules are operating at 500 W/m^2 (i.e., G^{pr}=500 W/m^2 and G^S=250 W/m^2).

In all the above scenarios, $V_{1,1}$ represents the voltage across an illuminated PV module, whereas $V_{10,1}$ represents the voltage across a shaded PV module. Furthermore, the cloud is considered to be moving from the left to the right of the layout shown in Figure 2.1. Thus, the shade is moving across the module width (w=1 m) [67]. The shading starts at t_1=50 ms. Figure 2.9 shows that the $V_{1,1}$ and $V_{10,1}$ waveforms during Δt under the four

shading scenarios are sigmoidal. Moreover, the steepness of the sigmoidal curve is affected by v_c, G^{pr}, and G^S, which is reflected on Δt. For instance, Δt of $V_{10,1}$ under high v_c in $Shd1$ is 23.9 ms (Figure 2.9a), which is smaller than the 38.4 s attained under lower v_c in $Shd2$ (Figure 2.9b). Similarly, the low G^{pr} and G^S in $Shd3$ causes Δt of $V_{10,1}$ to be 34.9 ms (Figure 2.9c), which is larger than the 23.9 ms obtained under high G^{pr} and G^S in $Shd1$. In addition, the high r_1^S in $Shd4$ results in smaller $\Delta V_{10,1}$=13.32 V (i.e., $PV_{10,1}$ remains forward-biased) and larger Δt=25.9 ms (Figure 2.9d) than the 31.02 V and 23.9 ms attained under low r_1^S in $Shd1$, respectively.

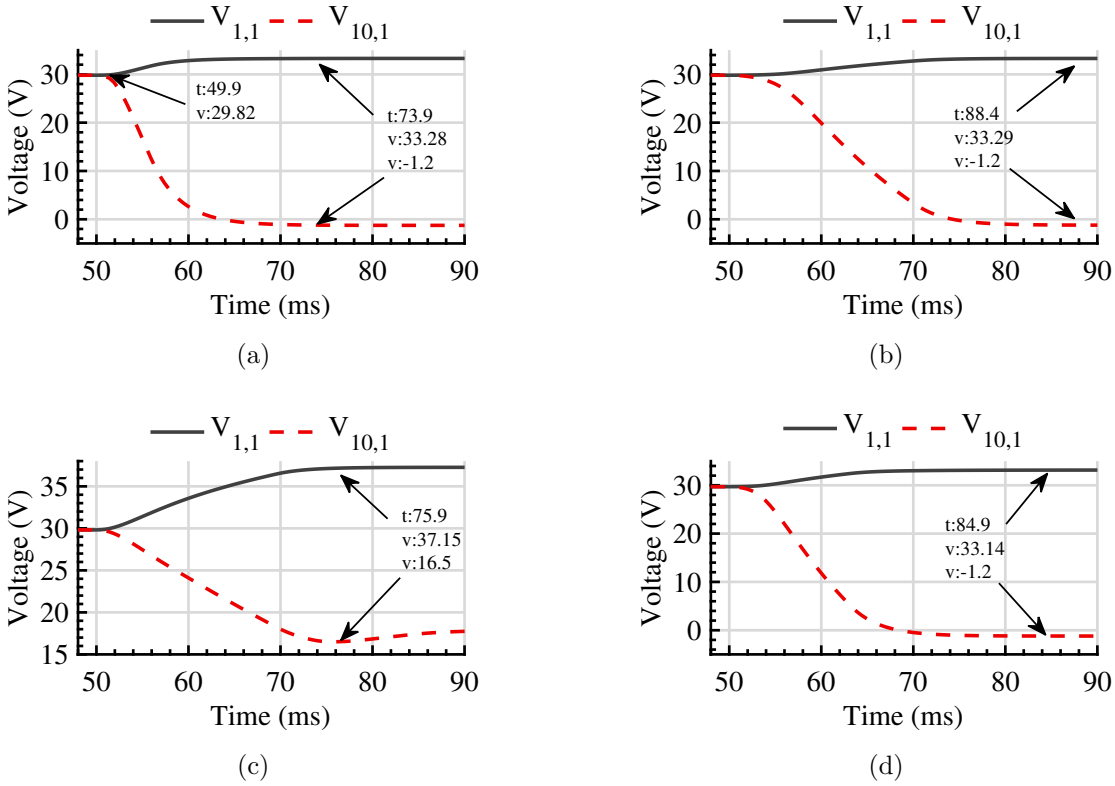

Figure 2.9: $V_{1,1}$ and $V_{10,1}$ under a) $Shd1$, b) $Shd2$, c) $Shd3$, and d) $Shd4$.

2.4 Proposed Protection Scheme

Two voltage transducers per string are used to measure the voltages across $PV_{1,m}$ and $PV_{N,m}$. Each module has a positive and a negative output terminal, and thus the voltage transducer is connected in parallel to these two external terminals. The voltage measurements are processed using an Intelligent Electronic Device (IED), which is located at the inverter (Figure 2.1). The acquired signals are first filtered using a first-order low-pass Butterworth filter to attenuate the noise. The output of this filter is sampled by the IED at 10 kHz. The proposed method consists of the following three stages.

2.4.1 Stage 1: Disturbance Detection

As shown in section 2.2, (2.1) can indicate the presence of a disturbance in a string. Therefore, the following two difference equations are defined based on (2.1).

$$\delta_m^1 = \left| \frac{V_{pv}}{N} - V_{1,m} \right| \tag{2.13}$$

$$\delta_m^2 = \left| \frac{V_{pv}}{N} - V_{N,m} \right| \tag{2.14}$$

During disturbance-free conditions, δ_m^1 and δ_m^2 are zero. However, upon a disturbance occurrence, δ_m^1 and δ_m^2 capture the deviation of $V_{1,m}$ and $V_{N,m}$ from the normal operating voltage at $\frac{V_{pv}}{N}$, respectively. A disturbance is detected at time t_1 in string m if δ_m^1 or δ_m^2 exceed a predefined threshold. The threshold is set to a value that takes into account the 2% maximum string voltage drop during normal operation [69], plus a security margin to account for measurement error. The maximum voltage drop across individual PV module in a string during normal operation becomes $\frac{2\%}{N}$. Moreover, in commercial protective devices, the measured error tolerance is often specified as ±5 percent of the measured value [77]. The threshold can be expressed as $\frac{V_{pv}}{N}\ \frac{2\%}{N}1.05$ V, where V_{pv} is set to the maximum power voltage. Accordingly, for this PV array, the threshold is set to 0.063 V.

2.4.2 Stage 2: Fault and Partial Shading Discrimination

A distinctive feature between faults and partial shading is the module voltage waveform. It was shown in Sections 2.2 and 2.3 that exponential voltage waveforms are observed during faults, whereas partial shading results in sigmoidal voltage waveforms. As indicated by (2.13) and (2.14), δ_m^1 and δ_m^2 waveforms are the absolute of the negative of $V_{1,m}$ and $V_{N,m}$, respectively. The second derivative is an effective tool to differentiate between exponential and sigmoidal waveforms. Therefore, the second derivative of δ_m^1 and δ_m^2, denoted by $D_t^2\delta_m^1$ and $D_t^2\delta_m^2$, is used to identify whether a disturbance is a fault or a partial shading. During faults, $D_t^2\delta_m^1$ and $D_t^2\delta_m^2$ have negative waveforms throughout Δt. On the contrary, during partial shading, $D_t^2\delta_m^1$ and $D_t^2\delta_m^2$ within Δt switch from a positive to a negative value, indicating the presence of the previously-discussed inflection point, which is a sigmoid curve signature. On this basis, if $D_t^2\delta_m^1$ and $D_t^2\delta_m^2$ are negative during Δt, the disturbance is a fault; otherwise, it is a partial shading condition.

As shown in Sections 2.2 and 2.3, Δt size is affected by the fault and the partial shading conditions, and is thus unpredictable. Meanwhile, the end of Δt, i.e., t_2, occurs, by definition, when δ_m^1 and δ_m^2 settle down and become constant. Therefore, the first derivatives of δ_m^1 and δ_m^2, denoted by $D_t\delta_m^1$ and $D_t\delta_m^2$, are used to determine t_2. t_2 for δ_m^1 and δ_m^2 is determined whenever $D_t\delta_m^1$ and $D_t\delta_m^2$ drop below a predefined threshold. The threshold is set to 0.01 V so as to accommodate a signal-to-noise ratio of 10 dB.

2.4.3 Stage 3: Fault Classification and Location

Upon a detection of fault at t_2 in stage 2, V_{pv}, $V_{1,m}$, and $V_{N,m}$ of the faulted strings are acquired to be analyzed for fault classification and location. Faults are classified by analyzing the way that $V_{1,m}$ and $V_{10,m}$ violate (2.1) and relating that violation to the properties of SG, SS, and OC faults mentioned in section 2.2.

Basically, if only one string is faulted and (2.15) and (2.16) are satisfied, the fault is an SG fault [section 2.2.1].

$$\frac{V_{pv}}{N} < V_{1,m} \tag{2.15}$$

$$\frac{V_{pv}}{N} > V_{N,m} \tag{2.16}$$

If only one string is faulted and (2.17) and (2.18) are satisfied, the fault is an OC fault [section 2.2.3].

$$\frac{V_{pv}}{N} < V_{1,m} \tag{2.17}$$

$$\frac{V_{pv}}{N} < V_{N,m} \tag{2.18}$$

If two strings are faulted and (2.19), (2.20), (2.21), and (2.22) are satisfied, the fault is an SS fault [section 2.2.2].

$$\frac{V_{pv}}{N} < V_{1,m'} \tag{2.19}$$

$$\frac{V_{pv}}{N} > V_{1,m''} \tag{2.20}$$

$$\frac{V_{pv}}{N} > V_{N,m'} \tag{2.21}$$

$$\frac{V_{pv}}{N} < V_{N,m''} \tag{2.22}$$

Finally, both SG and SS faults can be located by using (2.2) to solve for N_m^f on each of the faulted strings. Unlike SG and SS faults, an OC fault introduces to the string an additional voltage drop, which is across the fault. Hence, this method identifies the faulty string for OC faults, but is not able to determine its exact location within the string. Moreover, it is worth noting that if the method fails to capture the voltage waveforms, the disturbance can still be detected by applying stage 1 of the proposed method, however, stages 2 and 3 cannot be performed. Meanwhile, it is important to note that continuous measurement of voltage (i.e., not missing any part of the voltage waveform) is a reasonable and practically-valid assumption or fault protection purposes.

2.5 Performance Evaluation

2.5.1 Scheme Performance Under Sharp Irradiance Change

Figure 2.10 shows the irradiance level on 31/08/2015 in Eugene, Oregon with 1-min resolution [78]. The data represents the irradiance level on a typical sunny day and a 25 ^oC

constant temperature is assumed. Simulation duration is 60 seconds, starting at minute 648. The change in irradiance level during that period (i.e., from 844.9 to 160.6 W/m^2) represents the sharpest change during that day.

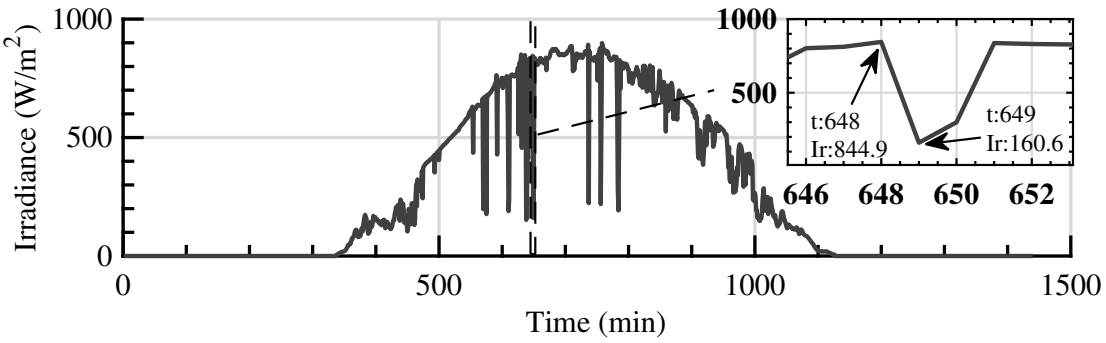

Figure 2.10: Irradiance level during 31/08/2015 in Eugene, Oregon [78].

Fault $Flt5$ occurs at 20 s after the beginning of the 648-th minute. Figure 2.11 presents a) V_{pv}, as well as $V_{1,m}$ and $V_{10,m}$ for three strings namely: b) string 1, representing the healthy strings, c) string 2, representing the faulted string at $F_{5,2}$, and d) string 3, representing the faulted string at $F_{6,3}$. Figure 2.12 shows the captured δ_m^1 and δ_m^2 along with their first and second derivatives for the three strings of interest.

For string 1, (2.1) is not violated as $V_{1,1}$=$V_{10,1}$=V_{pv}/N=30.35 V (Figure 2.11), the corresponding δ_m^1 and δ_m^2 do not exceed 0.063 V (Figure 2.12a–1). Therefore, string 1 is flagged as healthy. Similarly, all other healthy strings have the same response. On the contrary, strings 2 and 3 clearly violate (2.1). This violation is reflected on δ_m^1 and δ_m^2 of both strings as they exceed 0.063 V at t_1= 20 s (Figures 2.12b–1 and 2.12c–1). Therefore, there is a disturbance affecting strings 2 and 3. To determine whether the disturbance is a fault or a partial shading condition, $D_t^2\delta_m^1$ and $D_t^2\delta_m^2$ of both strings are computed within Δt. $D_t\delta_m^1$ and $D_t\delta_m^2$ of both strings drop below 0.01 V at t_2=20.015 s (Figures 2.12b–2 and 2.12c–2). Figures 2.12b–3 and 2.12c–3 show that $D_t^2\delta_m^1$ and $D_t^2\delta_m^2$ of both strings within the interval between t_1 and t_2 (i.e., Δt) are negative. Therefore, strings 2 and 3 are flagged as faulty after 15 ms of the fault occurrence. The above analysis shows that the proposed protection scheme is selective as it can trip only the faulted strings while the remaining healthy part of the PV array continues to operate seamlessly.

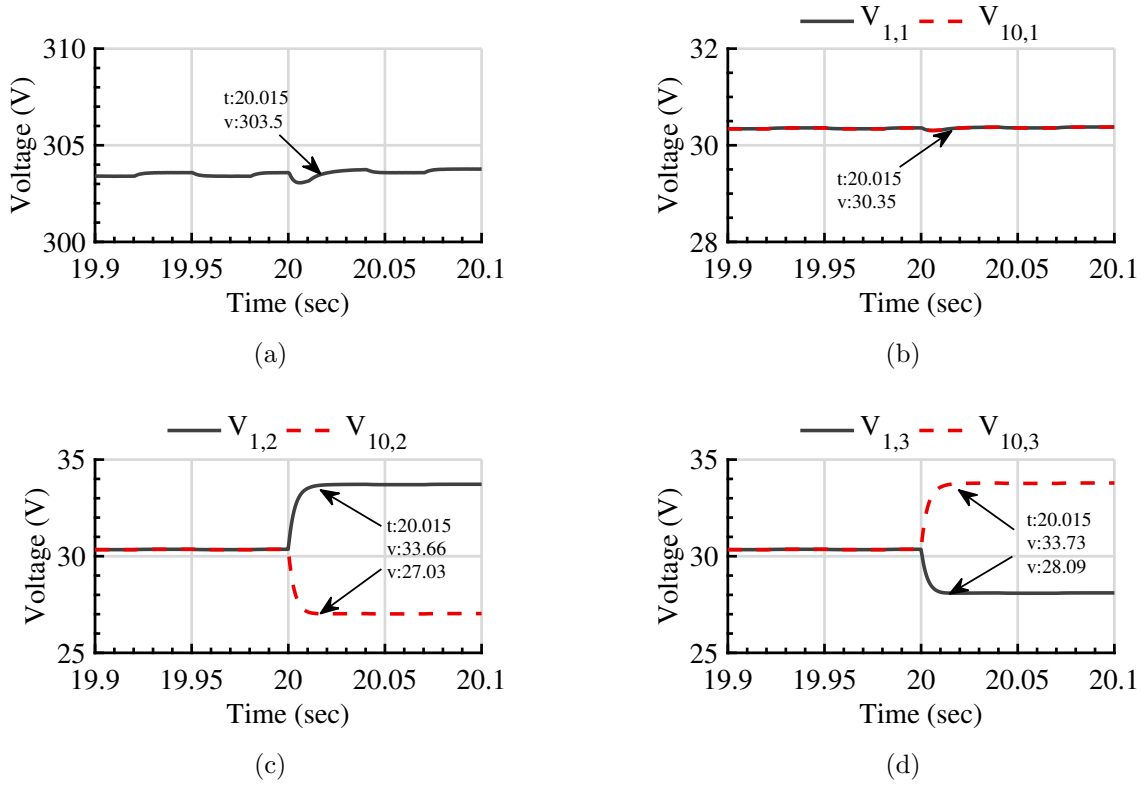

Figure 2.11: *Flt*5: a) V_{pv}, $V_{1,m}$ and $V_{10,m}$ for b) string 1, c) string 2, and d) string 3.

Since strings 2 and 3 are faulted and (2.19), (2.20), (2.21), and (2.22) are satisfied (Figures 2.11c and 2.11d), the fault is classified as an SS fault. By solving (2.2), the fault location represented by N_2^f and N_3^f is found to be 5 and 4 for string 2 and 3, respectively.

2.5.2 Scheme Performance Under Moving Clouds

A 2 m long cloud moving horizontally across the PV array from string 1 to 10, with v_c=51.3 m/s and casting shade on $PV_{9,m}$ and $PV_{10,m}$ is simulated. The shade cast by the cloud starts moving towards the PV array at 50 ms. The PV array is operating under the STC. Figure 2.13 shows that the irradiance seen by $PV_{9,m}$ and $PV_{10,m}$ in strings a) 1, b) 2, and c) 3 starts dropping sequentially at 50 ms, 69.4 ms, and 88.9 ms, respectively. As a

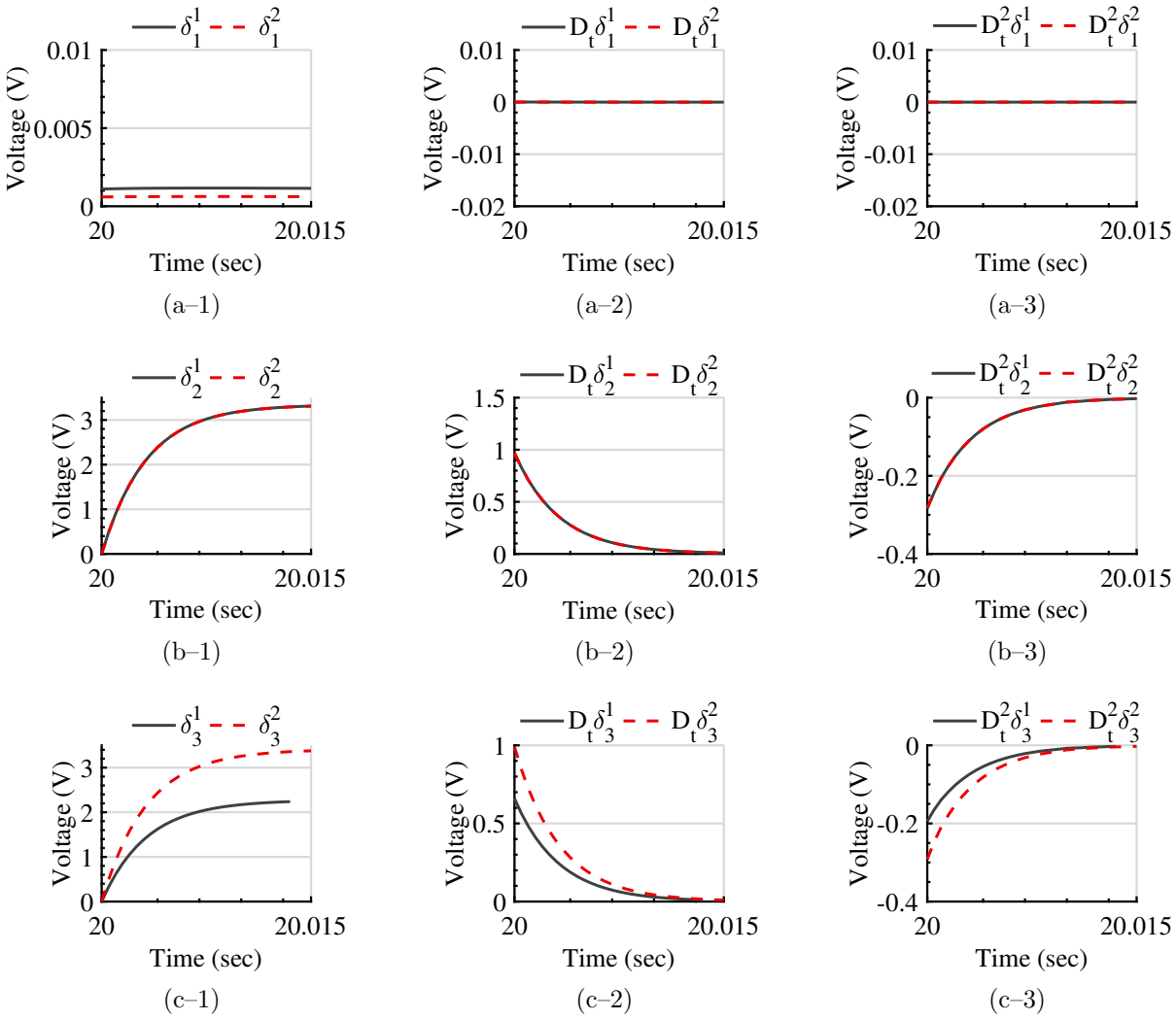

Figure 2.12: *Flt*5: δ_m^1 and δ_m^2 along with their first and second derivatives for a) string 1, b) string 2, and c) string 3.

consequence, Figure 2.14 shows that (2.1) is violated sequentially for the three mentioned strings. Correspondingly, the violation is captured by δ_m^1 and δ_m^2 of strings 1, 2, and 3 as they exceed 0.063 V at t_1, equal to 50 ms, 69.4 ms, and 88.9 ms, respectively (Figures 2.15a–1, 2.15b–1, and 2.15c–1). Therefore, there is a disturbance affecting all three strings, but at different times. $D_t\delta_m^1$ and $D_t\delta_m^2$ of strings 1, 2, and 3 drop below 0.01 V at t_2, equal

to 76 ms, 97 ms, and 125 ms, respectively (Figures 2.15a–2, 2.15b–2, and 2.15c–2). Figures 2.15a–3, 2.15b–3, and 2.15c–3 show that $D_t^2\delta_m^1$ and $D_t^2\delta_m^2$ of strings 1, 2, and 3 within their corresponding Δt switch from a positive to a negative value, indicating the presence of inflection points in the analyzed signals. Therefore, strings 1, 2, and 3 are flagged as partially shaded. Accordingly, no protective action is required.

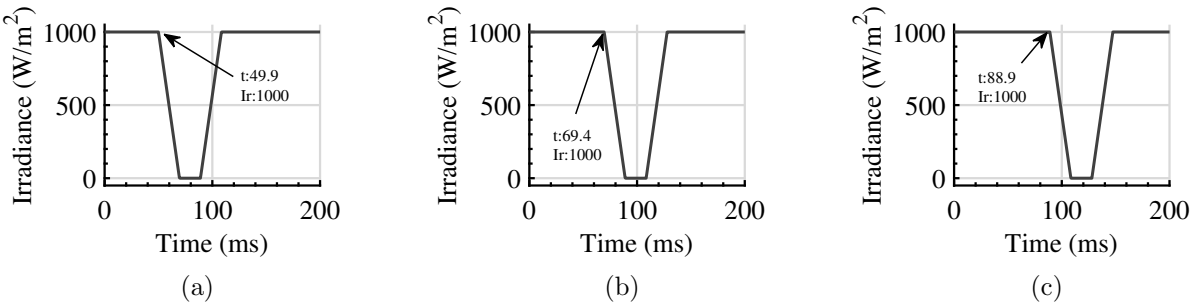

Figure 2.13: Irradiance seen by $PV_{9,m}$ and $PV_{10,m}$ in strings a) 1, b) 2, and c) 3.

To demonstrate the performance of the proposed method under dispersed shade patterns, three clouds moving horizontally across the PV array with v_c=51.3 m/s are simulated. The lengths of the shade casted due to clouds 1, 2, and 3 are 6 m, 3 m, and 2 m, respectively. Furthermore, clouds 1, 2, and 3 cast a shade on $PV_{10,m}$, $PV_{2-4,m}$, and $PV_{8-9,m}$ of each string, respectively. The shade casted by cloud 1, 2, and 3 starts moving towards the PV array at 50 ms, 250 ms and 650 ms, respectively. The PV array is operating under the STC. Figure 2.16 shows the irradiance seen by the modules that are affected by the three clouds. From Figures 2.17 and 2.18, it can be seen that (2.1) is violated sequentially more than once and at various occasions as the strings undergo partial shading. Correspondingly, the violation is captured by δ_m^1 and δ_m^2 of all ten strings when they exceed the 0.063 V threshold several times as the shades move in and out of each string (Figure 2.19). Accordingly, a disturbance is detected at different and several times on each of the ten strings. Figure 2.20 shows that $D_t^2\delta_m^1$ and $D_t^2\delta_m^2$ of all ten strings switch from a positive to a negative value whenever the strings experience the disturbance, indicating the presence of inflection points in the analyzed signals. Therefore, all ten strings are flagged as partially shaded.

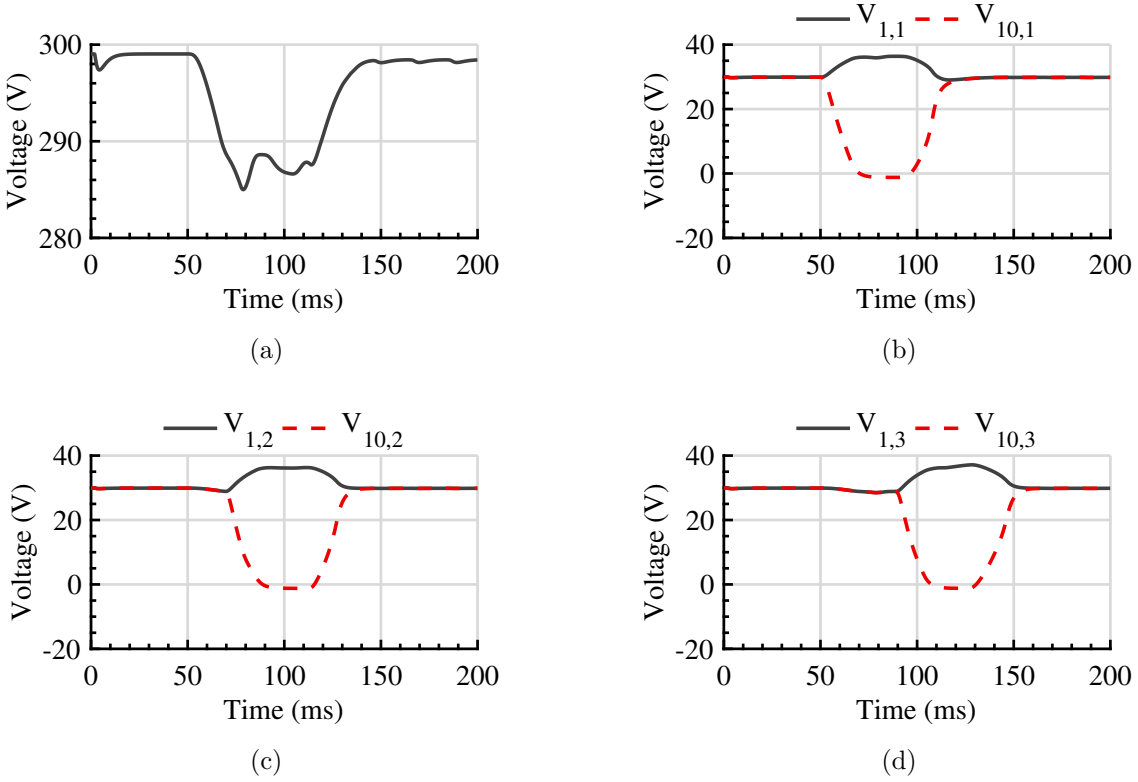

Figure 2.14: $PV_{9,m}$ and $PV_{10,m}$ shading: a) V_{pv}, $V_{1,m}$ and $V_{10,m}$ for b) string 1, c) string 2, and d) string 3.

Five additional partial shading case studies are simulated to assess the performance of the proposed method in differentiating between fault and partial shading conditions. Each case study takes into account different conditions that affect the shape of the voltage waveforms as explained in Section 2.3. These conditions include the number and location of the shaded modules, the pre-shade irradiance, the shading percentage, and the cloud speed and direction. Table 2.1 summarizes the partial shading conditions at which each case study is simulated along with the resulting positive and negative peaks of $D_t^2\delta_m^1$ and $D_t^2\delta_m^2$, and detection time. It can be seen that $D_t^2\delta_m^1$ and $D_t^2\delta_m^2$ for all cases switch from a positive to a negative value, indicating the presence of inflection points in δ_m^1 and δ_m^2. Therefore, string 1 in each case is flagged as partially shaded. Moreover, it can be seen

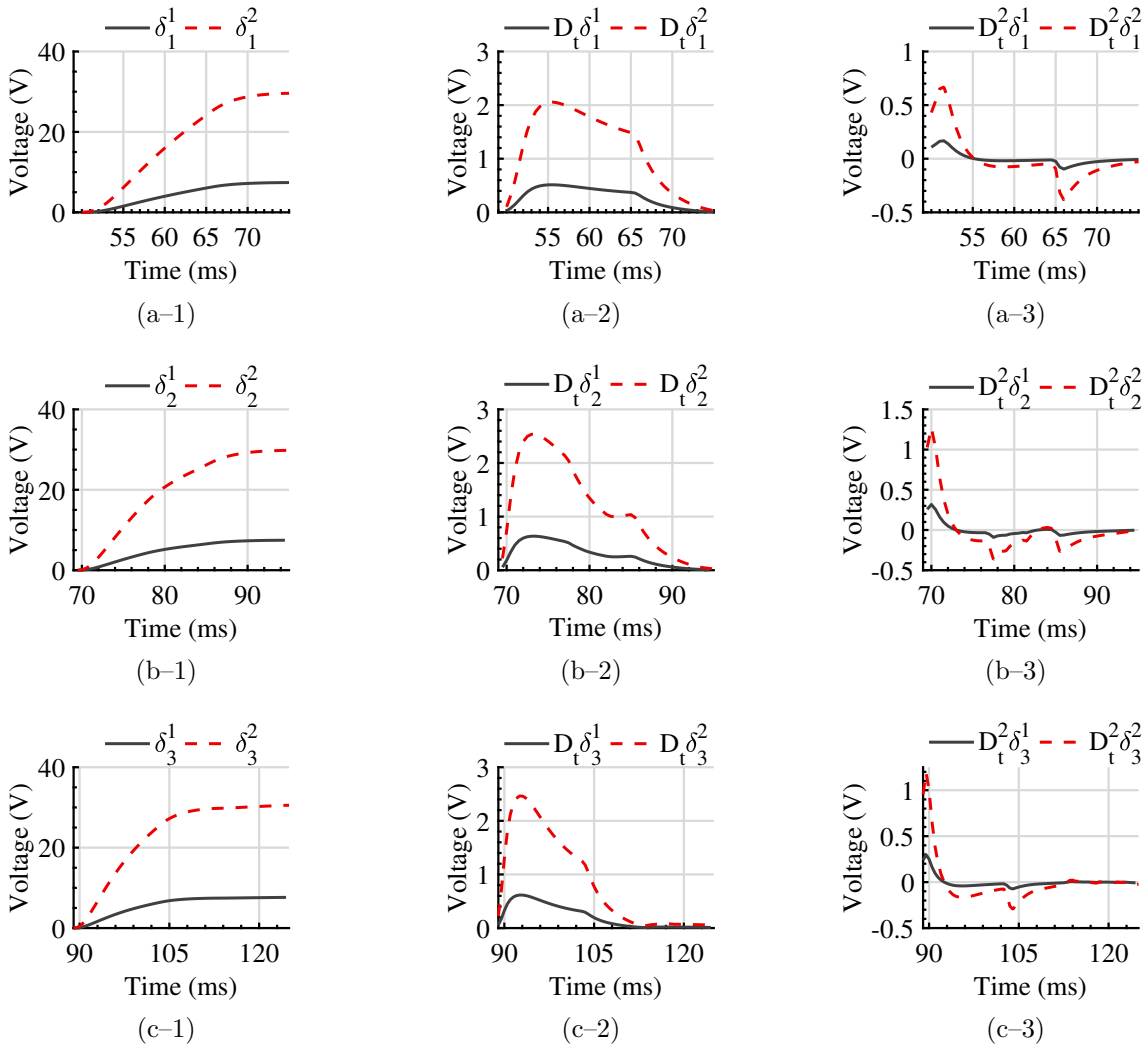

Figure 2.15: $PV_{9,m}$ and $PV_{10,m}$ shading: δ_m^1 and δ_m^2 along with their first and second derivatives for a) string 1, b) string 2, and c) string 3.

from cases 1 to 4 that the detection time reduces with increase in v_c. In addition, the shade in case 4 moves vertically along the string, casting a shade on one module at a time, whereas the shade in case 5 moves horizontally across the string, casting a shade on all seven modules at the same time. Hence, r_1^S in case 4 is lower than that in case 5. Accordingly, with the same v_c, the detection time of case 5 is lower than that for case

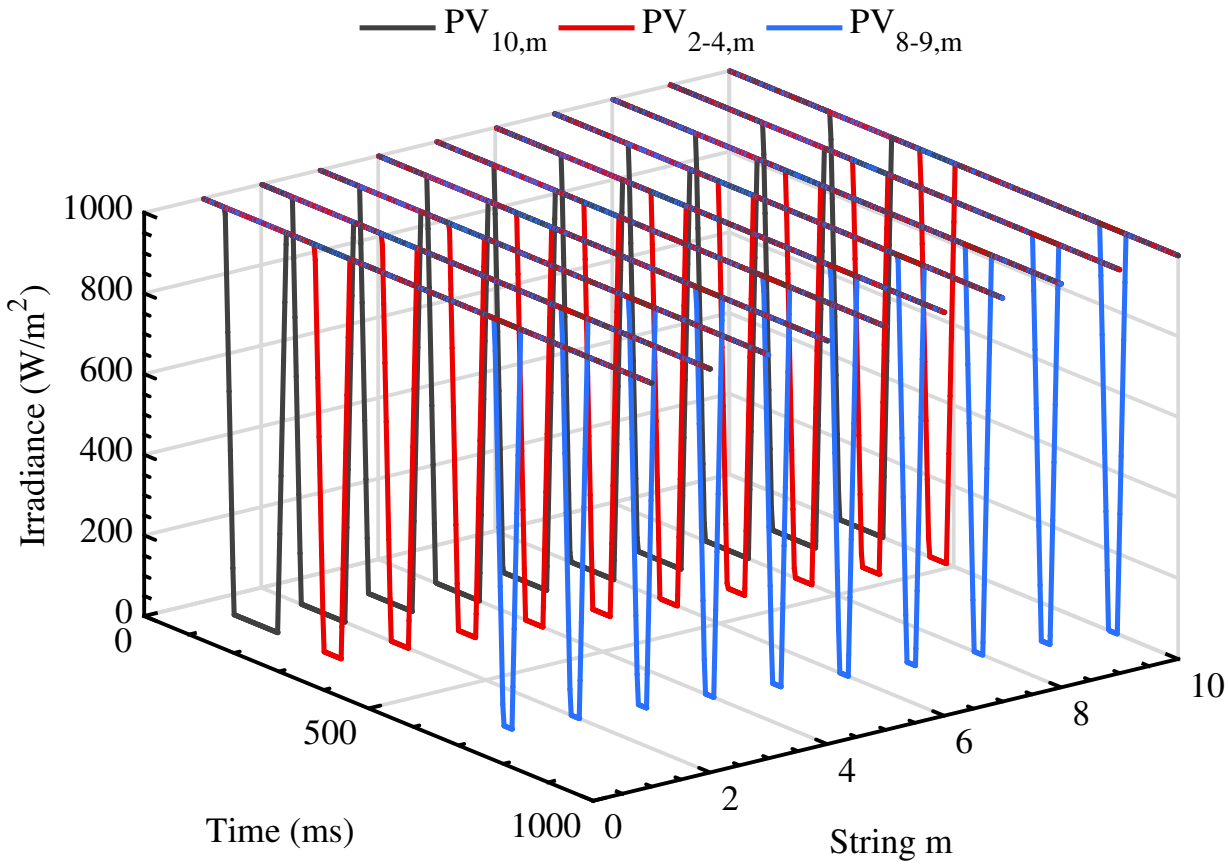

Figure 2.16: Irradiance seen by $PV_{10,m}$, $PV_{2-4,m}$, and $PV_{8-9,m}$.

4. However, Table 2.1 indicates that G^{pr} and the percentage shade have no visible effect on the speed of the proposed method in differentiating between fault and partial shading condition.

2.5.3 Scheme Performance Under High Fault Resistance

This subsection presents two case studies to assess the performance of the proposed scheme under high fault resistance: $Flt2$ and $Flt5$ with R_f= 100 Ω. The PV array is operating

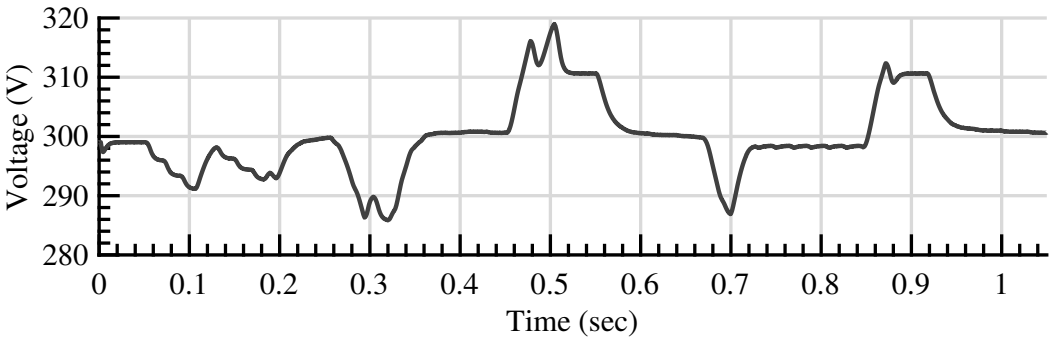

Figure 2.17: V_{pv} due to the shade casted by the three clouds.

Table 2.1: Case Studies of Partial Shading of String 1

Cases		Case 1	Case 2	Case 3	Case 4	Case 5
N_m		1	3	5	All	7
Shaded PVs		$PV_{10,1}$	$PV_{1-3,1}$	$PV_{3-7,1}$	All	$PV_{2-8,1}$
G^{pr} (W/m^2)		900	250	500	1000	750
Percentage Shade		40%	25%	75%	60%	10%
v_c (m/s)		5	15	30	51.3	51.3
Direction		Hor	Hor	Hor	Ver	Hor
$D_t^2\delta_1^1$ (V)	$+ve$ peak	0.076	0.218	0.062	0.422	0.024
	$-ve$ peak	-0.072	-0.410	-0.028	-0.404	-0.016
$D_t^2\delta_1^2$ (V)	$+ve$ peak	0.684	0.093	0.062	0.046	0.024
	$-ve$ peak	-0.649	-0.176	-0.028	-0.045	-0.016
Detection time (ms)		152	85	42	35	26

under the STC and the faults occur at 50 ms.

For $Flt2$, δ_1^1 and δ_1^2 exceed 0.063 V at t_1= 50 ms (Figure 2.22a), whereas $D_t\delta_1^1$ and $D_t\delta_1^2$

drop below 0.01 V at t_2=61.4 ms (Figure 2.22b), indicating a disturbance. Figure 2.22c shows that $D_t^2\delta_1^1$ and $D_t^2\delta_1^2$ within the interval between t_1 and t_2 are negative, flagging string 1 as faulted after 11.4 ms of the fault inception. Since only string 1 is faulted,

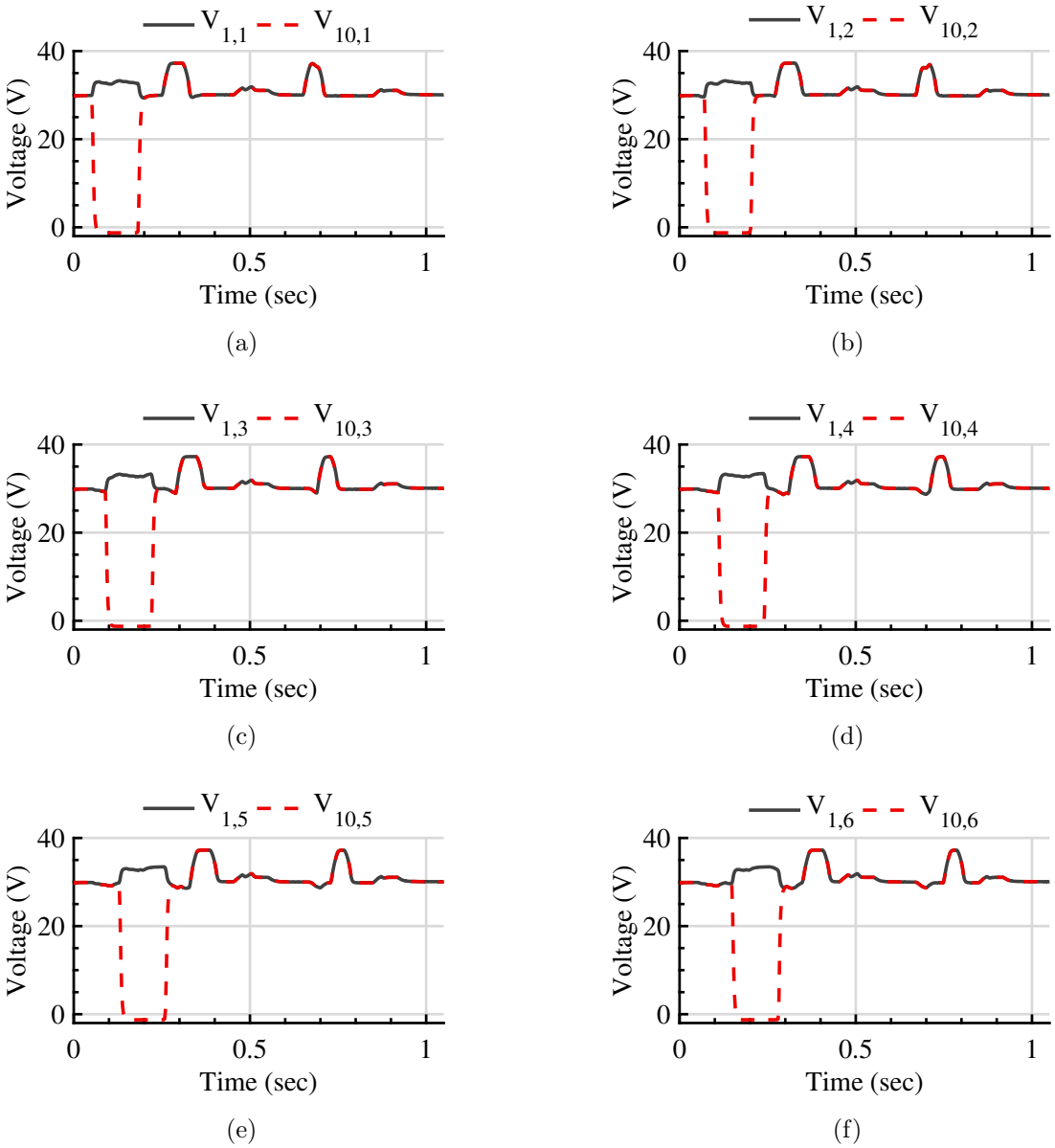

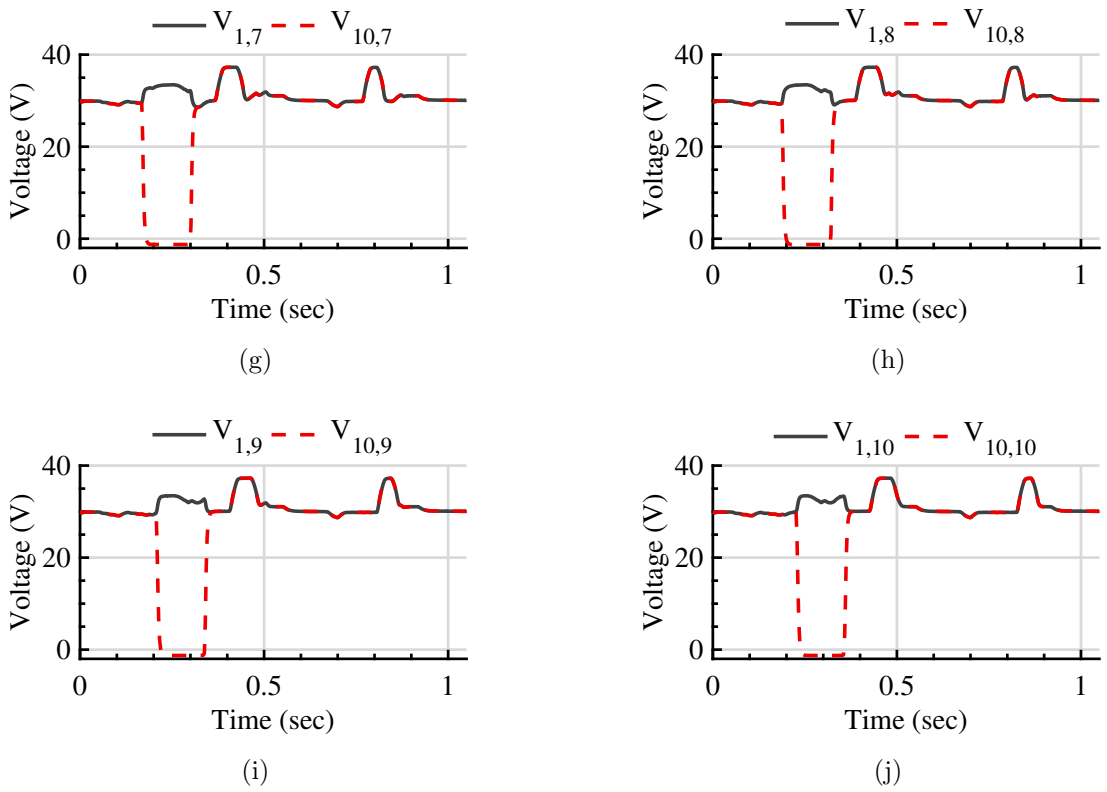

Figure 2.18: $PV_{10,m}$, $PV_{2-4,m}$, and $PV_{8-9,m}$ shading: $V_{1,m}$ and $V_{10,m}$ for string a) 1, b) 2, c) 3, d) 4, e) 5, f) 6, g) 7, h) 8, i) 9, j) 10.

and (2.15) and (2.16) are satisfied (Figure 2.21), the fault is classified as an SG fault. By solving (2.2), the fault location represented by N_1^f is equal to 1.

Similarly, for $Flt5$, δ_m^1 and δ_m^2 exceed 0.063 V of strings 2 and 3 at t_1= 50 ms (Figures 2.24a–1 and 2.24b–1), whereas $D_t\delta_m^1$ and $D_t\delta_m^2$ drop below 0.01 V at t_2=58.4 ms (Figures 2.24a–2 and 2.24b–2), indicating a disturbance. Figures 2.24a–3 and 2.24b–3 show that $D_t^2\delta_m^1$ and $D_t^2\delta_m^2$ of strings 2 and 3 within the interval between t_1 and t_2 are negative, flagging strings 2 and 3 as faulted after 8.4 ms of the fault inception. Since strings 2 and 3 are faulted, and (2.19), (2.20), (2.21), and (2.22) are satisfied (Figure 2.23), the fault is classified as an SS fault. By solving (2.2), the fault location represented by N_2^f and N_3^f are found to be 5 and 4 for string 2 and 3, respectively. The above results show that the

proposed scheme is sensitive to SG and SS faults with resistance up to R_f= 100 Ω.

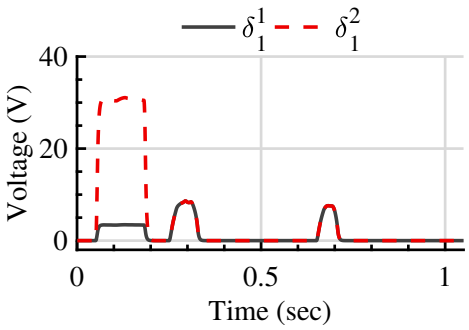

(a)

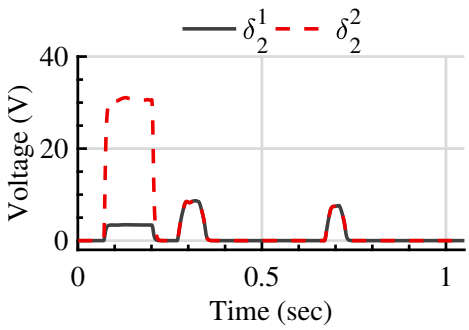

(b)

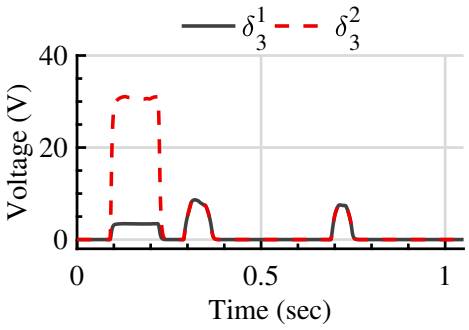

(c)

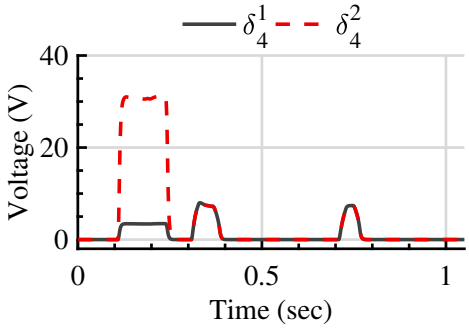

(d)

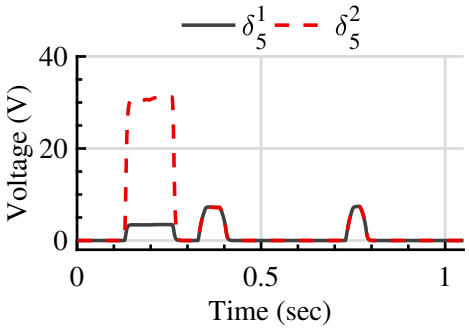

(e)

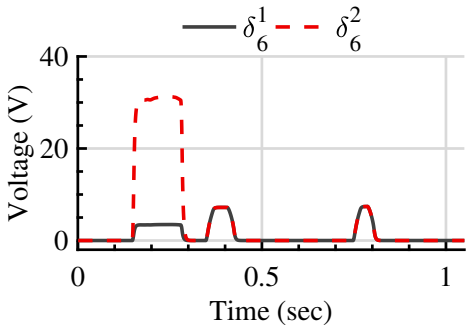

(f)

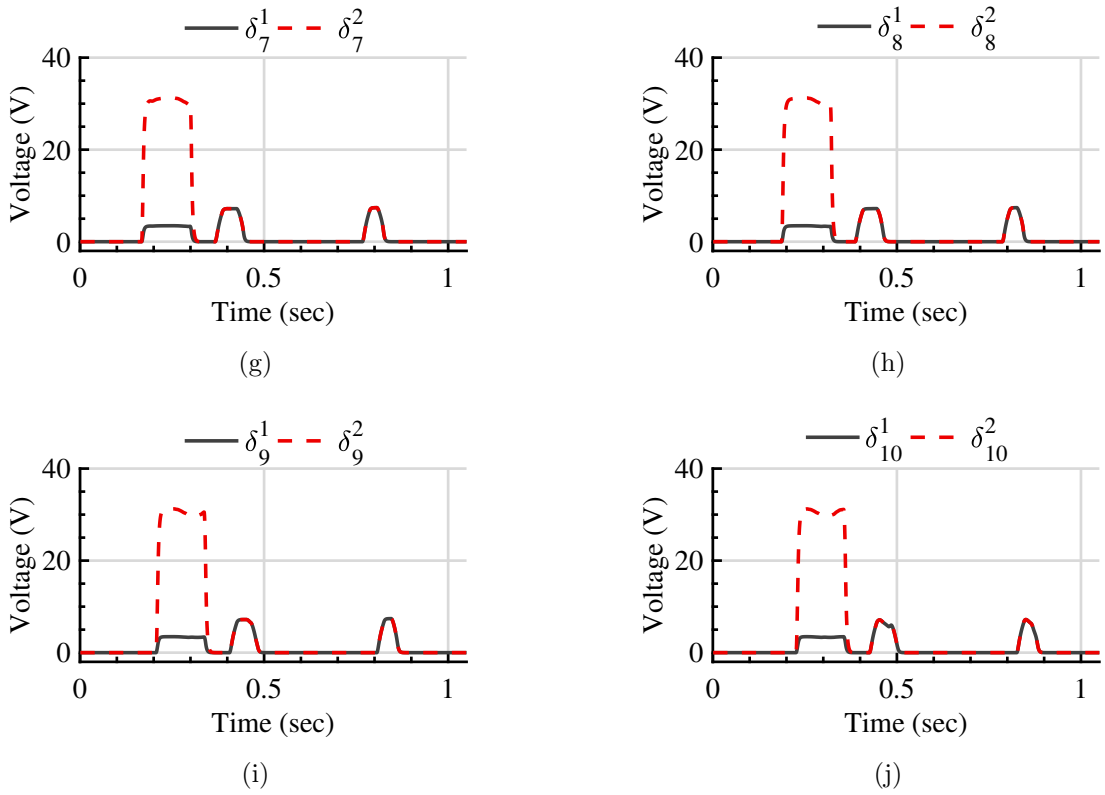

Figure 2.19: $PV_{10,m}$, $PV_{2-4,m}$, and $PV_{8-9,m}$ shading: δ_m^1 and δ_m^2 for string a) 1, b) 2, c) 3, d) 4, e) 5, f) 6, g) 7, h) 8, i) 9, j) 10.

2.5.4 Scheme Performance in a Large PV Array

This subsection presents a case study to assess the performance of the proposed scheme in a large PV array. The rated voltage of utility-scale PV arrays normally ranges from 300 to 1000 V [79]. Therefore, a 33 × 125, 970 kW, 1000 V testbed is used to model a large PV array. An SS fault at $F_{16,2}$-$F_{17,3}$ with 10% location mismatch is conducted at 50 ms.

During the fault, δ_m^1 and δ_m^2 exceed 0.019 V, i.e., $\frac{V_{pv}}{N}\frac{2\%}{N}$1.05 V, where V_{pv}=995 V, of strings 2 and 3 at t_1= 50 ms (Figures 2.26a–1 and 2.26b–1), whereas $D_t\delta_m^1$ and $D_t\delta_m^2$ drop below 0.01 V at t_2=60.9 ms (Figures 2.26a–2 and 2.26b–2), indicating a disturbance. Figures 2.26a–3 and 2.26b–3 show that $D_t^2\delta_m^1$ and $D_t^2\delta_m^2$ of strings 2 and 3 within the

interval between t_1 and t_2 are negative, flagging strings 2 and 3 as faulted after 10.9 ms of the fault inception. Since strings 2 and 3 are faulted, and (2.19), (2.20), (2.21), and (2.22) are satisfied (Figure 2.25), the fault is classified as an SS fault. By solving (2.2), the

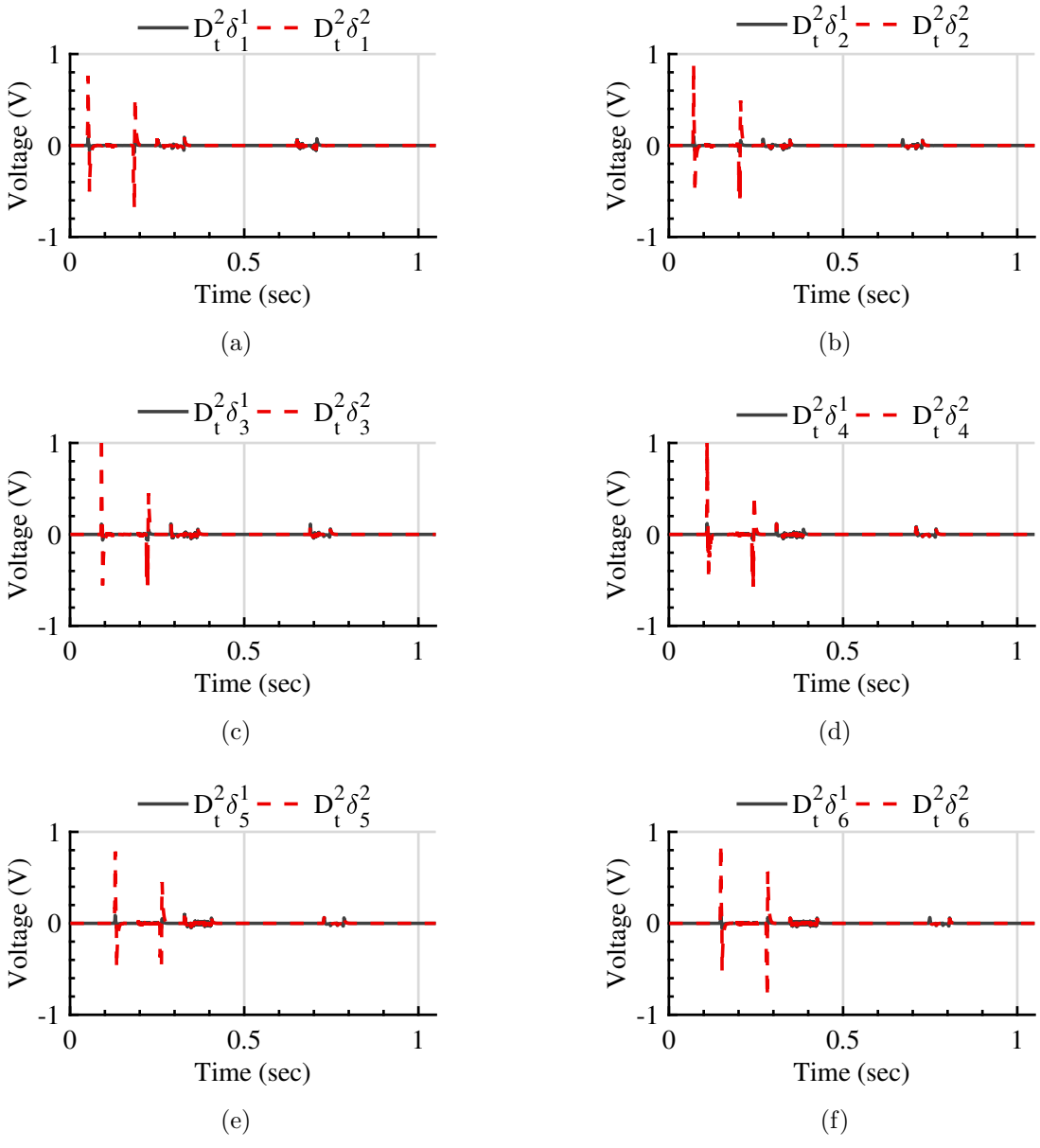

(a) (b) (c) (d) (e) (f)

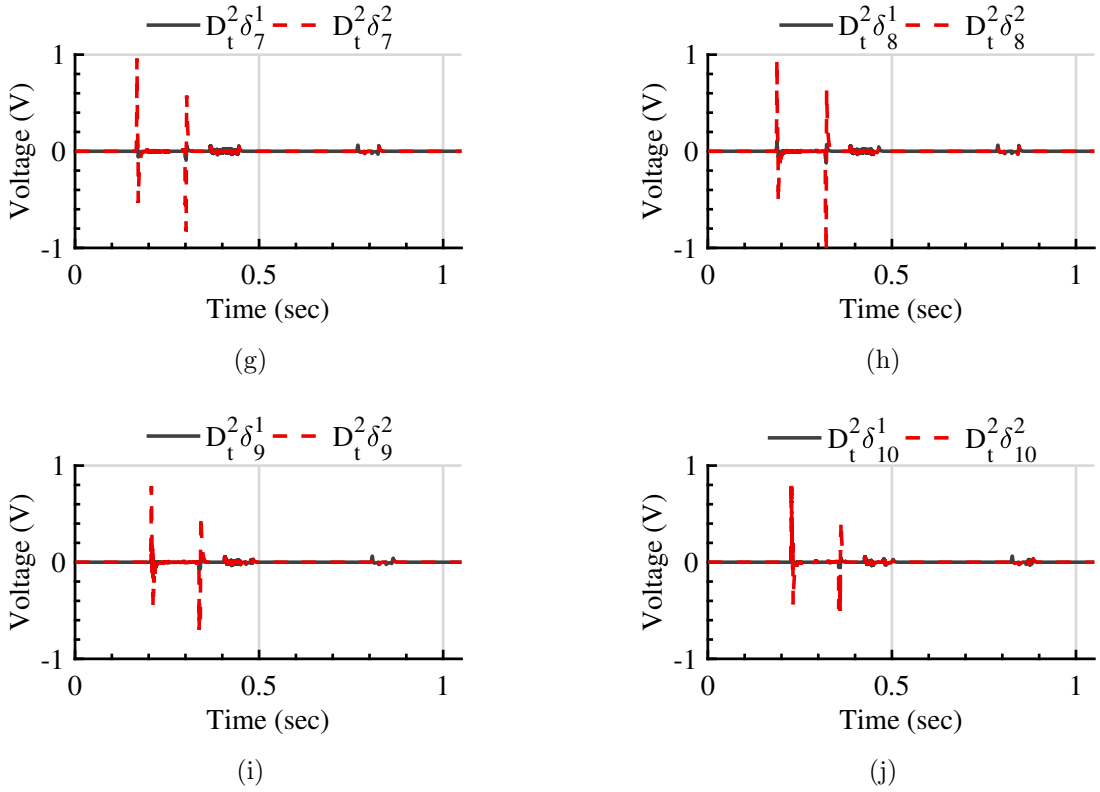

Figure 2.20: $PV_{10,m}$, $PV_{2-4,m}$, and $PV_{8-9,m}$ shading: $D_t^2\delta_m^1$ and $D_t^2\delta_m^2$ for string a) 1, b) 2, c) 3, d) 4, e) 5, f) 6, g) 7, h) 8, i) 9, j) 10.

fault locations represented by N_2^f and N_3^f are found to be 17 and 16 for strings 2 and 3, respectively.

Additionally, the performance of the proposed method is assessed under a partial shading case study for the 33×125 PV array. A 2 m long cloud moving horizontally across the PV array from string 1 to 125 with v_c=51.3 m/s and casting shade on $PV_{32,m}$ and $PV_{33,m}$ is simulated. The shade cast by the cloud starts partially covering the PV array at 50 ms. The PV array is operating under the STC before the shade starts. Figure 2.13 shows the irradiance seen by $PV_{32,m}$ and $PV_{33,m}$ in strings a) 1, b) 2, and c) 3. As a consequence of the irradiance drop caused by the shade, Figure 2.27 shows that (2.1) is violated sequentially for the three mentioned strings. Correspondingly, the violation is captured by δ_m^1

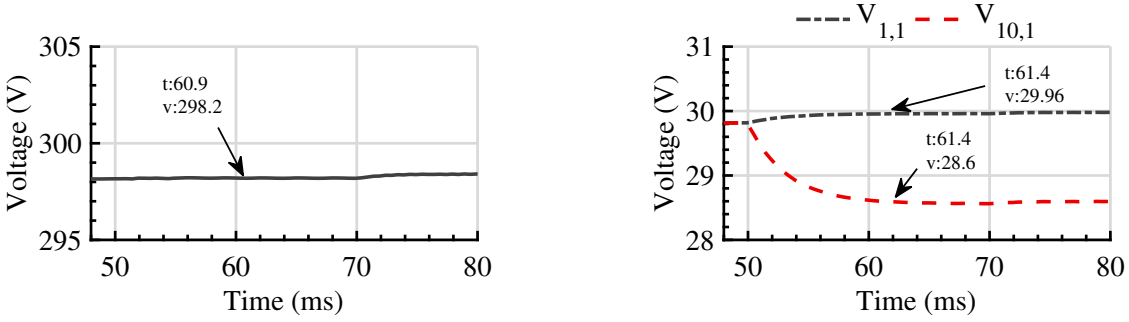

Figure 2.21: *Flt*2 with R_f= 100 Ω: a) V_{pv} b) $V_{1,1}$ and $V_{10,1}$.

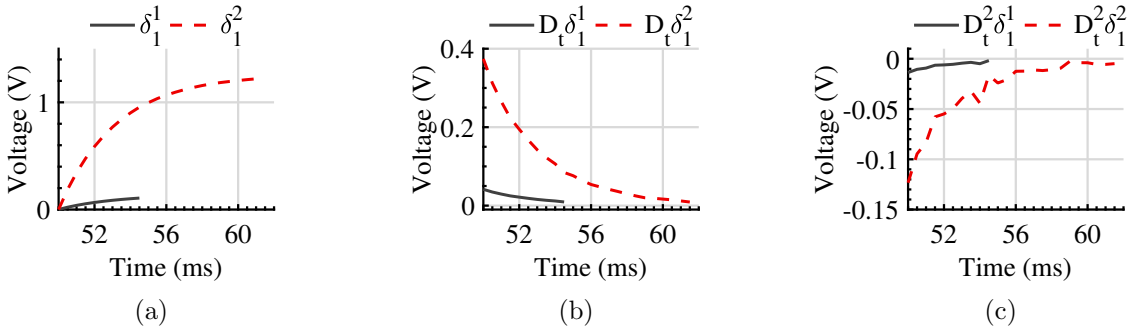

Figure 2.22: *Flt*2 with R_f= 100 Ω: a) δ_1^1 and δ_1^2 along with their b) first derivatives, and c) second derivatives.

and δ_m^2 of strings 1, 2, and 3 as they exceed 0.019 V at t_1 equal to 50 ms, 69.4 ms, and 88.9 ms, respectively (Figures 2.28a–1, 2.28b–1, and 2.28c–1). Therefore, there is a disturbance affecting all three strings, but at different times. $D_t\delta_m^1$ and $D_t\delta_m^2$ of strings 1, 2, and 3 drop below 0.01 V at t_2 equal to 76 ms, 97 ms, and 125 ms, respectively (Figures 2.28a–2, 2.28b–2, and 2.28c–2). Figures 2.28a–3, 2.28b–3, and 2.28c–3 show that $D_t^2\delta_m^1$ and $D_t^2\delta_m^2$ of strings 1, 2, and 3 switch from a positive to a negative value within their corresponding Δt, indicating the presence of inflection points in δ_m^1 and δ_m^2. Therefore, strings 1, 2, and 3 are flagged as partially shaded. The above results show that the proposed approach preforms effectively in large PV arrays, which highlights the scalability of the proposed protection

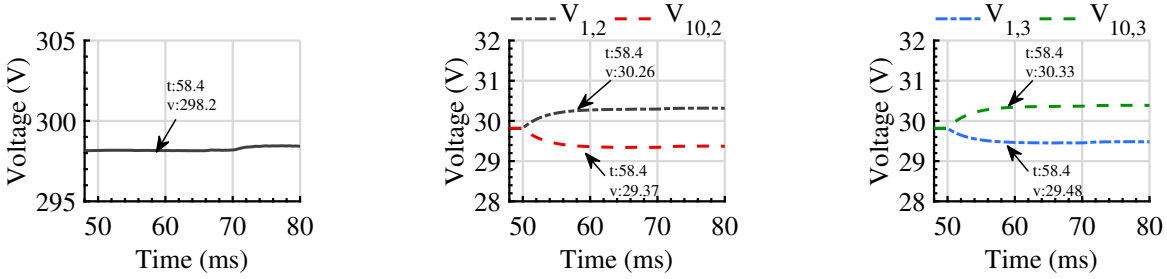

Figure 2.23: *Flt*5 with R_f= 100 Ω: a) V_{pv} b) $V_{1,2}$ and $V_{10,2}$, and c) $V_{1,3}$ and $V_{10,3}$.

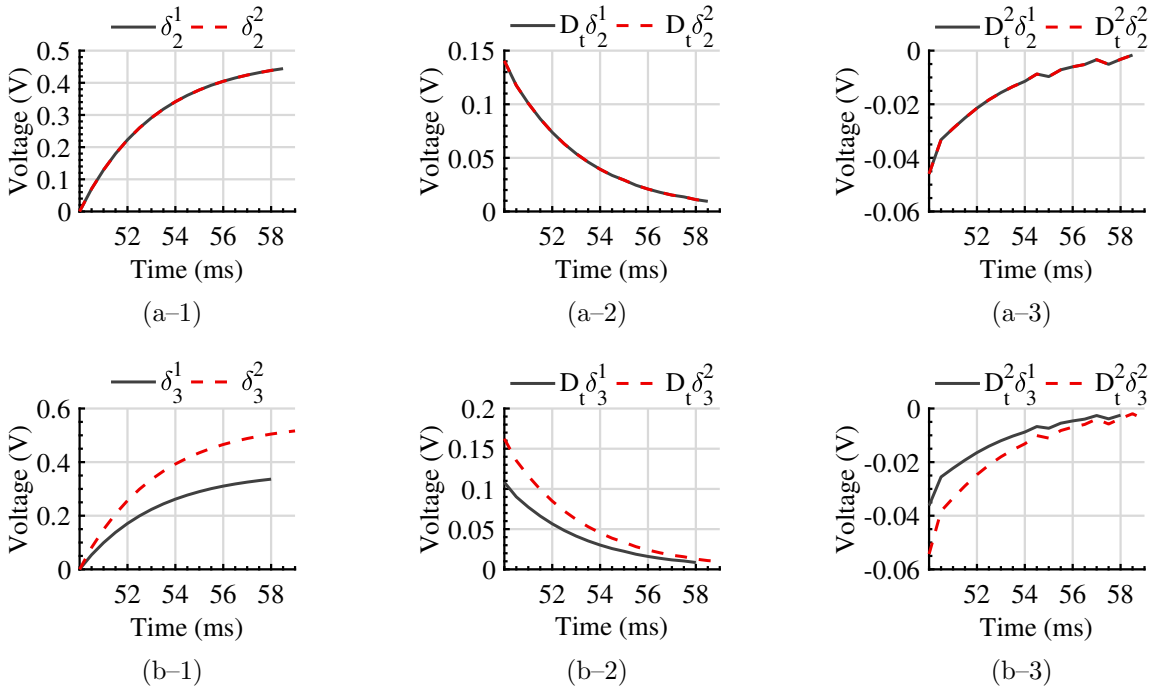

Figure 2.24: *Flt*5 with R_f= 100 Ω: δ_m^1 and δ_m^2 along with their first and second derivatives for a) string 2 and b) string 3.

scheme.

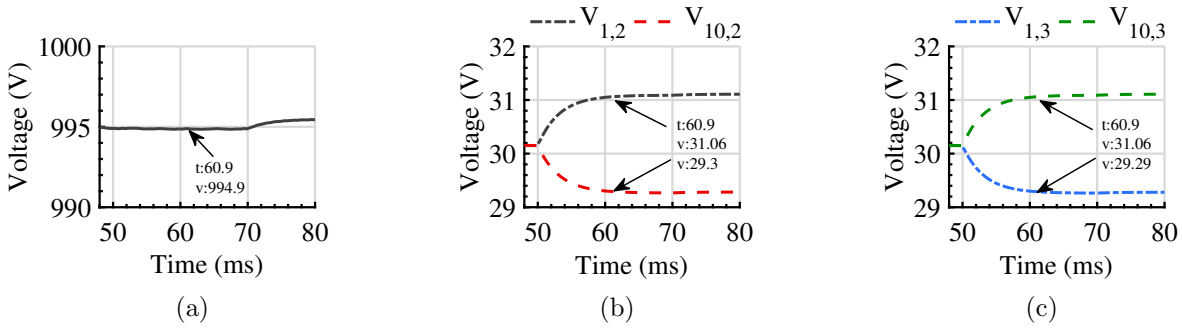

Figure 2.25: SS fault in large array: a) V_{pv}, $V_{1,m}$ and $V_{10,m}$ for strings b) 2 and c) 3.

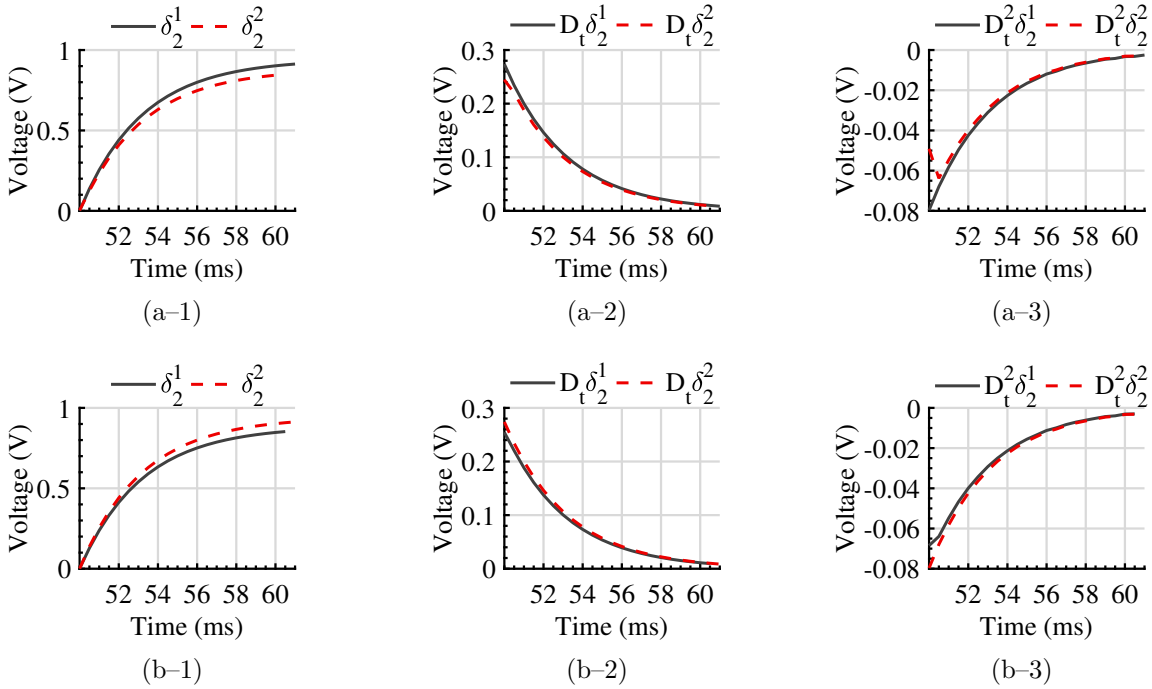

Figure 2.26: SS fault in large PV Array: δ_m^1 and δ_m^2 along with their first and second derivatives for a) string 2 and b) string 3.

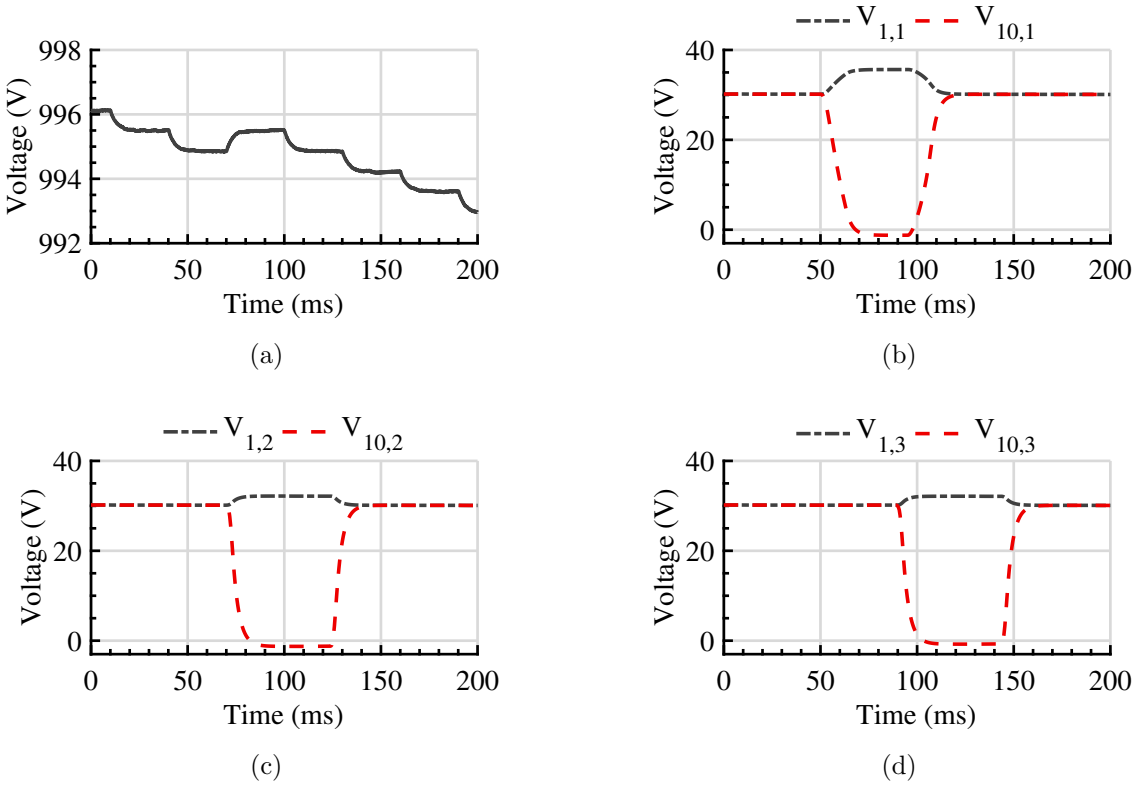

Figure 2.27: $PV_{32,m}$ and $PV_{33,m}$ shading: a) V_{pv}, $V_{1,m}$ and $V_{33,m}$ for b) string 1, c) string 2, and d) string 3.

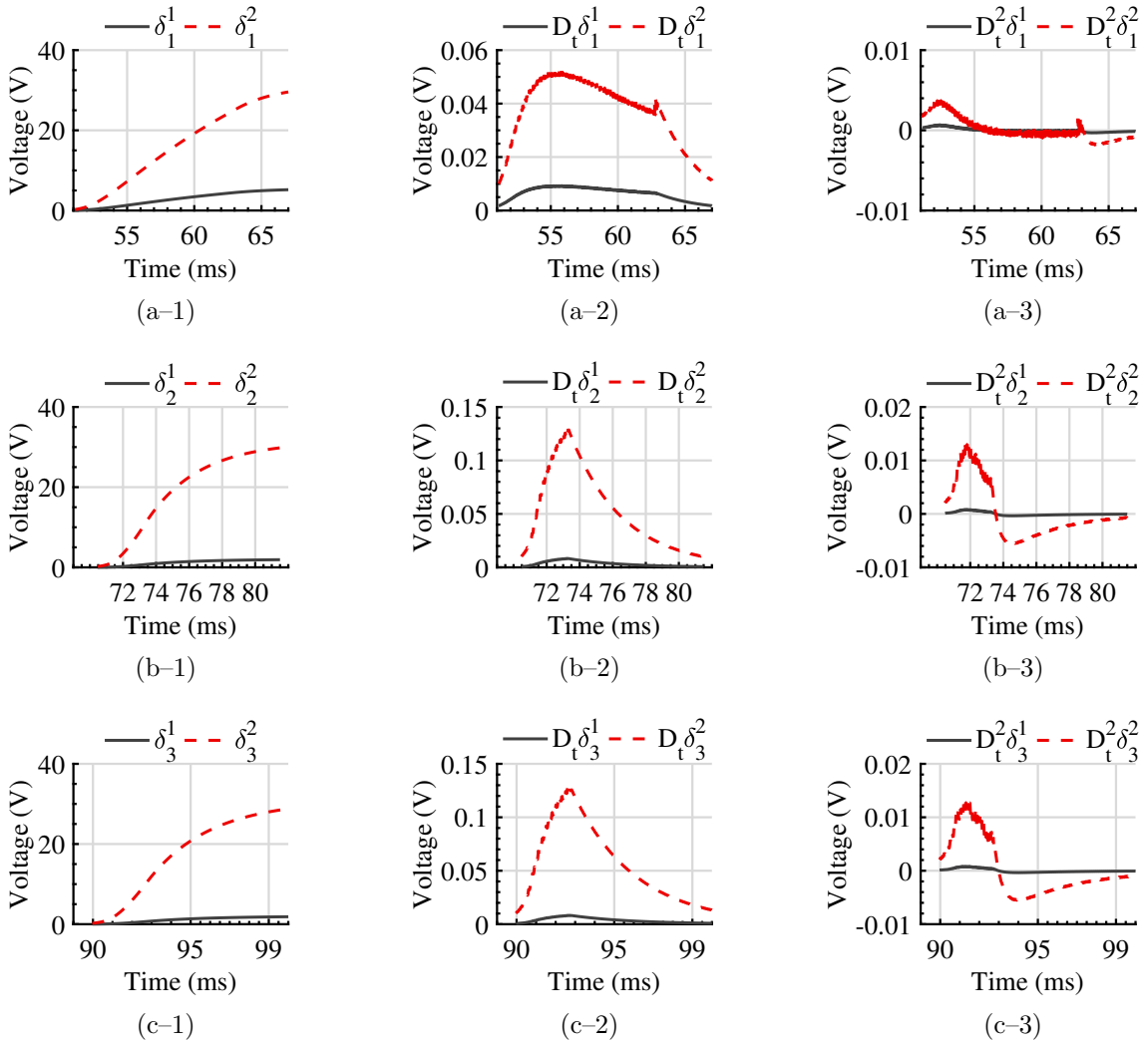

Figure 2.28: $PV_{32,m}$ and $PV_{33,m}$ shading: δ_m^1 and δ_m^2 along with their first and second derivatives for a) string 1, b) string 2, and c) string 3.

2.6 Experimental Performance Verification

Figure 2.29 shows a small-scale grid-connected PV system, which is utilized to verify the performance of the proposed method. The 5×3 PV array consists of 15 identical 4.5 W polycrystalline-silicon panels with V_{mp}= 5 V and I_{mp}= 850 mA at STC. Each PV module is equipped with one IN5817 Schottky bypass diode (i.e. N_d= 1) with V_d= 0.45 V when the forward current is 1 A. The PV array is connected to a 300 W centralized grid-tie inverter that converts a 10.5∼28 V to a 110 V AC output. The inverter is equipped with an MPPT algorithm. A four channel digital storage Tektronix TPS2024B oscilloscope is used to capture the voltage waveforms. The measurements are imported to MATLAB, in which the proposed method is implemented. Three toggle switches are used to conduct OC, SG, and SS faults. An SM206 Dr.Meter solar power meter is used to measure the irradiance during the experiments. The experiments were conducted during a partly sunny day, and thus the irradiance ranged from 600 to 900 W/m^2. It should be mentioned that the proposed method does not require irradiance measurement, and the irradiance meter is used only to indicate the irradiance level under which the method is tested.

2.6.1 SG Fault

A bolted SG fault at $F_{4,1}$ with 20% location mismatch is conducted by closing the normally-open left toggle switch in Figure 2.29. Figure 2.30 shows $V_{1,1}$, $V_{5,1}$, and V_{pv} waveforms captured by the oscilloscope. Each horizontal time division (i.e., the big grid square) is 1 ms. The measurements are filtered using a first-order low-pass Butterworth filter with a cut-off frequency of 1.5kHz to attenuate noise. Figure 2.31 presents a) the measured and b) the filtered and down-sampled V_{pv}, $V_{1,1}$, and $V_{5,1}$. Figure 2.32 shows δ_1^1 and δ_1^2 along with their first and second derivatives.

δ_1^1 and δ_1^2 exceed 0.021 V, i.e., $\frac{V_{pv}}{N}\frac{2\%}{N}$1.05 V, at t_1= −1.36 ms (Figure 2.32a), whereas $D_t\delta_1^1$ and $D_t\delta_1^2$ drop below 0.01 V at t_2=−0.96 ms (Figure 2.32b), indicating a disturbance. Figure 2.32c shows that $D_t^2\delta_1^1$ and $D_t^2\delta_1^2$ are negative between t_1 and t_2, flagging string 1 as faulted after 0.4 ms of the fault inception. Since only string 1 is faulted, and (2.15) and (2.16) are satisfied (Figure 2.31b), the fault is classified as an SG fault. By solving (2.2),

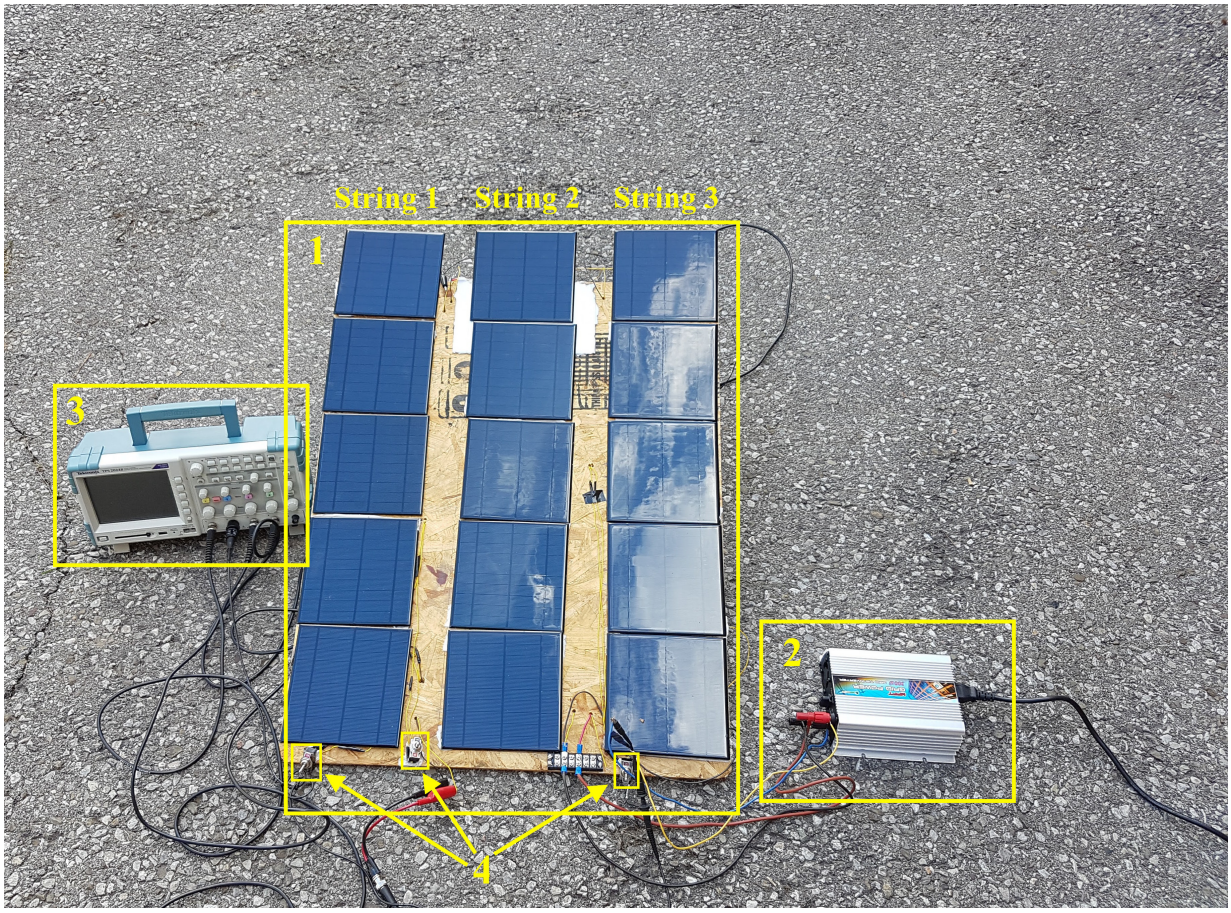

Figure 2.29: Experimental grid-connected PV system setup: 1) PV array, 2) grid-tie inverter, 3) oscilloscope, and 4) toggle switches.

N_1^f is equal to 1, so the fault location is correctly identified.

2.6.2 SS Fault

A bolted SS fault at $F_{2,2}$-$F_{3,3}$ with 20% location mismatch is conducted by closing the normally-open right toggle switch in Figure 2.29. Figure 2.33 shows $V_{1,2}$, $V_{5,2}$, $V_{5,3}$, and V_{pv} waveforms captured by the oscilloscope. Given that the oscilloscope used for this setup has only four channels for measurement, $V_{1,3}$ could not be measured, and all of the required

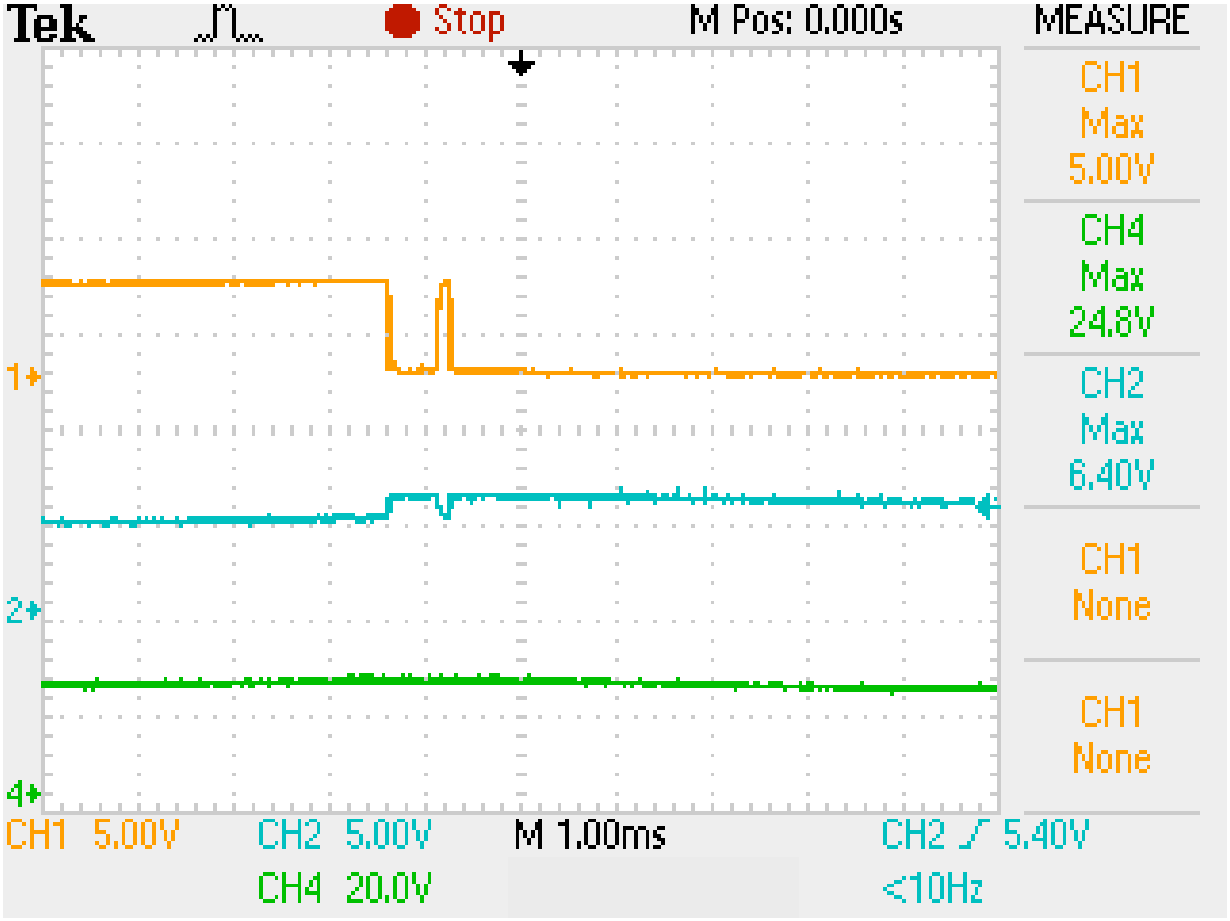

Figure 2.30: Oscilloscope measurements under an SG fault at $F_{4,1}$: CH1: $V_{5,1}$, CH2: $V_{1,1}$, and CH4: V_{pv}.

information for exact fault location along string 3 is not available for this case study, but the fault can successfully be detected and the fault location along string 2 can correctly be identified. δ_m^1 and δ_m^2 exceed 0.021 V for strings 2 and 3 at $t_1 = -0.44$ ms in Figures 2.35a–1 and 2.35b–1, whereas $D_t\delta_m^1$ and $D_t\delta_m^2$ drop below 0.01 V at $t_2 = -1.18$ ms in Figures 2.35a–2 and 2.35b–2, indicating a disturbance. Figures 2.35a–3 and 2.35b–3 show that $D_t^2\delta_m^1$ and $D_t^2\delta_m^2$ for strings 2 and 3 are negative between t_1 and t_2, hence flagging strings 2 and 3 as faulted 0.74 ms after the fault inception. Since strings 2 and 3 are faulted, and (2.19), (2.21), and (2.22) are satisfied (Figure 2.35b), the fault is classified as an SS fault. By

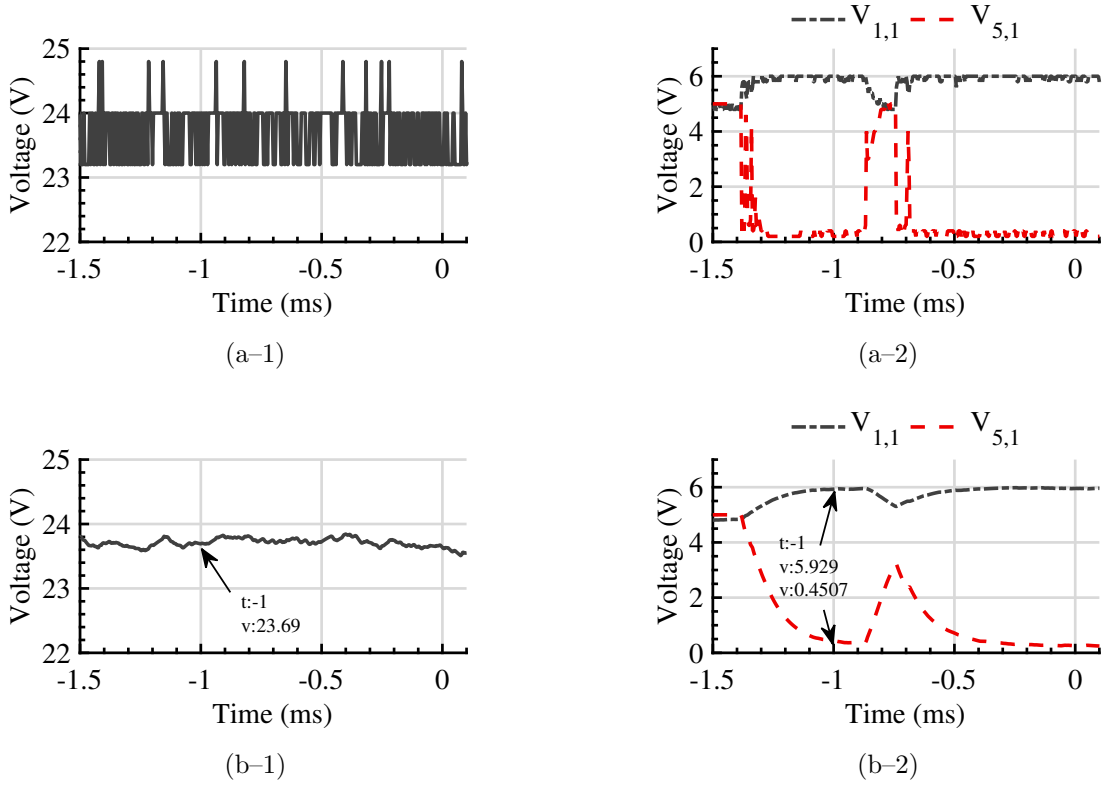

Figure 2.31: SG fault at $F_{4,1}$: V_{pv}, $V_{1,1}$, and $V_{5,1}$ a) Measured b) Filtered and down-sampled.

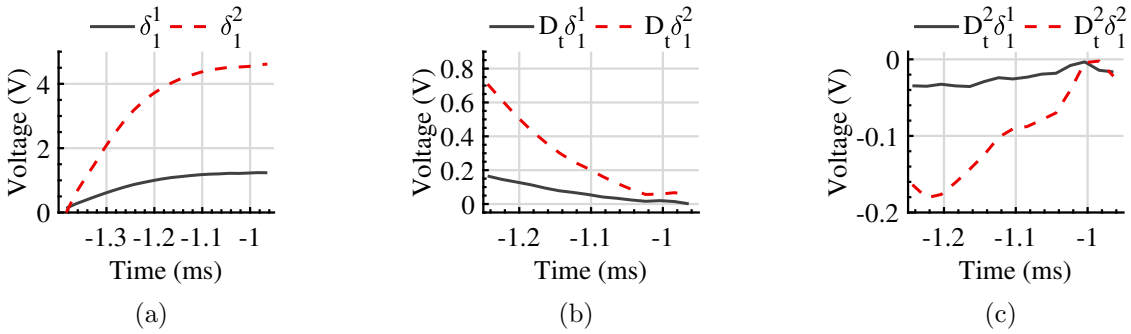

Figure 2.32: SG fault at $F_{4,1}$: a) δ_1^1 and δ_1^2 along with their b) first derivatives, and c) second derivatives.

solving (2.2), the fault location N_2^f is found to be 3 for string 2.

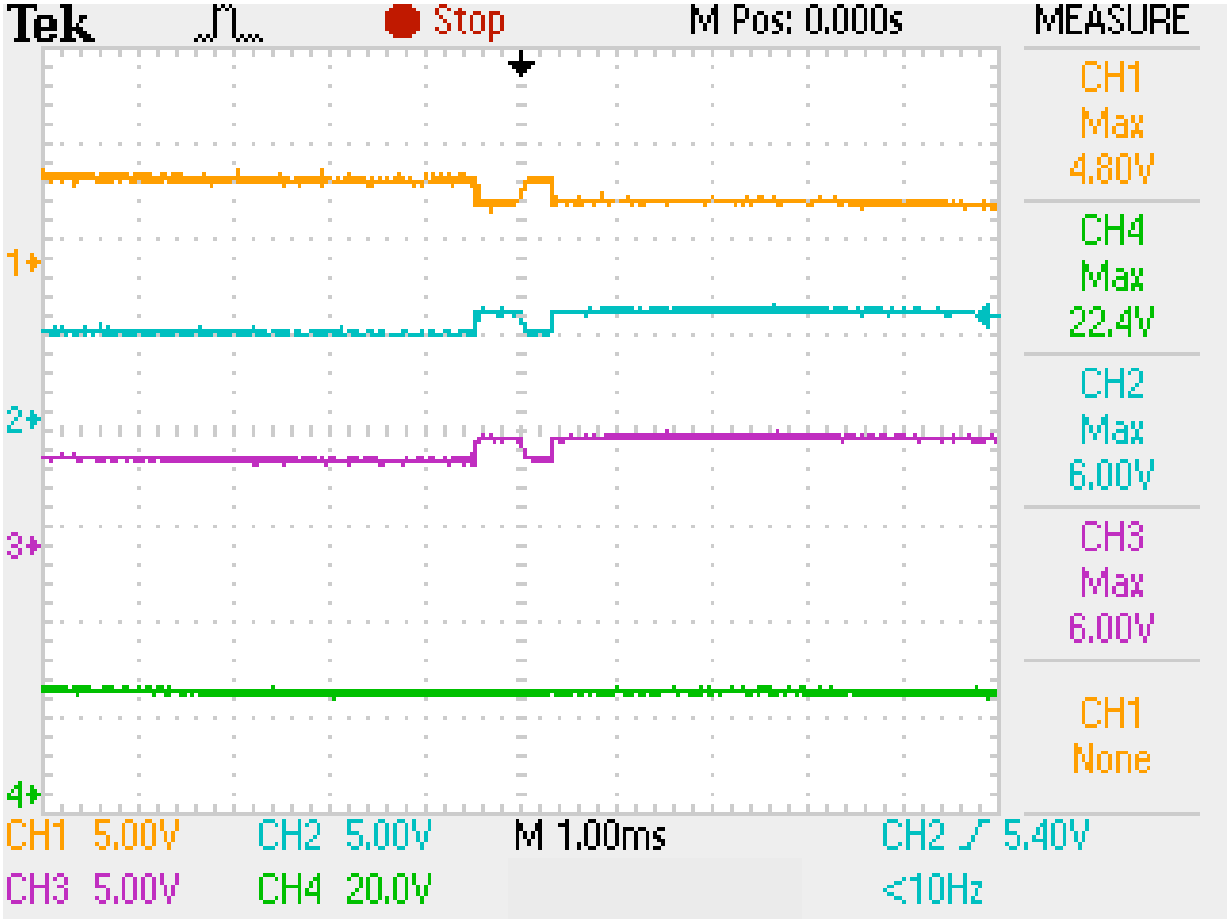

Figure 2.33: Oscilloscope measurements under an SS fault at $F_{2,2}$-$F_{3,3}$: CH1: $V_{5,2}$, CH2: $V_{1,2}$, CH3: $V_{5,3}$, and CH4: V_{pv}.

2.6.3 OC Fault

An OC fault at $F_{3,1}$ is conducted by opening the normally-closed middle toggle switch in Figure 2.29. Figure 2.36 shows $V_{1,1}$, $V_{5,1}$, and V_{pv} waveforms captured by the oscilloscope. δ_1^1 and δ_1^2 exceed 0.021 V at t_1= 0.016 ms (Figure 2.38a), whereas $D_t\delta_1^1$ and $D_t\delta_1^2$ drop below 0.01 V at t_2=0.356 ms (Figure 2.38b), indicating a disturbance. Figure 2.38c shows

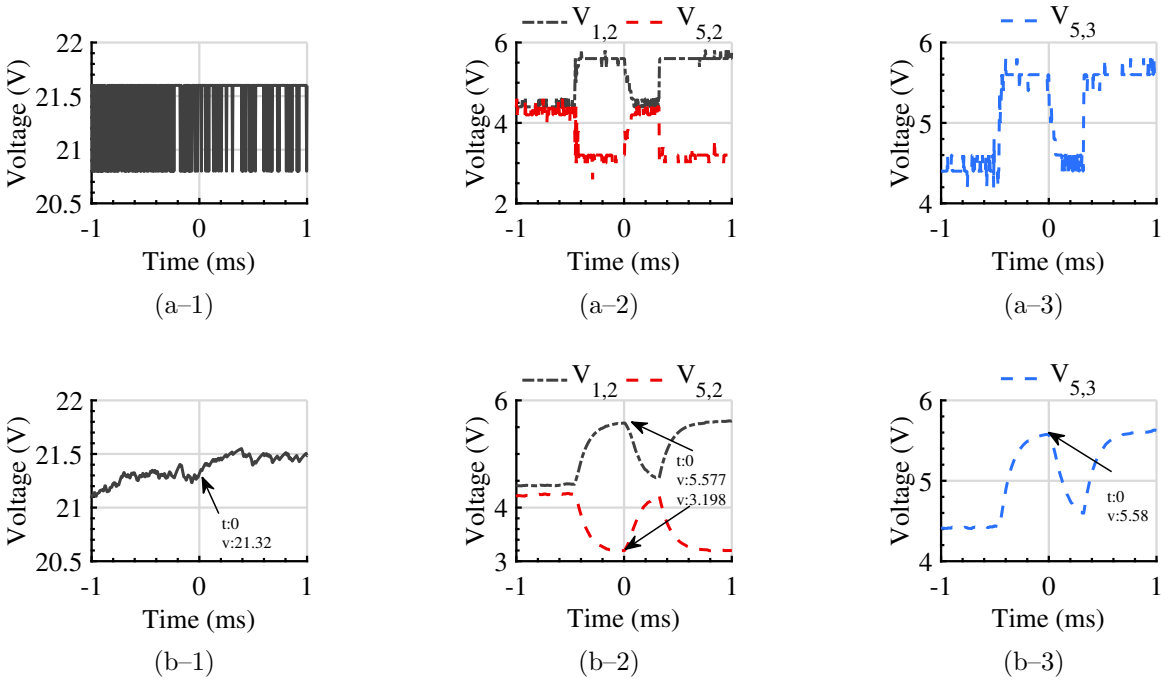

Figure 2.34: SS fault at $F_{2,2}$-$F_{3,3}$: V_{pv}, $V_{1,2}$, $V_{5,2}$, and $V_{5,3}$ a) Measured b) Filtered and down-sampled.

that $D_t^2\delta_1^1$ and $D_t^2\delta_1^2$ are negative between t_1 and t_2, and thus string 1 is flagged as faulted 0.34 ms after the fault inception. Since only string 1 is faulted, and (2.17) and (2.18) are satisfied (Figure 2.37b), the fault is classified as an OC fault.

2.6.4 Partial Shading Condition

Partial shading is conducted by moving a 20 cm ×20 cm cardboard as fast as possible from the right to the left of the PV array to apply shade over first $PV_{5,3}$, then $PV_{5,2}$. Figure 2.39 shows $V_{1,2}$, $V_{5,2}$, $V_{5,3}$, and V_{pv} waveforms measured by the oscilloscope.

Figure 2.40b2 and 2.40b3 illustrate the expected sigmoid-like shape of the shaded modules voltage drop, that is, $V_{5,2}$ and $V_{5,3}$, from the pre-fault V_{mp} to V_d= −0.36 V, whereas the unshaded module voltage $V_{1,2}$ increases slightly above the pre-fault V_{mp} with a sigmoid-like

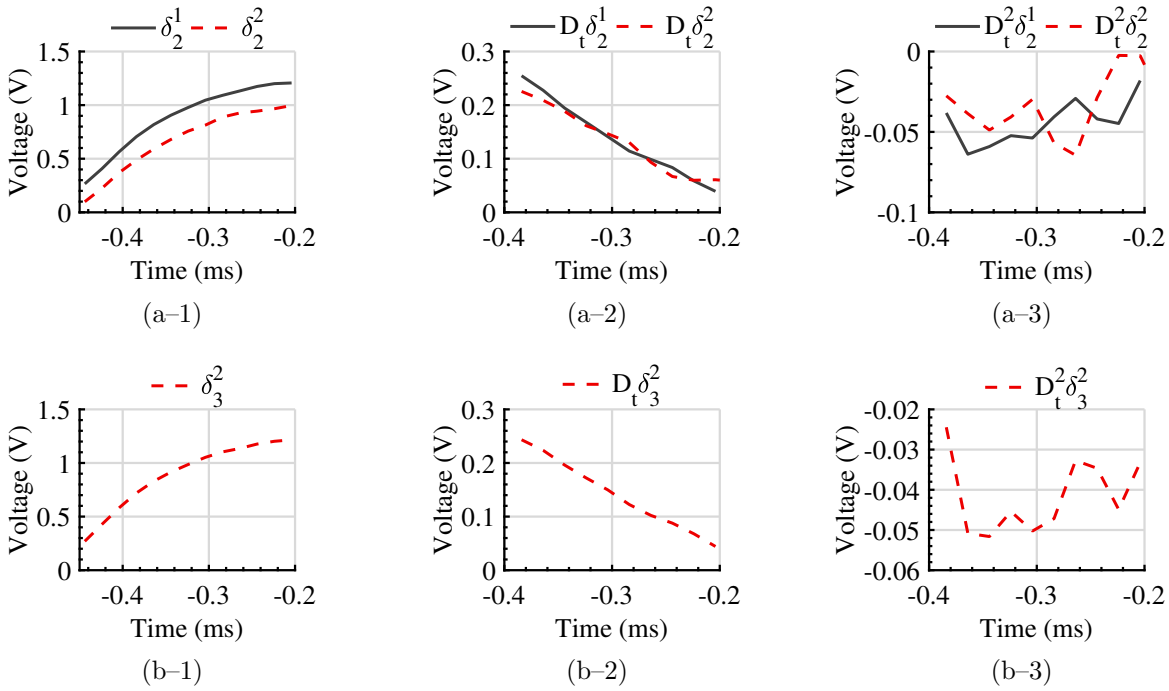

Figure 2.35: SS fault at $F_{2,2}$-$F_{3,3}$: δ_m^1 and δ_m^2 along with their first and second derivatives for a) string 2 and b) string 3.

shape. In addition, it can be noticed that the drop in $V_{5,3}$ (Figure 2.40b3) started earlier and is steeper than the drop in $V_{5,2}$ (Figure 2.40b2), which indicates that the shade cast first on $PV_{5,3}$ and then on $PV_{5,2}$.

Moreover, Figure 2.40 shows that (2.1) is violated for strings 3 and 2, sequentially. Correspondingly, the violation is captured by δ_m^1 and δ_m^2 of strings 3 and 2 as they exceed 0.021 V at t_1 equal to 0.994 s and 1.004 s, respectively (Figures 2.41b1 and 2.41a1). Therefore, there is a disturbance affecting the two strings, but at different times. $D_t\delta_m^1$ and $D_t\delta_m^2$ of strings 3 and 2 drop below 0.01 V at t_2 equal to 1.094 s and 1.154 s, respectively (Figures 2.41b2 and 2.41a2). Figures 2.41a3 and 2.41b3 show that $D_t^2\delta_m^1$ and $D_t^2\delta_m^2$ of strings 2 and 3 switch from a positive to a negative value within their corresponding Δt, indicating the presence of inflection points in δ_m^1 and δ_m^2. Therefore, strings 2 and 3 are flagged as partially shaded. Accordingly, no protective action is required.

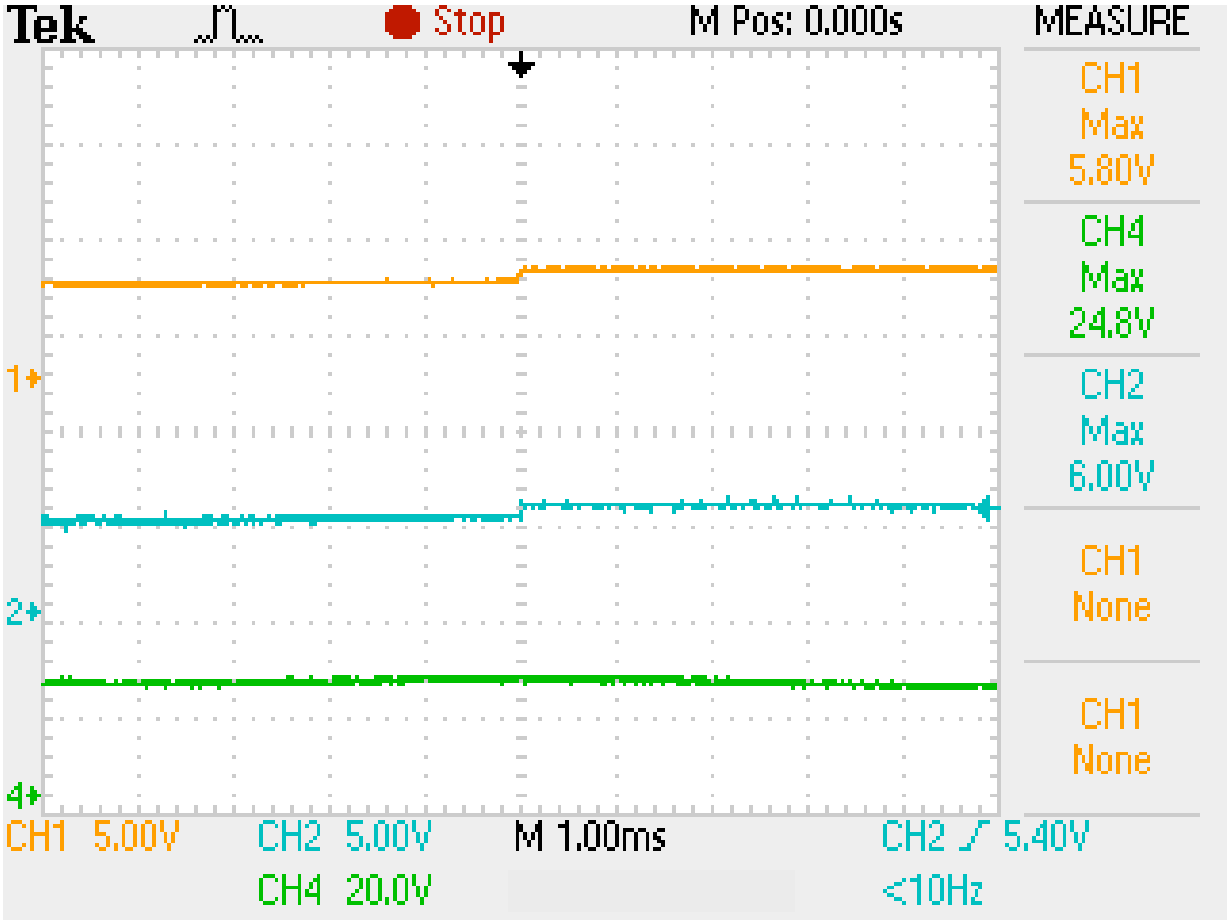

Figure 2.36: Oscilloscope measurements under an OC fault at $F_{3,1}$: CH1: $V_{5,1}$, CH2: $V_{1,1}$, and CH4: V_{pv}.

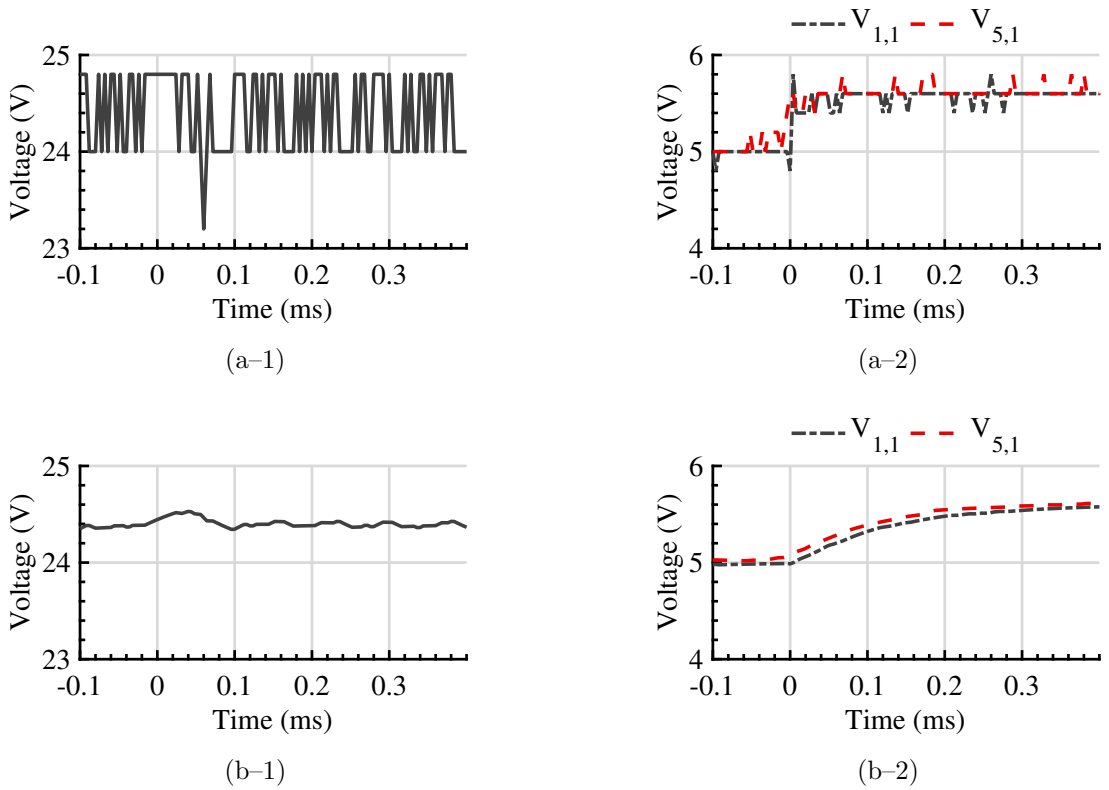

Figure 2.37: OC fault at $F_{3,1}$: V_{pv}, $V_{1,1}$, and $V_{5,1}$ a) Measured b) Filtered and down-sampled.

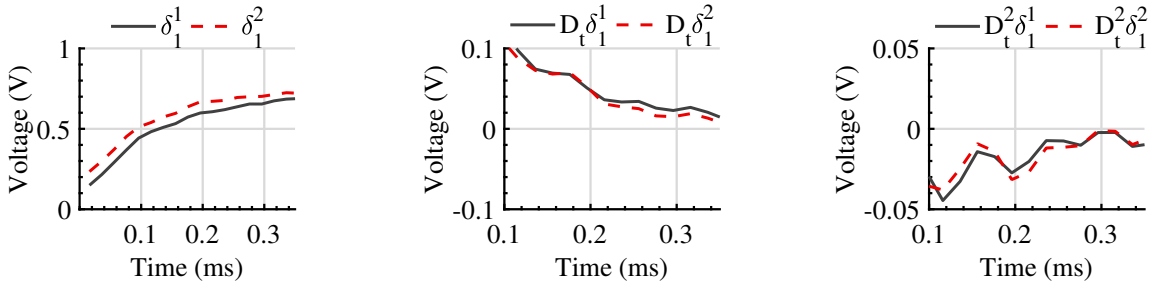

Figure 2.38: OC fault at $F_{3,1}$: a) δ_1^1 and δ_1^2 along with their b) first derivatives, and c) second derivatives.

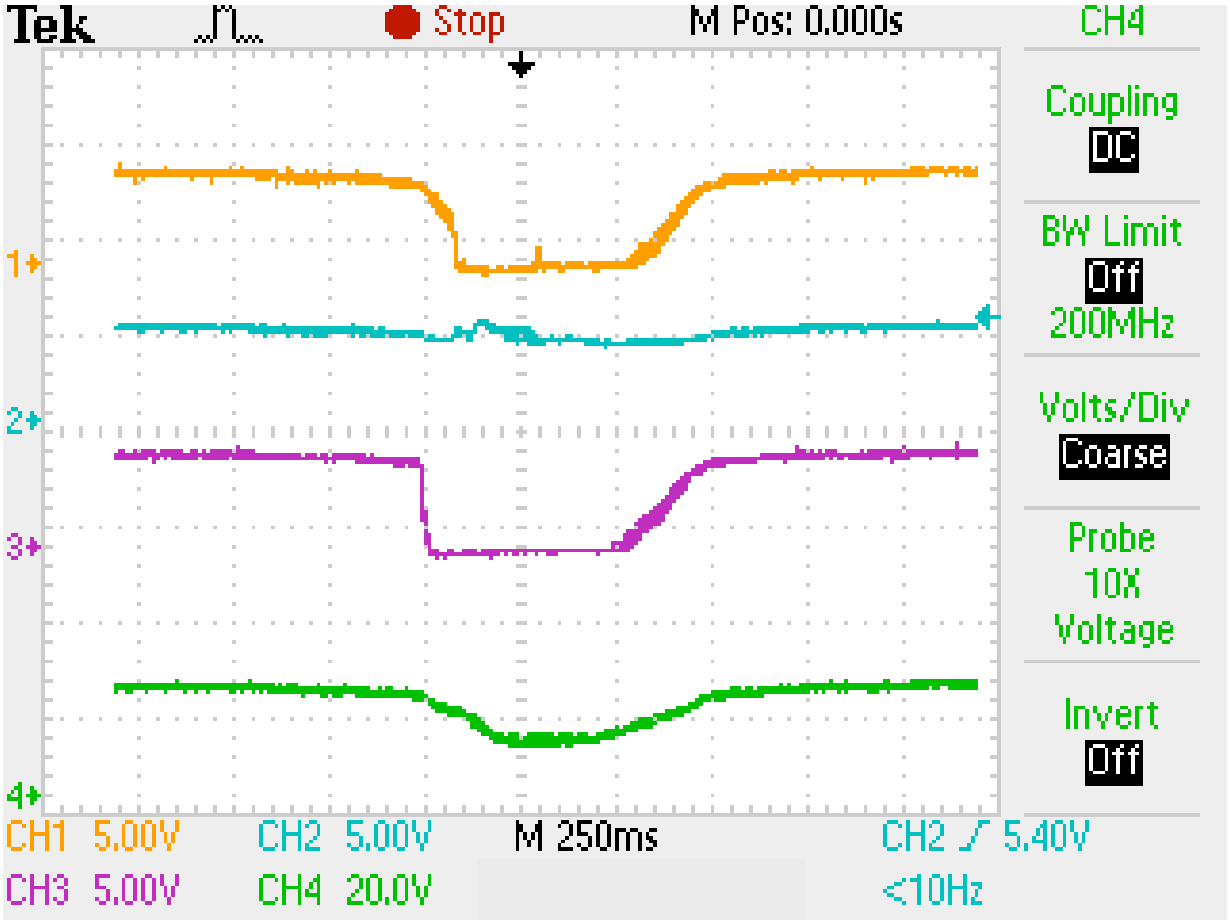

Figure 2.39: Oscilloscope measurements under a partial shading condition: CH1: $V_{5,2}$, CH2: $V_{1,2}$, CH3: $V_{5,3}$, and CH4: V_{pv}.

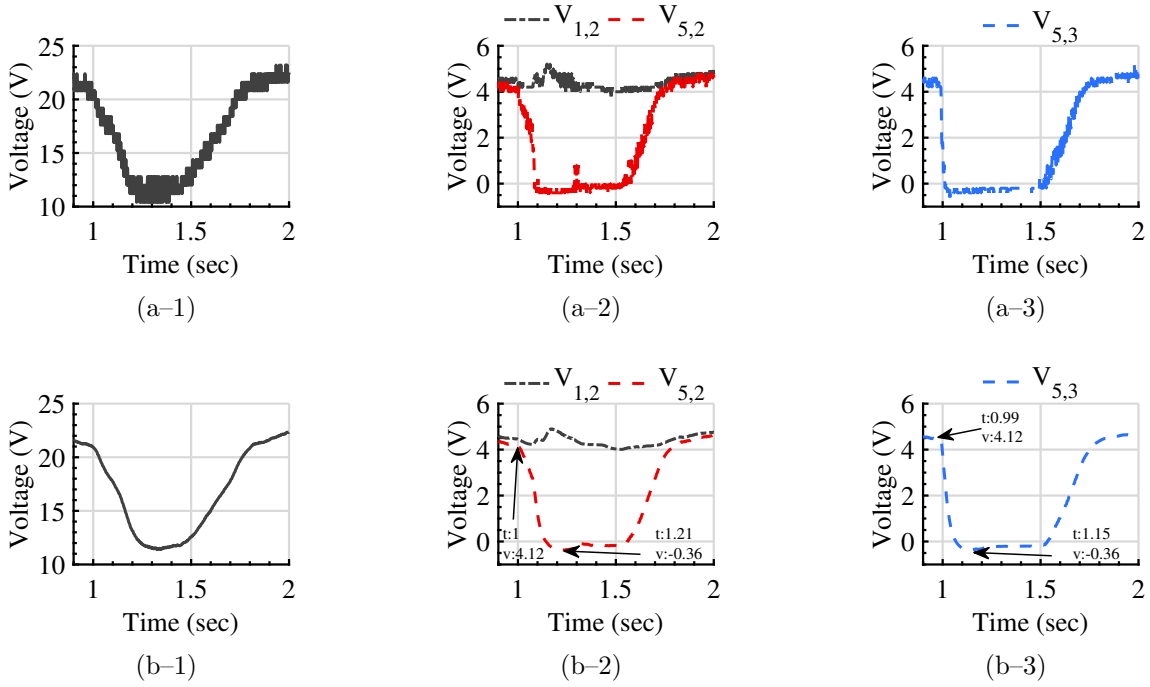

Figure 2.40: Partial shading condition: V_{pv}, $V_{1,2}$, $V_{5,2}$, and $V_{5,3}$ a) Measured b) Filtered and down-sampled.

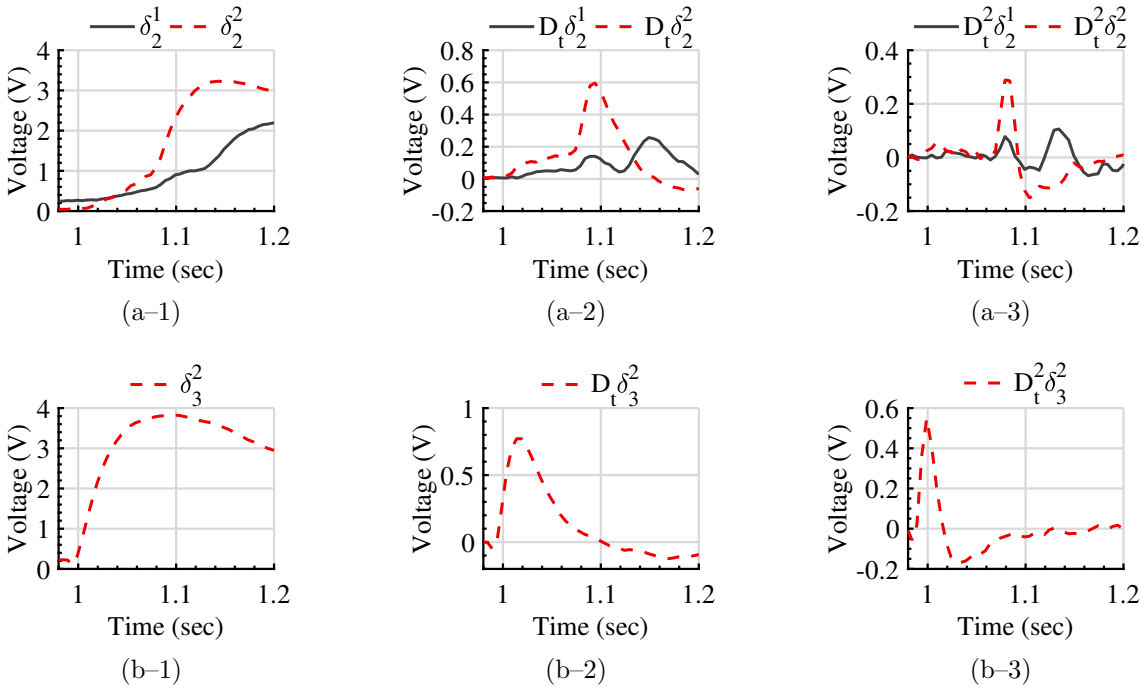

Figure 2.41: Partial shading condition: δ_m^1 and δ_m^2 along with their first and second derivatives for a) string 2 and b) string 3.

2.7 Conclusion

This chapter proposed a protection scheme that detects, classifies, and locates SG, SS, and OC faults in utility-scale grounded PV arrays. The scheme relies on a central IED located at the inverter, in addition to two voltage transducers on each string. The simulation and experimental results highlight the following features of the proposed method.

- Selectivity: Unlike existing schemes that trip an entire PV array with central inverter configuration during ground faults, the proposed scheme isolates the faulted string only while allowing normal operation of the healthy strings.
- Sensitivity: Section 2.5.3 demonstrates that, unlike conventional PV protection methods, the proposed scheme is sufficiently sensitive to detect, classify and locate high-impedance (up to 100 Ω) SG and SS faults with small location mismatch that have very low fault current.
- Speed: The proposed method detects faults in less than 15 ms.
- Scalability: The successful operation of the proposed method is demonstrated for three different PV array sizes, namely: 1) 10×10, 2) 33×125, and 3) 5×3.
- Model independence: The proposed scheme is model independent as 1) the underlying concepts of the proposed method were analytically proved for generic PV modules in Sections 2.2 and 2.3, 2) the proposed method was validated using PSCAD/EMTDC's built-in model of PV panel [80], [81], and 3) the proposed method was verified experimentally using polycrystalline-silicon panels (Section 2.6).
- Fault classification: This feature facilitates identifying and removing the cause of the fault.
- Fault location: The proposed method accurately locates SG and SS faults within the faulted strings.

In future works, attempts will be made to extend this work to PV systems with micro-inverters. Moreover, the partial shading detection capability makes the proposed method

valuable for partial shading mitigation studies. Hence, the proposed method can be further extended for such studies to detect the number and location of partially shaded modules.

Chapter 3

Hybrid Passive-Overcurrent Protection Scheme for LVDC Microgrids

As stated in Chapter 1, detection of high-resistance faults on meshed LVDC microgrids poses a challenge as such faults have very low fault current magnitudes. This chapter proposes a hybrid passive-overcurrent relay to overcome this problem. The proposed relay consists of one current and one voltage transducer as well as two passive elements; an inductor and a capacitor. For bolted and relatively low-resistance faults, the relay uses a simple overcurrent function to detect the resultant high fault current magnitudes within 2 ms. On the other hand, for relatively high-resistance faults, a real-time discrete DWT is used to detect the voltage transients generated by the relay passive elements in less than 5 ms. Furthermore, the proposed relay is inherently capable of identifying the type of fault. The proposed approach relies on local-bus measurements to detect and classify various types of faults with resistance up to 200 Ω. Analytical modelling proves that the proposed approach is system independent. Testing the hybrid passive-overcurrent relay on a ±750 V meshed TN-S DC microgrid reveals that the proposed relay is fast, sensitive, and selective under various conditions.

3.1 Meshed LVDC Test Microgrid

The LVDC test microgrid of Figure 3.1, developed using PSCAD/EMTDC, is structurally similar to the distribution portion of the IEEE 14-bus system architecture [82]. Two-level VSCs are utilized to interface the LVDC microgrid with the AC grid, sources, and loads. As can be seen in Figure 3.1, the meshed LVDC microgrid is connected to a 1 MVA AC-grid at bus 1, which acts as the slack bus. Furthermore, two AC sources, rated at 200 kVA and 300 kVA, are interfaced to the LVDC microgrid at Buses 3 and 6, respectively. The VSC at bus 1 controls the DC voltage of the microgrid and operates at unity power factor. Additionally, a generic model is developed for the three PV DGs rated at 500 kW, 300 kW, and 200 kW, that are connected to Buses 2, 4, and 5, respectively. Each PV station is interfaced with the LVDC microgrid through a DC/DC boost converter that is controlled by a MPPT algorithm. Finally, a resistive load rated at 500 kW is interfaced through an open loop controlled DC/DC buck converter at bus 7.

The operating DC voltage is chosen to be ±750 V to follow European Union (EU) LVD2006/95/EC guidelines [8]. The cables are represented using the frequency dependent distributed parameter model available in PSCAD/EMTDC. Accordingly, 0.6/1 kV 1000 mm^2 single core cables with a copper conductor, XLPE insulation (2.8 mm thick) and PVC sheathing (2.4 mm thick) are adopted [83]. For each line, two identical cables (one for each pole) are buried 1 m deep, with a horizontal separation of 0.4 m. The resultant DC cable resistance and inductance are 0.017204 Ω/km and 3.3 mH/km, respectively. The cable length is assumed to be 1 km for all of the network lines. Figure 3.1 shows nodes F1 to F8, each of which represents either a PP or a PPG fault.

The grounding configuration most commonly recommended by the EU and international standards is the TN-S grounding scheme [84], which provides midpoint grounding at each converter station. Finally, the developed microgrid is equipped with 16 relays, placed on the DC side to cover the eight lines. Each line consists of two poles, and thus the relays on the positive pole are denoted by superscript p, and those on the negative pole by superscript n. The forward direction of all the relays is set facing towards the lines.

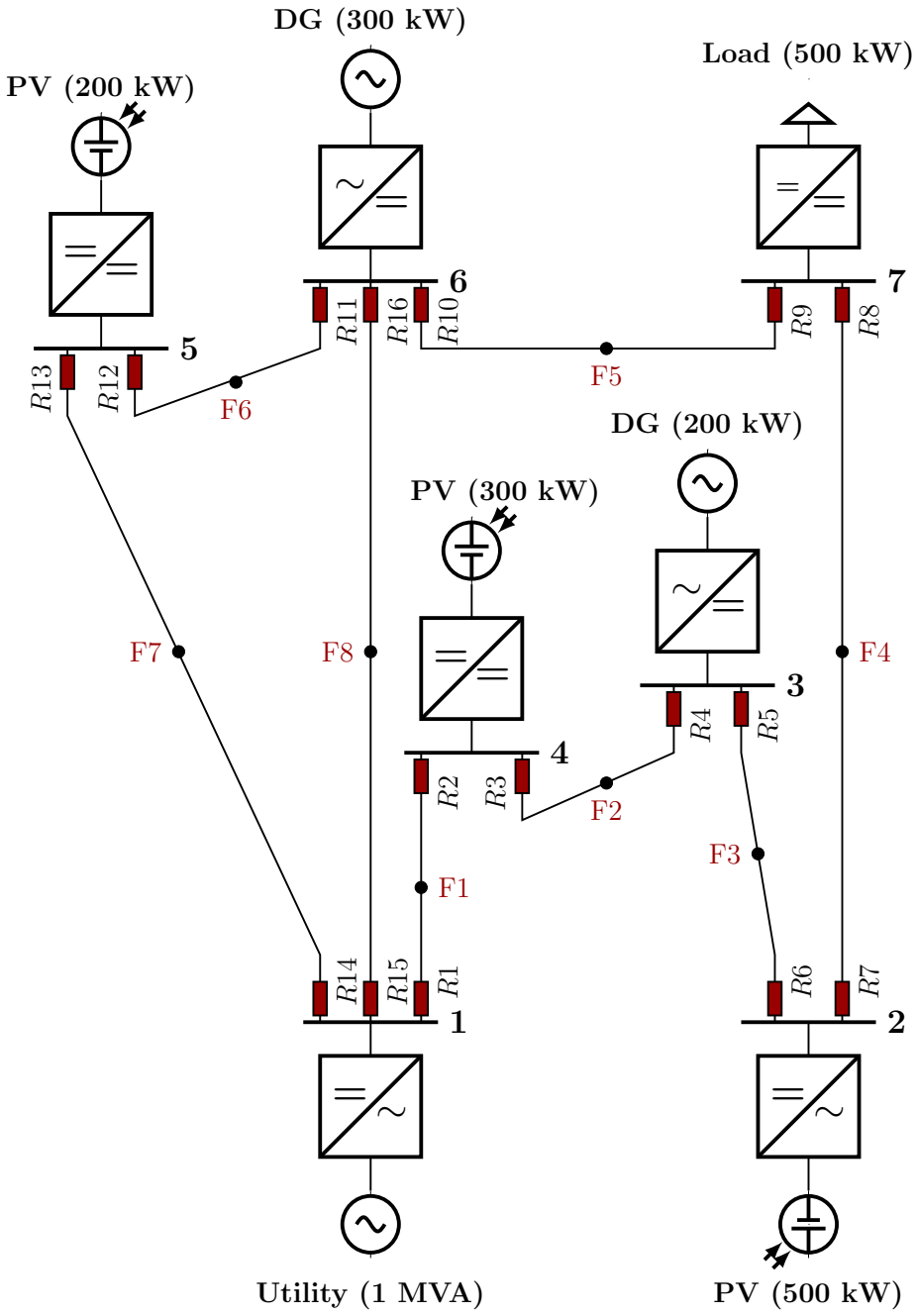

Figure 3.1: Single line diagram of the developed meshed LVDC test microgrid.

3.2 High-Resistance Fault Detection Problem

Several DC fault scenarios are investigated on the LVDC microgrid shown in Figure 3.1. First, bolted midpoint PPG and PP faults that occur on the line between Bus 1 and Bus 6 (F8) at 50 ms are simulated to investigate the most severe faults. Figure 3.2 shows the fault currents seen at the positive and negative poles of $R15$, denoted by by $R15^p$ and $R15^n$, respectively. For the bolted PP fault, both $R15^p$ and $R15^n$ sense huge fault current magnitudes reaching 4 kA within 2 ms. On the other hand, for the bolted PPG fault, only $R15^p$ senses large fault current magnitude reaching 4 kA within 17 ms, while $R15^n$ remains unaffected. The high fault current magnitude originates from the capacitor discharge stage of the DC fault [14], [36]. Therefore, PP faults should be detected before the diode freewheeling fault stage starts, to avoid damage to the converter switches and diodes [14]. PPG fault detection should also take place during the positive pole capacitor discharge stage, otherwise the system later goes into steady-state with the faulted positive pole grounded and the healthy negative pole operating at the full DC voltage (-1.5 kV) [40].

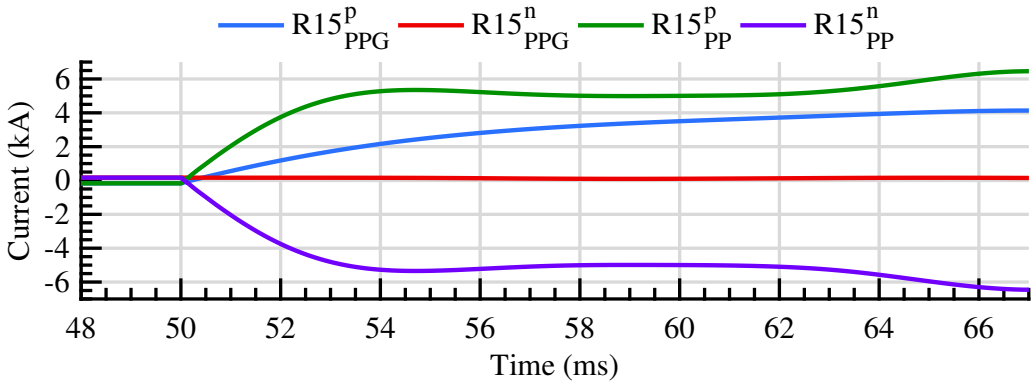

Figure 3.2: Fault currents seen by $R15^p$ and $R15^n$ due to bolted midpoint PP and PPG faults at F8.

Figure 3.3 indicates the fault current magnitudes denoted by I_f passing through the 10 Ω and 200 Ω fault resistances for both PP and PPG faults that occur at 50 ms on node F8. It can be noticed that the DC fault current still features a very high rate of change but

with a very low magnitude, which is limited by the fault resistance. Given the pole-to-pole 1.5 kV DC voltage, a 10 Ω PP fault results in a fault current magnitude of 150 A, while a 10 Ω PPG fault causes a fault current magnitude of 75 A. Similarly, the fault currents attained from 200 Ω PP and PPG faults are 7.5 A and 3.75 A, respectively.

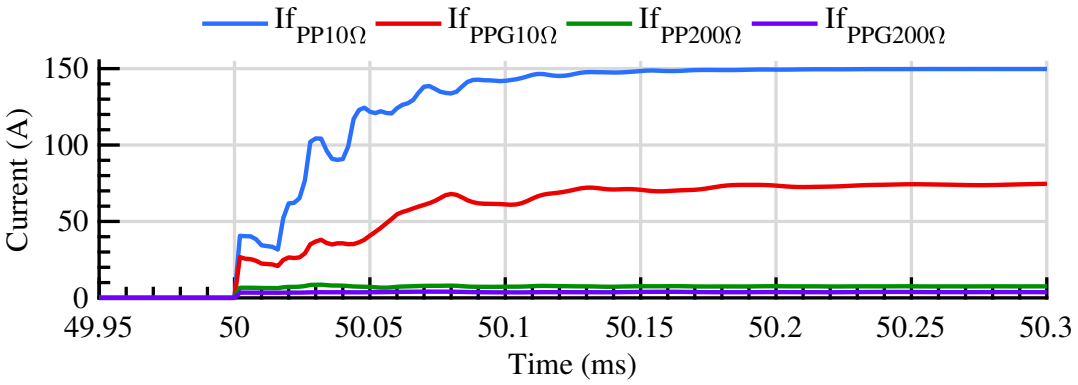

Figure 3.3: I_f passing through the 10 Ω and 200 Ω fault resistances for midpoint PP and PPG faults at F8.

The fault current seen by any relay is a fraction of the total fault current, because the LVDC test microgrid is meshed. Figure 3.4 shows the currents seen by one of the relays on the faulted line ($R15^p$ and $R15^n$) during the aforementioned faults. Before the fault, the currents measured by $R15^p$ and $R15^n$ are the same as the load current and equal to −167 A and +167 A, respectively. Based on the relays' direction convention noted earlier, the load current is flowing from Bus 1 to Bus 6. Once one of the above-mentioned non-bolted faults occurs at F8, the currents seen by $R15^p$ and $R15^n$ appear to decrease in magnitude with respect to the load current magnitude. The current seen by $R15^p$ reduces from −167 A to −92.5 A, −130.7 A, −163.6 A, and −165.6 A during 10 Ω PP, 10 Ω PPG, 200 Ω PP, and 200 Ω PPG faults, respectively. The currents seen by $R15^n$ for PP faults have the same magnitudes as $R15^p$ with opposite directions, while remaining unaffected for PPG faults. The fault current seen by a relay on one side of a faulted line $I_{f_{Rx}}$ can be computed using the following equation:

$$I_{f_{Rx}} = ||I_{load_{Rx}}| - |I_{fault_{Rx}}|| \tag{3.1}$$

where $I_{load_{Rx}}$ is the current seen by the relay in pre-fault condition, while $I_{fault_{Rx}}$ denotes the total current seen by the relay in fault condition. Accordingly, $I_{f_{R15}}$ for a 10 Ω PP, 10 Ω PPG, 200 Ω PP, and 200 Ω PPG fault is 74.5 A, 36.3 A, 3.4 A, and 1.4 A, respectively. None of the aforementioned faults results in $I_{f_{R15}}$ higher than $I_{load_{R15}}$ to be able to change the direction of the fault current to be towards the fault location. Hence, any relay located on the side with the current flowing out of the line (negative load current) experiences a reduction in the current magnitude if $I_{f_{Rx}}$ is lower than $I_{load_{Rx}}$ rather than an overcurrent. For such relays to sense overcurrent, the magnitude of $I_{f_{Rx}}$ should be at least twice $I_{load_{Rx}}$ to be able to first change the direction of the current to be towards the fault location (reaching zero), and then exceed it. This is clearly the case during the bolted faults indicated in Figure 3.2.

It can be noticed that the above-mentioned problem exists on LVDC microgrids not only for high-resistance faults such as 200 Ω, but also for faults with resistance of 10 Ω and lower. Conventional protection approaches fail to detect such faults. For instance, an overcurrent relay will sense a reduction in current during these faults, and thus does not operate. In a similar manner, it is difficult to set a threshold for a differential relay to effectively distinguish between non-fault transients and high-resistance faults such as 200 Ω ones. From the aforementioned results, it is concluded that even low-resistance faults in LVDC microgrids can limit the DC fault current magnitudes, which results in fault detection problems. Accordingly, an approach that does not depend on fault current magnitude is necessary.

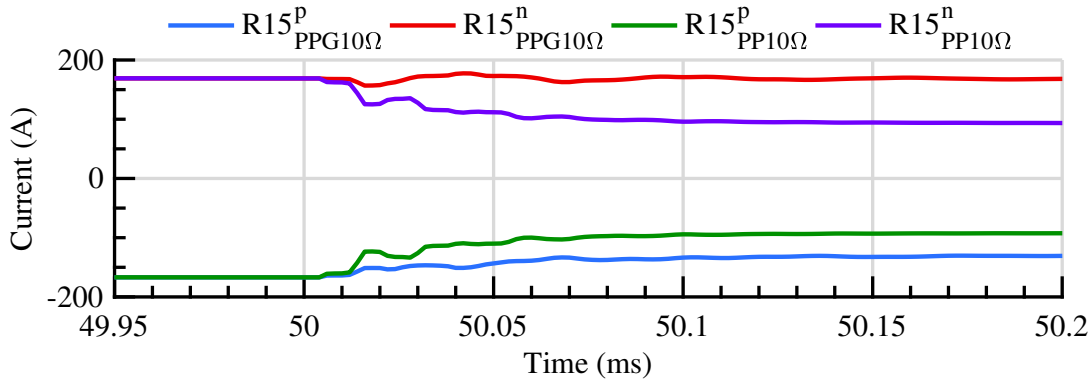

(a)

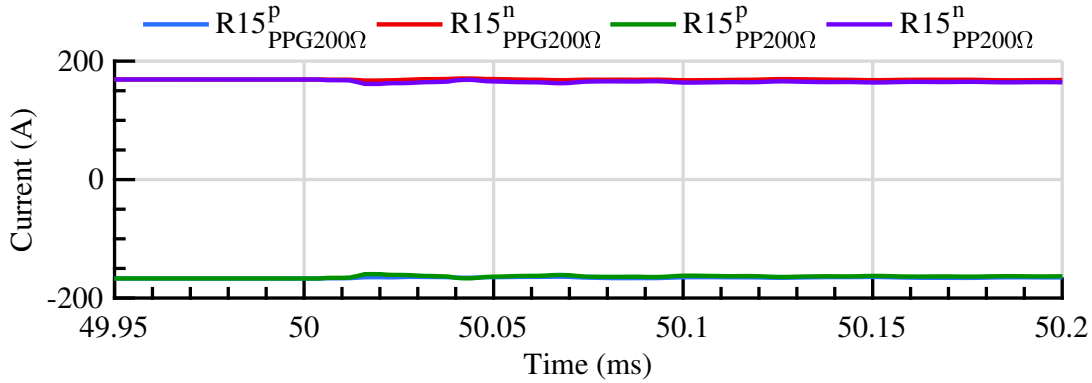

(b)

Figure 3.4: Fault currents seen by $R15^p$ and $R15^n$ due to a) 10 Ω and b) 200 Ω fault resistances midpoint PP and PPG faults at F8.

3.3 Hybrid Passive-Overcurrent Relay

3.3.1 Proposed Relay Analytical Modelling

The proposed relay is equipped with a simple passive circuit consists of a series inductor L_R that is in parallel with a capacitor C_R on each pole. In addition, the relay utilizes a current transducer that measures the pole current I_R, and a voltage transducer that measures the voltage V_R across the C_R. During steady-state conditions, L_R acts as a

short-circuit while C_R becomes an open-circuit, and hence, the existence of the relay does not affect steady-state operation. Yet, during DC fault conditions, the fault RLC circuit is formed, which drives the relay passive elements to resonance and consequently generating a damped frequency component F_d. Therefore, the idea is to design the relay passive elements to generate a specific F_d during DC faults that can be detected by an appropriate digital signal processing tool. The damped frequency F_d is a function of the natural radian frequency ω_n and the damping factor α_{dp}. Later in this subsection, analytical modelling will be presented indicating that α_{dp} value is negligible. Thus, the relays passive elements can be tuned to achieve the natural frequency F_n, as F_d becomes approximately equal to F_n and can be expressed as:

$$F_d = \frac{1}{2\pi\sqrt{L_R C_R}} \tag{3.2}$$

An appropriate F_d should be:

1. Higher than any frequency generated due to various non-fault transients. Under the assumption that the LVDC microgrid is fully interfaced with VSCs and DC/DC converters, the frequencies imposed by any non-DC-fault transients on the LVDC microgrid are limited by the converters. For AC/DC VSCs, sinusoidal components with frequencies of $2\omega_0$ and $6\omega_0$ are the most dominant harmonic frequencies that can be imposed on the LVDC microgrid due to non-fault or AC faults transients, where ω_0 is the AC-side fundamental radian frequency [85], [86]. Accordingly, 360 Hz is the highest frequency that can be imposed on an LVDC microgrid by any AC-side transients. Alternatively, for DC/DC buck and boost converters, the radian frequencies that exists on the LVDC microgrid are given by $\frac{1}{\sqrt{L_{conv}C_{conv}}}$ and $\frac{(1-D)}{\sqrt{L_{conv}C_{conv}}}$, respectively, where D is the duty cycle, and L_{conv} and C_{conv} are the respective converters' parameters [87]. In this study, 550 Hz is the highest frequency component that can be generated in the LVDC grid by transients from the DC/DC converters. Taking into account 10% as an additional safety factor, F_d must be higher than 605 Hz.

2. High enough to reduce the footprint and cost of the utilized passive elements based on users' design specifications. As indicated in (3.2), F_d is inversely proportional to the size of both passive elements.

3. Low enough to reduce the relay required sampling frequency. Most of the available commercial relays have sampling rates that can reach up to 8 kHz [88]. Thus, the selected F_d shall not exceed 8 kHz.

4. Set to a value that lies on the frequency band edge of one of the DWT signal decomposition levels. This criterion makes the number of samples per cycle equal to 2^L, where L is the signal decomposition level attained by DWT, which ensures a proper capture of F_d at the selected decomposition level [89].

Appropriately, F_d can be set to any value that satisfies the above criteria. To achieve good compromise between the footprint and cost of both passive elements, in this study, L_R and C_R are set to 50 μH and 50 μF, respectively, resulting in F_d equal to 3183 Hz, based on (3.2). It is worth noting that any other combination of L_R and C_R that results in F_d can also be considered.

The relay always operates during the capacitor discharge stage, because for bolted or low-resistance faults, the high current magnitudes occur during capacitor discharge stage. Moreover, for high-resistance faults, only a capacitor discharge stage takes place, because the DC voltage does not drop below the AC grid voltage, and hence eliminating the two latter diode freewheeling and grid injection stages [36]. Accordingly, Figure 3.5 shows the circuit models of the proposed relay during the capacitor discharge stage of PPG and PP faults, respectively. For brevity, detailed analytical modelling is presented only for the PPG fault circuit, whereas conclusions are drawn for both PPG and PP faults circuits.

The PPG fault circuit of Figure 3.5a consists of the positive pole capacitor ($2C_{dc}$), the relay passive elements (L_R^p, C_R^p), the cable parameters ($R_c{}^p$, $L_c{}^p$), and R_f. A switch with voltage V_{SW} is used to model the instance at which the fault occurs. A PPG fault is modelled by closing the switch SW, forming the capacitor discharge circuit, which is a fourth order RLC circuit. A state-space model is derived for this circuit (Figure 3.5a), in order to analyze the impact of system parameters and fault resistance on F_d by the proposed relay. The relay inductor current ($I_{Lr}{}^p$), the current passing through the cable $I_R{}^p$, the voltage across the relay capacitor C_R^p (V_R^p), and the positive pole DC link capacitor voltage ($V_c{}^p$) are the model state variables. V_{SW} is considered as the model input, and V_R^p

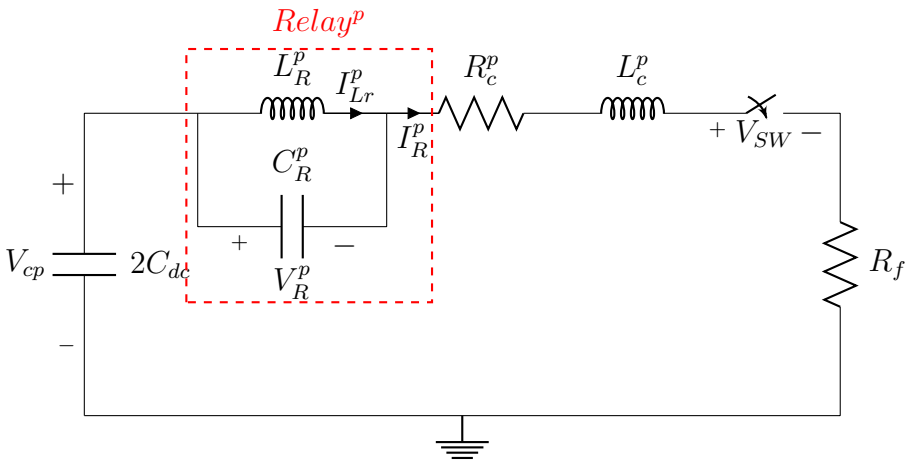

(a)

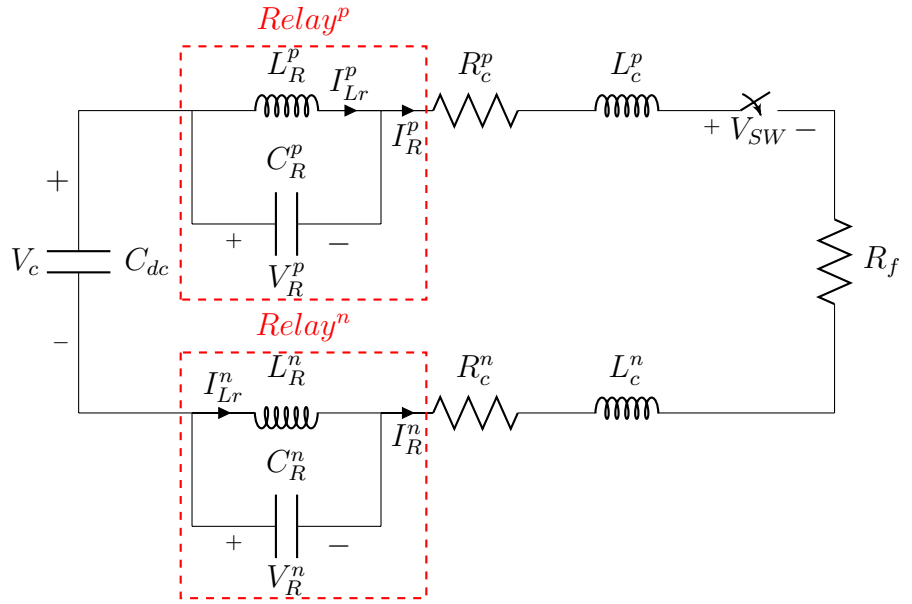

(b)

Figure 3.5: Circuit model of the proposed relay during the capacitor discharge stage of a) PPG and b) PP faults.

as its output. Below is the state-space representation for the the proposed relay during the

capacitor discharge stage of a PG fault:

$$\begin{bmatrix} \dot{i}_{Lr}^{p} \\ \dot{i}_{R}^{p} \\ \dot{v}_{R}^{p} \\ \dot{v}_{c}^{p} \end{bmatrix} = \begin{bmatrix} 0 & 0 & \frac{1}{L_R^p} & 0 \\ 0 & -\frac{R_c^p + R_f}{L_c^p} & -\frac{1}{L_c^p} & \frac{1}{L_c^p} \\ -\frac{1}{C_R^p} & \frac{1}{C_R^p} & 0 & 0 \\ 0 & \frac{1}{2C_{dc}} & 0 & 0 \end{bmatrix} \begin{bmatrix} i_{Lr}^{p} \\ i_{R}^{p} \\ v_{R}^{p} \\ v_{c}^{p} \end{bmatrix} + \begin{bmatrix} 0 \\ -\frac{1}{L_c^p} \\ 0 \\ 0 \end{bmatrix} v_{SW} \tag{3.3}$$

$$y(t) = \begin{bmatrix} 0 & 0 & 1 & 0 \end{bmatrix} \begin{bmatrix} i_{Lr}^{p} \\ i_{R}^{p} \\ v_{R}^{p} \\ v_{c}^{p} \end{bmatrix} + \begin{bmatrix} 0 \end{bmatrix} v_{SW} \tag{3.4}$$

Additionally, from the above state-space model, the following transfer function can be obtained [90]:

$$\frac{V_R^p(s)}{V_{SW}(s)} = \frac{z(s)}{p(s)} \tag{3.5}$$

where

$$z(s) = L_R^p s^2 \tag{3.6}$$

$$p(s) = C_R^p L_R^p L_c^p s^4 + \left(C_R^p L_R^p (R_c^p + R_f)\right) s^3 + \left(L_R^p + L_c^p - \frac{C_R^p L_R^p}{2C_{dc}}\right) s^2 + \left(R_c^p + R_f\right) s - \frac{1}{2C_{dc}} \tag{3.7}$$

It can be seen that this model results in one zero and four poles. One way to determine the effect of different circuit components on F_d and α_{dp} is to derive an expression for each pole. The poles' symbolic expressions are, however, very large, which makes it difficult to draw any useful conclusion. Therefore, numerical values are used to analyze the four poles. In order to mimic the LVDC grid, the cable parameters R_c^p and L_c^p are set as 0.017204 Ω/km and 3.3 mH/km, respectively. Moreover, $2C_{dc}$ is set to 17 mF, representing one of the VSC DC link capacitors. The relay passive elements are set as per design values ($L_R^p = 50$ μH and $C_R^p = 50$ μF). The model is examined under two scenarios: one with a bolted fault (R_f=0 Ω), and one with a high-resistance fault (R_f=200 Ω). Figure 3.6 shows the pole-zero map for both scenarios.

As expected, the bolted fault results in instability, as one of the poles is on the right of the imaginary axis (Figure 3.3.1). Whereas the 200 Ω fault does not cause instability,

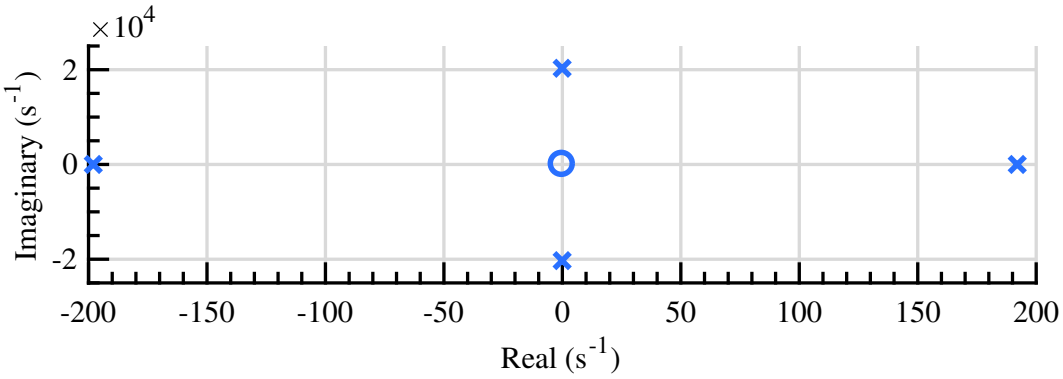

(a)

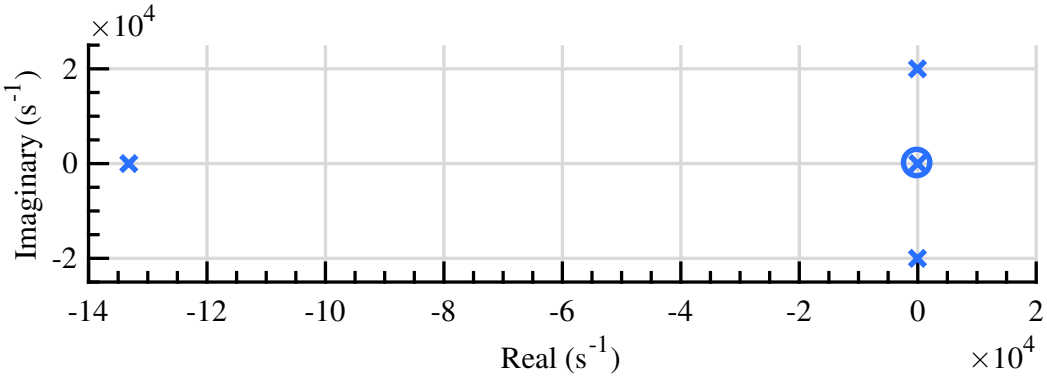

(b)

Figure 3.6: Pole-zero map for a) a bolted and b) 200 Ω fault.

as all of the poles are on the left of the imaginary axis (Figure 3.6b). The two poles out of four that changed dramatically with the change in fault resistance correspond to the system parameters ($2C_{dc}$, R_c^p, L_c^p). Yet, it can be noticed that the two other poles encounter minimal impact with the change in fault resistance. These poles correspond to the relay passive elements (C_R^p, L_R^p). In the case of a bolted fault, these two poles are $-0.0925 \pm 20300j$, while for a 200 Ω fault, they are $-48.9 \pm 20000j$. The change in the fault resistance affects α_{dp} (the real part). As fault resistance increases, α_{dp} increases slightly, corresponding to higher damping. Such result is in line with typical RLC circuits

responses. On the other hand, change in the fault resistance have minimal impact on ω_d (the imaginary part). Since $\omega_d = \sqrt{\omega_n^2 - \alpha_{dp}^2}$ and α_{dp} is negligible with respect to ω_d, then ω_d approximately becomes ω_n. Therefore, regardless of the fault resistance, the relay passive elements will generate F_d that is very close to F_n, easing the fault detection. On the other hand, if the relay passive elements do not exist, the fault response can change widely depending on the fault resistance, making detection very difficult. The fact that α_{dp} is small means that the generated transient will remain on the faulted pole for a long time (in the range of seconds). This situation does not raise any concern since the faulted pole will be tripped.

Figure 3.7 presents the impact of varying $2C_{dc}$ and cable parameters (R_c^p, L_c^p) on F_d under three scenarios; 10 Ω, 50 Ω, and 200 Ω fault resistances. The variation of the cable parameters (R_c^p = 0.017204 Ω/km and L_{cp} = 3.3 mH/km) is implemented by changing the length of the cable up to 40 km. It can be observed that for high-resistance faults (200 Ω), changes in the system parameters have no impact on F_d as it remains at 3183 Hz. However, as the fault resistance decreases, the cable parameters start to have a small impact on F_d, while F_d remains unaltered by the changes in the DC link capacitor. F_d tends to increase only slightly for near-end faults (below 1 km) with lower values of R_c^p and L_c^p. In conclusion, this analysis proves that the proposed approach is neither system nor fault resistance dependent.

The circuit model of the proposed relay during the capacitor discharge stage of PP fault is a sixth-order RLC circuit (Figure 3.5b). Similar analysis can be conducted to obtain the six poles for this circuit. Four of these poles will correspond to the positive and negative pole relays. Hence, the conclusions drawn for PPG faults also apply to PP faults.

For simplicity, the aforementioned analysis assumed ideal inductor and capacitor, that is to say without losses or any parasitic elements. However, in practice, both the inductor and capacitor of the relay exhibit parasitic effects. According to [91], an LC tank resonant circuit experiences small signal attenuation and downward shift in the desired oscillation frequency due to the presence of these parasitics. Yet, as with the system parameters discussed above, slight changes to F_d do not affect the proposed method.

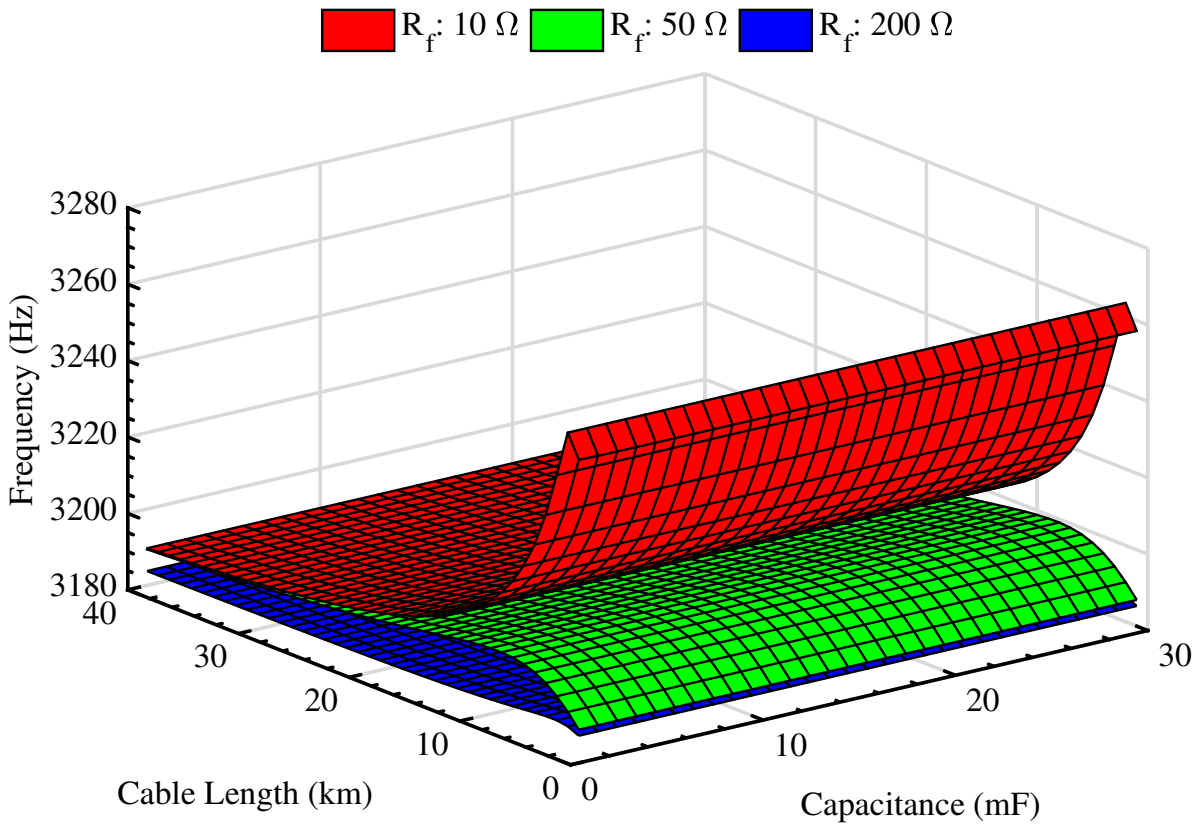

Figure 3.7: Plot of F_d versus changes in the DC link capacitor $2C_{dc}$ and cable parameters for 10 Ω, 50 Ω, and 200 Ω faults.

3.3.2 Proposed Relay Algorithm

Figure 3.8 shows the flowchart of the proposed algorithm for relays on the positive poles. The same algorithm is implemented for relays on the negative pole, but with opposite notations. The algorithm consists of two sequential parts: fault detection and classification. The algorithm starts by measuring both I^p_{Ri} and V^p_{Ri} at a given sampling frequency F_s, where the subscript i denotes the examined relay. If I^p_{Ri} exceeds the later-discussed pickup current I_{pu} threshold, then the relay utilizes the overcurrent function; otherwise, DWT is applied on V^p_{Ri} to detect the fault. This condition is set to enable the detection of

DC faults with very high rate of current change and magnitude within a short period to avoid converter damage. According to [14], high magnitudes are attained within the capacitor discharge stage, which affects only the cables. In general, the cables have high thermal inertia [14]. The maximum permissible short circuit current is 490 kA for 0.1 s [83]. Therefore, to ensure that the relay operates only for fault conditions, and that the fault is detected before the diode freewheeling stage, I_{pu} is set to 1 kA, which is the value of the current rating of the cable with an additional 10% safety factor [83]. Overcurrent function is selected since it provides fast and accurate fault detection for faults with high magnitudes while relying on local measurements only. On the other hand, if I^p_{Ri} does not exceed I_{pu}, then DWT is used to detect any DC fault that does not have a high current magnitude. The details of overcurrent and DWT functions are discussed below.

Overcurrent Function

Once the fault current seen by the relay I^p_{Ri} exceeds I_{pu}, it is necessary to check whether the fault is on the protected line or an adjacent one. To achieve this function, the following equation is introduced:

$$I^p_{Ri} = \sum_{j,j\neq i}^{N} I^p_{Rj} + I^p_{conv} \tag{3.8}$$

where j refers to a relay on the examined bus, and N is the total number of relays on that bus. ${I_{conv}}^p$ is the current contribution from the converter on the same investigated bus. If (3.8) holds, a fault is detected on the protected line/pole at time ${tf_i}^p$. Otherwise, the fault is on another line and the relay should not operate. It is worth noting that the proposed method requires measurements of only the relays installed at the same bus (local-bus measurements) and is independent of any communication between different buses.

DWT function

DWT is a powerful signal processing tool that is capable of capturing detailed frequency features of a signal and localizing them in the time domain accurately [39], [89]. The DWT model of PSCAD is used in this study. Detail one signal decomposition level, $D1$, is used

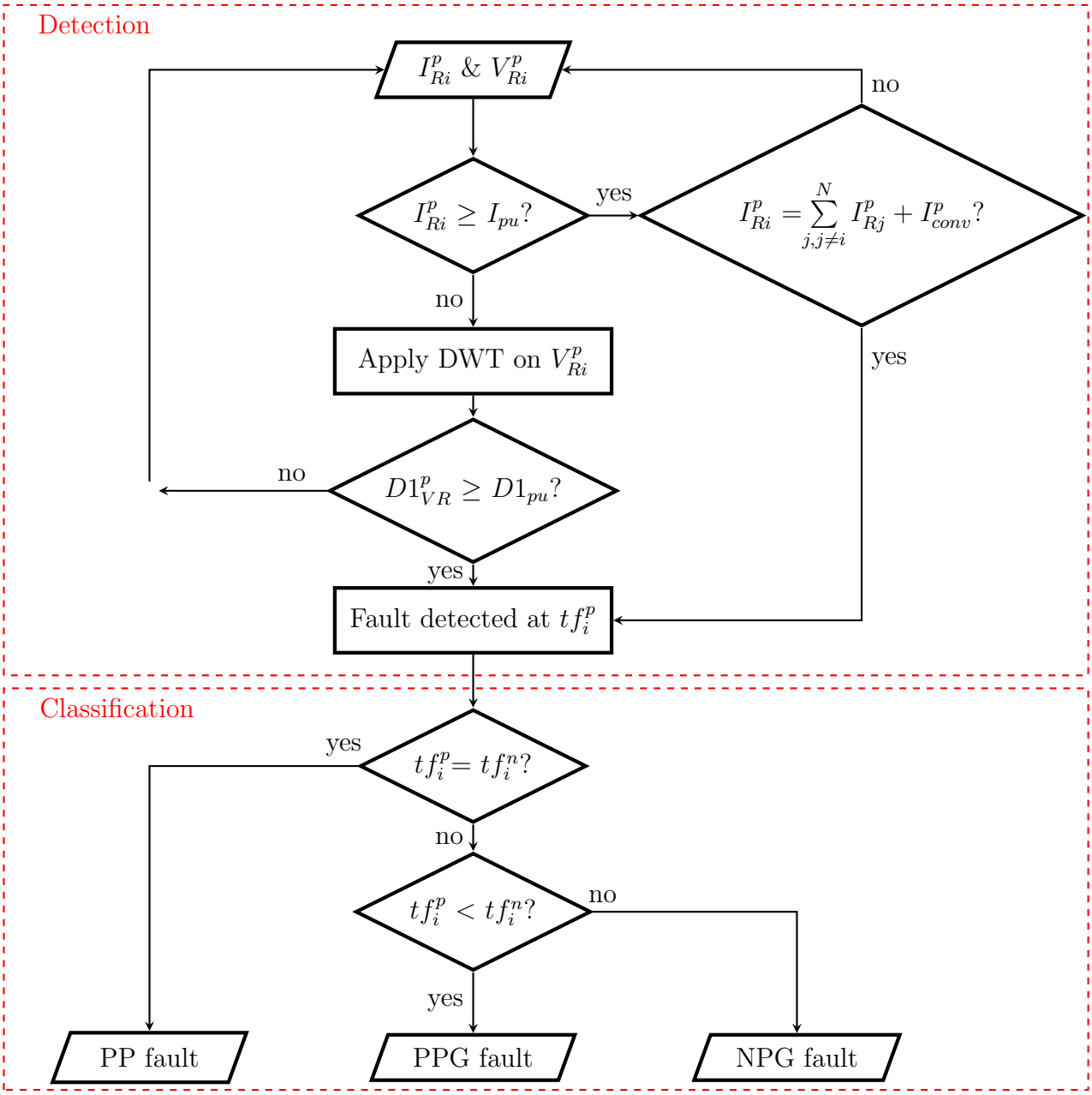

Figure 3.8: Proposed algorithm for relays on the positive poles.

to capture F_d. The frequency band of $D1$ is between $\frac{F_s}{2^L}$ and $\frac{F_s}{2(2^L)}$. Since F_d is 3183 Hz, a reasonable frequency band is between 1600 Hz and 3200 Hz to satisfy the above-mentioned F_d selection criteria. Accordingly, the relay sampling frequency, F_s, is set to 6.4 kHz.

Moreover, the type of mother wavelets used impacts the performance of DWT. There are several orthogonal wavelet families, among which Daubechies dbM are the most popular, where M is the order of the wavelet function [39]. Higher orders of the mother wavelet are more localized in the frequency domain and less localized in the time domain than the lower orders and vice versa. In this study, $db8$ is used, favouring frequency domain over time domain localization. Consequently, such mother wavelets hinders the fault detection speed of the DWT function. Nonetheless, the proposed method uses DWT to detect high-resistance faults during which the system is not in danger, and thus slow fault detection is permissible.

Based on the aforementioned discussion, the relay compares the 1st level detail wavelet coefficients of the capacitor voltage, denoted by $D1^p_{V_R}$ with a pre-defined Detail 1 pickup voltage $D1_{pu}$ (Figure 3.8). The value of $D1_{pu}$ is set to 1 V, which is much higher than the signal noise, and hence cannot be exceeded unless the analyzed signal contains frequencies spanning the band between 1600 Hz and 3200 Hz. Consequently, if $D1^p_{V_R}$ exceeds $D1_{pu}$, $D1^p_{V_R}$ captures F_d and a fault is detected at time tf^p_i. Otherwise, the algorithm keeps scanning the signal. Furthermore, as indicated in Figure 3.7, in some fault scenarios, F_d can go slightly above the $D1$ frequency band (3200 Hz). As the filters of DWT do not have ideal cut-off frequency characteristics [89], the faults are still detectable by $D1$. Hence, even for low fault resistances (F_d exceeding 3200 Hz), $D1$ can be used to detect F_d.

After the fault is detected at tf^p_i, the fault is classified by comparing tf^p_i with tf^n_i, which is the fault detection time of the relay i placed on the negative pole of the same line. If the fault is detected by the positive and negative pole parts of the relay and the respective detection times are almost equal, the fault is identified as PP. In commercial relays the measurement error tolerance is often specified as ± 5 percent of the measured value [77]. In this case, tf^p_i should be within $\pm 1.05 tf^n_i$ for the fault to be identified as PP. On the other hand, if the relay positive pole measurement detects the fault only, or does so before the negative pole relay, the fault is identified as PPG and vice versa.

It is worth mentioning that the proposed relay does not require fault resistance information. As illustrated in the flowchart of Figure 3.8, the proposed relay applies the overcurrent function first. If a fault is detected, the algorithm proceeds to the fault type classification subroutine. Otherwise, the DWT function is applied. Therefore, a threshold to choose between the overcurrent and DWT functions is not required.

3.4 Performance Evaluation

This section presents various case studies illustrating the performance of the proposed relay under a variety of fault conditions for the meshed LVDC microgrid of Figure 3.1.

3.4.1 Steady-State Analysis

This subsection assesses the performance of the proposed relay as well as its effect on the LVDC test microgrid under steady-state operation and non-fault transients. Initially, all buses operate at their rated powers. The power delivered and absorbed at different buses of the LVDC microgrid are varied in a stepwise manner by changing their respective set points to simulate non-fault transients at 800 ms, 1500 ms, 1650 ms, 1800 ms, 2000 ms, and 2200 ms, respectively. Figure 3.9 shows the positive pole load currents seen at different locations in the LVDC microgrid without the proposed relays ($R4^{p}_{w/o-Rel}$, $R7^{p}_{w/o-Rel}$, and $R15^{p}_{w/o-Rel}$), and with the proposed relays ($R4^{p}_{w-Rel}$, $R7^{p}_{w-Rel}$, and $R15^{p}_{w-Rel}$). It is clear that the load currents throughout the LVDC microgrid do not get affected by the presence of the passive elements of the proposed relay during steady-state operation and non-fault transient conditions. The reason behind such outcome is that none of the aforementioned conditions drive the LVDC microgrid to resonance, and thus the relay inductor ideally acts as a short-circuit and the capacitor acts as an open-circuit.

Furthermore, Figure 3.10 show V_R and $D1_{V_R}$ of the two relays ($R15$, $R16$) located on the line connecting buses 1 and 6 under the same non-fault transients and power variations throughout the system. It can be noticed that V_R transients can reach a magnitude of 1.2 V, yet these transients are not captured by the relay $D1_{V_R}$ as the magnitudes reach up

to 0.04 V only. This situation occurs because none of the these transients span the $D1_{V_R}$ frequency band. Thus, the relays' $D1_{V_R}$ do not reach the $D1_{pu}$ 1 V threshold, in line with the first criterion of F_d selection discussed in Section 3.3.1.

3.4.2 Faults With High Current Magnitude

This subsection presents the performance of the proposed relay overcurrent function in detecting a PPG bolted fault occurring on node F8 at 50 ms. Figure 3.11 presents the currents seen by $R15^p$, $R14^p$, $R1^p$, as well as the converter current I^p_{conv} located on different lines of bus 1 for the aforementioned fault. It is clear that all three relays as well as the

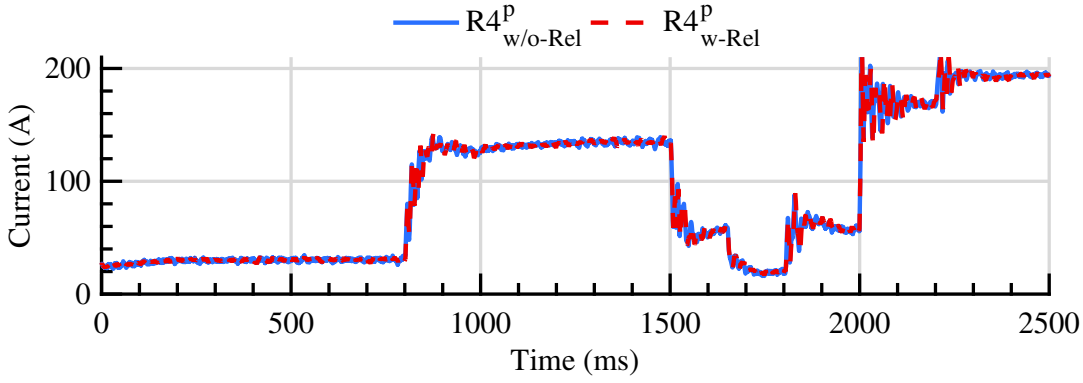

(a)

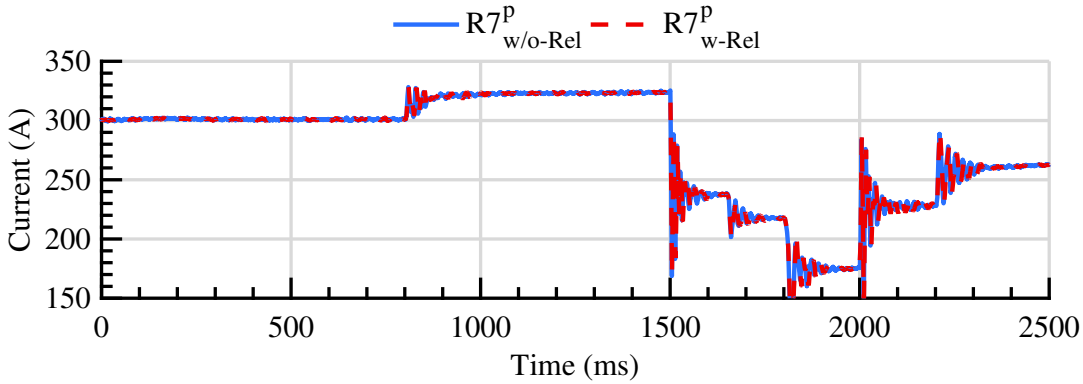

(b)

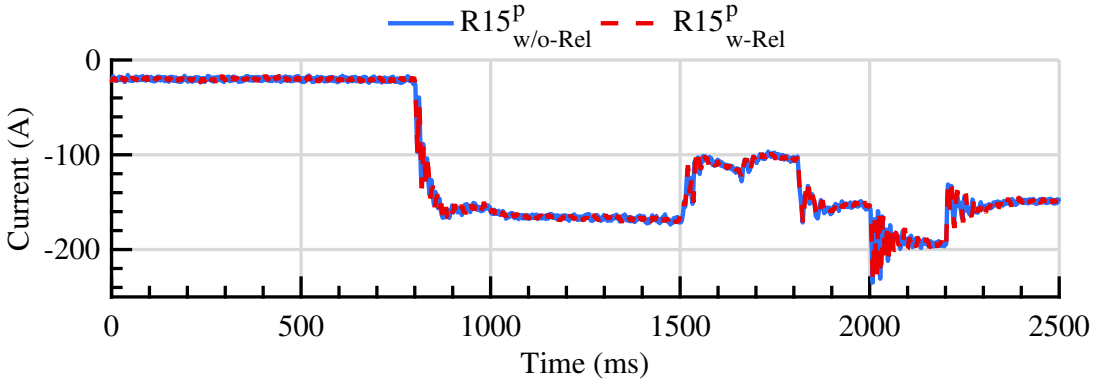

(c)

Figure 3.9: Positive pole load currents seen at a) $R4$, b) $R7$, and c) $R15$ on the LVDC microgrid without and with the proposed relays.

converter fault current contribution experience overcurrent. However, based on the relay proposed algorithm (Figure 3.8), $R15^p$ is the first to exceed I_{pu} (1 kA) after 1.78 ms of the fault occurrence. Once the threshold is passed, the condition expressed by (3.8) is checked, which corresponds to the following expression:

$$I^p_{R15} = I^p_{R14} + I^p_{R1} + I^p_{conv} \tag{3.9}$$

From Figure 3.11, it can be noticed that the summation of I^p_{R14}, I^p_{R1}, and I^p_{conv} is equal to I^p_{R15} at 51.78 ms. Hence, an in-zone fault is detected at $tf^p_{15} = 1.78$ ms.

3.4.3 Relay Sensitivity

To assess the sensitivity of the proposed relay, the fault with the lowest current magnitude in this study is presented. For the remaining case studies, all the stations of the LVDC microgrid are operating at their rated capacity. Figure 3.12 illustrates the V_R and $D1_{V_R}$ of the same two relays ($R15_{pn}$, $R16_{pn}$) under a 200 Ω PP midpoint fault at node F8 at 50 ms. It is observed that V_R of the two relays experiences sinusoidal decaying transients with a frequency of 3183 Hz that appear at the instance of the fault (Figure 3.12a). Yet,

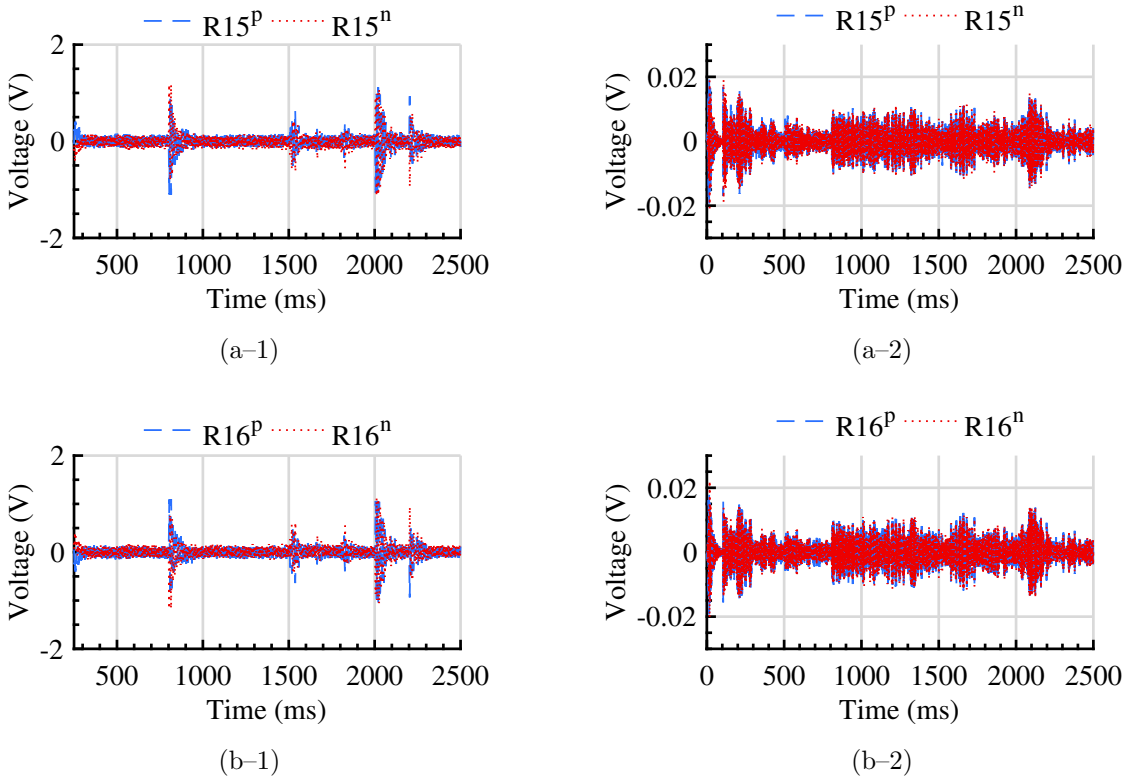

Figure 3.10: V_R and $D1_{V_R}$ of a) R15 and b) R16 under various non-fault transients.

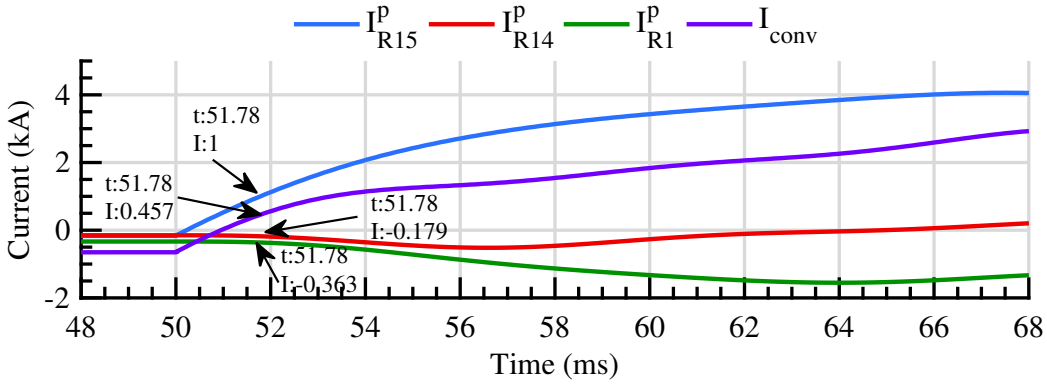

Figure 3.11: Currents at bus 1 for PPG bolted fault on node F8.

$R15^p$ and $R16^p$ experience exactly equal transients in magnitude and frequency because it is a midpoint fault, which is equal but opposite to the corresponding $R15^n$ and $R16^n$ because it is a PP fault. As expected, these signals are captured by DWT at the 1st detail (Figure 3.12b). It is clear that the two relays start crossing the $D1_{pu}$ threshold after 4.56 ms of the fault occurrence. It can be seen that $R15^p$ and $R16^p$ cross the negative threshold at the same time as $R15^n$ and $R16^n$ cross the positive one. Therefore, this fault can be accurately identified as a PP fault.

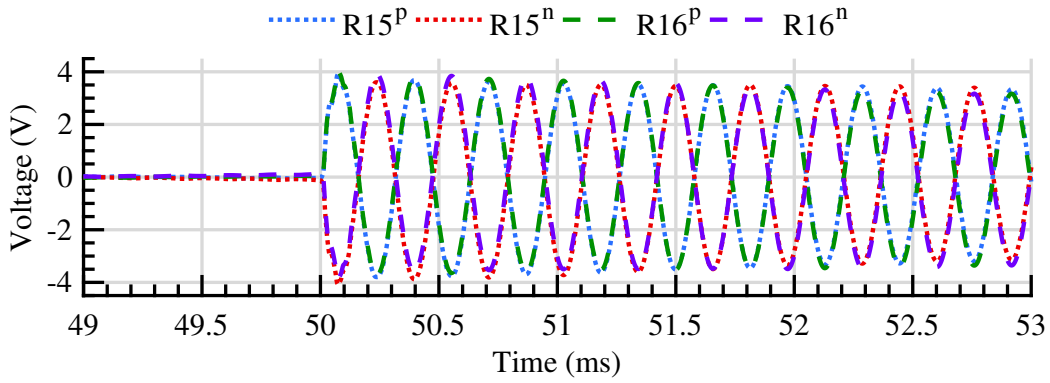

(a)

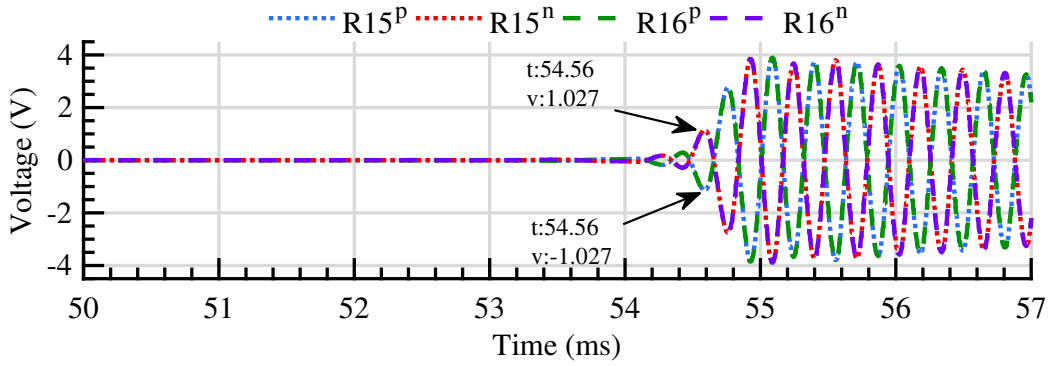

(b)

Figure 3.12: $R15$ and $R16$ a) V_R and b) $D1_{V_R}$ under midpoint 200 Ω PP fault on node F8.

3.4.4 Relay Selectivity

To ensure the selectivity of the proposed relay, Figure 3.13 shows $D1_{V_R}$ of the four relays $R1$, $R10$, $R11$, and $R14$ surrounding the faulted line for a midpoint 200 Ω PP fault at F8. It is clear that those relays do not see F_d, because all of the converters are grounded according to the TN-S configuration, making the generated traveling wave die once it reaches the converters' grounds and not propagate to other lines.

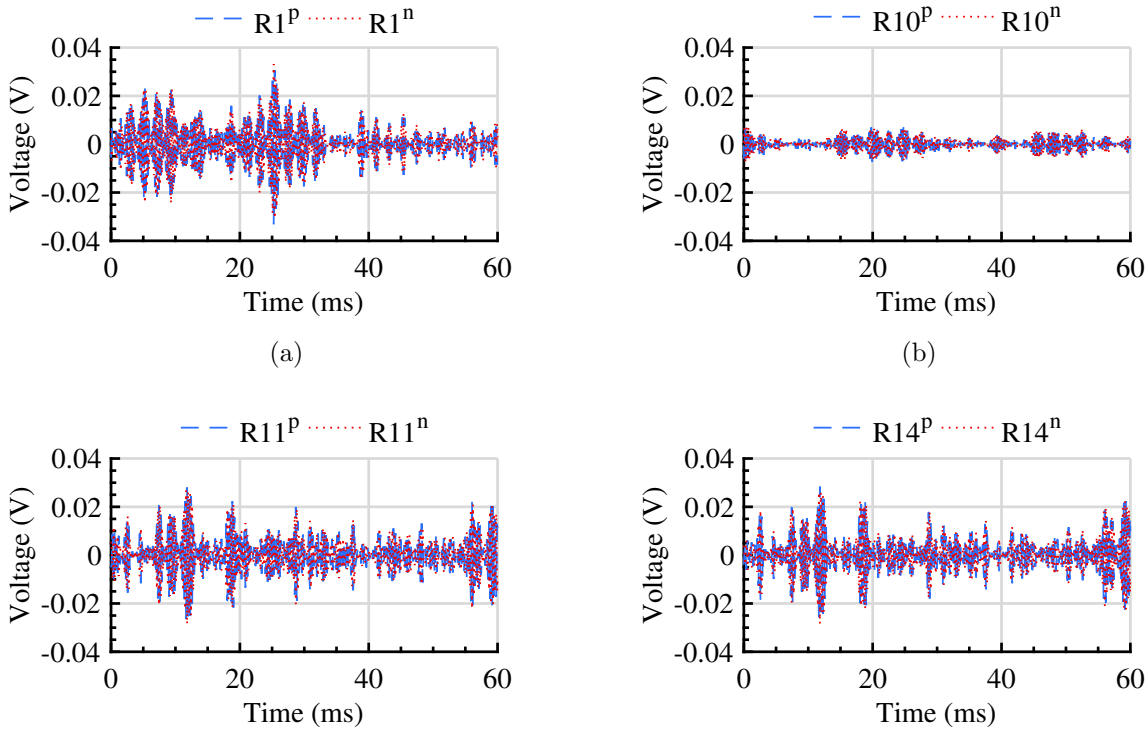

Figure 3.13: $D1_{V_R}$ of a) $R1$, b) $R10$, c) $R11$, and d) $R14$ under midpoint 200 Ω PP fault on node F8.

Figure 3.14 shows $D1_{V_R}$ of the two relays located on the faulted line for a midpoint 200 Ω PPG fault at F8. Only $R15^p$ and $R16^p$ respond to the fault, by generating F_d with a magnitude exceeding $D1_{pu}$, whereas, $R15^n$ and $R16^n$ are not affected. Since the fault is

detected only by $R15^p$ and $R16^p$ at $tf_{15}^p = 4.71$ ms and $tf_{16}^p = 4.71$ ms, respectively, the fault can be accurately identified as a PPG fault.

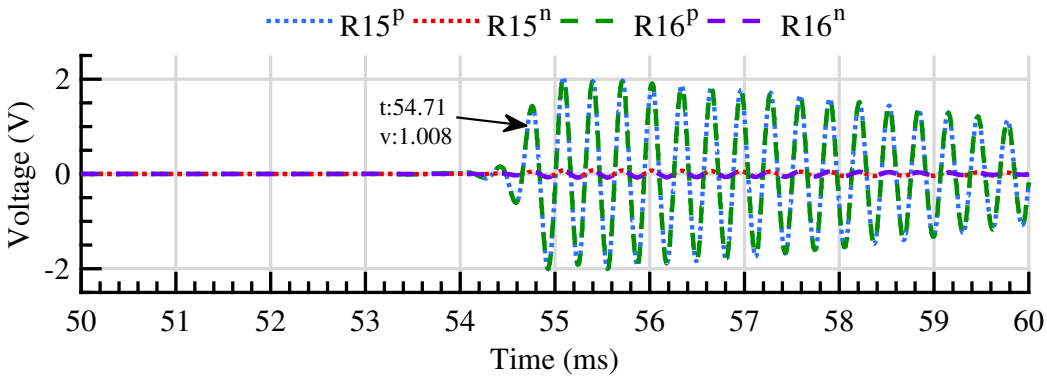

Figure 3.14: $D1_{V_R}$ of $R15$ and $R16$ under midpoint 200 Ω PPG fault on node F8.

3.4.5 Fault Resistances

To test the effectiveness of the proposed relay under various fault resistances, ten midpoint PPG faults are placed at F8 with different fault resistances ranging from 0 Ω to 200 Ω. Figure 3.15 compares the fault detection times of $R15^p$ for PG faults at F8 with different resistances. As can be seen, $R15^p$ is able to detect all PPG faults in less than 5 ms.

3.4.6 Fault Locations

Several 10 Ω PPG and PP faults are conducted on three different lines and three locations on each line (Near-End, Midpoint, and Far-End) of the test LVDC microgrid. Table 3.1 presents the fault detection times of the respective relays on the faulted line for each fault scenario. It can be seen that 10 Ω faults are always detected in less than 5 ms. It is also noticed that for near-end and far-end faults, the relay closer to the fault operates faster than the one on the other side of the line. Yet, for midpoint faults, both relays located on the faulted line operate at the same time. In addition, Table 3.1 indicates that

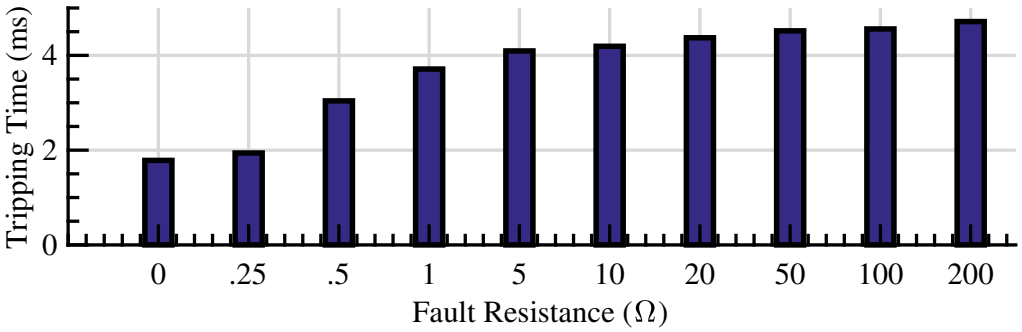

Figure 3.15: $R15^p$ detection times due to midpoint PG faults on node F8 with different fault resistances.

exactly the same operating times are obtained for the fault scenarios conducted at F1 (on the line connecting AC/DC and DC/DC boost converters), F4 (connecting DC/DC boost and DC/DC buck converters), and F8 (connecting two AC/DC converters). This occurs because all converters used in an LVDC microgrid have a DC link capacitor irrespective of their typology. Consequently, any converter will have the same initial DC fault response, namely, the capacitor discharge stage.

3.4.7 Mother Wavelets

This subsection assesses the performance of lower-order mother wavelets such as $db1$ against the proposed relay with its high-order mother wavelets such as $db8$ to detect a 200 Ω near-end PPG fault that occurs on node F8. Figure 3.16 illustrates the corresponding $D1_{V_R}$ of $R15^p$ and $R16^p$. It can be seen that by utilizing $db1$, $R15^p$ located near the fault can detect the fault within 310 μs (cross $D1_{pu}$ threshold). This makes $db1$ much faster than its $R15^p$ counterpart that uses $db8$ as it detects the fault after 4.69 ms. On the other hand, $R16^p$ located far from the fault cannot detect the fault (does not cross $D1_{pu}$ threshold) if $db1$ is used, but it can detect the fault after 5.53 ms if $db8$ is utilized. Consequently, despite the superiority of $db1$ over $db8$ in terms of fault detection speed, it can potentially fail to operate under such fault conditions, while the proposed relay with $db8$ is clearly

Table 3.1: Detection Times of 10 Ω Faults at Different Locations

Fault location		Fault Detection Times (ms)			
		PG Faults		PP Faults	
F1	Near-End	$R1^p$: 4.176	$R2^p$: 4.514	$R1$: 3.756	$R2$: 4.362
	Midpoint	$R1^p$: 4.192	$R2^p$: 4.192	$R1$: 4.148	$R2$: 4.148
	Far-End	$R1^p$: 4.514	$R2^p$: 4.176	$R1$: 4.362	$R2$: 3.756
F4	Near-End	$R7^p$: 4.176	$R8^p$: 4.514	$R7$: 3.756	$R8$: 4.362
	Midpoint	$R7^p$: 4.192	$R8^p$: 4.192	$R7$: 4.148	$R8$: 4.148
	Far-End	$R7^p$: 4.514	$R8^p$: 4.176	$R7$: 4.362	$R8$: 3.756
F8	Near-End	$R15^p$: 4.176	$R16^p$: 4.514	$R15$: 3.756	$R16$: 4.362
	Midpoint	$R15^p$: 4.192	$R16^p$: 4.192	$R15$: 4.148	$R16$: 4.148
	Far-End	$R15^p$: 4.514	$R16^p$: 4.176	$R15$: 4.362	$R16$: 3.756

more sensitive.

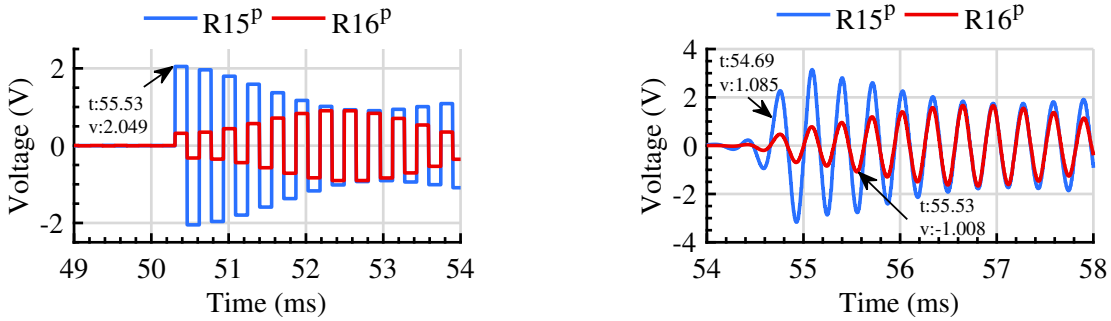

(a) (b)

Figure 3.16: $D1_{V_R}$ of $R15^p$ and $R16^p$ with a) $db1$ and b) $db8$ due to a 200 Ω far-end PG fault on node F8.

3.5 Conclusion

This chapter first presented the meshed LVDC test microgrid model and after that discussed the problems associated with detecting high-resistance faults in meshed LVDC microgrids and the shortcomings of present protection schemes. A hybrid passive-overcurrent relay is proposed to effectively detect low and high-resistance faults. The relay is equipped with two passive elements that generate a specific damped frequency during fault conditions. DWT is utilized to capture that frequency, and hence detect and identify the DC faults. For faster detection of bolted and low-resistance faults, an overcurrent function is used. The proposed relay operates based on local-bus measurements and requires a moderate sampling frequency. Analytical modelling has confirmed that the proposed method is system independent. Furthermore, in case studies conducted on a ±750 V meshed LVDC microgrid to assess performance, the proposed relay was shown to be fast, sensitive, and selective for both types of DC faults, with different resistances that can occur at various locations.

Chapter 4

Time-Domain TW-Based Protection Scheme for MVDC Microgrids

As discussed in Chapter 1, fast detection of dc faults in MVDC microgrids poses a challenge as such faults can cause severe damage to VSC within few milliseconds. This chapter proposes a new time-domain TW-based method to detect, classify, and locate different DC fault types in MVDC microgrids. Unlike the existing TW-based protection and fault location methods, the proposed technique (i) utilizes only the first locally measured TW after the inception of a fault, and (ii) focuses on the waveshape properties and polarity of the TW, rather than its arrival time. Therefore, the proposed method is faster than the existing techniques, and also requires no form of communication. As a result, it can effectively operate as both primary and backup protection. The proposed method is robust against high-resistance faults, and has been tested for fault resistances of up to 200 Ω. The performance of the proposed scheme has been assessed using a ±2.5 kV TN-S grounded MVDC microgrid under various conditions. The results verify the scheme's ultra-high-speed, accuracy, sensitivity, selectivity, and independence from system configuration. The concepts discussed in this chapter are independent of the voltage level. Thus, the proposed method can be applied to other types of DC grids as well.

4.1 MVDC Test Microgrid

The 12-bus test MVDC microgrid of Figure 4.1, modeled using PSCAD/EMTDC, is structurally similar to a portion of the DC microgrid in [46]. Two-level VSCs are utilized to interface the MVDC microgrid with the ac grid at bus 1 and the ac DG at bus 9. The voltage level is ±2.5 kV, which is typical for MVDC systems [65]. The VSC at bus 1 controls the dc voltage of the grid. Additionally, two PV DG units are connected to buses 4 and 12. Each PV unit is interfaced with the MVDC microgrid through a DC/DC boost converter that is controlled by an MPPT algorithm. Finally, DC loads are connected to buses 3, 7, and 11 using DC/DC buck converters.

The cables are represented using the frequency-dependent distributed parameter model available in PSCAD/EMTDC. Single-core 1.9/3.3 kV 1000 mm^2 cables with copper conductor, XLPE insulation (2.8 mm thick) and PVC sheathing (2.5 mm thick) are adopted [83]. For each line, two identical cables (one for each pole) are buried 0.6 m deep, with a horizontal separation of 0.4 m. The cable lengths between different buses range from 0.4 to 3 km.

The grounding scheme is TN-S, which is commonly recommended by different standards [84], and provides midpoint grounding at each converter station. Each line is equipped with two relays—one per terminal—that receive only the local current measurements of the positive and negative poles. The relay between buses i and j, next to bus i, is denoted by Rij. In this system configuration PP, PPG, and NPG faults can occur.

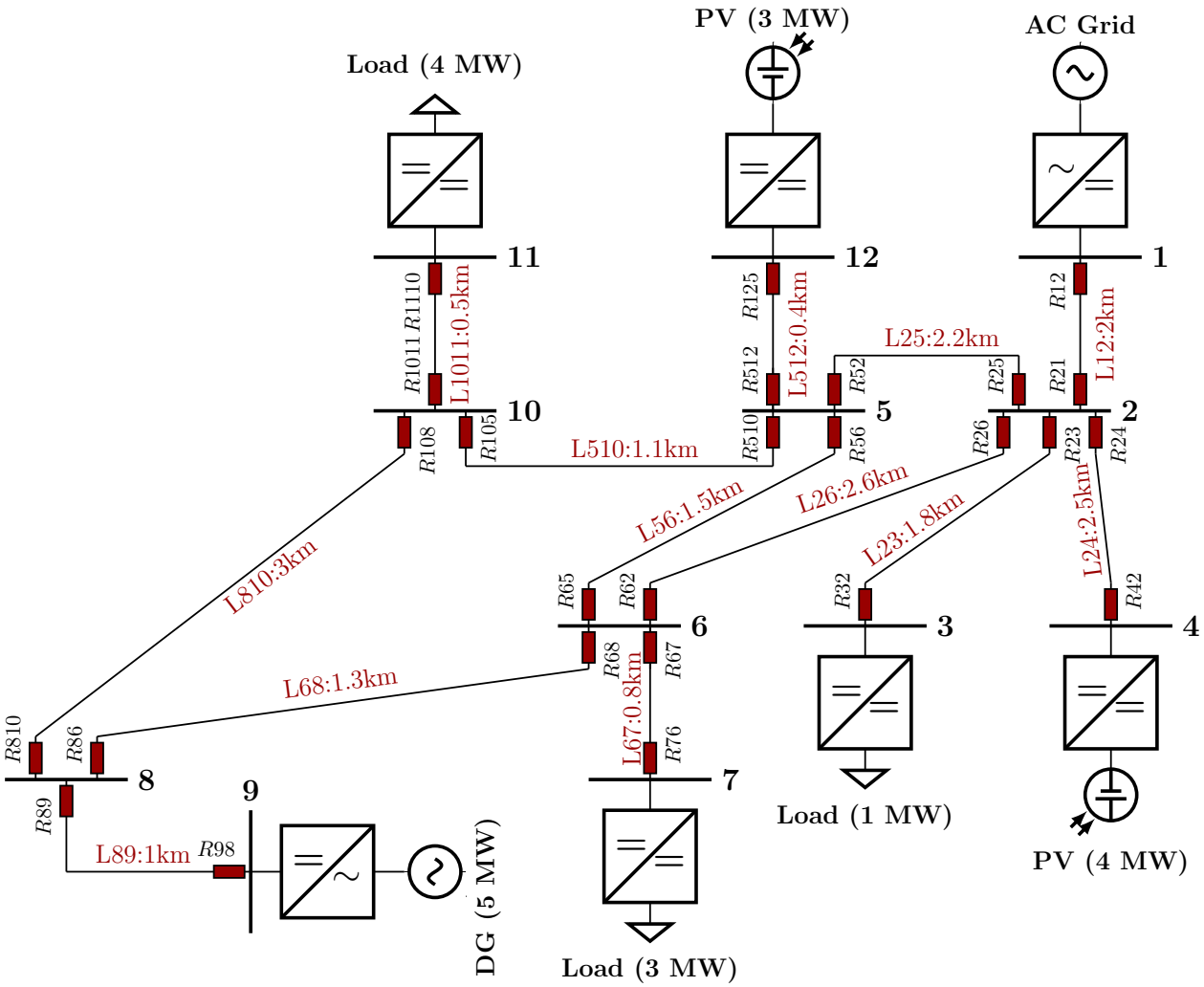

Figure 4.1: Single-line diagram of the test MVDC microgrid

4.2 Scrutiny of TW Signals

A fault launches voltage (v_{TW}) and current TWs (i_{TW}) that propagate in both directions from the fault location towards the line (or cable) terminals. i_{TW} is utilized in this chapter because its polarity can be used to identify the fault direction. The following elaborates on the two TW properties used to develop the proposed method.

4.2.1 Waveshape Properties

Once an incident TW reaches a junction or line terminal, a part of the TW is transmitted while the rest is reflected. i_{TW} can be expressed as [92]:

$$i_{TW}(\chi, t) = i_i(t)e^{-\gamma\chi} + i_r(t)e^{\gamma\chi} \tag{4.1}$$

where i_i and i_r are the incident and reflected current TWs, respectively. χ is the distance travelled by the TW from the fault to the measurement location. γ is the propagation constant, given by:

$$\gamma = \alpha + j\beta = \sqrt{(R_x + j\omega L_x)(G_x + j\omega C_x)} \tag{4.2}$$

where R_x, L_x, and C_x are the per unit length of line/cable resistance, inductance, and capacitance, respectively. Gx is the conductance per unit length of the cable's dielectric. ω is the angular frequency. The real part of γ is the attenuation constant (α), and the imaginary part represents the phase constant (β). The propagation velocity (v) varies for different frequency components of a TW and is expressed as [93]:

$$v = \frac{\omega}{\beta} \tag{4.3}$$

This relation shows that high frequency-components of a TW travel faster than low-frequency components. This phenomenon, referred to as dispersion, results in separation of different frequency components in the waveshape of a TW as it propagates through a conductor. The waveshape of a TW is also affected by the fact that the attenuation rate for different frequency components is not the same when a TW propagates through a conductor. α—the main cause of the TW attenuation—depends on R_x, which is directly proportional to the square root of the frequency of a component due to the skin effect [93], [94]. Thus, higher frequency components undergo more severe attenuation.

The frequency-dependent attenuation of the TW makes the higher frequency components of the spectrum relatively smaller. In addition, the lower velocity and late arrival of low-frequency components raise the settling time of the TW waveshape. As a result, propagation through a conductor diminishes the high-frequency share of a TW spectrum, which changes the shape of the TW. The longer the TW propagates, the more significant the waveshape changes [93].

To illustrate this phenomenon, a voltage that consists of three sinusoidal components with zero phase angle and frequencies equal to 2 MHz, 1 MHz, and 100 kHz is applied to a 3 km cable with specifications presented in Section 4.1. Figure 6.2 shows a 5 μs window of applying this voltage to the cable at two different locations. It is evident that the voltage waveform is smoothed as the voltage propagates along the cable. To investigate the attenuation rate of each frequency component as it travels through the cable, Fast Fourier Transformer (FFT) is applied to obtain the normalized spectrum of the two waveforms in Figure 6.2. Figure 4.3a shows that the three frequency components have equal amplitudes at the beginning of the cable. However, as the signal reaches the end of the cable, the 1 and 2 MHz components decline while the 100 kHz component remains the same (Figure 4.3b). Consequently, the cable functions, in effect, like a low-pass filter for the voltage of Figure 4.2a.

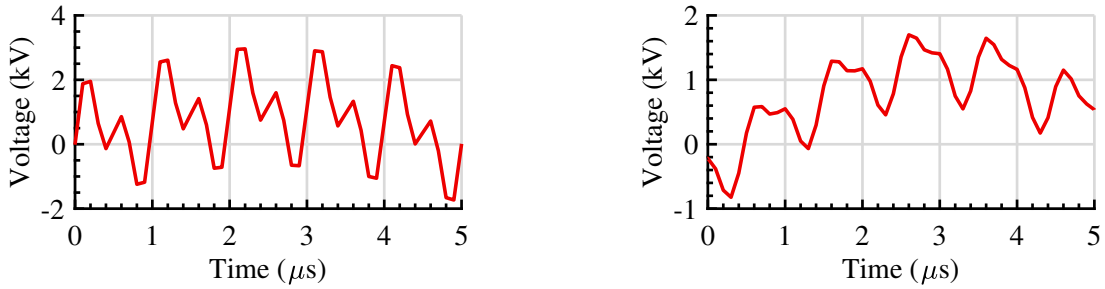

(a) (b)

Figure 4.2: A three-component voltage waveform at a) the beginning and b) the end of a 3 km cable.

The cable has similar effect on a fault-initiated TW, which has a step shape and thus an infinite spectrum at the fault location. To demonstrate this issue, consider a bolted PG fault on line $L12$ of the system in Figure 4.1. The fault is 0.95 km away from $R12$, 1.05 km away from $R21$ and $R23$, and 2.85 km away from $R32$. Figure 4.4 shows i_{TW} measured by $R21$ and $R32$ together with i_{TW} measured at the fault location. It can be seen that the sharp edge of the step TW waveshape at the fault location becomes smoother as it propagates through the system and reaches the relays. The decline in the high-frequency

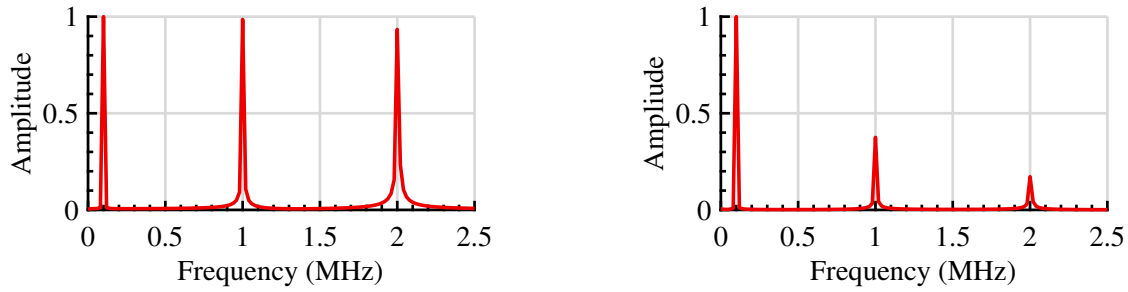

(a) (b)

Figure 4.3: The normalized spectrum of the voltage waveform at a) the beginning and b) the end of a 3 km cable.

components of the step waveshape as the TW moves away from the fault location makes the TW waveshape measured at relay locations approach an exponential shape. The farther is the relay from the fault location, the longer is the settling time of this exponential.

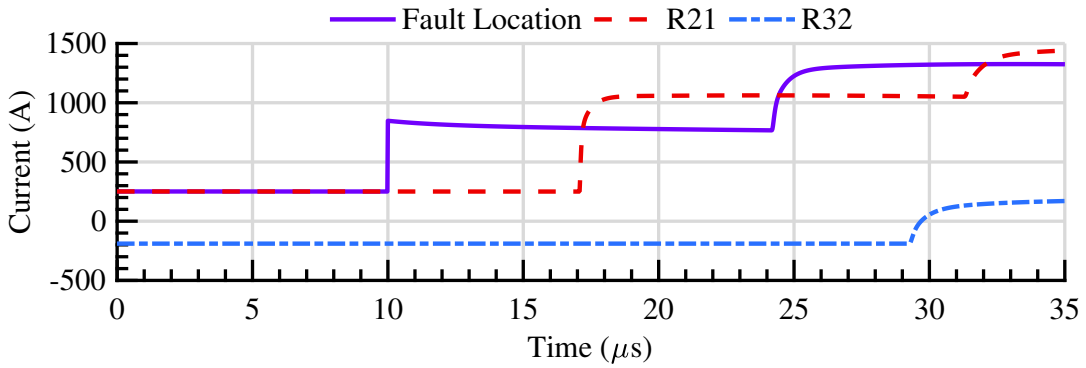

Figure 4.4: i_{TW} at the fault location, $R21$, and $R32$ due to a bolted PPG fault on $L12$.

The above variations of the TW waveshapes are undesired in most applications. For example, it limits the data transfer rate in fiber cables used in communication systems [95]. For existing TW-based fault protection and location schemes, these waveshape variations from a step change make precise identification of the TW arrival time difficult and can

potentially result in significant location errors [63]. This chapter, however, exploits such waveshape properties to develop a fast and effective protection method.

4.2.2 Polarity

In order to investigate the polarity of the TWs, the convention for the direction of current measurement should be determined. In this chapter, the current measurement units on the positive poles are set to face towards the line, whereas the units on the negative poles are set to face outwards. This convention simplifies fault direction identification using current TWs. Figure 4.5 illustrates this convention on the positive and negative poles of a 3-bus system. For a fault on the line between buses A and B, $R1$, $R2$, and $R4$ should see a forward fault, but $R3$ should see a reverse fault.

As can be seen from Figure 4.5a, a fault on the positive pole results in a decreasing v_{TW}. When the the fault is forward for the relay, the direction of i_{TW} and the direction of the above convention for current measurement are opposite. Such a scenario leads to an opposite pattern for the waveform of i_{TW} with respect to that of v_{TW} [96]. Therefore, an increasing i_{TW} is seen by the relay. Accordingly, the rising i_{TW} waveform detected by $R1$, $R2$, and $R4$ indicate a forward fault (Figure 4.5a). However, unlike the condition for a forward fault, the direction of i_{TW} and the direction of the adopted convention for current measurement are the same during a reverse fault. For such a condition, v_{TW} and i_{TW} have the same waveform [96]. Therefore, a reducing i_{TW} is measured by the relay. For instance, Figure 4.5a shows the falling i_{TW} waveform detected by $R3$, which indicates a reverse fault.

As a representative case, consider the bolted PPG fault on line $L12$, discussed in the last subsection. This fault is forward for $R21$ and reverse for $R23$. Figure 4.6 shows i_{TW}^{P} measured by these two relays (superscript P denotes positive-pole quantities). It can be seen that i_{TW}^{P} measured by $R21$ rises, and so a forward fault is detected. Conversely, i_{TW}^{P} measured by $R23$ drops to around zero, hence detecting a reverse fault.

A similar concept can be applied to determine the direction of the faults on the negative pole. The only difference is that such faults increase the algebraic magnitude of the negative-pole voltage. Therefore, a rising v_{TW} waveform is obtained. Using the earlier-discussed relations for the pattern of i_{TW} waveform, forward and reverse faults on the

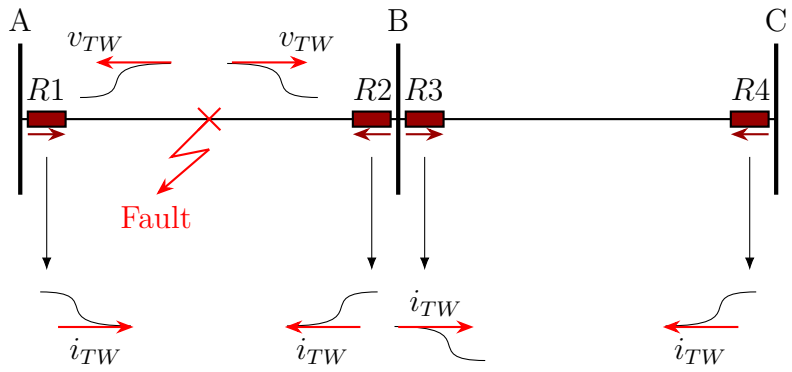

(a)

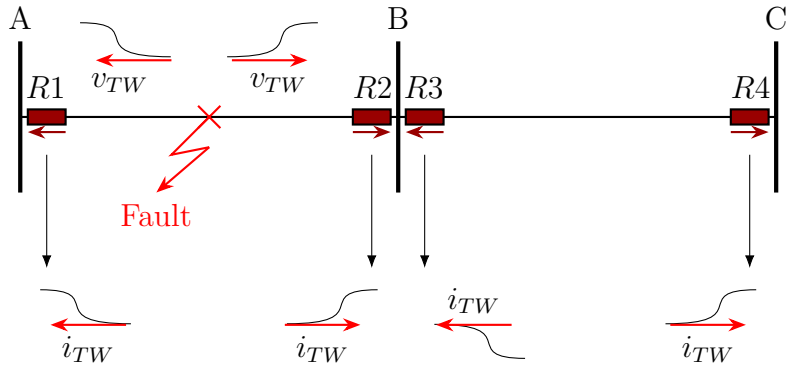

(b)

Figure 4.5: i_{TW}s as seen by four relays for a fault on a) a positive and b) a negative pole of a 3-bus system.

negative pole result in rising and falling i_{TW} for the relay, respectively. For example, Figure 4.5b shows that $R1$, $R2$, and $R4$ see a rising i_{TW} waveform, indicating a forward fault, but $R4$ detects a falling i_{TW} waveform, which signifies a reverse fault.

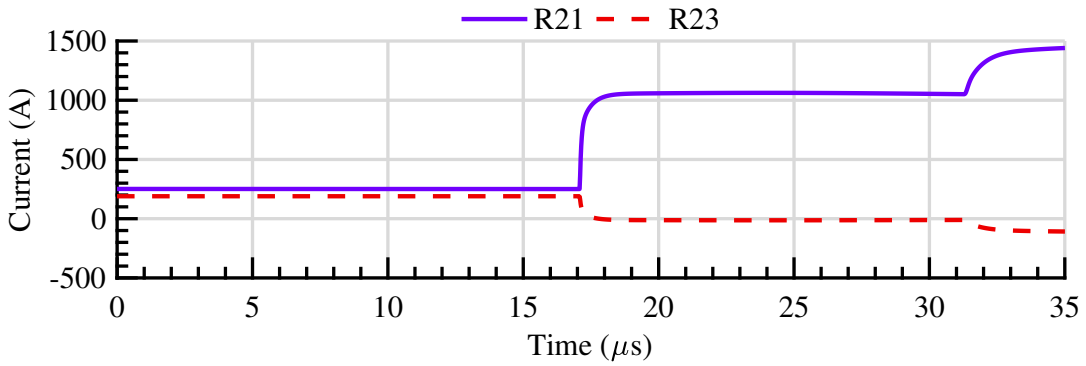

Figure 4.6: i_{TW}^{P} measured by $R21$ and $R23$ during a bolted PPG fault on $L12$.

4.3 Proposed TW-Based Protection Method

The proposed TW-based protection method consists of four units that operate sequentially. The following discusses each unit in detail.

4.3.1 TW Capturing Unit

The function of this unit is to extract the TW waveshape. Figure 4.7 shows the block diagram of the TW capturing unit. Given that the bulk of the TW energy is in the megahertz range [66], the acquired measurements are passed through an analog first-order high-pass Butterworth filter. By removing the DC component, this filter changes the exponential shape of the TW to a pulse-like signal [97]. The high-pass filtered signal is passed through an Analog-to-Digital (ADC) to obtain i_{hp} for each pole current. i_{hp} is used to extract the waveshape of the TW. It is also used to develop a directional element, which is utilized by the other units of the proposed relay. In order to extract a TW waveshape, the absolute value of i_{hp} is compared to a pre-defined threshold Ψ. The boundaries of the period during which the pulse-like waveshape of $|i_{hp}|$ is higher than Ψ are denoted by t_1 and t_N. The value of Ψ is selected such that:

1. It is sensitive to high-resistance and far-end faults that result in small TWs.

2. It captures the entire length of a TW waveshape.

3. It is higher than non-fault measurement noise. Typical current measurement units are designed to maintain a minimum Signal-to-Noise Ratio (SNR) of 85 dB [98].

4. It factors in sufficient security margin for the above three criteria. In commercial protective devices, the measured error tolerance is often specified as ±5 percent of the measured value [77].

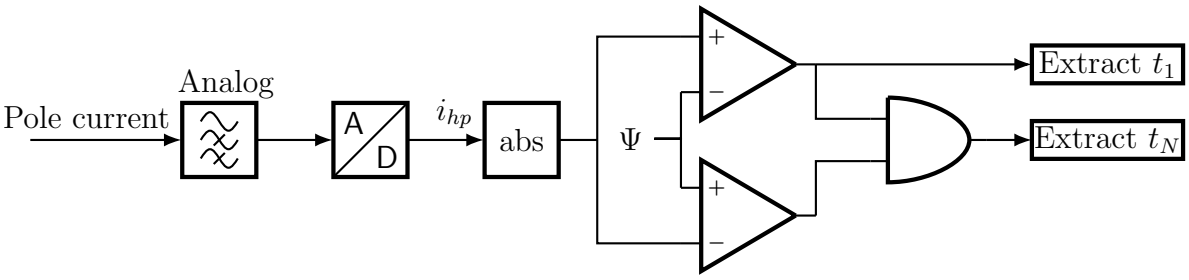

Figure 4.7: Block diagram of the TW capturing unit.

For instance, the lowest i_{TW} and its correspondingly $|i_{hp}|$ in the MVDC system of Figure 4.1 are seen by $R42$ when it operates as the backup protection for a 200 Ω PPG fault on $L26$ close to bus 6, i.e., the farthest (5.1 km away) high-resistance fault in this MVDC microgrid. Figure 6.5 shows $|i_{hp}|$ for this scenario after the white noise with SNR=85 dB is added to it. This figure illustrates that Ψ=5 mA satisfies the above four criteria. The selected Ψ is: (i) 23 times lower than the pinpointed i_{hp} peak (criterion 1), (ii) captures the TW waveshape between t_1=34.66 μs and t_N=39.22 μs (criterion 2), and (iii) is 67% higher than measurement noise (criteria 3 and 4).

4.3.2 Time Constant Estimation Unit

The time constant (τ) of the exponential i_{TW} is an effective tool to examine the TW's waveshape and locate the fault. The definition of τ depends on whether i_{TW} is rising or falling: τ is the time for a rising i_{TW} to grow from zero to $1 - \frac{1}{e}$ of its maximum; for a falling i_{TW}, on the other hand, τ is the time it takes to reach $\frac{1}{e}$ of the maximum of i_{TW}.

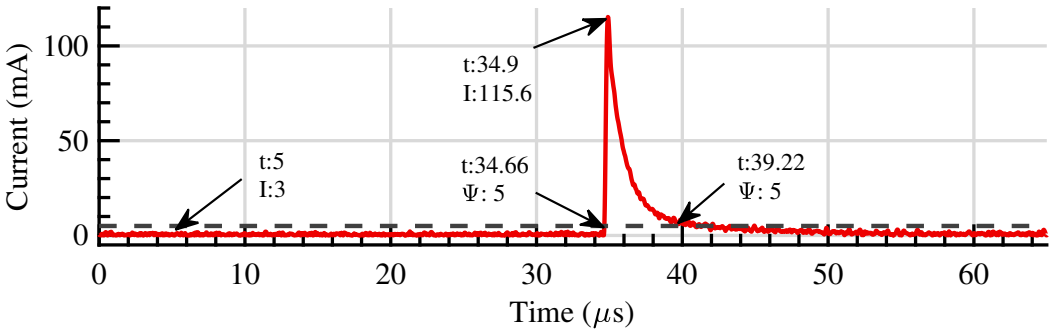

Figure 4.8: $|i_{hp}|$ of $R42$ for a 200 Ω PPG fault on $L26$ close to bus 6.

Figure 4.9 shows the block diagram of the time constant estimation unit. t_1 given by the TW capturing unit can be used to remove the time offset of the TW samples:

$$t'_n = t_n - t_1 \qquad \forall n = 1, 2, \ldots, N \tag{4.4}$$

where t_n is the *n-th* sampling instant of a recorded current, and t'_n is the corresponding sampling instant after removing the time offset. To make the estimation of the time constant immune to noise, $i_{TW}(t'_1 : t'_N)$ is smoothed using Savitzky-Golay filter [99]. In addition, to enhance the accuracy of τ estimation, especially for close-in faults with few TW samples, $i_{TW}(t'_1 : t'_N)$ is up-sampled using non-linear spline interpolation method [100]. The i_{TW} sample between t'_1 and t'_N that corresponds to τ is denoted by $i_{TW}(\tau)$ and can be calculated by:

$$i_{TW}(\tau) = \min(i_{TW}) + [\max(i_{TW}) - \min(i_{TW})]\, K \tag{4.5}$$

where K is $1 - \frac{1}{e}$ for a rising i_{TW} (which occurs for a forward fault) and $\frac{1}{e}$ for a falling i_{TW} (which occurs for a reverse fault). A rising i_{TW} is detected if i_{hp} is greater than Ψ, whereas a falling i_{TW} is detected if i_{hp} less than Ψ. $i_{TW}(t'_n)$ for $n = 1, \ldots, N$ is then subtracted from $i_{TW}(\tau)$ to obtain $|\Delta i_{TW}|$, which is the absolute difference between the captured i_{TW} samples and the closest i_{TW} sample to τ. t'_n that results in minimum $|\Delta i_{TW}|$ is τ.

To demonstrate the operation of the time constant estimation unit, Table 4.1 shows the parameters used to obtain τ for $R12$ during a bolted PPG fault 950 m away from $R12$

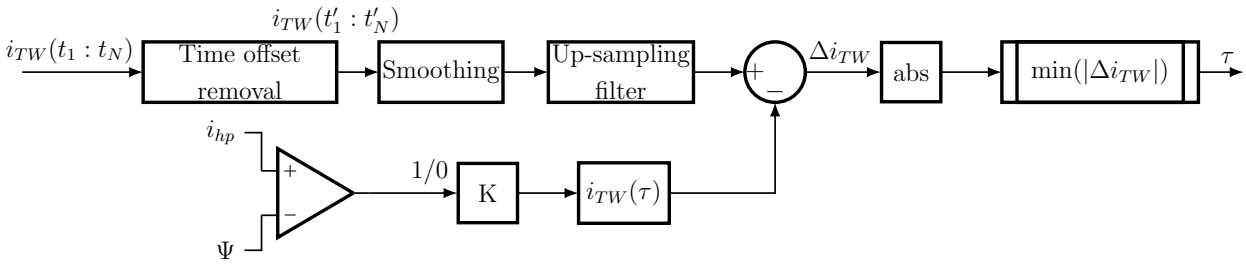

Figure 4.9: Block diagram of the time constant estimation unit.

on $L12$ in the MVDC system of Figure 4.1. Only 10 samples are shown for brevity. i_{hp} exceeds Ψ at sample 1 and then becomes less than Ψ again at sample 7900. Therefore, t_1 and t_N are 506.4205 and 507.9998 μs, respectively. Using (6.3), t'_1 and t'_N are 0 and 1.5798 μs, respectively. The minimum and maximum i_{TW} samples among the samples between t'_1 and t'_N are -268.31 and 590.74 A, respectively. Moreover, since i_{hp} exceeds Ψ, the fault is forward and thus K is $1 - \frac{1}{e}$. Using (4.5) and the aforementioned parameters, $i_{TW}(\tau)$ is 279.76 A. By subtracting $i_{TW}(t'_n)$ for $t'_n = 1, \ldots, 7900$ from $i_{TW}(\tau)$, the minimum $|\Delta i_{TW}|$ is 0.0626 A, which corresponds to t'_{504}. Therefore, using Table 4.1, τ=t'_{504}=100.6 ns.

4.3.3 Fault Detection and Real-Time Fault Location Unit

As discussed in Section 4.2, the farther is a fault from the relay location, the longer is the settling time, or equivalently, the τ of i_{TW}. This relation is shown in Figure 4.10 for i_{TW} measured during bolted faults at various locations on $L810$. Therefore, fault detection and location can be developed based on the relationship between χ and τ.

Fault Detection

Figure 4.11 shows the proposed trip logic which involves fault detection. This logic has three main elements, namely: 1) directional, 2) fault detection, and 3) backup protection element. The directional element was discussed in Section 4.3.2. The following focuses on the fault detection element, and the last element will be discussed in Section 4.3.4.

Table 4.1: Measurements of $R12$ for a Bolted PPG Fault on L12.

Sample	i_{hp} (A)	t_n (μs)	t'_n (ns)	i_{TW} (A)	$\lvert\Delta i_{TW}\rvert$ (A)
1	**80.4**	**506.4205**	**0**	**−268.31**	**548.08**
⋮	⋮	⋮	⋮	⋮	⋮
250	125.7	506.4738	49.8	134.19	145.58
⋮	⋮	⋮	⋮	⋮	⋮
502	52.7	506.5202	100.2	278.96	0.805
503	52.6	506.5204	100.4	279.33	0.433
504	**52.4**	**506.5206**	**100.6**	**279.70**	**0.0626**
505	52.2	506.5208	100.8	280.07	0.3068
506	52.1	506.5210	101	280.44	0.6753
507	51.9	506.5212	101.2	280.81	1.0429
⋮	⋮	⋮	⋮	⋮	⋮
4000	1.63	507.2198	799.8	561.34	281.57
⋮	⋮	⋮	⋮	⋮	⋮
7900	**0.0049**	**507.9998**	**1579.8**	**590.74**	**310.97**

Figure 4.11 shows that the relay trips if the directional element identifies a forward fault and the fault detection element picks up. The fault detection element compares τ of a captured i_{TW} with a threshold ζ_1, which is based on i_{TW} for the fault at the relay reach setting. For each relay, faults at the reach settings of the protection zones are simulated, and the time constants of the corresponding i_{TW}s' are used to set the thresholds. The reach for the primary protection zone of each relay is set to cover the entire line length. For instance, ζ_1 of $R12$ is set to be the time constant of i_{TW} launched by a fault at 2.2 km, i.e., length of $L12$.

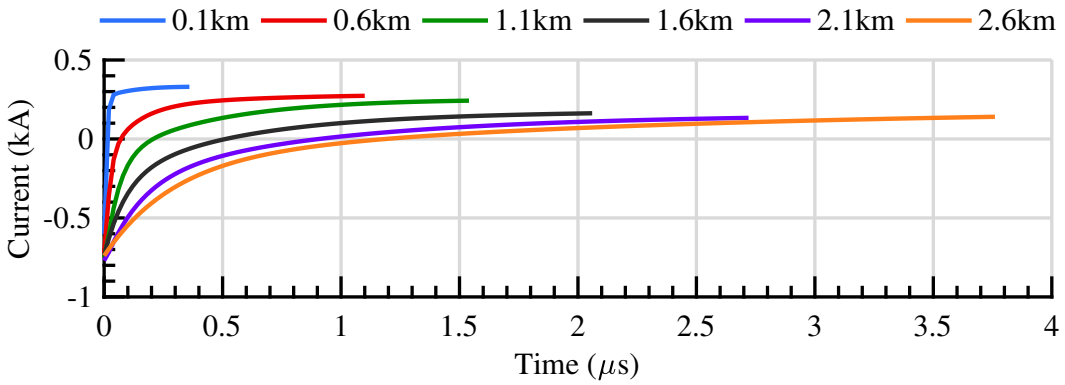

Figure 4.10: i_{TW} due to bolted faults at various locations on line $L810$.

Fault Location

Based on the relationship between fault location and the waveshape of i_{TW}, τ-χ lookup table for each cable type can be generated. This lookup table is completely independent of the microgrid topology. For the test system of Figure 4.1, there is only one lookup table since one cable type is used in this MVDC microgrid. The lookup table is created offline by simulating faults at different locations along that cable. Alternatively, the lookup table can also be created experimentally by injecting a step voltage or current wave and then measuring τ of the wave at given distances along the cable. The attained lookup table is uploaded to the fault location unit of each relay.

As an example, for the test system of Figure 4.1, the lookup table is created by simulating a fault at every 100 m along the 3-km $L810$. To further enhance the accuracy of the fault location unit, the distance resolution is increased from 100 m to 1 m using the spline interpolation method [100]. Figure 4.12 shows a graphical representation of the lookup table for the system of Figure 4.1, including the simulated samples as well as the samples obtained using the spline interpolation method. Using the measured time constant and this lookup table, the fault location can be identified.

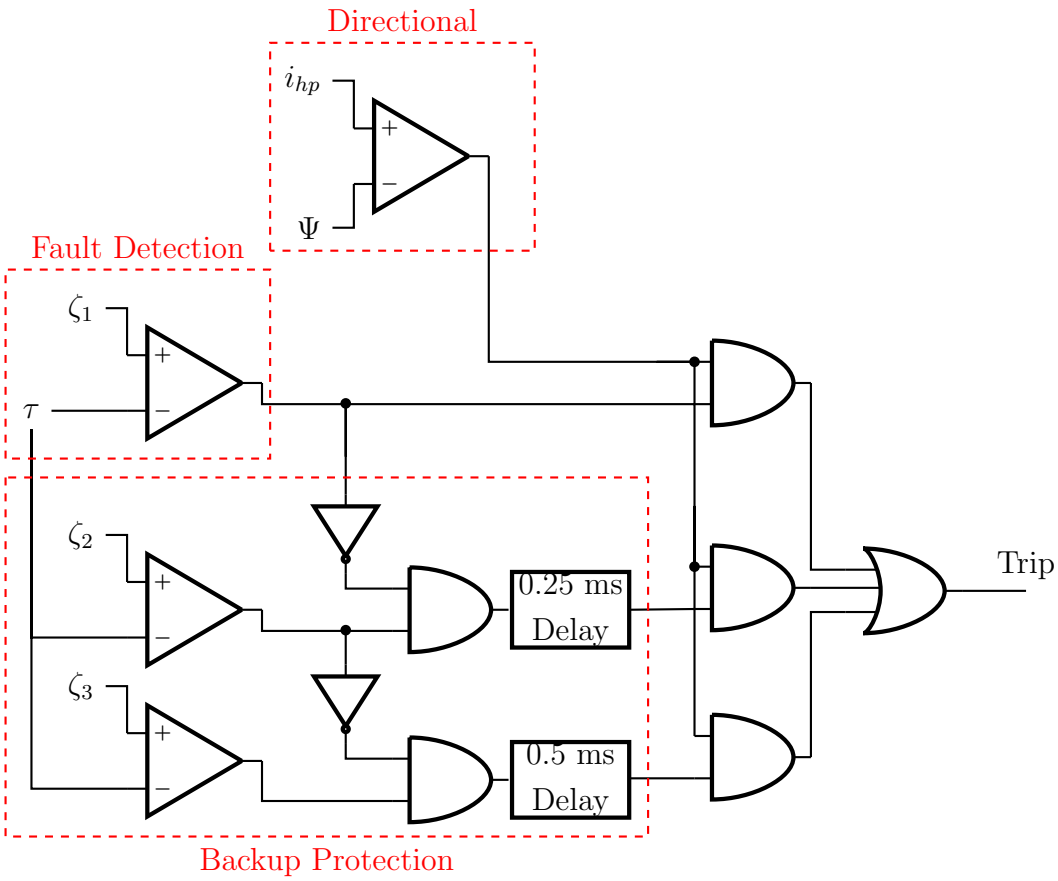

Figure 4.11: Tripping logic of the proposed relay.

4.3.4 Backup Protection Unit

Each relay has three zones of operation: 1) primary, 2) first backup, and 3) second backup zone. The proposed relay operates in the primary, first backup, or second backup zone if τ is within thresholds ζ_1, ζ_2, or ζ_3, respectively. The primary zone is set to protect the full length of the line. The first and the second backup zones protect the shortest and the longest adjacent lines, respectively.

For instance, the reach for the primary zone of $R12$ in the test MVDC microgrid (Figure 4.1) is 2 km, the reach of the first backup zone is 2+1.8=3.8 km, and the second backup

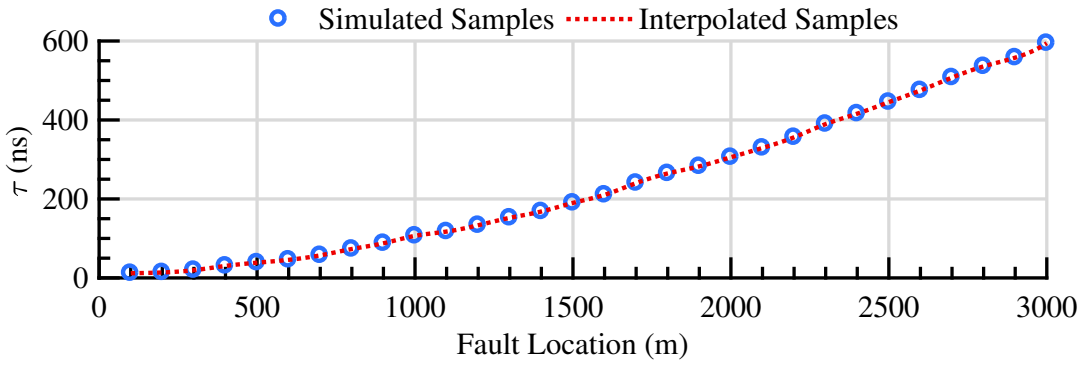

Figure 4.12: The simulated and interpolated samples of the τ-χ lookup table.

zone reaches 2+2.6=4.6 km. Table 4.2 summarizes the zone reaches and their respective thresholds for each relay in the MVDC microgrid of Figure 4.1. It is worth noting that the relays facing converter ends, such as $R21$, $R23$, $R512$, $R67$, $R89$, and $R1011$, have no remote backup because the converter buses have no adjacent lines.

As shown in Figure 4.11, the faults in the relay's primary zone are tripped instantaneously, whereas the ones in the first and second backup zones are tripped if the fault persists after a delay of 0.25 ms and 0.5 ms, respectively. The 0.25 ms Coordination Time Interval (CTI) is selected based on the following criteria:

1. The CTI must be larger than the maximum OT of the primary zone. For the test system in Figure 4.1, this time is 4.2 μs, which corresponds to the time required for the i_{TW} launched by the far-end fault on line $L810$ (the longest line in the system) to reach $R810$.

2. The CTI must be higher than the OT of solid-state dc circuit breaker, which is within 200μs [14], [47].

3. The CTI must include a sufficiently high security margin.

Table 4.2: Relays Zone Reaches and Thresholds in the Test Microgrid

Relay	Primary Zone		First Backup Zone		Second Backup Zone	
	Reach (km)	ζ_1 (ns)	Reach (km)	ζ_2 (ns)	Reach (km)	ζ_3 (ns)
R12	2	306	3.8	675	4.6	839
R21	2	306	–	–	–	–
R23	1.8	265	–	–	–	–
R32	1.8	265	3.8	675	4.4	831
R24	2.5	445	–	–	–	–
R42	2.5	445	4.3	825	5.1	947
R25	2.2	356	2.6	475	3.3	615
R52	2.2	356	4	818	4.7	886
R26	2.6	475	3.4	645	3.9	693
R62	2.6	475	4.4	831	5.1	947
R56	1.5	190	2.3	390	2.8	536
R65	1.5	190	1.9	283	2.6	475
R510	1.1	117	1.6	210	–	–
R105	1.1	117	1.5	190	3.3	615
R512	0.4	30	–	–	–	–
R125	0.4	30	1.5	190	2.6	475
R67	0.8	73	–	–	–	–
R76	0.8	73	2.1	329	3.4	645
R68	1.3	152	2.3	390	4.3	825
R86	1.3	152	2.1	329	3.9	693
R89	1	107	–	–	–	–
R98	1	107	2.3	390	4	818
R810	3	594	3.5	656	–	–
R108	3	594	4	818	–	–
R1011	0.5	39	–	–	–	–
R1110	0.5	39	1.6	210	3.5	656

4.4 Performance Evaluation

This section presents various case studies to demonstrate the performance of the proposed relay under a variety of fault conditions for the MVDC microgrid of Figure 4.1.

4.4.1 Bolted PPG Fault

A bolted PPG fault on $L810$, 2397 m away from bus 8 is studied in this section. The measurements on the positive and negative poles of the primary relays covering this fault, i.e., $R810$ and $R108$, are displayed with respect to t'_n in Figure 4.13. As shown in Figures 4.13a–2 and 4.15a–1, $|i^P_{hp}|$ measured by these relays exceeds Ψ= 5 mA, but $|i^N_{hp}|$ (superscript N denotes the negative pole) does not exceed Ψ, and thus each relay is able to flag the fault as a PPG fault. Moreover, the larger magnitude of i^P_{hp} than Ψ for $R810$ and $R108$ correctly indicates that the fault is forward for these two relays.

For the same fault, the measurements on the positive pole of the relays on the adjacent lines—i.e., $R68$, $R86$, $R89$, $R98$, $R510$, $R105$, $R1011$, and $R1110$—are displayed with respect to t'_n in Figures 4.14 and 4.15. All of the aforementioned relays correctly detect a PPG fault because $|i^P_{hp}|$ measured by these relays exceeds Ψ, as shown in Figures 4.14b and 4.15b. Meanwhile, it can be seen that only $R98$, $R510$, and $R1110$ have i^P_{hp} that exceeds Ψ, whereas i^P_{hp} of $R68$, $R86$, $R89$, and $R105$ is below Ψ. Hence, $R98$, $R510$, and $R1110$ flag a forward fault and can accordingly operate as backup relays to $R810$ and $R108$. On the other hand, $R68$, $R86$, $R105$, and $R1011$ identify a reverse fault, which blocks their operation based on the tripping logic of Figure 4.11.

It is worth noting that due to the different distances between the fault and various relays, the magnitude of i_{TW} measured by different relays is not the same. Therefore, i_{hp} does not drop below Ψ at the same time for different relays, making the time length of the TWs shown in Figures 4.13 to 4.15 different.

Using the minimum and maximum samples of i_{TW} between t'_1 and t'_N in (4.5), the time constant estimation unit of each relay computes its respective $i_{TW}(\tau)$. $i_{TW}(\tau)$ for $R810$, $R108$, $R98$, $R510$ and $R1110$ is 734, 86.4, 1191, 745.3, and -395.7 A, and its

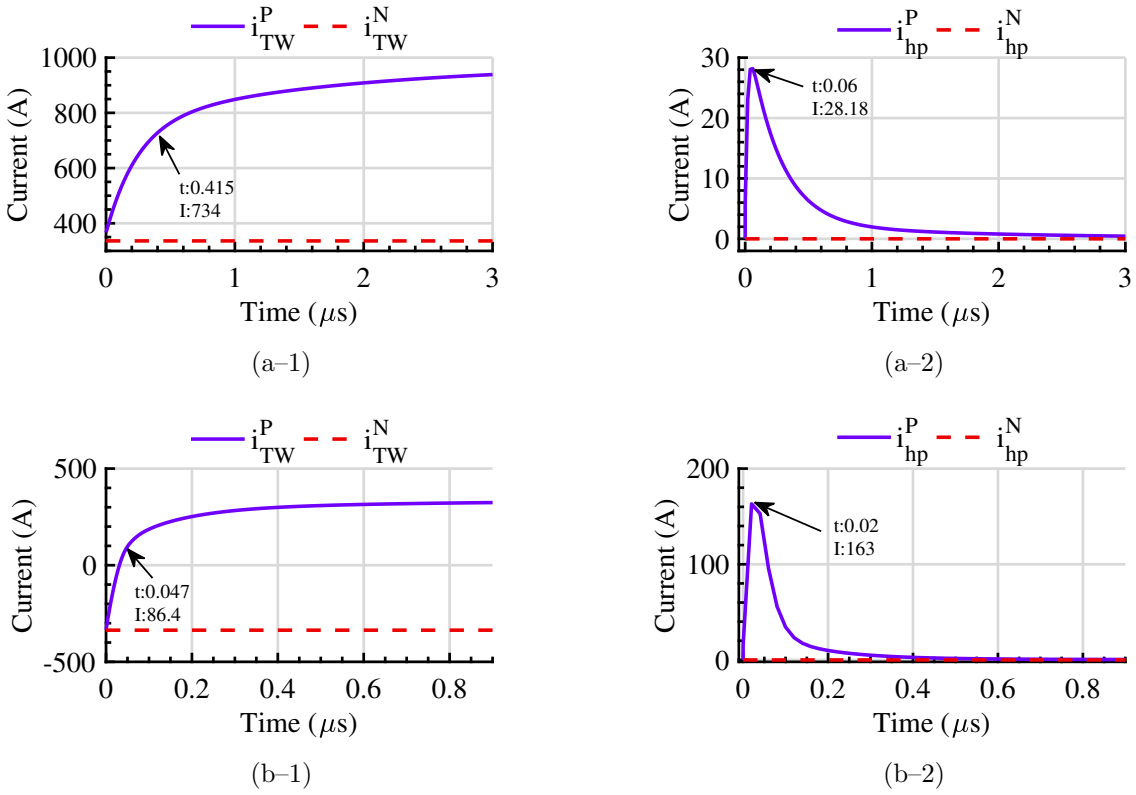

Figure 4.13: i_{TW} and i_{hp} of primary relays for bolted PPG fault on L810, a) R810, b) R108.

corresponding τ is 41.5, 47, 739.8, 246, and 147.2 ns, respectively (Figures 4.13a–1, 4.14b–1, 4.14a–2, and 4.15a). These time constants are used by the fault detection unit of each relay to determine if the fault is in-zone. The time constants for $R810$ and $R108$ are 41.5 and 47 ns, respectively, and are less than ζ_1=594 ns (Table 4.2). Thus, the primary relays trip instantaneously. On the other hand, the time constant for $R98$ is 739.8 ns, which is greater than ζ_1=107 ns and ζ_2=390 ns, but less than ζ_3=818 ns (Table 4.2). Therefore, $R98$ correctly detects that the fault is in its second backup zone. Similarly, the time constant of $R1110$ is 147.2 ns, which is greater than ζ_1=39 ns, but less than ζ_2=210 ns (Table 4.2). Hence, $R1110$ correctly detects a fault in its first backup zone. Meanwhile, the time constant of $R510$ is 246 ns, which is greater than ζ_1=117 ns and ζ_2=210 ns (Table 4.2). In

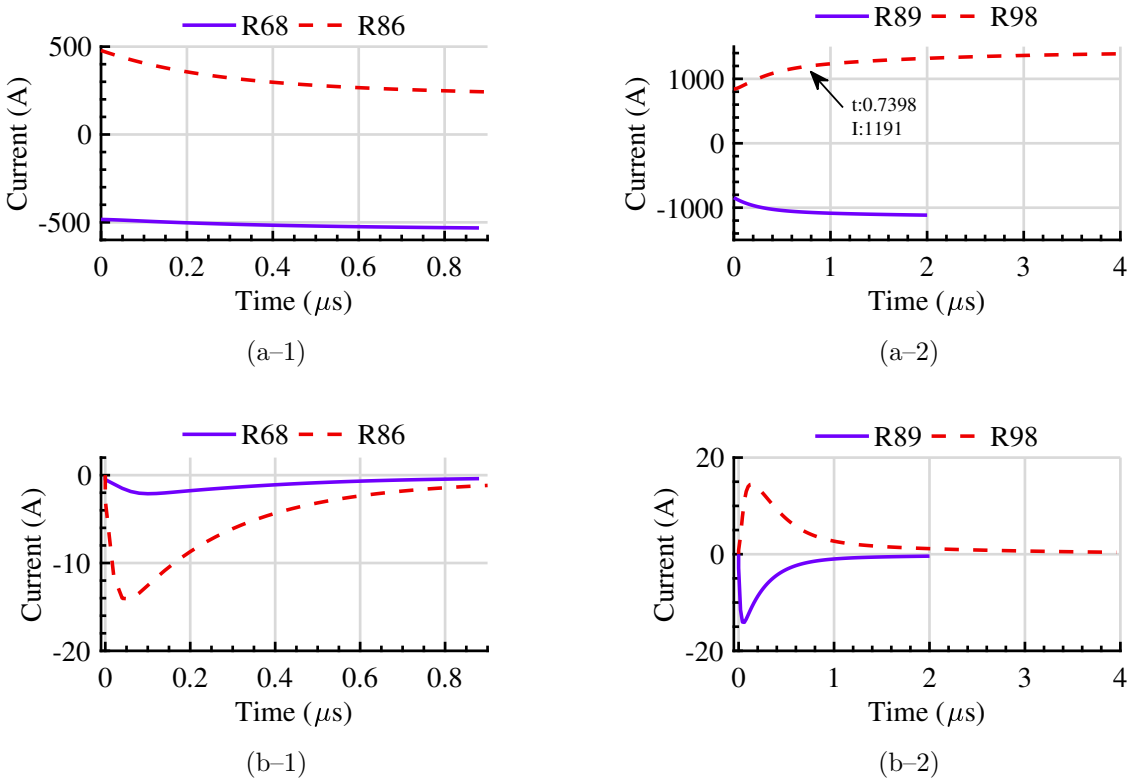

Figure 4.14: a) i^P_{TW} and b) i^P_{hp} of adjacent relays for bolted PPG fault on L810.

addition, R510 does not have a second backup zone. Therefore, this relay does not trip.

Based on t'_N and the relay's operation zones, the OT of R810, R108, R98, and R1110 is 3.18 (Figure 4.13a–1), 0.98 (Figure 4.14b–1), 500+4=504 (Figure 4.14a–2), and 250+1=251 μs (Figure 4.15a–2), respectively. Therefore, in addition to the primary relays—whose OT remain well below 4 μs—the backup relays also satisfy the speed requirement for the protection of MVDC microgrids.

Finally, the previously-mentioned 41.5 and 47 ns time constants calculated by R810 and R108 are used along with the lookup table illustrated in Figure 4.12 to estimate the fault location. The actual distance between the fault and R108 is 603 m and the estimated χ is 613 m. Thus, the error in fault location is only 10 m. Similarly, the actual and estimated fault locations for R810 are 2397 and 2396 m, resulting in 1 m error.

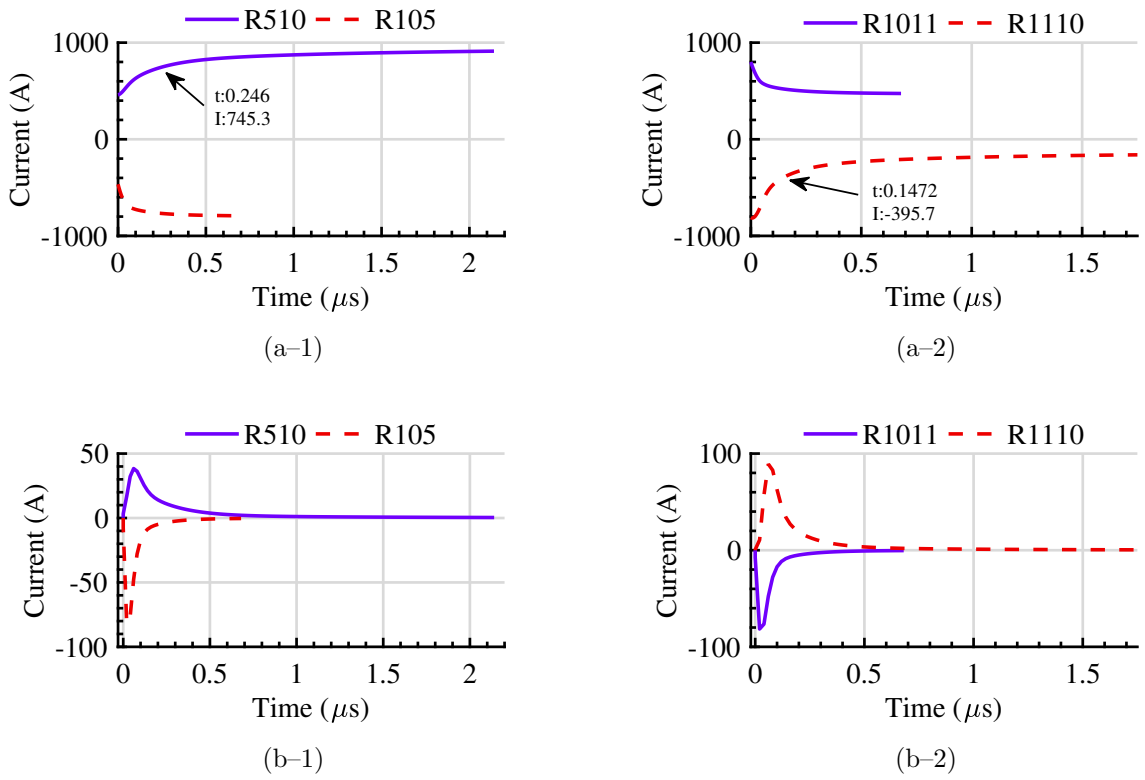

Figure 4.15: a) i_{TW}^{P} and b) i_{hp}^{P} of adjacent relays for bolted PPG fault on L810.

4.4.2 Different System Configurations

The following three case studies are presented to assess the effect of different system configurations on the primary and backup protection.

DG Addition

A 1 MW ac DG is connected through a two-level VSC to bus 8 of the MVDC test microgrid of Figure 4.1. A bolted PPG fault is applied to $L89$, 400 m away from bus 8 in the presence and absence of the aforementioned DG. Figure 4.16 shows that connecting the DG to bus 8 has a negligible effect on the magnitudes of i_{TW}^{P} and i_{hp}^{P} of primary relays $R89$ and $R98$.

Therefore, τ for $R89$ under the PPG fault in the MVDC microgirds with and without the DG at bus 8 is equal to 31.2 ns. Moreover, τ for $R98$ is equal to 47.2 ns under these two conditions. Since τ of the i_{TW} detected by $R89$ and $R98$ is less than ζ_1=107 ns (Table 4.2), both relays correctly detect a fault in their primary zone. Therefore, the addition of a new DG has no impact on the primary protection.

On the other hand, Figure 4.17 shows that connecting the DG to bus 8 considerably impacts the magnitudes of i^P_{TW} and i^P_{hp} of backup relays $R68$ and $R108$. $i_{TW}(\tau)$ for $R68$ under the PPG fault in the MVDC microgirds with and without the DG at bus 8 is equal to 380.8 and 21.81 A, respectively (Figure 4.17a–1). However, the change in magnitude of $i_{TW}(\tau)$ has a minimal effect on the τ computed by $R68$, which is equal to 238.6 and 239.8 ns in the presence and absence of the new DG at bus 8, respectively. Such a small difference in τ has negligible impact on the accuracy of the proposed protection scheme. The τ calculated for $R68$ in both cases (238.6 and 239.8 ns) is greater than ζ_1=152 ns, but less than ζ_2=390 ns (Table 4.2). Hence, $R68$ correctly detects a fault in the first backup zone for both cases. Similarly, Figure 4.17b–1 shows that the difference in $i_{TW}(\tau)$ magnitudes detected by $R108$ in the presence and absence of the new DG at bus 8 has a negligible impact on the computed τ. Accordingly, τ calculated by $R108$ in the presence and absence of the new DG is 629.6 and 639.2 ns, which is greater than ζ_1=594 ns, but less than ζ_2=818 ns (Table 4.2). Thus, $R108$ correctly detects a fault in the first backup zone for both cases. As a result, this case study illustrates that addition of a DG does not affect the operation of the backup protection as well.

DG and Load Addition

A new 1 MW DC load is connected through a DC/DC buck converter to bus 6 of the MVDC test microgrid of Figure 4.1. The ac DG at bus 8, added in the previous subsection, is still in service. A bolted PPG fault is applied to $L89$, 400 m away from bus 8 in this new microgrid configuration. Figure 4.18 shows that the addition of a new DG and load changes $i^P_{TW}(\tau)$ for all of the primary and backup relays with respect to the case study in Section 4.4.2 (Figures 4.16 and 4.17), but has no noticeable effect on τ.

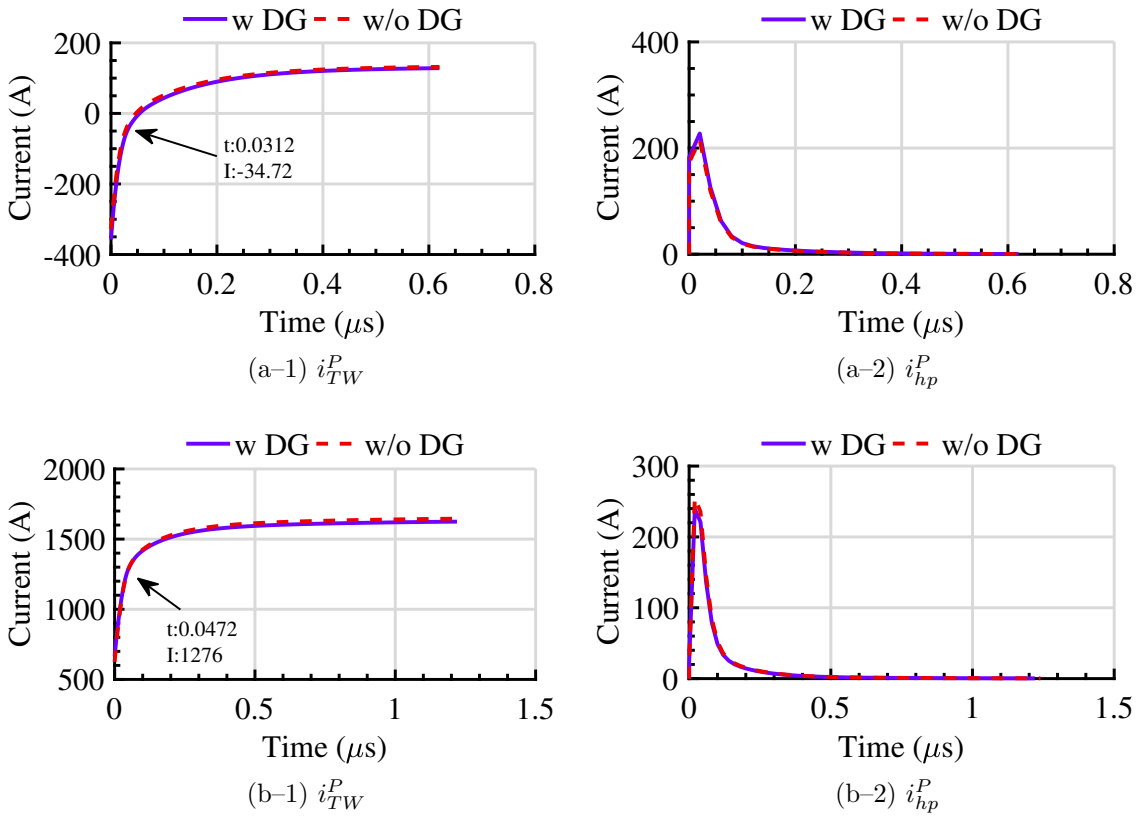

(a–1) i_{TW}^{P} (a–2) i_{hp}^{P}

(b–1) i_{TW}^{P} (b–2) i_{hp}^{P}

Figure 4.16: i_{TW}^{P} and i_{hp}^{P} of primary a) R89 and b) R98 for a bolted PPG fault on $L89$ with and without a DG at bus 8.

Line Outage

In this case study, line $L510$ is disconnected. The same bolted PPG fault is applied to $L89$, 400 m away from bus 8 in this new microgrid configuration. Since the line outage changes the pre-fault current flow in $L89$, Figure 4.19 shows that $i_{TW}^{P}(\tau)$ of all of the primary and backup relays is different from the one obtained in the two case studies in Sections 4.4.2 and 4.4.2 (Figures 4.16 and 4.17, and 4.18), but τ remains unaffected.

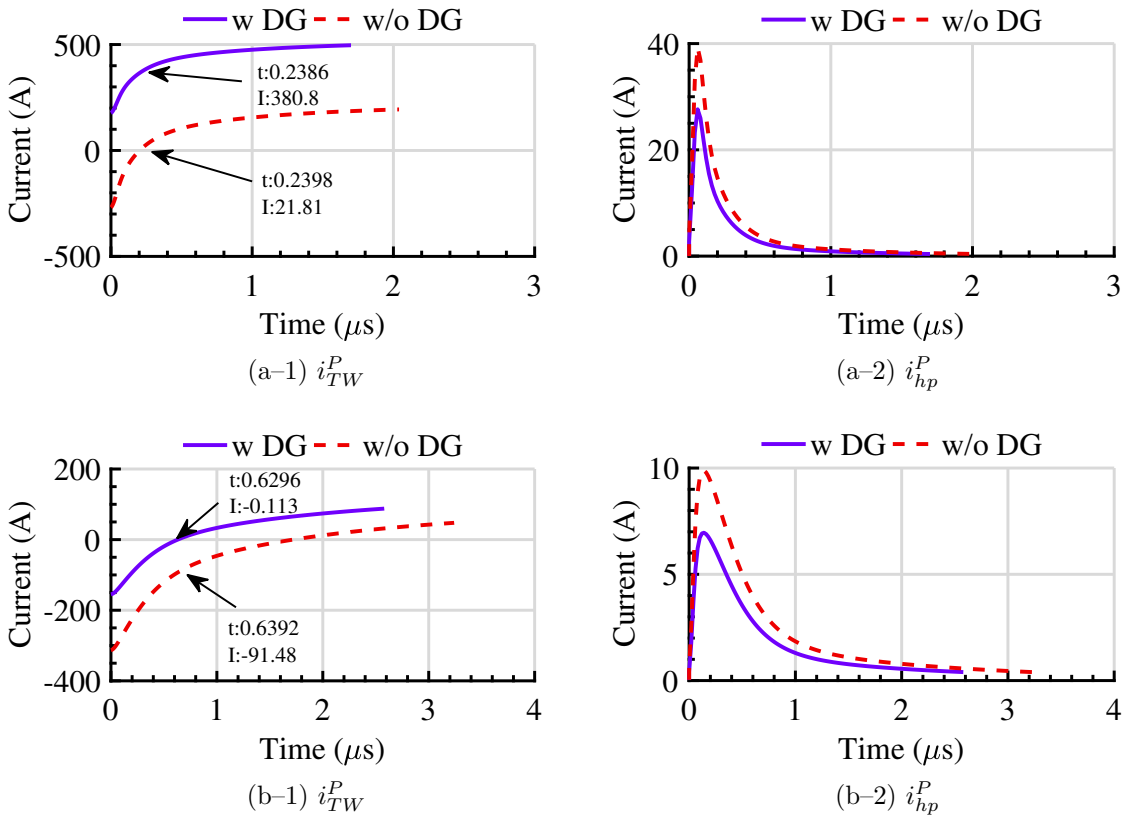

(a–1) i_{TW}^{P} (a–2) i_{hp}^{P}

(b–1) i_{TW}^{P} (b–2) i_{hp}^{P}

Figure 4.17: i_{TW}^{P} and i_{hp}^{P} of backup a) R68 and b) R108 for a bolted PPG fault on L89 with and without a DG at bus 8.

4.4.3 Fault Types

To assess the selectivity of the proposed scheme, bolted NPG and PP faults are conducted on $L810$, 2397 m away from bus 8 (i.e., the same location for the PPG fault of the last subsection). During an NPG fault, only $|i_{hp}^{N}|$ exceeds Ψ (Figures 4.20a–2 and 4.20b–2), whereas both $|i_{hp}^{P}|$ and $|i_{hp}^{N}|$ exceed Ψ during a PP fault (Figures 4.21a–2 and 4.21b–2). Therefore, the proposed scheme can selectively trip the faulted pole. Moreover, the computed τ of $R810$ under all three fault types in Figures 4.13a–1, 4.20a–1, and 4.21a–1 ranges between 407.4 and 415 ns, which is almost the same. Similarly, τ of $R108$ under all three fault types in Figures 4.13b–1, 4.20b–1, and 4.21b–1 ranges between 46.8 and 47 ns,

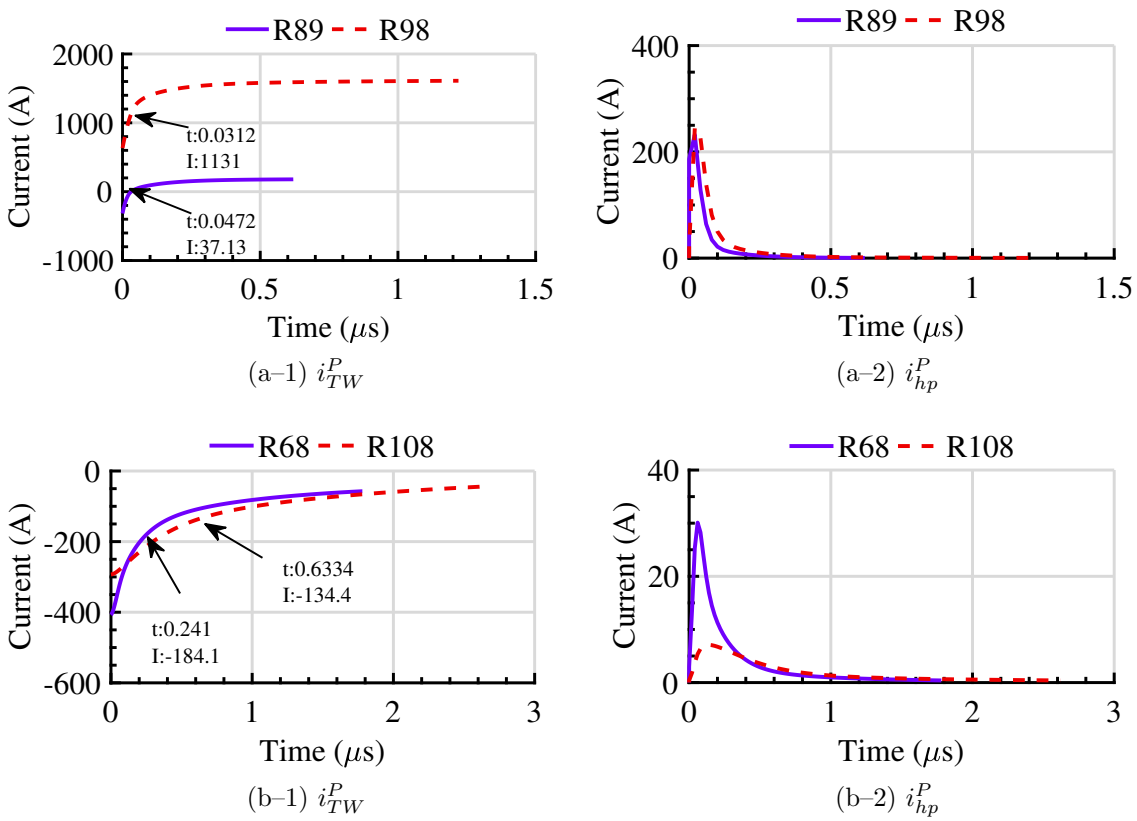

(a–1) i_{TW}^{P} (a–2) i_{hp}^{P}

(b–1) i_{TW}^{P} (b–2) i_{hp}^{P}

Figure 4.18: i_{TW}^{P} and i_{hp}^{P} of a) primary and b) backup relays for a bolted PPG fault on $L89$ in MVDC.

which is almost the same. Accordingly, neither the speed nor the accuracy of the proposed method is affected by the change in the fault type.

4.4.4 Fault Resistances

To assess the sensitivity of the proposed scheme, PPG faults with R_f equal to 10, 100, and 200 Ω are conducted on $L810$, 2397 m away from bus 8. Figure 4.22 shows that R_f has a significant effect on the magnitudes of i_{TW}^{P} and $|i_{hp}^{P}|$ of both $R810$ and $R108$. Therefore, $i_{TW}(\tau)$ for $R810$ under the PPG faults with R_f=10, 100, and 200 Ω is equal to 426, 366.1, and 362.1 A, respectively. In addition, $i_{TW}(\tau)$ for $R108$ is equal to −276, −348,

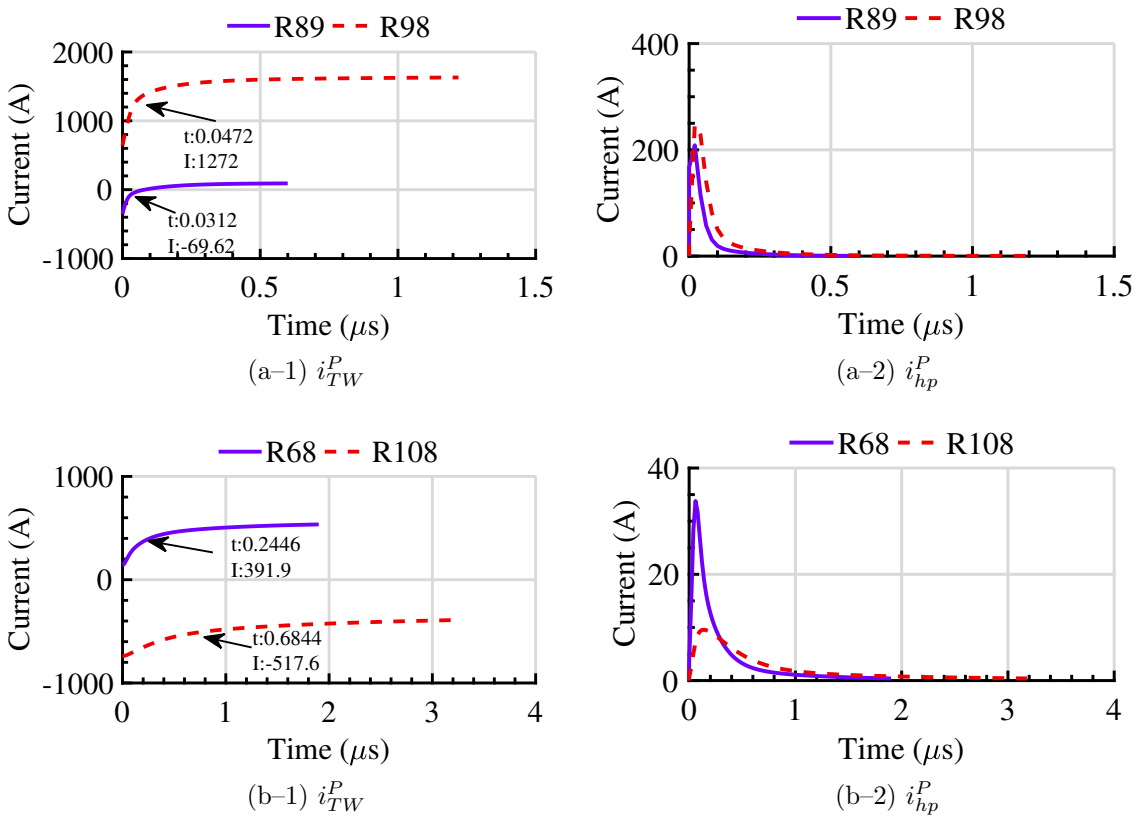

Figure 4.19: i_{TW}^{P} and i_{hp}^{P} of a) primary and b) backup relays for a bolted PPG fault on $L89$ in MVDC.

and -352 A, respectively. However, the variation of $i_{TW}(\tau)$ has a minimal effect on the τ computed by $R810$, which is equal to 411.8, 413.4, and 407.6 ns for R_f=10, 100, and 200 Ω, respectively. Moreover, τ for $R108$ is equal to 49, 49, and 48.2 ns under R_f=10, 100, and 200 Ω, respectively. Such small differences in τ have negligible impact on the speed and accuracy of the proposed protection scheme. The OT of $R810$ for R_f=10, 100, and 200 Ω is 2.34, 2.24, and 2.12 μs, while the OT of $R810$ OT is 0.84, 0.8, and 0.74 μs, respectively. Furthermore, the fault location estimated by $R810$ for R_f=10, 100, and 200 Ω is 2384, 2390, and 2367 m away from the relay, resulting in 13, 7, and 30 m errors, respectively. Similarly, the fault location estimated by $R108$ for R_f=10, 100, and 200 Ω is 634, 634, and 626 m away from the relay, causing only 31, 31, and 23 m errors, respectively.

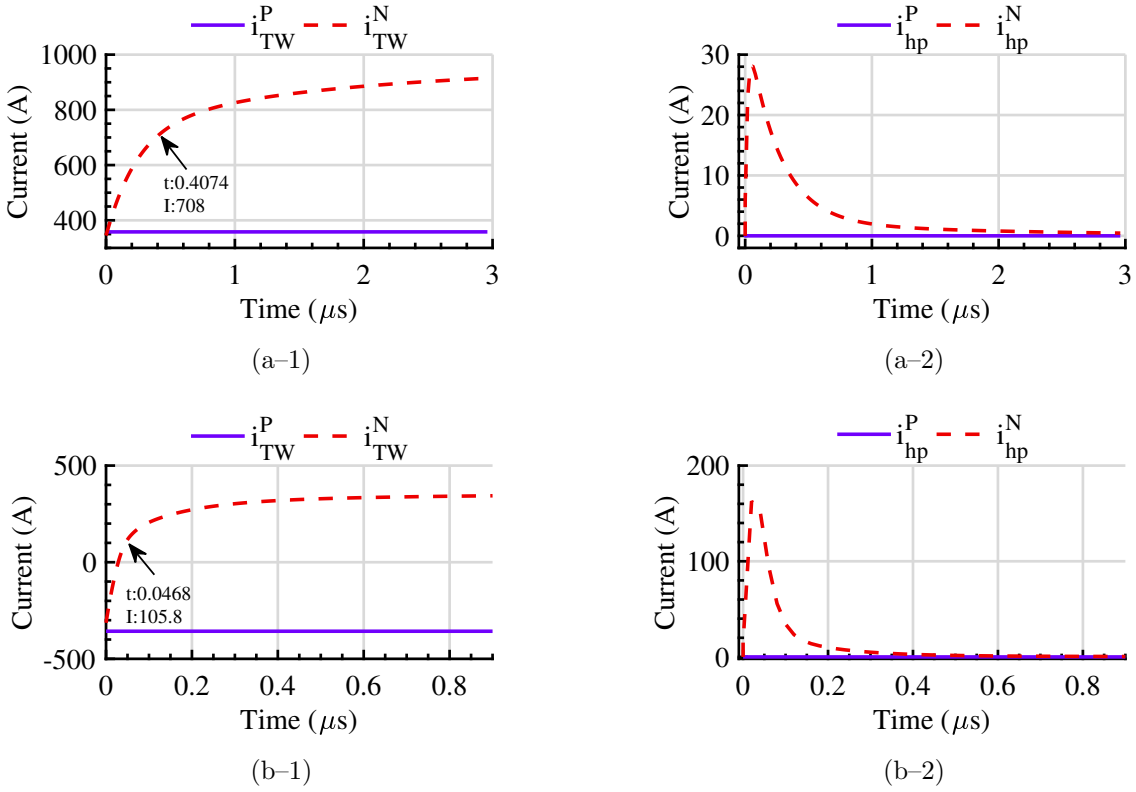

Figure 4.20: i_{TW} and i_{hp} of primary relays for bolted NPG fault on L810, a) R810, b) R108.

4.4.5 Fault Locations

To assess the speed and accuracy of the proposed scheme, bolted PPG faults are conducted at various locations on the 13 lines of the test MVDC microgrid. Table 4.3 summarizes the time constant and OT of the primary and backup relays for different fault locations. This table shows that the OT of the primary relays does not exceed 3.18 μs for any of the fault locations. Table 4.4 summarizes the fault location estimations for the faults in Table 4.3 as seen by the relays at both ends of the faulted lines. It can be seen that 38 m is the largest estimation error for χ.

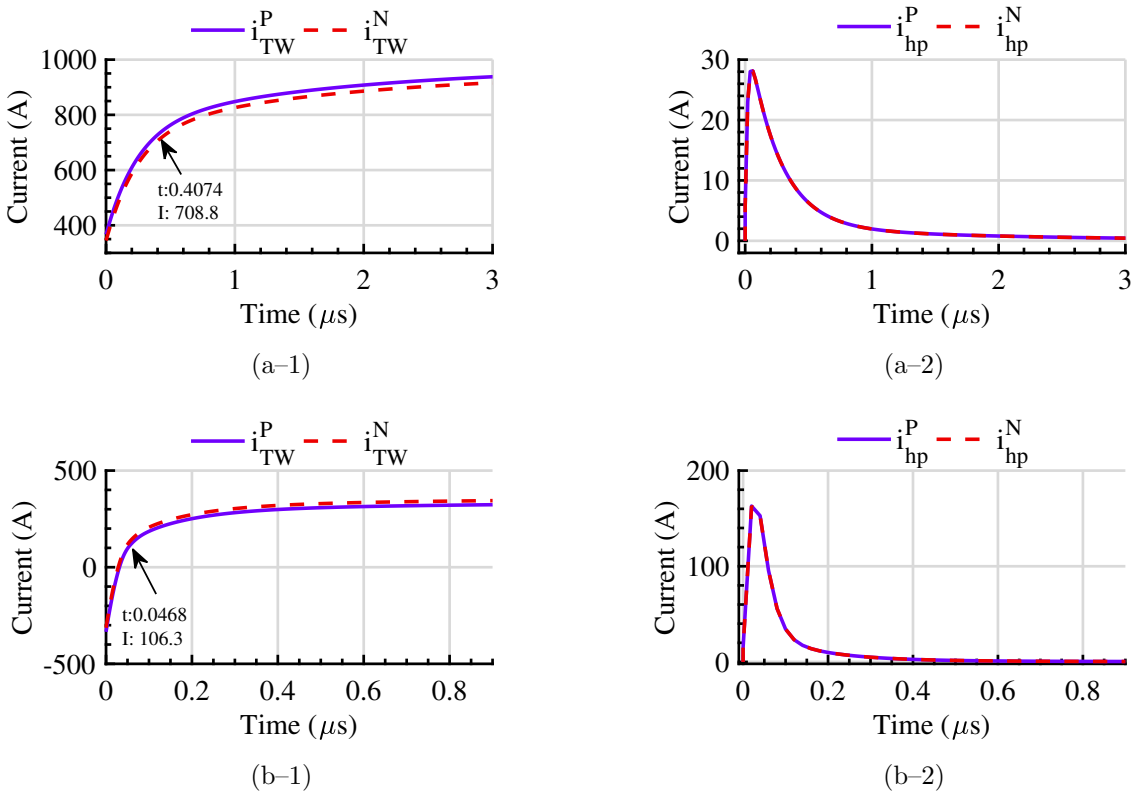

Figure 4.21: i_{TW} and i_{hp} of primary relays for bolted PP fault on L810, a) R810, b) R108.

Table 4.3: Primary and Backup Relay τ and OTs for PPG Faults in the Test Microgrid

Line	χ (m)	Primary Zone Relay	τ (ns)	OT (μs)	First Backup Zone Relay	τ (ns)	OT (μs)	Second Backup Zone Relay	τ (ns)	OT (μs)
L12	950	R12	101	1.58	–	–	–	–	–	–
	1050	R21	112	1.42	R32 R42	485 651	252 252	– –	– –	– –

					R52	541	252	–	–	–
					R62	653	252	–	–	–
L23	435	R23	34.6	0.76	R12	393	252	–	–	–
					R42	504	252	–	–	–
					R52	412	252	–	–	–
					R62	512	252	–	–	–
	1365	R32	166	1.82	–	–	–	–	–	–
L24	1035	R24	107	1.34	R12	536	252	–	–	–
					R32	481	252	–	–	–
					R52	543	252	–	–	–
					R62	651	252	–	–	–
	1465	R42	187	1.94	–	–	–	–	–	–
L25	754	R25	65.6	1.06	R12	467	252	–	–	–
					R32	424	252	–	–	–
					R42	583	252	–	–	–
	1446	R52	186	1.64	–	–	–	R105	398	502
					–	–	–	R125	259	502
L26	1168	R26	130	1.46	R12	552	252	–	–	–
					R32	512	252	–	–	–
					R42	686	252	–	–	–
	1432	R62	181	1.88	–	–	–	R56	511	502
					–	–	–	R86	459	502
					–	–	–	R76	363	502
L56	621	R56	50.2	1.04	R25	385	252	R105	287	502
					R125	160	252	–	–	–
	879	R65	88	1.16	R76	193	252	–	–	–

					R86	271	252	–	–	–
L510	394	R510	31.4	0.58	R25	426	251	–	–	–
					R65	265	252	–	–	–
					R125	79.4	252	–	–	–
	706	R105	58	0.96	R1110	161	252	–	–	–
L512	148	R512	12.4	0.08	R25	361	252	–	–	–
					R65	224	251	–	–	–
					R105	142	251	–	–	–
	252	R125	15	0.10	–	–	–	–	–	–
L67	275	R67	20.8	0.16	R26	505	252	–	–	–
					R56	249	252	–	–	–
					R86	201	252	–	–	–
	525	R76	39.6	0.96	–	–	–	–	–	–
L68	843	R68	82.2	1.5	R56	386	252	–	–	–
	457	R86	32.6	0.88	R76	248	252	–	–	–
					R98	217	252	–	–	–
L89	583	R89	47	0.86	R68	282	252	–	–	–
					R108	695	252	–	–	–
	417	R98	32.2	0.68	–	–	–	–	–	–
L810	2397	R810	415	3.18	–	–	–	R98	740	504
	603	R108	47	0.98	R1110	147	251	–	–	–
L1011	180	R1011	14.4	0.20	R510	170	252	–	–	–
					R810	603	252	–	–	–
	320	R1110	24	0.42	–	–	–	–	–	–

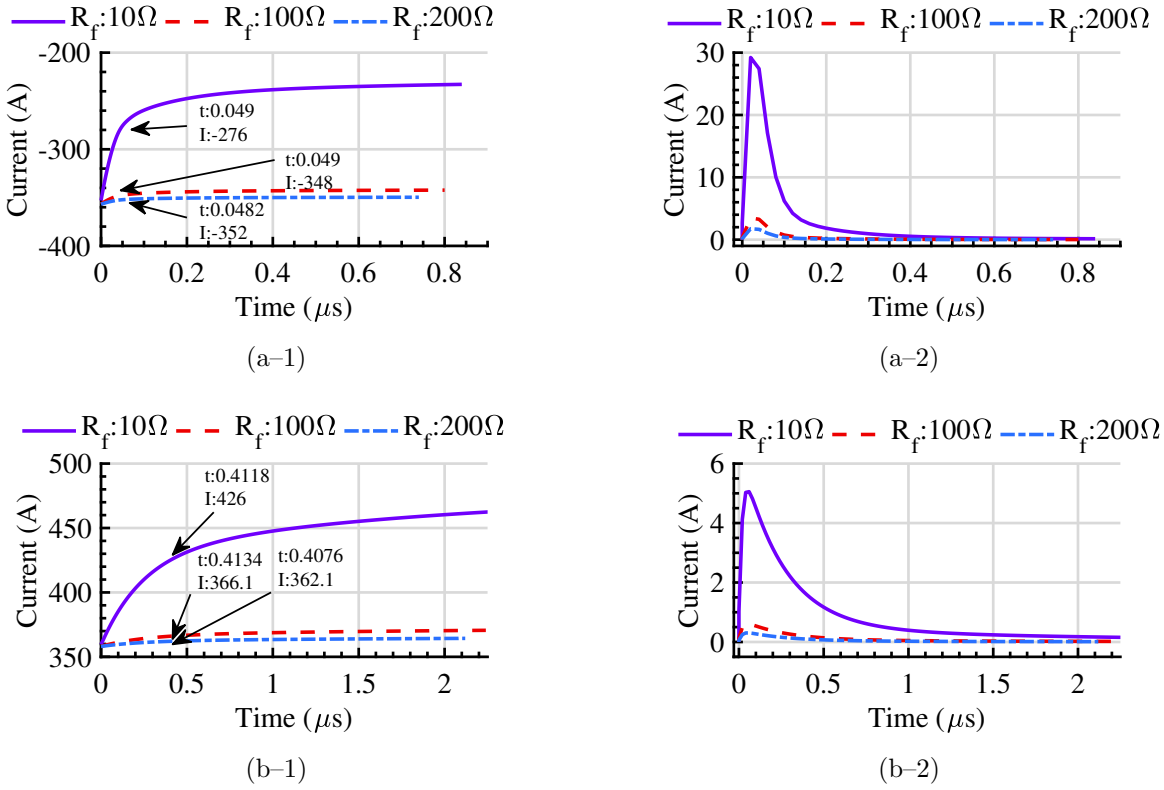

Figure 4.22: i^P_{TW} and i^P_{hp} of primary relays for PPG faults with R_f equal to 10, 100, and 200 Ω on L810, a) R810 and b) R108.

4.4.6 Signal-to-Noise-Ratios

To assess the noise immunity of the proposed scheme, White Gaussian Noise (WGN) with various SNRs is added to the TW seen by R12 during a bolted PG fault on $L12$, 950 m away from bus 1. The WGN is generated using MATLAB. Each time WGN is generated by MATLAB for the same SNR level, different values are obtained for the added noise, resulting in a potentially different effect on the estimated fault location. Therefore, in this study, 100 simulation runs are conducted for each SNR. Table 4.5 summarizes the average and worst fault location estimations for 100 runs of the TW with various SNRs. The deviation of the estimated χ due to noise (ΔN) is computed as the absolute value of

Table 4.4: Fault Location Estimation for Various Faults in the Test Microgrid

Line	Length (km)	Relay	Act. χ (m)	Est. χ (m)	Error (m)	Relay	Act. χ (m)	Est. χ (m)	Error (m)
L12	2	R12	950	965	−15	R21	1050	1044	6
L23	1.8	R23	435	446	−11	R32	1365	1389	−24
L24	2.5	R24	1035	1006	29	R42	1465	1485	−20
L25	2.2	R25	754	753	1	R52	1446	1489	−34
L26	2.6	R26	1168	1182	−14	R62	1432	1461	−29
L56	1.5	R56	621	645	−24	R65	879	901	−22
L510	1.1	R510	394	410	−16	R105	706	705	1
L512	0.4	R512	148	139	9	R125	252	231	21
L67	0.8	R67	275	313	**−38**	R76	525	515	10
L68	1.3	R68	843	865	−22	R86	457	423	34
L89	1	R89	583	613	−30	R98	417	418	−1
L810	3	R810	2397	2396	1	R108	603	613	−10
L1011	0.5	R1011	180	217	−37	R1110	320	342	−22

the estimated χ for a given SNR minus the estimated χ without noise, i.e., 965 m from Table 3.1. The error is computed as the actual χ for a given SNR minus the estimated χ, i.e., 950 m. It can be seen that the WGN with SNR of up to 40dB has an average and maximum impact of 11 m and 47 m on the estimation for χ, respectively. The resulting average and maximum overall error are 26 m and 62 m, respectively.

Table 4.5: Fault Location Estimation for Various SNRs

SNR (dB)	Average estimations and errors			Worst estimations and errors		
	χ (m)	ΔN (m)	Error (m)	χ (m)	ΔN (m)	Error (m)
70	965	0	−15	966	1	−16
60	965	0	−15	968	3	−18
50	968	3	−18	981	16	−31
40	976	11	−26	1012	47	−62

4.5 Conclusion

This chapter proposed a method to effectively detect, classify, and locate PP, PPG, and NPG faults in MVDC microgrids. Both the primary and the backup element of the proposed relay fulfill the speed requirement for the protection of dc systems. Unlike the existing TW-based protection methods, the proposed scheme is independent of the arrival times of TWs, and focuses on the waveshape properties of only the first TW initiated by a fault. The direction of the TW is identified based on the sign of the current TW. The estimated time constant for the current TW is used to identify the fault zone and fault location with an error that is less than ±38 m. Unlike existing two-terminal TW-based protection methods, the proposed scheme operates entirely based on local measurements, hence avoiding the delay and vulnerability to the failure of the communication system. This method is also superior to existing single-terminal TW-based protection methods since it is faster and also eliminates the complexities of detecting the second TW after the fault inception, e.g., the small magnitude of the second TW for high-resistance faults. In addition, independence from the TW arrival time makes the proposed method applicable to short distribution lines. The proposed relay is sufficiently sensitive to detect and locate high-resistance faults with R_f up to 200 Ω.

Chapter 5

Time-Domain TW-Based Protection Scheme for Hybrid AC/DC Microgrids

Low AC and high DC fault current magnitudes in hybrid AC/DC microgrids pose a major protection challenge. This chapter proposes a new TW-based method to detect, classify, and locate both AC and DC faults in hybrid AC/DC microgrids. Similar to the method proposed in Chapter 4, the proposed technique (i) utilizes only the first locally measured TW after the inception of a fault, and (ii) focuses on the waveshape properties and polarity of the TW, rather than its arrival time. Therefore, the proposed method is faster than the existing techniques, and also requires no form of communication. PSCAD/EMTDC simulation studies verify the performance of this new method. The results verify the scheme's ultra-high-speed, accuracy, sensitivity, selectivity, and independence from system configuration.

5.1 Hybrid AC/DC Test Microgrid

The 10-bus test hybrid AC/DC microgrid of Figure 5.1, is modeled using PSCAD/EMTDC [101]. The test microgrid has a PV station connected in the DC microgrid and supplying power to the main AC grid and local AC loads in the AC microgrid. The AC and DC microgrids are interlinked by a two-level VSC between buses 1 and 10. The test microgrid can operate in both grid-connected and islanded modes by closing and opening the main Circuit Breaker (CB), respectively. The voltage level in the AC and DC microgrids is 11 kV and ±2.5 kV, respectively. The interlinking VSC controls the DC voltage of the DC microgrid. Additionally, the PV station is connected to buses 5 and is interfaced with the DC microgrid through a DC/DC boost converter that is controlled by an MPPT algorithm. Moreover, two AC loads are connected to buses 8 and 9. Finally, a DC load is connected to bus 4 using DC/DC buck converters.

The cables are represented using the frequency-dependent distributed parameter model available in PSCAD/EMTDC. In both the AC and DC microgrids, single-core 6.35/11 kV 800 mm^2 cables with copper conductor, XLPE insulation (3.4 mm thick) and PVC sheathing (2.5 mm thick) are adopted [83]. For each line, the cables (one for each phase and pole) are buried 0.6 m deep, with a horizontal separation of 0.4 m. The cable lengths between different buses range from 1 to 3 km.

The grounding scheme of the DC microgrid is TN-S. Each line is equipped with two relays—one per terminal—that receive only the local current and voltage measurements. The relay between buses i and j, next to bus i, is denoted by Rij. The current measurement units of all relays are facing towards the line. In this system configuration three phase, Single-Line-to-Ground (SLG), Line-to-Line-to-Ground (LLG), Line-to-Line (LL), PP, PPG, and NPG faults can occur.

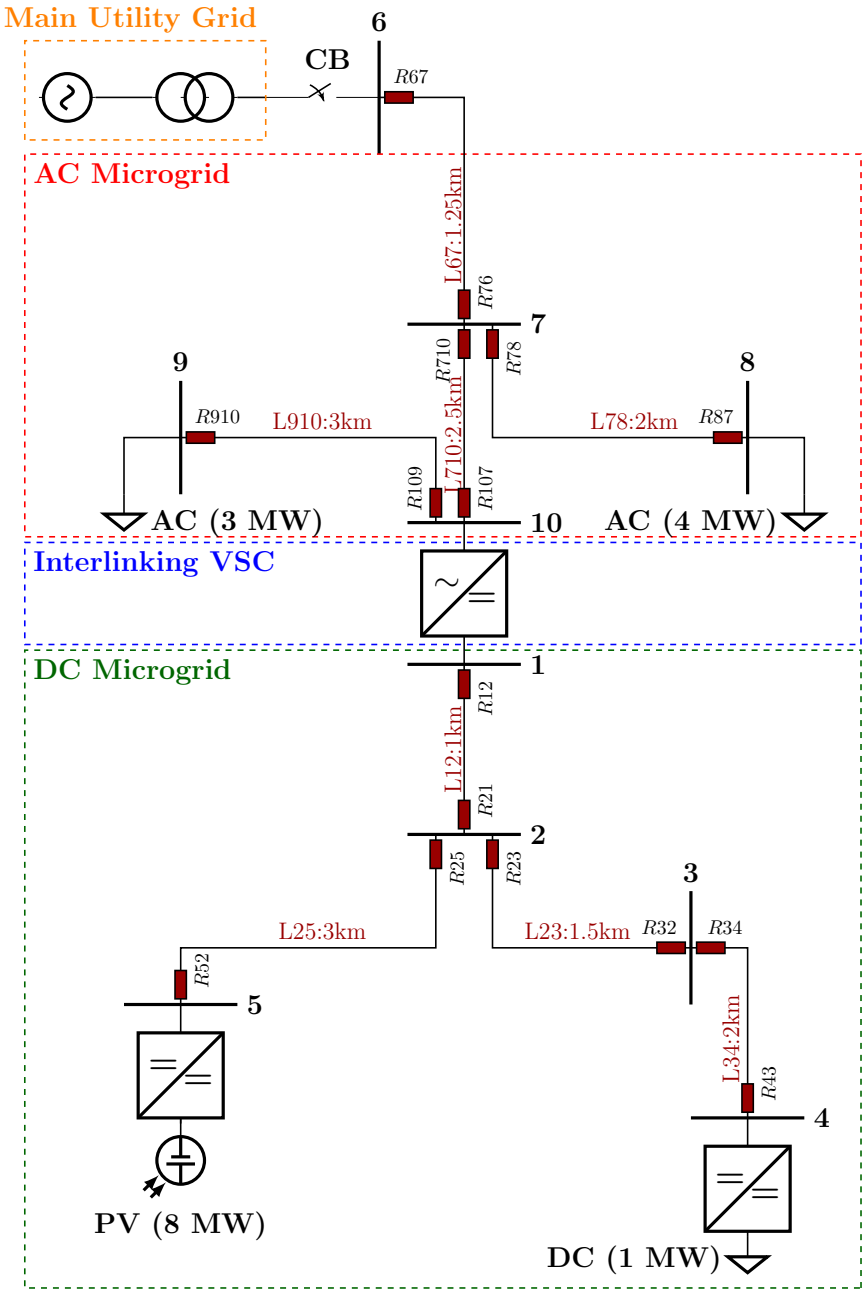

Figure 5.1: Single-line diagram of the test hybrid AC/DC microgrid

5.2 Proposed TW-Based Protection Method

Using the waveshape and polarity properties of the TWs discussed in Sections 4.2.1 and 4.2.2, respectively, another time-domain TW-based protection method for hybrid AC/DC microgrids is developed in this section. Different stages of this new method are summarized in the flowchart of Figure 5.2 and discussed in detail below.

5.2.1 Computation of Fault Discriminant Functions

To analyze the propagation of TWs in AC systems, a modal analysis to decouple the wave propagation modes is required [102]. In modal analysis, the phase signals are linear combinations of the mode signals, and vice versa. Clarke transformation is used to convert the three phases A, B, and C to α, β and 0 components [103]. In order to cover all fault types, three sets of voltage and current Clarke components with reference to phase A, B, and C are used. (5.1), (5.2), and (5.3) show the current Clarke components. Similar voltage Clarke components are computed.

$$\begin{bmatrix} I_\alpha^A \\ I_\beta^A \\ I_0^A \end{bmatrix} = \frac{1}{3} \begin{bmatrix} 2 & -1 & -1 \\ 0 & \sqrt{3} & -\sqrt{3} \\ 1 & 1 & 1 \end{bmatrix} \begin{bmatrix} I_A \\ I_B \\ I_C \end{bmatrix} \tag{5.1}$$

$$\begin{bmatrix} I_\alpha^B \\ I_\beta^B \\ I_0^B \end{bmatrix} = \frac{1}{3} \begin{bmatrix} -1 & 2 & -1 \\ -\sqrt{3} & 0 & \sqrt{3} \\ 1 & 1 & 1 \end{bmatrix} \begin{bmatrix} I_A \\ I_B \\ I_C \end{bmatrix} \tag{5.2}$$

$$\begin{bmatrix} I_\alpha^C \\ I_\beta^C \\ I_0^C \end{bmatrix} = \frac{1}{3} \begin{bmatrix} -1 & -1 & 2 \\ \sqrt{3} & -\sqrt{3} & 0 \\ 1 & 1 & 1 \end{bmatrix} \begin{bmatrix} I_A \\ I_B \\ I_C \end{bmatrix} \tag{5.3}$$

On the other hand, in DC systems, the current and voltage measurements on the positive and negative poles are decoupled. Thus, all fault types are covered using two sets of measurements only.

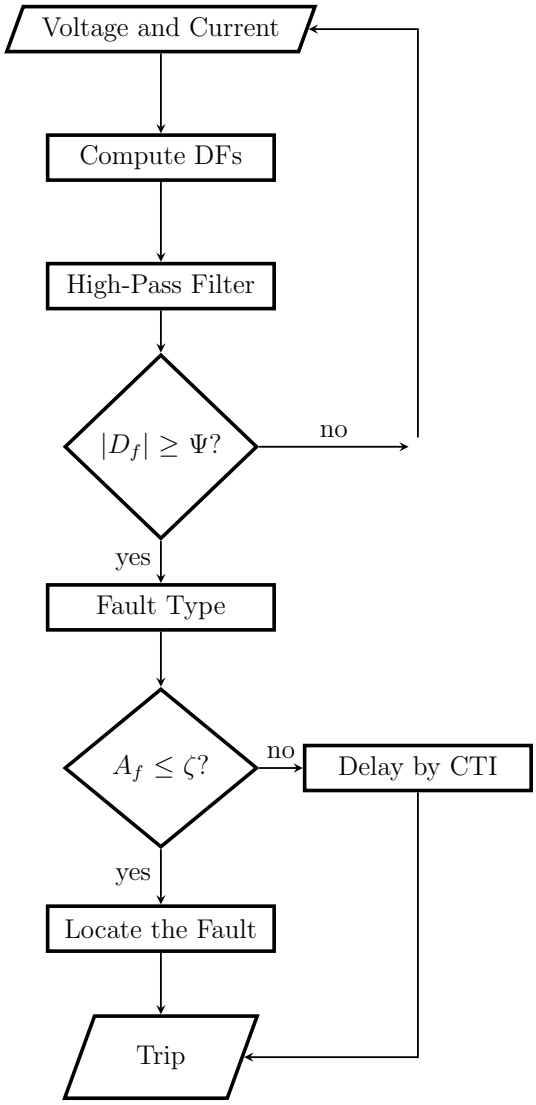

Figure 5.2: Flowchart of the proposed protection scheme.

Discriminant Functions (DF)s derived from the voltage and current TWs were introduced by [59]. The functions depend on the polarity properties of the voltage and current TWs discussed in Section 4.2.2. Salient features of this function, includes its line termination independence and polarity sensitivity [59]. DFs consist of a Forward Discriminant Function (FDF) and a Reverse Discriminant Function (RDF), corresponding to forward

and reverse faults, respectively and are expressed as:

$$\text{FDF} = v_{TW} - Z_c i_{TW} \tag{5.4}$$

$$\text{RDF} = v_{TW} + Z_c i_{TW} \tag{5.5}$$

where Z_c is the cable's characteristic impedance, expressed as:

$$Z_c = \sqrt{\frac{(R_x + j\omega L_x)}{(G_x + j\omega C_x)}} \tag{5.6}$$

Given that the bulk of the TW energy is in the megahertz range [66], FDF and RDF are passed through a first-order high-pass Butterworth filter. By removing the low-frequency content, this filter changes the exponential shape of the TWs in FDF and RDF to a pulse-like signals designated by D_f and D_r, respectively. In the AC microgrid, nine D_fs and nine D_rs are computed corresponding to the nine modal components. For instance, the D_f corresponding to the α Clarke component with respect to phase A is denoted as $D_f^{\alpha|A}$. On the other hand, in the DC microgrid, two D_fs and two D_rs are computed corresponding to the positive and negative pole measurements. For example, the D_r corresponding to the negative pole measurement is denoted as D_r^n.

5.2.2 Fault Detection and Direction Identification

In this section, D_f and D_r are used to detect the fault and determine its direction. The first TW launched by a fault is detected by comparing the absolute values of D_f and D_r to a pre-defined threshold Ψ. The boundaries of the period during which the pulse-like waveshape of $|D_f|$ and $|D_r|$ is higher than Ψ are denoted by t_1 and t_N. Ψ is selected based on the criteria mentioned in Section 4.3.1.

Moreover, during a forward fault, D_f exceeds Ψ while D_r does not. On the other hand, during a reverse fault, D_r exceeds Ψ while D_f does not. The aforementioned observation is deduced from the polarities of the voltage and current TWs [Section 4.2.2] expressed in (5.4) and (5.5). Therefore, based on Figure 5.2, if the fault is forward, i.e., D_f exceeds Ψ, the relay algorithm proceeds, otherwise, the algorithm keeps scanning for forward faults.

For instance, the lowest i_{TW} and v_{TW} and their corresponding $D_f^{\alpha|A}$ in the hybrid AC/DC grid of Figure 5.1 is seen by $R910$ for a 200 Ω SLG fault on phase A of $L710$, close to bus 7, i.e., the farthest (5.5 km away) high-resistance fault in this microgrid. Figure 5.3 shows $|D_f^{\alpha|A}|$ for this scenario after the white noise with SNR=85 dB is added to its associated i_{TW}s and v_{TW}s. During non-fault conditions, the $|D_f^{\alpha|A}|$ caused by noise is 0.9 V. Figure 5.3 illustrates that Ψ=5 V satisfies the four criteria of Section 4.3.1. The selected Ψ is: (i) 1.95 times lower than the pinpointed $|D_f^{\alpha|A}|$ peak (criterion 1), (ii) captures the TW waveshape between t_1=37.46 μs and t_N=38.66 μs (criterion 2), and (iii) is 5.6 times higher than measurement noise (criteria 3 and 4).

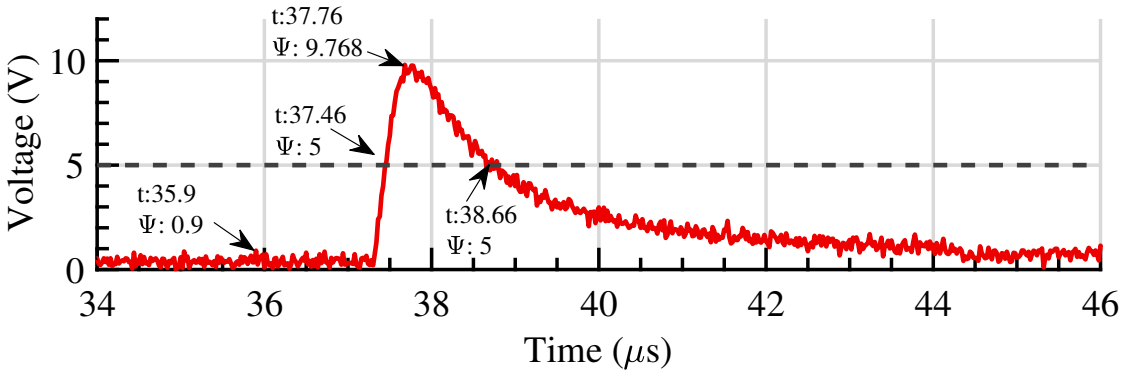

Figure 5.3: $|D_f^{\alpha|A}|$ of $R910$ for a 200 Ω SLG fault on $L710$ close to bus 7.

5.2.3 Fault Type

Depending on the fault type, some of the $|D_f|$ components detect the fault. i.e., $|D_f|$ exceeds Ψ, whereas others do not. Tables 5.1 and 5.2 show an AC and DC truth tables that can be used to determine the type of AC and DC faults, respectively. In the aforementioned truth tables, 1 represents a fault detected by the respective $|D_f|$, while a 0 denotes no detection. For example, during a SLG fault on phase A, all $|D_f|$ components detect the fault except $|D_f^{\beta|A}|$. This effect is mainly due to the fact that from (5.1), I_β^A and V_β^A are computed using the healthy phases B and C, while phase A is eliminated by the zero

multiplication. Similar justifications can be deduced for other AC fault types. It is worth noting that in case of LLG faults, all nine D_fs detect them, and thus it is not possible to identify the faulted phases. For PPG faults in the DC microgrid, only $|D_f^p|$ detects the fault while $|D_f^n|$ does not (Table 5.2). Similar observations are made for the other two DC fault types.

Table 5.1: Forward Discriminant Functions Truth Table for AC Faults

D_f	Fault Types									
	3ϕ	SLG			LLG			LL		
		A	B	C	AB	BC	AC	AB	BC	AC
$\alpha\|A$	1	1	1	1	1	1	1	1	0	1
$\beta\|A$	1	0	1	1	1	1	1	1	1	1
$0\|A$	0	1	1	1	1	1	1	0	0	1
$\alpha\|B$	1	1	1	1	1	1	1	1	1	0
$\beta\|B$	1	1	0	1	1	1	1	1	1	1
$0\|B$	0	1	1	1	1	1	1	0	0	1
$\alpha\|C$	1	1	1	1	1	1	1	0	1	1
$\beta\|C$	1	1	1	0	1	1	1	1	1	1
$0\|C$	0	1	1	1	1	1	1	0	0	1

Table 5.2: Forward Discriminant Functions Truth Table for DC Faults

D_f	Fault Types		
	PP	PPG	NPG
p	1	1	0
n	1	0	1

5.2.4 Fault Zone

As discussed in Section 4.2, the farther is a fault from the relay location, the longer is the settling time of the TW. This relation is shown in Figure 5.4a for FDF computed from measured i_{TW} and v_{TW} at $R910$ during bolted three phase fault on $L910$, 0.5 and 2.5 km away from $R910$. Moreover, Figure 5.4b shows that the corresponding $|D_f^{\alpha|A}|$s reflect the same relationship. Basically, the farther is a fault from the relay location, the wider is the $|D_f^{\alpha|A}|$. To eliminate the effect of different fault types and fault resistances on the magnitude of $|D_f^{\alpha|A}|$, the signal is normalized by its peak value as shown in Figure 5.4c. Figure 5.4c also shows that farther fault, i.e., 2.5 km away, has wider normalized $|D_f^{\alpha|A}|$, or equivalently larger normalized area (A_f) than closer fault. A_f is computed by summing the normalized $|D_f|$ samples between t_1 and t_N, and can be expressed as:

$$A_f = \frac{\sum_{i=1}^{N} D_f}{\max(D_f(t_1 : t_N))} \tag{5.7}$$

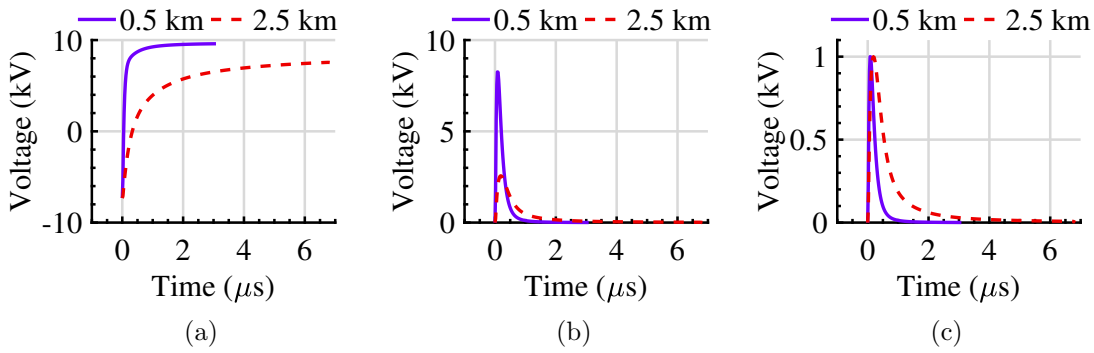

Figure 5.4: a) FDF, b) $|D_f^{\alpha|A}|$, and c) normalized $|D_f^{\alpha|A}|$ of $R910$ for a bolted three phase fault on $L910$ at 0.5 an 2.5 km away from $R910$.

The fault zone is determined by comparing A_f of a given D_f with a threshold ζ_a, which is based on A_f for the fault at the relay reach setting. For each relay, faults at the reach settings of the protection zones are simulated, and the normalized areas of the corresponding D_fs' are used to set the thresholds. The reach for the primary protection

zone of each relay is set to cover the entire line length. For instance, ζ_a of $R12$ is set to be the A_f of any D_f component launched by a fault at 1.25 km, i.e., length of $L12$. Table 5.3 summarizes the zone reaches and their respective thresholds for each relay in the hybrid AC/DC microgrid of Figure 5.1.

Each relay has primary and backup zones. The proposed relay operates in the primary zone if A_f is less than ζ_a (Figure 5.2). Otherwise, it operates in the backup zone. It is worth noting that the relays facing converter ends, such as $R21$, $R25$, $R34$, $R76$, $R109$, and $R78$, have no remote backup because the converter buses have no adjacent lines.

As shown in Figure 5.2, the faults in the relay's primary zone are tripped instantaneously, whereas the ones in the backup zone are tripped if the fault persists after the CTI. By following the CTI selection criteria stated in Section 4.3.4, the CTI for relays installed in the DC microgrid is set to 0.25 ms, while the ones installed in the AC microgrid have CTI=11 ms. The huge difference in the CTI values between the relays on the AC and DC microgrids is due to the difference in the operation time of the CBs. The fasted operation time of CB in the DC and AC microgrids is 200 μs and 10 ms, respectively.

5.2.5 Real-Time Fault Location

Based on the relationship between fault location and the area of D_fs, A_f-χ lookup table for each cable type can be generated. This lookup table is completely independent of the microgrid topology. For the test system of Figure 5.1, there is only one lookup table since one cable type is used in this hybrid AC/DC microgrid. The lookup table is created offline by simulating faults at different locations along that cable. The attained lookup table is uploaded to the fault location unit of each relay.

As an example, for the test system of Figure 5.1, the lookup table is created by simulating a fault at every 100 m along the 3-km $L910$. To further enhance the accuracy of the fault location unit, the distance resolution is increased from 100 m to 1 m using the spline interpolation method [100]. Figure 5.5 shows a graphical representation of the lookup table for the system of Figure 5.1, including the simulated samples as well as the samples obtained using the spline interpolation method. Using the measured time constant

Table 5.3: Relays Zone Reaches and Thresholds in the Test Microgrid

Relay	Reach (km)	ζ_a
R12	1	17.86
R21	1	17.86
R23	1.5	23.44
R32	1.5	23.44
R25	3	44.82
R52	3	44.82
R34	2	29.84
R43	2	29.84
R67	1.25	20.5
R76	1.25	20.5
R78	2	29.84
R87	2	29.84
R710	2.5	36.87
R107	2.5	36.87
R910	3	44.82
R109	3	44.82

and this lookup table, the fault location can be identified. After locating the fault, a trip signal is send to the respective CB to isolate the fault (Figure 5.2).

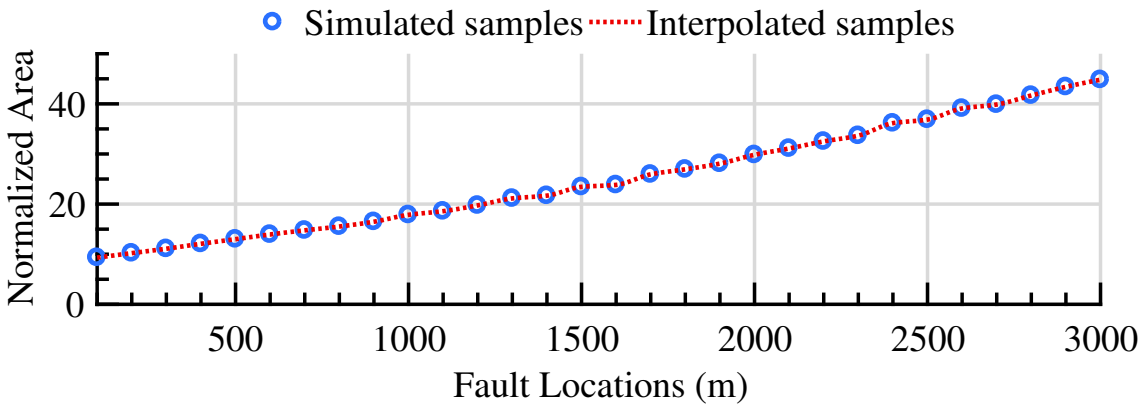

Figure 5.5: The simulated and interpolated samples of the A_f-χ lookup table.

5.3 Performance Evaluation

This section presents various case studies to demonstrate the performance of the proposed protection scheme under a variety of fault conditions for the hybrid ACDC microgrid of Figure 5.1.

5.3.1 Fault in the DC Microgrid

A bolted PPG fault on $L23$, 1 km away from bus 2 is studied in this section. The D_fs and D_rs of the positive and negative measurements of the primary relays covering this fault, i.e., $R23$ and $R32$, are shown in Figure 5.6. As shown in Figures 5.6a–1 and 5.6b–1, $|D_f^p|$ measured by these relays exceeds Ψ= 5 V, but $|D_f^n|$ does not exceed Ψ, and thus each relay is able to flag the fault as a PPG fault. Moreover, the smaller magnitude of $|D_r^p|$ than Ψ for $R23$ and $R32$ correctly indicates that the fault is forward for these two relays.

For the same fault, the measurements on the positive pole of the relays on the adjacent lines—i.e., $R12$, $R21$, $R25$, $R52$, $R34$, and $R43$—are shown in Figure 5.7. All of the aforementioned relays correctly detect a PPG fault because $|D_f^p|$ or $|D_r^p|$ measured by these relays exceed Ψ. Meanwhile, it can be seen that only $R12$, $R52$, and $R43$ have $|D_f^p|$ that exceeds Ψ, whereas $|D_r^p|$ of $R21$, $R25$, and $R34$ is the one exceeding Ψ. Hence, based

on the algorithm depicted in Figure 5.2, $R12$, $R52$, and $R43$ flag a forward fault and can accordingly operate as backup relays to $R23$ and $R32$. On the other hand, $R21$, $R25$, and $R34$ identify a reverse fault, which blocks their operation based on the algorithm of Figure 5.2.

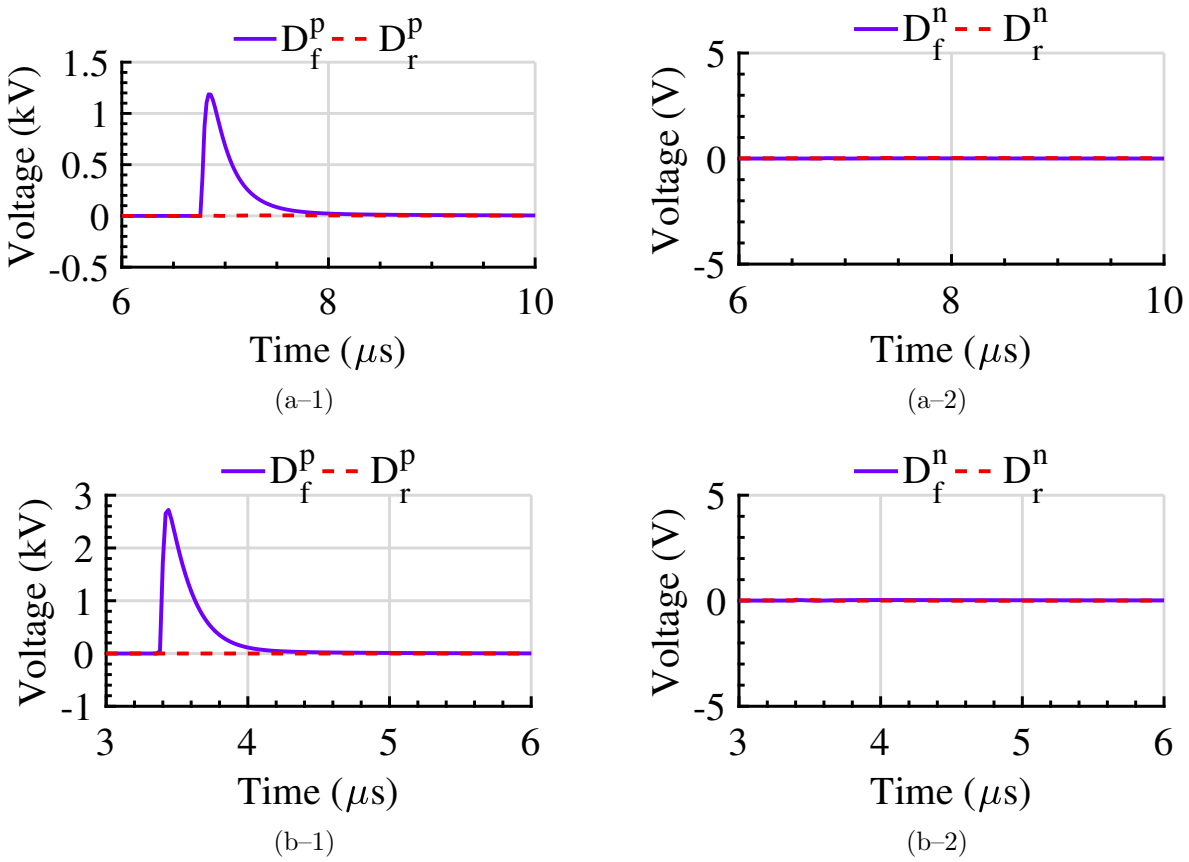

Figure 5.6: D_f and D_r of positive and negative pole primary relays for bolted PPG fault on L23, a) R23, b) R32.

Using (5.7), the normalized areas of the D_fs detected by the aforementioned relays are computed. A_f^p for $R23$, $R32$, $R12$, $R52$ and $R43$ is 16.57, 11.70, 28.69, 63.45, and 36.42, respectively (Figures 5.6a–1, 5.6b–1, 5.7a–1, 5.7b–2, and 5.7c–2).

These normalized areas are used by each relay to determine if the fault is in-zone. The normalized areas for $R23$ and $R32$ are 16.57 and 11.70, respectively, and are less than

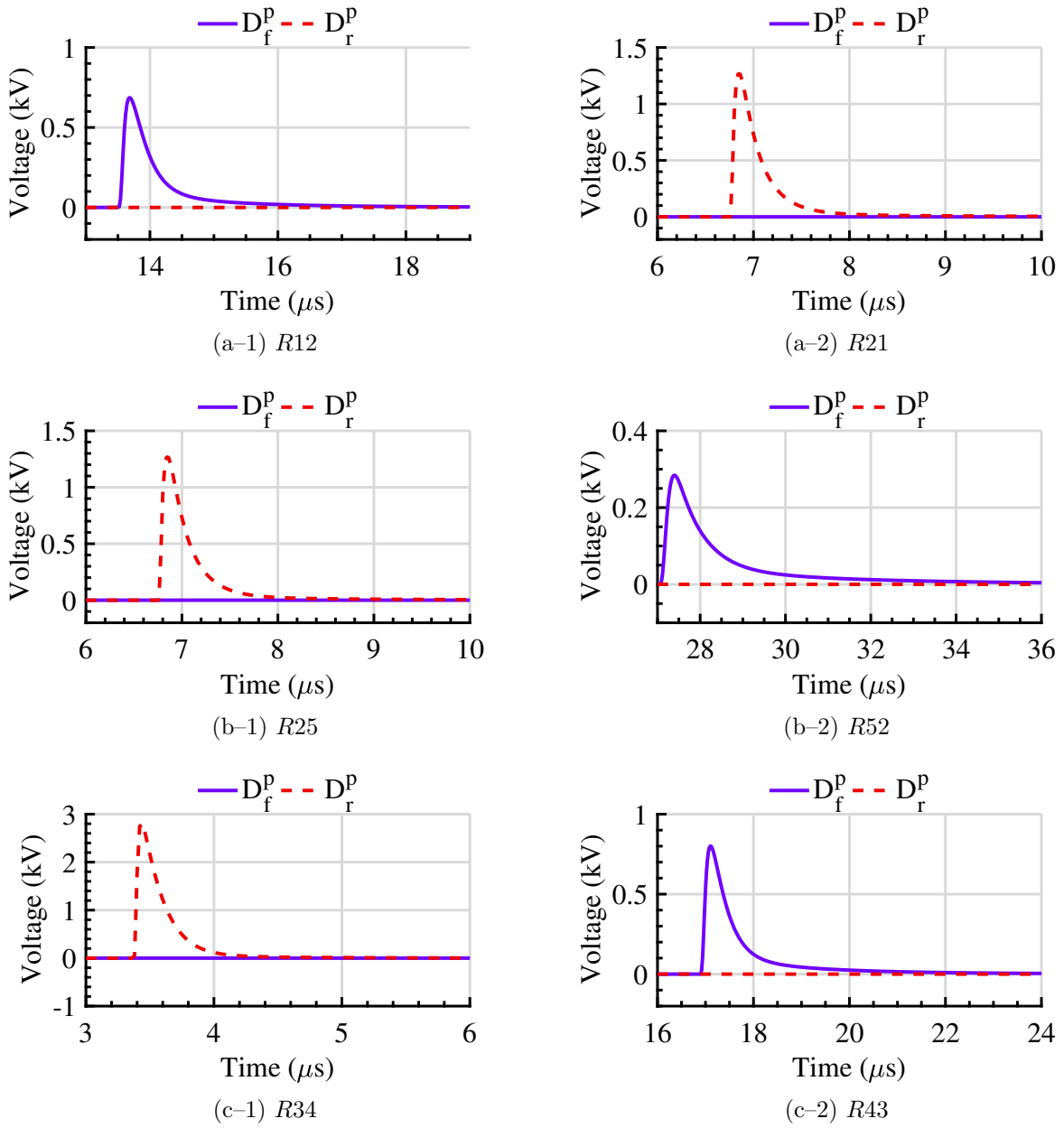

Figure 5.7: Positive pole D_fs and D_rs of adjacent relays on lines a) $L12$, b) $L25$, and c) $L34$ for bolted PPG fault on $L23$.

ζ_a=23.44 (Table 5.3). Thus, the primary relays trip instantaneously. On the other hand, the normalized area for $R12$, $R52$ and $R43$ is 28.69, 63.45, and 36.42, respectively, which is greater than their respective ζ_a=17.86, 36.87, and 29.84 (Table 5.3). Therefore, $R12$, $R52$ and $R43$ correctly detect that the fault is in their backup zones and a delay of 250 μs is added before tripping.

Based on the relay's operation zones, the operation time of $R23$, $R32$, $R12$, $R52$ and $R43$ is 7.68 (Figure 5.6a–1), 4.2 (Figure 5.6b–1), 250+14.84=264.84 (Figure 5.7a–1), 250+28.46=278.46 μs (Figure 5.7b–2), and 250+18.82=268.82 μs (Figure 5.7c–2), respectively. Therefore, in addition to the primary relays—whose operation time remain well below 8 μs—the backup relays also satisfy the speed requirement for the protection of DC microgrids.

Finally, the previously-mentioned 16.57 and 11.70 normalized areas calculated by $R23$ and $R32$ are used along with the lookup table illustrated in Figure 5.5 to estimate the fault location. The actual distance between the fault and $R23$ is 1000 m and the estimated χ is 1093 m. Thus, the error in fault location is only 93 m. Similarly, the actual and estimated fault locations for $R32$ are 500 and 448 m, resulting in 52 m error.

5.3.2 Faults in the AC Microgrid

A bolted SLG fault on phase A of $L67$, 0.5 km away from bus 6, with inception angle equal to 1 degree is studied in this section. The fault is conducted while the microgrid is in grid-connected mode. The nine D_fs and D_rs Clarke components of primary relay $R67$ are shown in Figure 5.8. Only $|D_f|$s exceed Ψ= 5 V, while $|D_r|$s remain unaffected. Thus, $R67$ is able to flag a forward fault. Moreover, all the $|D_f|$s detect the fault with the exception of $|D_f^{\beta|A}|$ (Figure 5.8a–2), which remains unaffected. Therefore, based on the truth table of Table 5.1, $R67$ correctly identify the fault as SLG on phase A and can selectively trip the faulted phase. The normalized area of $|D_f^{\alpha|A}|$, $|D_f^{0|A}|$, $|D_f^{\alpha|B}|$, $|D_f^{\beta|B}|$, $|D_f^{0|B}|$, $|D_f^{\alpha|C}|$, $|D_f^{\beta|C}|$, and $|D_f^{0|C}|$ is 12.24, 11.83, 11.78, 12.19. 11.83, 11.76, 12.19, and 11.83, respectively. All the aforementioned A_fs are smaller than ζ_a=20.5, and hence the fault is in-zone. From Figure 5.8, the operation time of $R67$ from all the D_f components is 3.9 μs. Since, all of the aforementioned A_fs correspond to the same fault, their average=12.2 is used along

with the lookup table illustrated in Figure 5.5 to estimate the fault location. The actual distance between the fault and $R67$ is 500 m and the estimated χ is 473 m. Thus, the error in fault location is only 27 m.

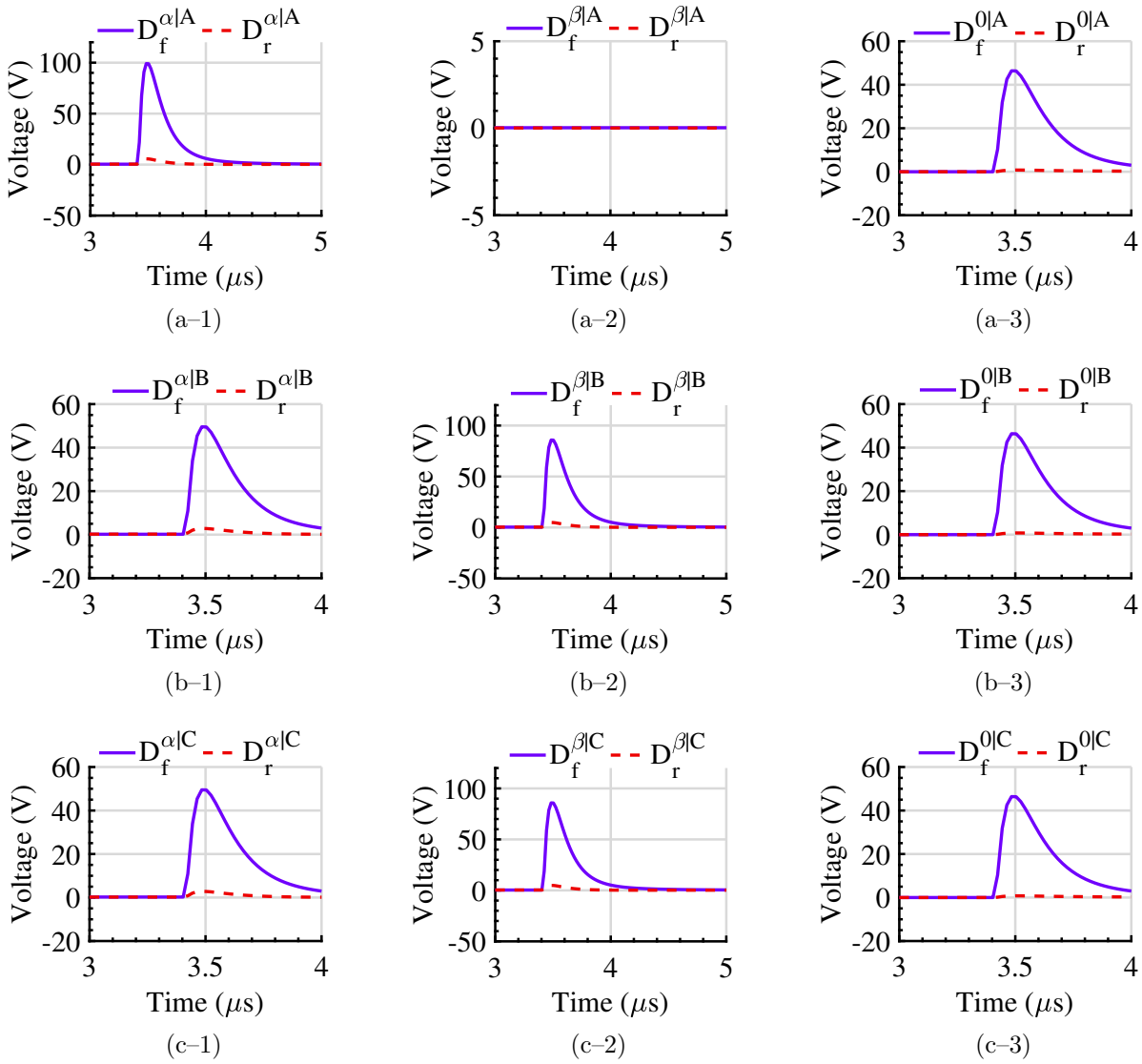

Figure 5.8: D_f and D_r Clarke components of $R67$ with reference to phase a) A, b) B, and c) C for bolted SLG fault on phase A of $L67$.

Another bolted SLG fault on phase B of $L67$, 0.5 km away from bus 6, with inception angle equal to 1 degree is conducted while the microgrid is in islanded mode. The nine D_fs and D_rs components of primary relay $R67$ are shown in Figure 5.9. Only $|D_f|$s exceed Ψ= 5 V, while $|D_r|$s remain unaffected. Thus, $R67$ is able to flag a forward fault. Moreover, all the $|D_f|$s detect the fault with the exception of $|D_f^{\beta|B}|$ (Figure 5.9b–2), which remains unaffected. Therefore, based on the truth table of Table 5.1, $R67$ correctly identify the fault as SLG on phase B. The normalized area of $|D_f^{\alpha|A}|$, $|D_f^{\beta|A}|$, $|D_f^{0|A}|$, $|D_f^{\alpha|B}|$, $|D_f^{0|B}|$, $|D_f^{\alpha|C}|$, $|D_f^{\beta|C}|$, and $|D_f^{0|C}|$ is 9.78, 11.14, 9.79, 10.95, 9.79, 9.75, 10.97, and 9.79, respectively. All the aforementioned A_fs are smaller than ζ_a=20.5, and hence the fault is in-zone. From Figure 5.9, the operation time of $R67$ from all the D_f components is 2.8 μs. The average A_f is 10.2. Hence, the actual and estimated fault locations for $R67$ are 500 and 414 m, resulting in 86 m error.

From the above case studies, it can be seen that microgrid configuration mode has a negligible effect on the speed and fault location accuracy of the proposed method. Yet, the proposed method was shown to be sensitive to very low fault current and voltage changes during microgrid islanded mode and faults with inception angle very close to zero.

5.3.3 Fault Types

To assess the selectivity of the proposed scheme, different types of bolted AC and DC faults are conducted on $L23$ and $L67$, respectively. AC faults are performed 0.5 km away from bus 6, i.e., the same location for the SLG fault of the last subsection. Similarly, DC faults are performed 1 km away from bus 2, i.e., the same location for the PPG fault of the Section 5.3.1. Tables 5.4 and 5.5, show the normalized areas of the different D_f components computed by $R67$ and $R23$ under different types of AC and DC faults, respectively. The different fault types trigger different set of D_f components that correspond to the truth tables in Tables 5.1 and 5.2. Therefore, the proposed method can accurately classify different AC and DC fault types and selectively trip the faulted pole. The average normalized area of D_f components corresponding to SLG, LLG, LL, and three phase faults in Table 5.4 ranges between 12.95 and 12.99, which is almost the same. Similarly, the average normalized area of D_f components corresponding to NPG and PP faults in Table

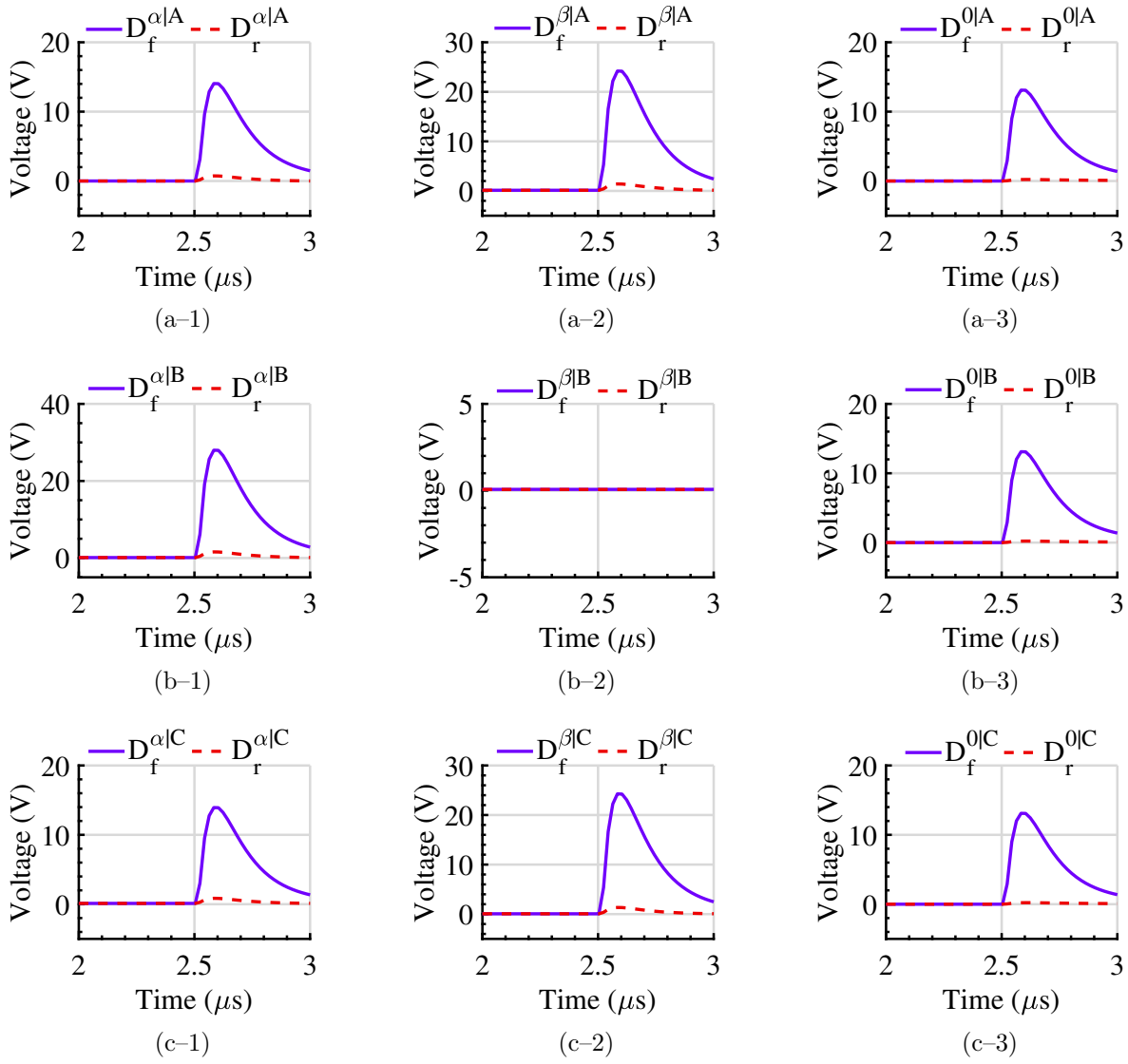

Figure 5.9: D_f and D_r Clarke components of $R67$ with reference to phase a) A, b) B, and c) C for bolted SLG fault on phase B of $L67$.

5.5 ranges between 16.56 and 16.57, which is almost the same. Accordingly, the accuracy of the proposed method is not affected by the change in the fault type.

Table 5.4: Normalized areas of D_f components computed by $R67$ for different fault types in the AC Microgrid

Fault Types	Phase	$A_f^{\alpha\|A}$	$A_f^{\beta\|A}$	$A_f^{0\|A}$	$A_f^{\alpha\|B}$	$A_f^{\beta\|B}$	$A_f^{0\|B}$	$A_f^{\alpha\|C}$	$A_f^{\beta\|C}$	$A_f^{0\|C}$
SLG	C	12.97	12.97	12.97	12.93	12.99	12.97	12.99	–	12.97
LLG	AC	12.98	12.97	12.92	12.88	12.99	12.92	12.99	12.94	12.92
LL	BC	–	13	–	12.99	12.98	–	13	12.96	–
3ϕ	ABC	12.96	13	–	12.99	12.99	–	13	13	–

Table 5.5: Normalized areas of D_f components computed by $R23$ for different fault types in the DC Microgrid

Fault Types	A_f^p	A_f^n
PPG	16.57	–
NPG	–	16.56
PP	16.56	16.56

5.3.4 Fault Resistances

To assess the sensitivity of the proposed scheme, PPG and three phase faults with R_f equal to 10, 100, and 200 Ω are conducted on $L23$ and $L67$ (same location as in other subsections), respectively. Figures 5.10 and 5.11 show that R_f has a significant effect on the magnitudes of D_f components. However, the variation of D_f components has a minimal effect on the normalized area computed by the relays. On the DC microgird, the normalized area computed by $R23$ is equal to 16.57, 16.25, and 16.1 for R_f=10, 100, and 200 Ω, respectively. Moreover, A_f^p for $R32$ is equal to 11.70, 11.3, and 10.9 under R_f=10, 100, and 200 Ω, respectively. Similarly, on the AC microgrid, the average normalized area of the D_f Clarke components computed by $R67$ is equal to 12.96, 12.63, 12.13 for R_f=10, 100, and 200 Ω, respectively. In addition, the average normalized area of the D_f Clarke components for $R76$ is equal to 15.12, 14.93, and 14.74 under R_f=10, 100, and 200 Ω,

respectively. Such small differences in A_f have negligible impact on the accuracy of the proposed protection scheme. Therefore, the proposed method is shown to be sensitive to high-resistance faults on the DC and AC microgrids.

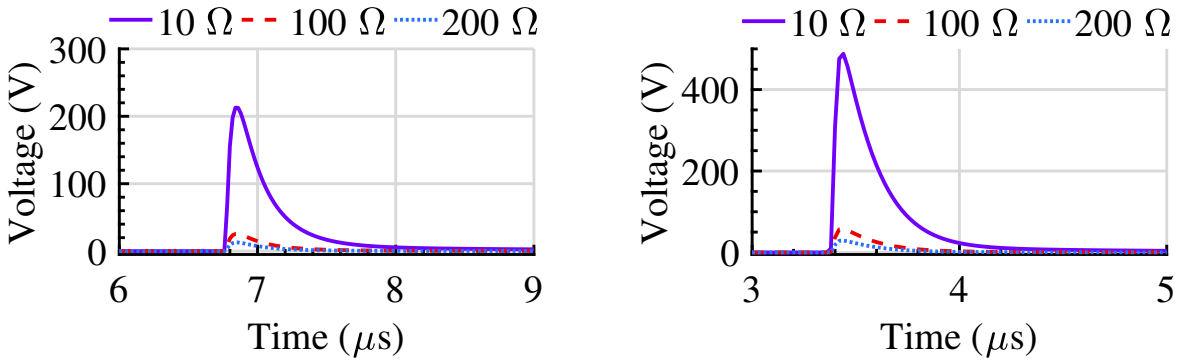

Figure 5.10: D_f^p of primary relays for PPG faults with R_f equal to 10, 100, and 200 Ω on L23, a) R23 and b) R32.

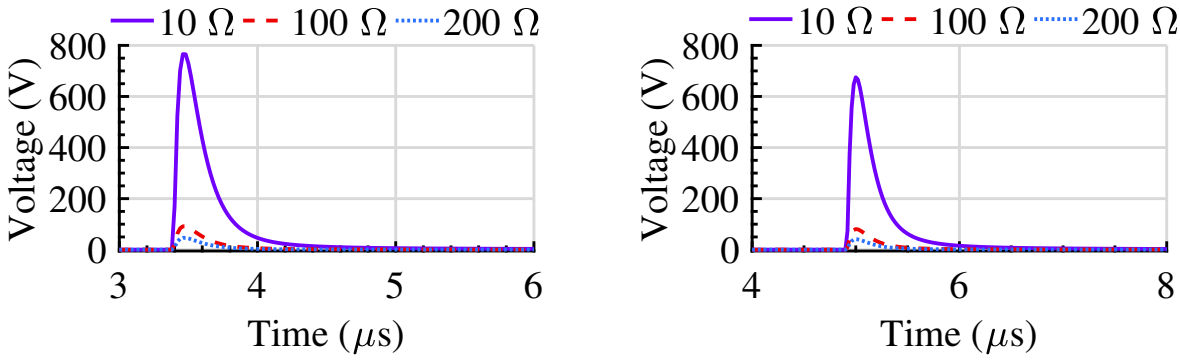

Figure 5.11: $D_f^{\alpha|A}$ of primary relays for three phase faults with R_f equal to 10, 100, and 200 Ω on L67, a) R67 and b) R76.

5.3.5 Fault Locations

To assess the accuracy of the proposed scheme, bolted faults are conducted at various locations on the 8 lines of the test hybrid AC/DC microgrid. Table 5.6 summarizes the fault location estimations for the faults in the test microgrid of Figure 5.1 as seen by the relays at both ends of the faulted lines. It can be seen that 93 m is the largest estimation error for χ.

Table 5.6: Fault Location Estimation for Various Faults in the Test Microgrid

Line	Length (km)	Relay	Act. χ (m)	Est. χ (m)	Error (m)	Relay	Act. χ (m)	Est. χ (m)	Error (m)
L12	1	R12	130	156	26	R21	870	848	22
L23	1.5	R23	1000	1093	93	R32	500	448	52
L25	3	R25	1265	1210	55	R52	1735	1744	9
L34	2	R34	442	463	21	R43	1558	1530	28
L67	1.25	R67	500	492	8	R76	725	737	12
L78	2	R78	888	801	87	R87	1112	1065	47
L710	2.5	R710	736	789	53	R107	1764	1682	82
L910	3	R910	2762	2758	4	R109	238	231	7

5.4 Conclusion

This chapter proposed a method to effectively detect, classify, and locate different AC and DC fault types in hybrid AC/DC microgrids. The direction of the fault is identified using a discriminant function based on the voltage and current TWs. The area under the high-pass filtered discriminant function is used to identify the fault zone and fault location with an error that is less than $\pm$100 m. The proposed scheme is sufficiently sensitive to detect and locate faults during islanded configuration, with inception angle close to zero, and with R_f

up to 200 Ω. Other salient features of this scheme include its ultra-high-speed, selective isolation of the faulted phase/pole and independence from grid configuration.

Chapter 6

Frequency-Domain TW-Based Protection Scheme for HVDC Grids

DC faults in HVDC grids can cause severe damage to VSCs and large loss of infeed within few milliseconds. Ensuring selectivity and sensitivity of the protection system within a short time window is a major challenge. This chapter proposes an ultra-high-speed method to detect and locate DC faults in HVDC grids. This new scheme uses, for the first time, the frequency-domain properties of TWs, and also does not require communication. The proposed method uses only the first TW caused by a fault, and so does not need to cope with the complexities for detecting the arrival time of the second TW. Another corollary is that the primary operation time of this method is less than 0.5 ms, which meets the speed requirement for protection of DC grids. Moreover, the high speed of the proposed primary protection method enables the design and coordination of a TW-based backup protection, enhancing the protection reliability. The proposed method is also robust against noise, and has been tested successfully for fault resistances of up to 200 Ω. The performance of the proposed scheme has been assessed using the CIGRE B4 HVDC test grid under various conditions. The results verify this method's ultra high speed, accuracy, sensitivity, selectivity, and independence from grid configuration.

6.1 CIGRE HVDC Test System

The 15-bus CIGRE HVDC test grid of Figure 6.1, modelled using PSCAD/EMTDC, is used for this study [104]. This grid connects offshore wind power plants and oil & gas platforms to onshore ac systems. The grid consists of three interconnected dc systems (DCS) namely: (a) DCS1 is a ±200 kV 2-terminal symmetric monopole HVDC link, (b) DCS2 is a ±200 kV 4-terminal symmetric monopole HVDC grid, and (c) DCS3 is a ±400 kV 5-terminal bipole HVDC meshed grid. A monopole ac-dc converter station consists of one MMC, whereas a bipole ac-dc converter station consists of two MMCs with a midpoint ground. DCS1 and DCS3 are interconnected through the ac system, whereas DCS2 and DCS3 are interconnected through the ac system as well as a dc-dc converter station between buses 8 and 11.

This grid consists of Overhead Line (OHL)s and Underground Cable (UGC)s, which are simulated using the frequency-dependent distributed parameter model available in PSCAD/EMTDC. The positive and negative poles of each OHL are both are 30 m above the ground, with a horizontal separation of 10 m. Each conductor consists of two bundled sub-conductors with a spacing of 0.45 m. Additionally, two ground wires are 7 m above the conductors, with a horizontal spacing of 9 m. The conductors and ground wires sag 20 and 14 m, respectively. The two conductors of each UGC are buried 1.5 m deep, with a horizontal separation of 0.5 m. The OHL lengths range from 100 to 500 km, and the UGC lengths range from 100 to 300 km. Only one type of conductor is used for all of the OHLs in the HVDC grid of Figure 6.1. The same applies for UGG.

Each line is equipped with two relays—one per terminal—that receive only the local current measurements of the positive and negative poles. The relay between buses i and j, next to bus i, is denoted by Rij. In both symmetric monopole and bipole system configurations, PP, PPG, and NPG faults can occur.

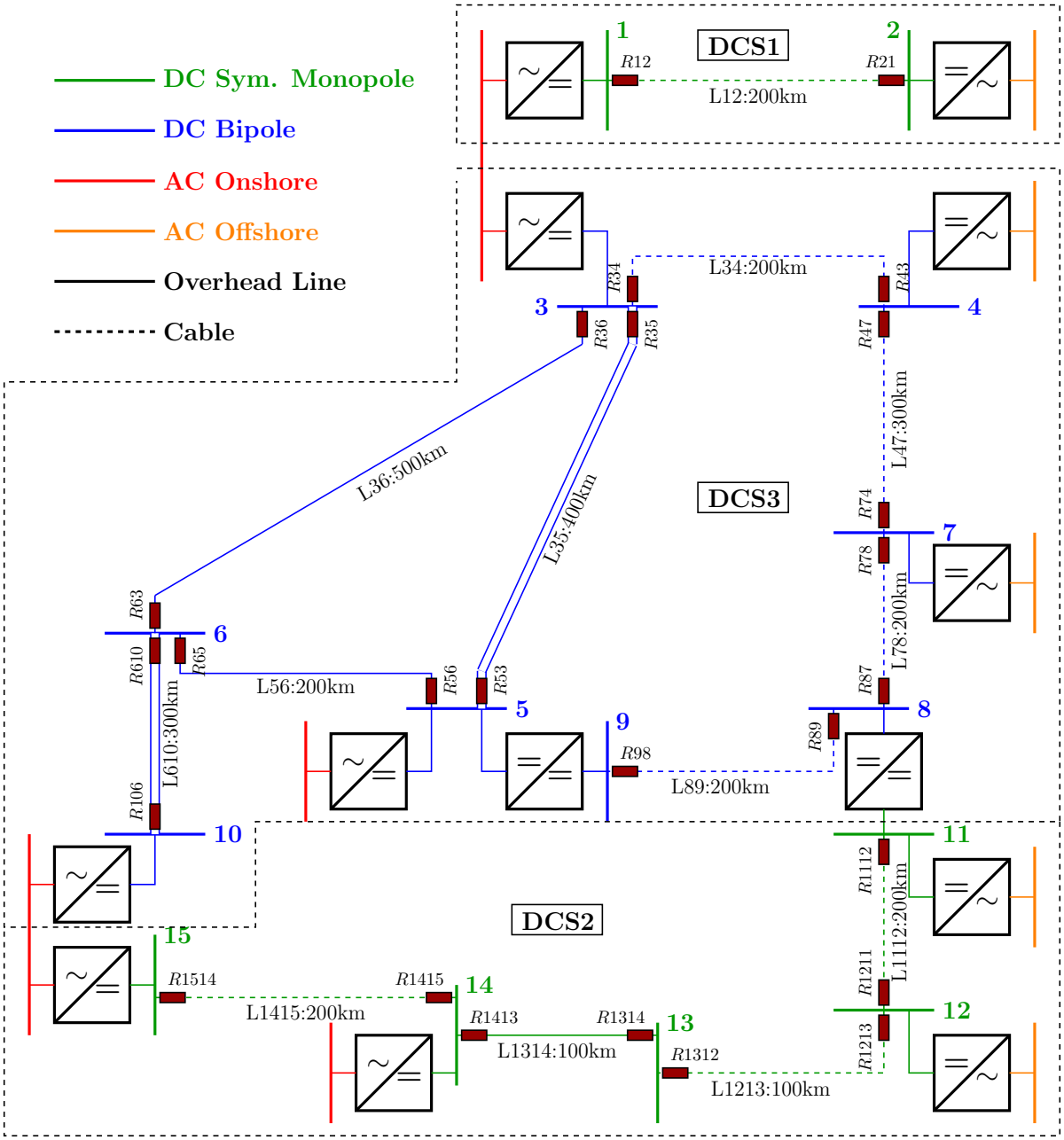

Figure 6.1: Single-line diagram of the CIGRE HVDC grid

6.2 TWs' Frequency Content

From (4.1), it can be seen that i_{TW} is a function of χ and γ. Moreover, (4.2) shows that the real part of γ is α, which is a frequency-dependent parameter and the main cause of the TW attenuation. α can be broken down into four loss components, namely: (a) skin-effect loss (α_S), (b) dielectric loss (α_D), (c) conductivity of dielectric loss (α_G), and (d) radiation loss (α_R) [105]. α_G and α_R have a negligible impact on the total α, and thus can be ignored [105], [106]. On the contrary, α_S—the main cause of the TW attenuation at lower frequencies—depends on R_x, which is directly proportional to the square root of the frequency of a component, and is given by [106]:

$$\alpha_S = \frac{R}{2Z_c} = \frac{1}{2Z_c}\sqrt{\frac{\pi\mu f}{\sigma}} \tag{6.1}$$

where σ is the conductor's conductivity, μ is the conductor's permeability, and f is the frequency of a given TW component. On the other hand, α_D dominates α at higher frequencies. It depends on C_x and is directly proportional to the frequency of a component, and is represented as [105], [106]:

$$\alpha_D = \frac{\omega C Z_c tan(\delta)}{2} = \frac{\pi\sqrt{\epsilon_r}tan(\delta)}{c} f \tag{6.2}$$

where $\tan(\delta)$ is the dielectric dissipation factor, ϵ_r is the relative dielectric constant, c is the speed of light. It can be seen from (6.1) and (6.2) that α_S and α_D are directly related to f, and so the higher frequency components undergo more severe attenuation. In addition, since α is related to the per-unit length quantities in (4.2), the total TW attenuation of each frequency component increases with the increase in the distance traveled by the TW.

To illustrate this phenomenon, a voltage that consists of seven sinusoidal components with frequencies equal to 125, 250, 375, 500, 625, 750, and 875 kHz, and zero phase angles is applied to a 500 km OHL with specifications presented in Section 6.1. Figure 6.2 shows a 50 μs window of applying this voltage to the OHL at three different locations. It is evident that the voltage waveform is smoothed as the voltage propagates along the OHL. To investigate the attenuation rate of each frequency component as it travels through the OHL, FFT is applied to obtain the normalized spectrum of the three waveforms in Figure

6.2. Figure 6.3 shows that the seven frequency components have equal amplitudes at the beginning of the OHL. However, as the signal reaches the middle and end of the OHL, all seven frequency components decline. The higher frequency components, such as the 875 kHz, experience more severe attenuation than the lower ones, such as the 125 kHz. Moreover, for every frequency component, the amplitude attenuation at the end of the OHL is higher than that at the middle of the OHL.

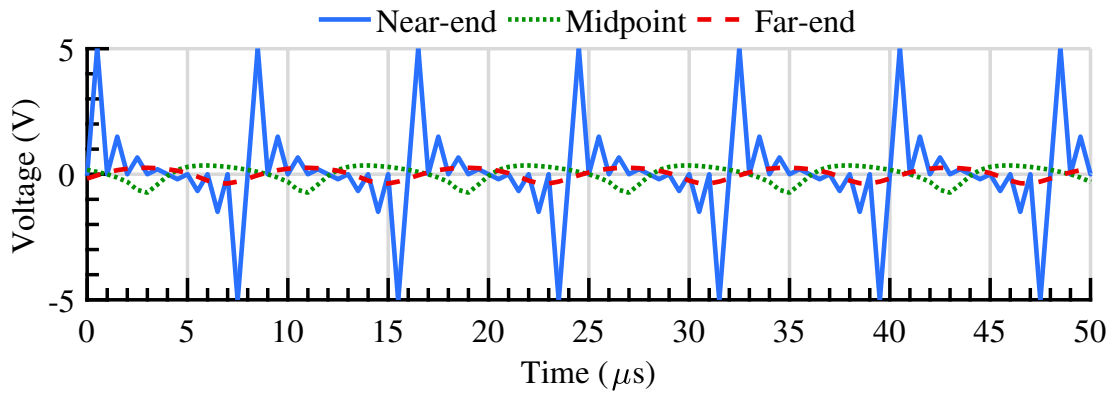

Figure 6.2: A seven-component voltage waveform at near end, midpoint, and far end of a 500 km OHL.

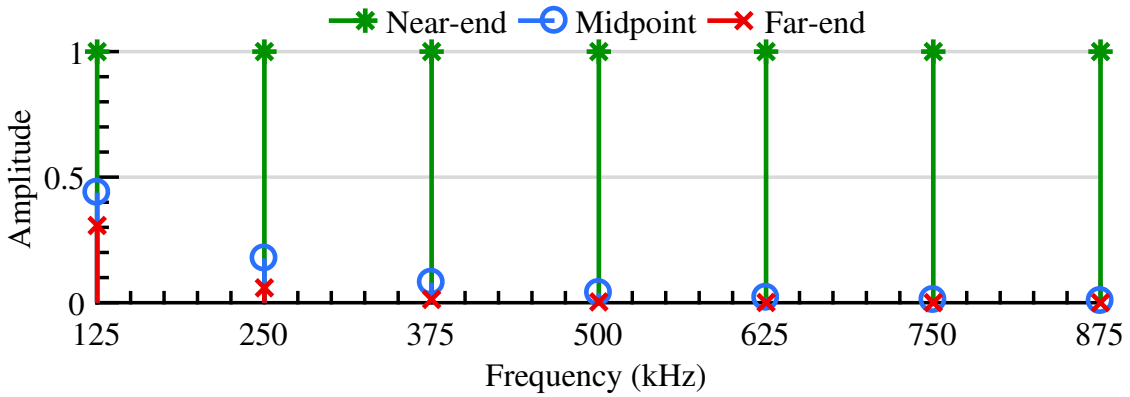

Figure 6.3: The spectrum of the voltage waveform at near end, midpoint, and far end of a 500 km OHL.

It is worth noting that the the reliance of α in (4.2) on L and C indicates that alpha

depends on the configuration and geometry of the conductors. Therefore, the TW attenuation is different for OHL and UGC. From (6.1) and (6.2), it can be seen that large Z_c results in low α_S and has no impact on α_D, and thus a low α is obtained. Since OHLs have higher Z_c than UGCs [107], OHLs have lower α, and accordingly lower frequency components attenuation rate than UGCs. Furthermore, since Z_c is directly proportional to the TW propagation velocity, TW propagate faster in OHLs (98% of c) than in UGCs (48% of c) [108]. Section 6.3 will demonstrate how the above characteristics can be used to locate DC faults.

6.3 Proposed TW-Based Protection Scheme

Using the frequency content and polarity properties of the TWs discussed in Sections 6.2 and 4.2.2, respectively, a frequency-domain TW-based protection method for HVDC grids is developed in this section. Different stages of this new method are summarized in the flowchart of Figure 6.4 and discussed in detail below.

6.3.1 TW Detection

Given that the bulk of the TW energy is in the megahertz range [66], the analog measurements are passed through a first-order high-pass Butterworth filter. By removing the low-frequency content, this filter changes the exponential shape of the TW to a pulse-like signal [97]. The high-pass filtered signal is passed through an ADC. The output of ADC for each pole current is designated by i_{hp}. i_{hp} is used to capture the first TW and determine the fault direction using the polarity properties. The directional element is discussed in Section 6.3.4 as it is used in other stages of the proposed method. In this section, the first TW is detected by comparing i_{hp} to a pre-defined threshold $\pm\Psi$. The boundaries of the period during which the pulse-like waveshape of i_{hp} is higher than $+\Psi$ or lower than $-\Psi$ are denoted by t_1 and t_N. Ψ is selected such that:

1. It is sensitive to high-resistance and far-end faults that result in small TWs.

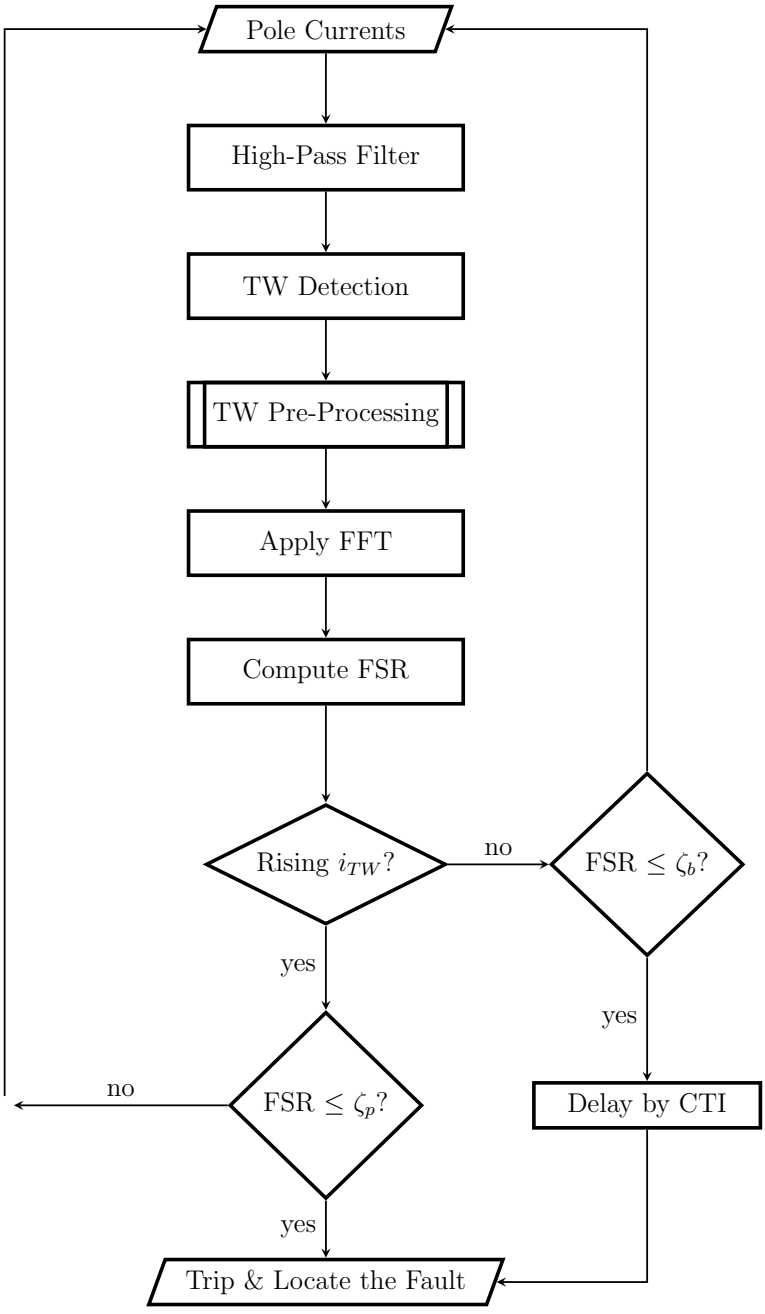

Figure 6.4: Flowchart of the proposed protection scheme.

2. It captures the entire length of a TW waveshape.

3. It is higher than non-fault measurement noise. Typical current measurement units are designed to maintain a minimum SNR of 85 dB [98].

4. It factors in sufficient security margin for the above three criteria. In commercial protective devices, the measured error tolerance is often specified as ±5 percent of the measured value [77].

For instance, the lowest i_{TW} and its correspondingly i_{hp} in the HVDC grid of Figure 6.1 are seen by $R47$ for a 200 Ω PPG fault on UGC $L47$, close to bus 7, i.e., the farthest (300 km away) high-resistance fault on an UGC in this HVDC grid. Figure 6.5 shows i_{hp} for this scenario after the white noise with SNR=85 dB is added to its associated i_{TW}. During non-fault conditions, the i_{hp} caused by noise is 4.9 mA. Figure 6.5 illustrates that Ψ=10 mA satisfies the above four criteria. The selected Ψ is: (i) 7 times lower than the pinpointed i_{hp} peak (criterion 1), (ii) captures the TW waveshape between t_1=1.536 ms and t_N=31.921 ms (criterion 2), and (iii) is 2.1 times higher than measurement noise (criteria 3 and 4).

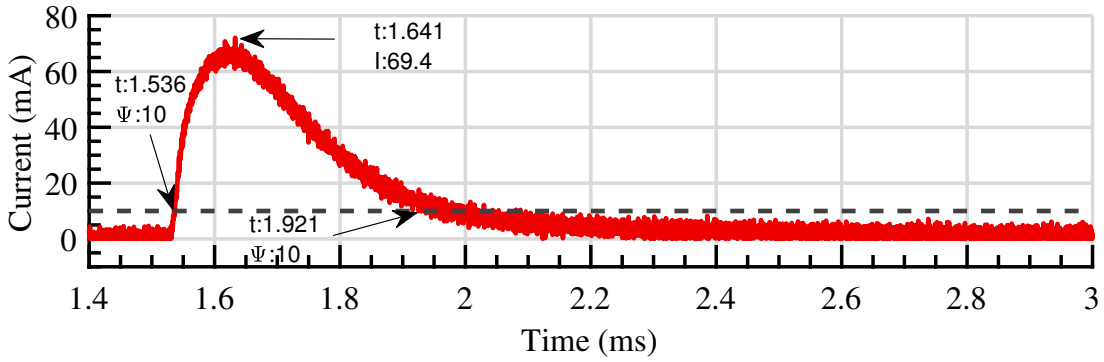

Figure 6.5: i_{hp} of $R47$ for a 200 Ω PPG fault on $L47$ close to bus 7.

6.3.2 TW Pre-processing

Prior to obtaining the detected TW's frequency spectrum, $i_{TW}(t_1{:}t_N)$ undergoes three pre-processing stages:

TW Normalization

The magnitude of $i_{TW}(t_1{:}t_N)$ varies based on the fault's type, resistance, and location. Such variation affects the frequency analysis outcome, which makes it difficult to draw an informative comparison between the TW frequency spectra associated with different fault conditions. Accordingly, to ensure that all $i_{TW}(t_1{:}t_N)$s have a similar magnitude, a min-max normalization technique is utilized and the normalized current TW, $i_{TW,N}$, is computed as [109]:

$$i_{TW,N} = \frac{i_{TW}(n) - \min(i_{TW})}{\max(i_{TW}) - \min(i_{TW})} \quad \forall n = 1, 2, \ldots, N \tag{6.3}$$

where $i_{TW}(n)$ is the *n-th* sampling instant of a recorded current between t_1 and t_N. To demonstrate the TW normalization stage, Figures 6.6a and 6.6b show a sample $i_{TW}(t_1{:}t_N)$ and its $i_{TW,N}$, respectively.

Window Selection

Due to the lower velocity and late arrival of low-frequency components, the longer the TW propagates, the higher the settling time of the TW waveshape becomes [Section 6.2]. As a result, the length of i_{TW} varies for different fault locations. The farthest fault location from the relay generates the longest i_{TW}. Moreover, the type of conductor affects the length of i_{TW} [Section 6.2]. In order to obtain the same resolution, i.e., number of bins, for the TW frequency spectrum associated with different fault locations on a given conductor, a fixed time-domain window size (W_F) should be used for each conductor type. Moreover, W_F is determined by the length of the longest i_{TW}, i.e., the farthest fault location, to ensure that the full length of $i_{TW}(t_1{:}t_N)$ for all of the faults inside the relay's protection zone is smaller than W_F.

For instance, Figures 6.6 and 6.7 show the longest i_{TW}s that can occur on the OHLs and UGCs of the test HVDC grid of Figure 6.1, respectively. For illustration purposes, the time axes offset are removed by subtracting t_1. Figure 6.6a shows that a fault on an OHL, 500-km away from the relay, results in a 39 μs long i_{TW}. Similarly, a fault on an UGC, 300-km away from the relay, causes a 385 μs long i_{TW} in Figure 6.7a. Accordingly, with the addition of a 20% security margin, W_F of the relays for the OHLs and UGCs of the HVDC grid in Figure 6.1 is selected to be 50 and 500 μs, respectively.

TW Zero-Padding

W_F is larger than the length of all of the TWs recorded by the relay. In the meantime, zero-padding a signal before finding its frequency spectrum is an effective method for interpolating the spectra of finite-duration signals and is commonly used in different applications [110]. Therefore, the W_F-long window is zero-padded between t_N and the end of the window. For rising $i_{TW,N}$s, such as the ones in Figures 6.6b and 6.7b, $i_{TW,N}(t_N)$ is equal to one. Zero-padding such signals will cause a step change at t_N, which negatively impacts the frequency analysis of $i_{TW,N}$. To avoid this negative impact, rising $i_{TW,N}$s are first flipped to make them falling. Hence, as shown in Figures 6.6c and 6.7c, $i_{TW,N}(t_N)$ is zero instead of one, and the zero-padding does not cause discontinuity in $i_{TW,N}$. In the case of a falling $i_{TW,N}$, no flipping is required.

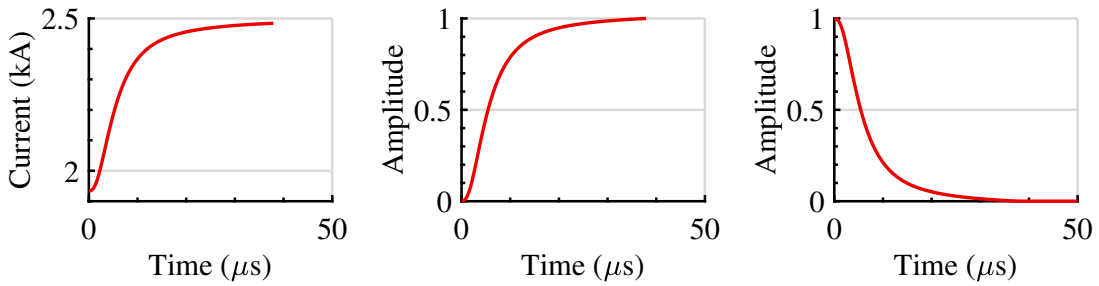

Figure 6.6: The a) captured, b) normalized, and c) zero-padded i_{TW} of $R63$ for a 200 Ω PPG fault on $L36$ close to bus 3.

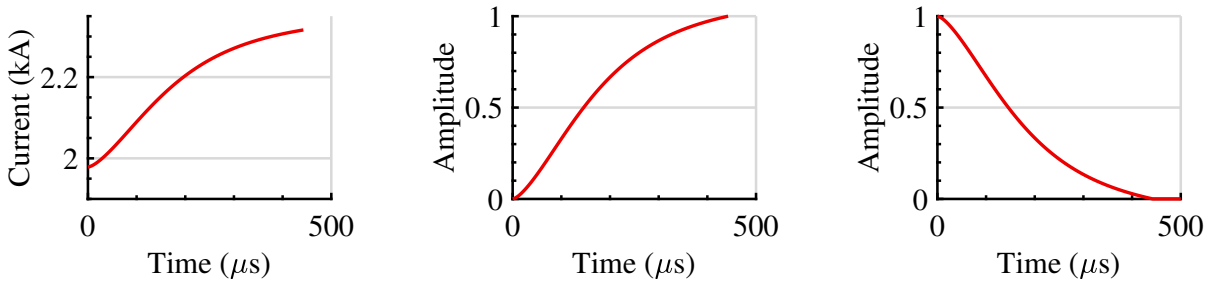

Figure 6.7: The a) captured, b) normalized, and c) zero-padded i_{TW} of $R47$ for a 200 Ω PPG fault on $L47$ close to bus 7.

6.3.3 TW Frequency Spectrum Analysis

FFT is an effective tool to examine the frequency content of the captured TW. FFT is applied to the TW inside W_F, which starts at t_1. In order to analyze the attenuation rates of different frequency components of a recorded TW, the Frequency Spectrum Ratio (FSR), which compares the low- and high-frequency components, is introduced:

$$FSR = \frac{\sum_{k=1}^{\lceil \frac{N}{2} \rceil} I[k]}{\sum_{k=\lceil \frac{N}{2} \rceil + 1}^{N} I[k]} \tag{6.4}$$

where $I[k]$ is the power of $k\text{-}th$ harmonic, and N is the total number of harmonics, computed as:

$$N = \lceil \frac{1}{2} . \frac{F_s}{\Delta F} \rceil \tag{6.5}$$

where F_s is the sampling frequency and ΔF is FFT's frequency resolution, which is computed by:

$$\Delta F = \frac{1}{W_F} \tag{6.6}$$

Section 6.2 proved that longer TW propagation through a conductor causes higher attenuation in the high-frequency components than the low-frequency ones. Therefore,

FSR is directly proportional to the distance to the fault location. For instance, FSR for near-end, midpoint and far-end locations discussed for Figures 6.2 and 6.3 is equal to 1.33, 19, and 324, respectively, confirming the above argument.

It can be seen that the FSR in (6.4) designates the first half of the frequency spectrum as low-frequency components and the second half as high-frequency components. Different designations of low and high frequency components result in different FSR values, yet the trend of higher FSR values for farther fault locations does not change. Moreover, since a range of frequency components—rather than individual frequency bins—are used in the numerator and denominator of (6.4), the defined FSR is robust against noise. This is attributed to the fact that the power of noise at a given SNR is distributed to various frequency components.

6.3.4 Fault Detection

The relation between fault location (χ) and FSR is used to determine the reach of the relay. Each relay has two reaches namely: (i) a primary reach set to cover the length of the primary line, and (ii) a backup reach set to cover the length of the longest line behind the relay. ζ_p is the threshold used to set the primary reach, whereas ζ_b is the threshold used to set the backup reach. A fault is detected in the primary zone by comparing the FSR of the measured i_{TW} with ζ_p, which is based on the i_{TW} for the fault at the relay reach setting. For each relay, faults at the reach settings of the primary and backup protection zones are simulated, and the FSRs of the corresponding i_{TW}s are used to set the thresholds. For instance, ζ_p of $R36$ is set to be the FSR of i_{TW} launched by a fault next to bus 6.

As discussed in Section 6.2, (6.1) and (6.2) show that the TW frequency attenuation depends on the configuration of the line/cable, meaning that the FSR for a certain location is fixed for one conductor type. Consequently, the same FSR is obtained for faults at 200-km on $L12$ and $L34$, which are UGCs with the same conductor type. However, different FSRs are obtained for faults at 200-km on $L12$ and $L56$, i.e., an UGC and an OHL with different conductor types. Table 6.1 summarizes the thresholds for different OHL and UGC lengths at which relays are installed in the HVDC grid of Figure 6.1. For example, the reach of $R1213$ and $R1314$ on UGC $L1213$ and OHL $L1314$ is 100-km, and ζ_p is 11480 and

41.27, respectively. Moreover, each relay has different ζ_p and ζ_b depending on its location. For instance, $R65$ has a primary reach of 200 km to cover $L56$ with ζ_p=143 and a backup reach of 500 km to cover $L36$ with ζ_b=926.5.

Table 6.1: Zone Reaches and Thresholds in the Test HVDC Grid

Reach (km)	ζ	
	OHL	UGC
100	41.27	11480
200	143	131500
300	347.1	209200
400	633.6	–
500	926.5	–

As shown in the flowchart of Figure 6.4, if the fault is forward, i.e., i_{hp} is greater than $+\Psi$ indicating a rising i_{TW}, and within the primary reach, i.e., FSR is less than ζ_p, then the primary zone of the relay will pick up. However, if the fault is reverse and within the backup reach, i.e., FSR is less than ζ_b, then the backup zone of the relay will pick up.

During a relay's backup operation, the trip signal is delayed by the CTI. In this chapter, the CTI is set to 1.55 ms to account for the maximum 500 μs operation time of the primary zone, 1 ms operation time of dc circuit breaker [14], and a security margin.

6.3.5 Real-Time Fault Location

Based on the relationship between the fault location and the frequency spectrum of i_{TW}s, an FSR-χ lookup table for each conductor type can be generated. This lookup table is completely independent of the HVDC grid topology, and depends only on α, which is a function of the conductor parameters in (4.2). Such dependence on conductor parameters is common in protection applications, e.g., distance relays require information about the impedance of the line, which depends on the parameters in (4.2). For the test system of

Figure 6.1, there are two lookup tables, one is for the OHLs and the other is for UGCs. The lookup tables are created offline by simulating faults at different locations along these conductors.

As an example, for the test system of Figure 6.1, the lookup tables are created by simulating a fault at every 100 m along the 500-km $L36$ OHL and the 300-km $L47$ UGC. To further enhance the accuracy of the fault location unit, the distance resolution is increased from 100 m to 1 m using the spline interpolation method [100], i.e., without increasing the number of simulations. Figures 6.8 and 6.9 show a graphical representation of the lookup tables for the system of Figure 6.1, including the simulated samples as well as the samples obtained using the spline interpolation method. Using the computed FSR given by these lookup tables, the fault location can be identified immediately after the onset of a fault.

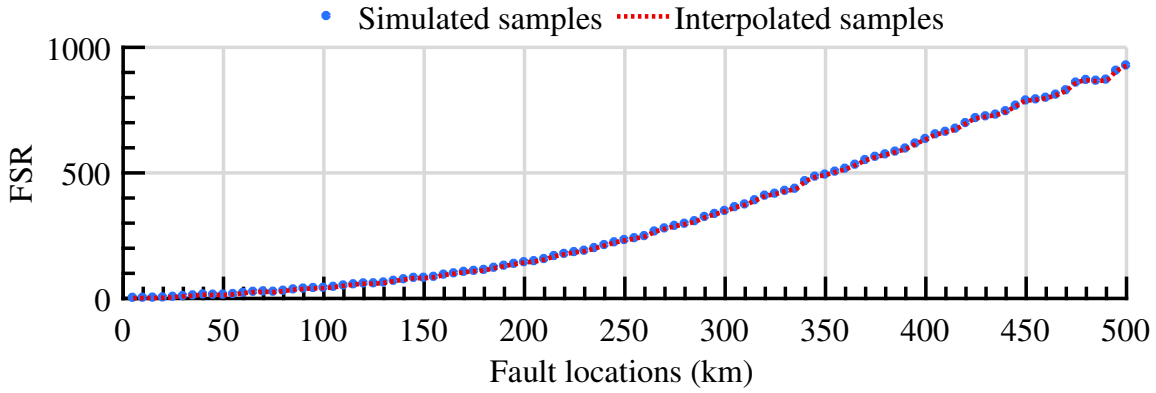

Figure 6.8: The simulated and interpolated samples of the OHL lookup table.

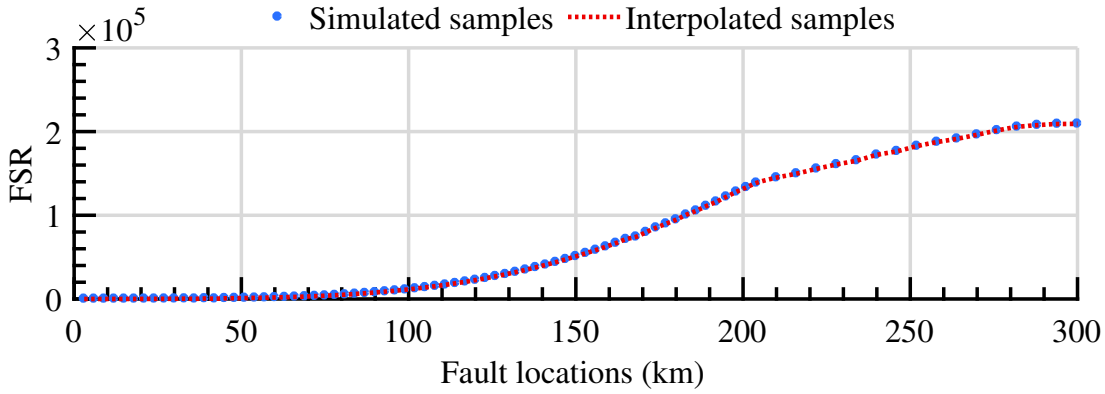

Figure 6.9: The simulated and interpolated samples of the UGC lookup table.

6.4 Performance Evaluation

This section presents various case studies to demonstrate the performance of the proposed protection scheme under a variety of fault conditions for the HVDC grid of Figure 6.1.

6.4.1 Bolted PP Fault on an OHL

A bolted PP fault on $L36$, 382 km away from bus 3 is studied in this section. The high-pass filtered and processed current TW measured on the positive pole of the relays on the faulted $L36$, i.e., $R36$ and $R63$, and adjacent $L56$, $L610$, $L34$, and $L35$—i.e., $R56$, $R65$, $R610$, $R106$, $R34$, $R43$, $R35$, and $R53$—are displayed in Figure 6.10. The same measurements are obtained for the negative pole since its a PP fault. As shown in Figure 6.10a–1, i_{hp}^{P} (superscript P denotes the positive pole) measured by the primary relays $R36$ and $R63$ exceeds the positive Ψ=10 mA, and thus each relay is able to flag the fault as a forward fault. On the other hand, Figure 6.10b–1 shows that i_{hp}^{P} of $R56$ drops below $-\Psi$, indicating a reverse fault, whereas $R65$ exceeds $+\Psi$, indicating a forward fault. Similarly, a reverse and forward fault are detected by $R610$ and $R106$, respectively (Figure 6.10c–1). Since a converter station is connected to bus 3 with a capacitive termination [104], Figures 6.10d−1 and 6.10e−1 show that i_{hp}^{P} of the relays on $L34$ and $L35$ do not exceed $\pm\Psi$; thus, they do not detect any TW. Such behaviour is attributed to the fact that capacitive

termination results in the full reflection of i_{TW} onto the faulted line, i.e., $L36$, and the annihilation of v_{TW} [96]. Thus, the relays on $L34$ and $L35$ do not detect a fault, and accordingly they do not trip.

Figures 6.10a–2, 6.10b–2, and 6.10c–2 show the normalized and zero-padded i^P_{TW} of the aforementioned relays that detected the TW. Figure 6.11 shows the corresponding frequency spectra of the six relays after applying FFT to $i^P_{TW,N}$s. In all six spectra, the high-frequency components attenuate more severely than the low-frequency components. Furthermore, Figure 6.11 shows that the higher frequency components of the relays that are farther away from the fault—i.e., $R36$, $R56$ and $R106$—attenuate more severely than those of the relays closer to the fault, i.e., $R63$, $R65$ and $R610$.

The FSR for relays $R36$, $R63$, $R56$, $R65$, $R610$, and $R106$, computed using (6.4), is 550.47, 58.29, 393.3, 58.29, 58.29, and 641.90, respectively. The FSRs for $R36$ and $R63$ are 550.47, 58.29, respectively, and are less than their ζ_p=926.5 of OHL $L36$ (Table 6.1). Since $R36$ and $R63$ flagged a forward fault, the primary relays trip instantaneously. However, FSR for $R56$ is 393.3, which is greater than its ζ_p=143 of OHL $L56$ (Table 6.1). Therefore, the fault is out of $R56$'s primary zone and according to the flowchart in Figure 6.4, this relay does not trip. Similarly, FSR for $R106$ is 641.90, which is greater than its ζ_p=347.1 of OHL $L610$ (Table 6.1). Therefore, the fault is outside the primary zone of $R106$ and does not trip. On the other hand, the FSR of $R65$ and $R610$ is 58.29, which is less than their ζ_b=926.5 of OHL $L36$. Therefore, $R65$ and $R610$ correctly detect that the fault is in their backup zones.

The primary relays $R36$ and $R63$ operate instantaneously after the time it takes to process the captured TWs, which is 50 μs for relays on the OHLs of the grid (Figure 6.10a–2). On the other hand, backup relays $R65$ and $R610$ are delayed by the 1.55 ms CTI. Therefore, in addition to the primary relays—whose operation times do not exceed 50 μs—the backup relays also satisfy the speed requirement for the protection of HVDC grids.

Finally, the previously-mentioned 550.47 and 58.29 FSRs calculated by $R36$ and $R63$ are used along with the OHL lookup table illustrated in Figure 6.8 to estimate the fault location. The actual distance between the fault and $R36$ is 382 km and the estimated χ

is 382.012 km. Thus, the error in fault location is only 12 m. Similarly, the actual and estimated fault locations for $R63$ are 118 and 118.008 km, resulting in 8 m error.

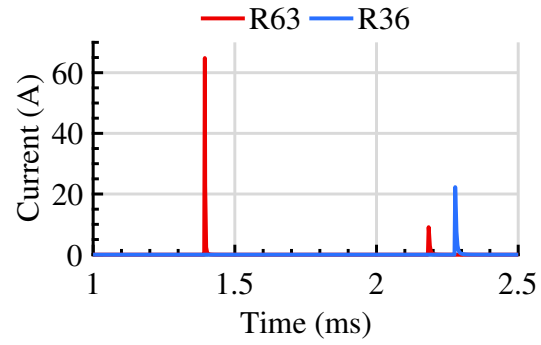

(a–1) i^P_{hp}

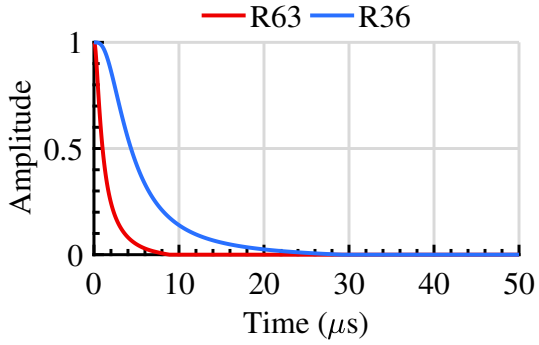

(a–2) $i^P_{TW,N}$

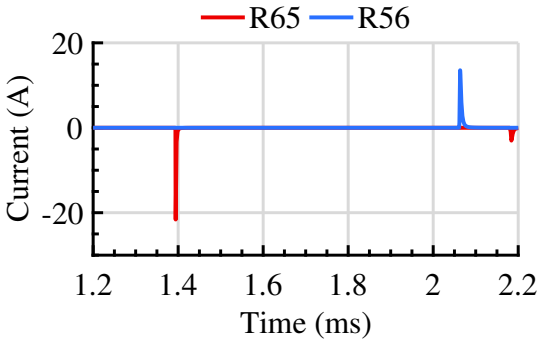

(b–1) i^P_{hp}

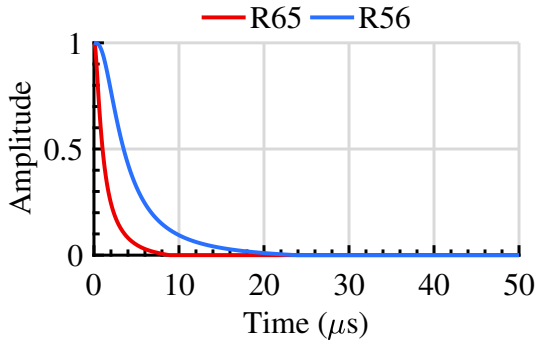

(b–2) $i^P_{TW,N}$

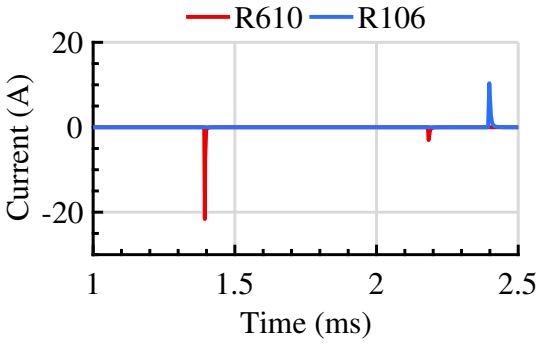

(c–1) i^P_{hp}

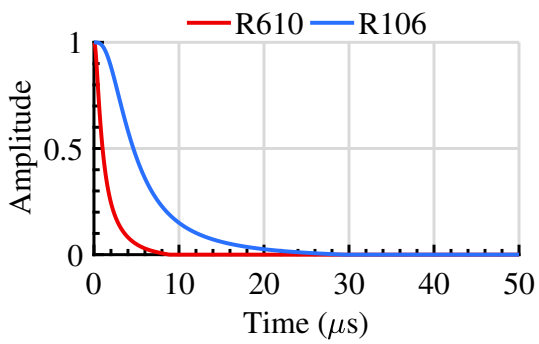

(c–2) $i^P_{TW,N}$

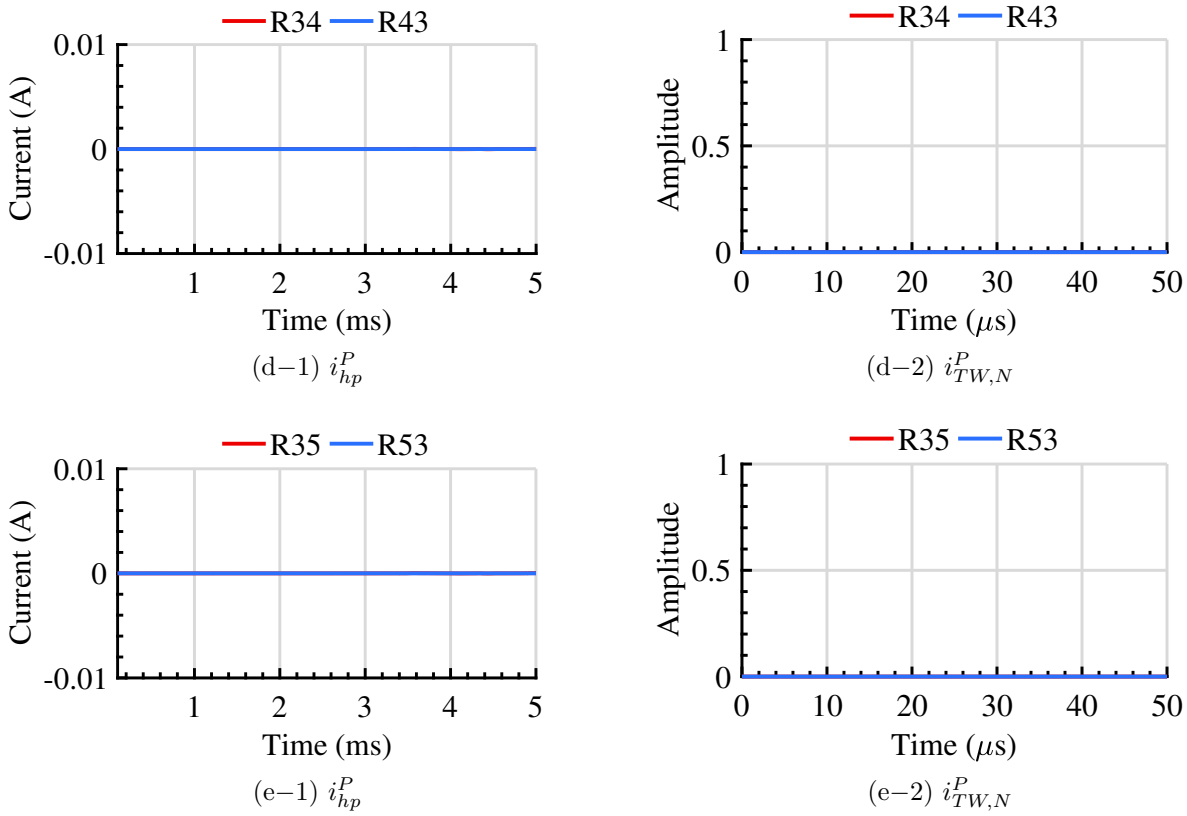

Figure 6.10: i^P_{hp} and $i^P_{TW,N}$ of relays on a) faulted $L36$ and adjacent lines b) $L65$, c) $L610$, d) $L34$, and e) $L35$ for a bolted PP fault on $L36$.

6.4.2 Fault Type

To assess the selectivity of the proposed scheme, bolted PP, PPG, and NPG faults are conducted on $L12$, 19 km away from bus 1. During a PP fault, both i^P_{hp} and i^N_{hp} (superscript N denotes the negative pole) exceed $+\Psi$ (Figures 6.12a–1 and 6.12b–1). On the other hand, only i^P_{hp} exceeds $+\Psi$ during a PPG fault (Figures 6.12a–2 and 6.12b–2). Moreover, only $|i^N_{hp}|$ exceeds $+\Psi$ during a NPG fault (Figures 6.12a–3 and 6.12b–3). Therefore, the proposed scheme can selectively trip the faulted pole. Moreover, the FSR of $R12$ under all three fault types in Figures 6.12a–1, 6.12a–2, and 6.12a–3 is 55.11. Similarly, FSR of $R21$ under all three fault types in Figures 6.12b–1, 6.12b–2, and 6.12b–3 is 74782. The

FSRs of both relays are below their ζ_p=131500 of a 200-km UGC (Table 6.1). Since $R12$ and $R21$ detect a forward and in-zone fault, they operate instantaneously after the time it takes to process the captured TWs, which is 500 μs for the relays protecting the UGCs of this system. Moreover, the FSRs of $R12$ and $R21$ are used along with the UGC lookup table illustrated in Figure 6.9 to estimate the fault location. The actual distance between the fault and $R12$ is 19 km and the estimated χ is 19.06 km. Thus, the error in fault location is only 60 m. Similarly, the actual and estimated fault locations for $R21$ are 181 and 180.953 km, resulting in 47 m error. Accordingly, neither the speed nor the accuracy of the proposed method is affected by the change in the fault type.

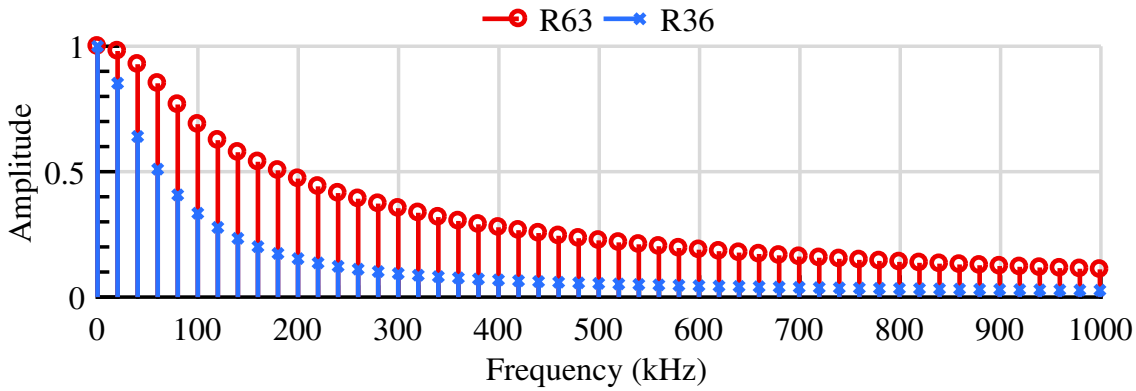

(a)

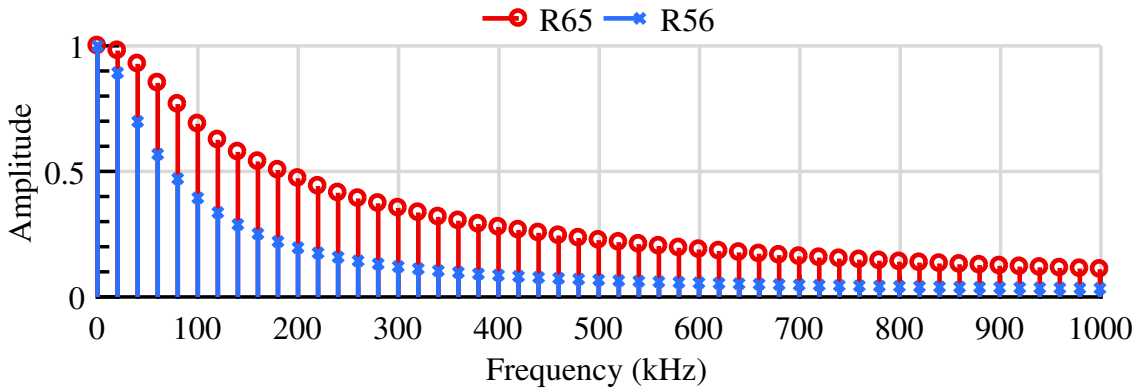

(b)

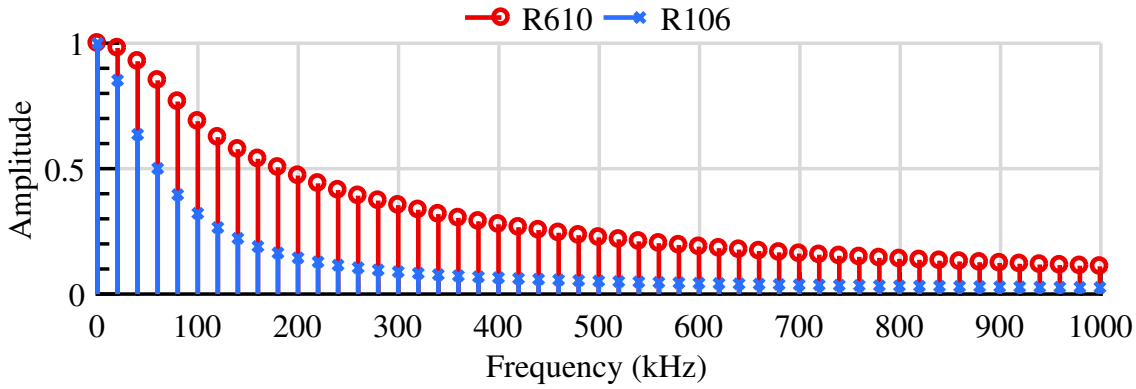

(c)

Figure 6.11: The spectra of $i^P_{TW,N}$ seen by relays on a) the faulted $L36$ and adjacent lines b) $L56$ and c) $L610$ for a bolted PP fault on $L36$.

6.4.3 Fault Resistance

To assess the sensitivity of the proposed scheme, PP faults with fault resistance (R_f) equal to 10, 100, and 200 Ω are conducted on $L36$, 382 km away from bus 3. Figures 6.13a–1 and 6.13b–1 show that R_f has a significant effect on the magnitudes of i^P_{hp} of both $R63$ and $R36$. However, Figures 6.13a–2 and 6.13b–2 show that the magnitude variation of i^P_{hp} has minimal impact on $i^P_{TW,N}$. Accordingly, these variations affect the FSR computed by $R36$, which is equal to 550.46, 550.43, 550.41 for R_f=10, 100, and 200 Ω, respectively. Moreover, FSR for $R63$ is equal to 58.30, 58.34, 58.36 under R_f=10, 100, and 200 Ω, respectively. Such small differences in FSR have negligible impact on the accuracy of the proposed scheme. The fault location estimated by $R36$ for R_f=10, 100, and 200 Ω is 382.015, 382.027, and 382.037 km away from the relay, resulting in 15, 27, and 37 m errors, respectively. Similarly, the fault location estimated by $R63$ for R_f=10, 100, and 200 Ω is 118.015, 118.049, and 118.063 km away from the relay, causing only 15, 49, and 63 m errors, respectively.

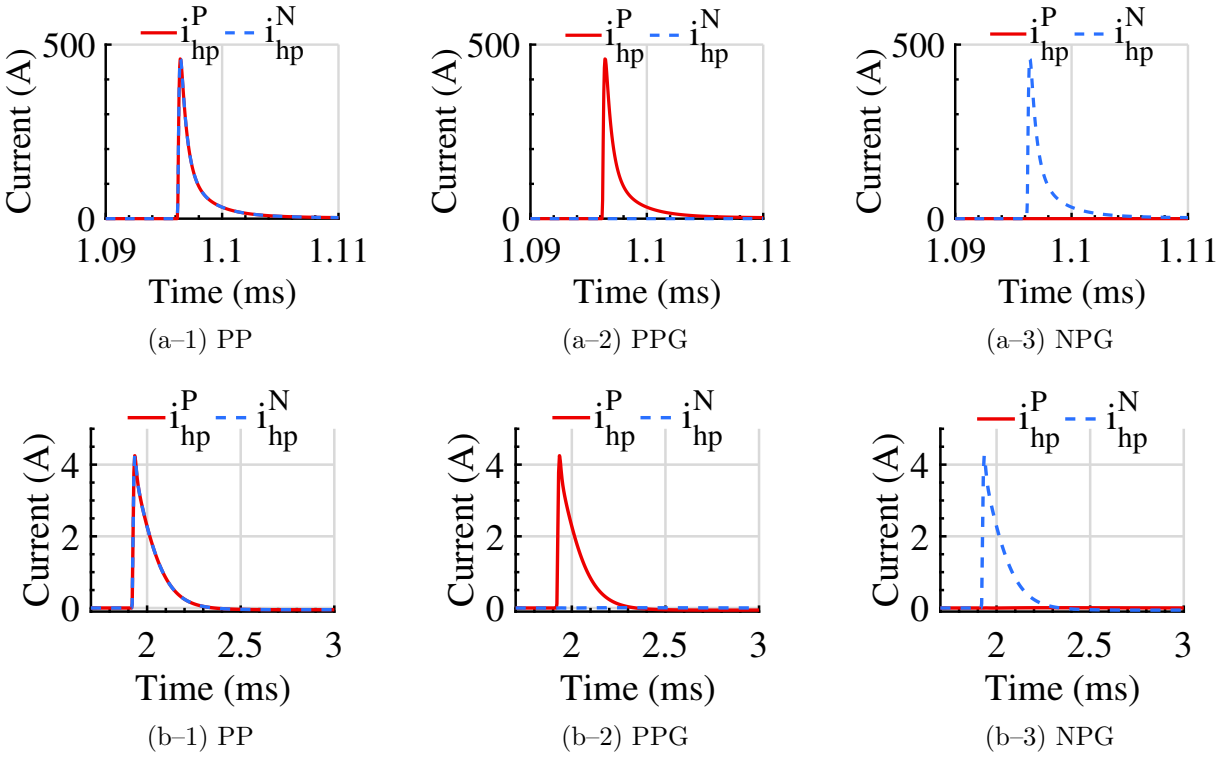

(a–1) PP (a–2) PPG (a–3) NPG

(b–1) PP (b–2) PPG (b–3) NPG

Figure 6.12: i^P_{hp} of a) $R12$ and b) $R21$ for a bolted PP, PPG, and NPG faults on $L12$.

6.4.4 Fault Location

To assess the accuracy of the proposed scheme, bolted PP faults are conducted at various locations on the 15 lines of the test HVDC grid. Table 6.2 summarizes the fault location estimations for various faults as seen by the relays at both ends of the faulted lines. It is observed that the largest estimation error for χ is 100 m. If the resolution of simulated fault locations is increased, this error will reduce even further.

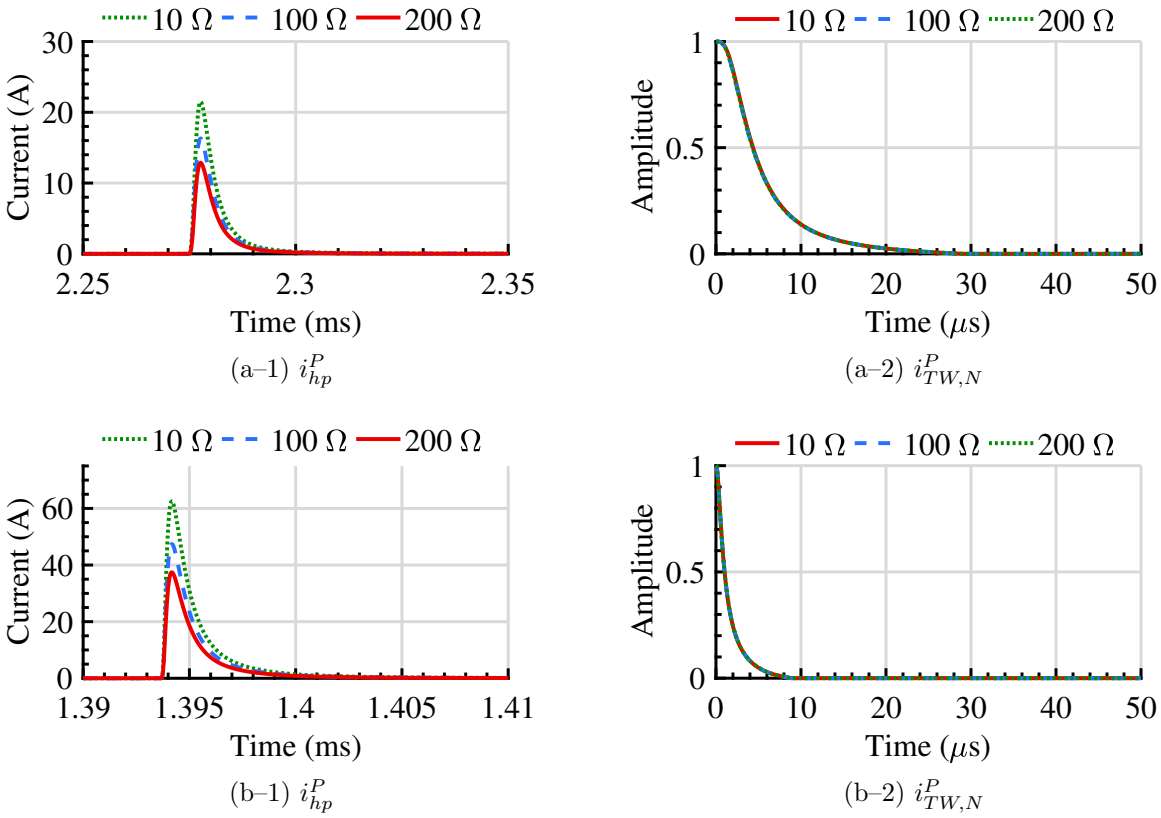

(a–1) i^P_{hp} (a–2) $i^P_{TW,N}$

(b–1) i^P_{hp} (b–2) $i^P_{TW,N}$

Figure 6.13: i^P_{hp} and $i^P_{TW,N}$ of primary relays a) $R63$ and b) $R36$ for PP faults with R_f equal to 10, 100, and 200 Ω on $L36$.

Table 6.2: Fault Location Estimation for Various Faults in the HVDC Grid

Line	Length (km)	Relay	Act. χ (km)	Est. χ (km)	Error (m)	Relay	Act. χ (km)	Est. χ (km)	Error (m)
L12	200	R12	19	19.06	60	R21	181	180.953	47
L34	200	R34	62	61.991	9	R43	138	138.025	25
L35	400	R35	147	147.01	10	R53	253	253.043	43
L36	500	R63	118	118.008	8	R36	382	382.012	12
L47	300	R47	105	104.988	12	R74	195	195.033	33
L56	200	R56	72	72.036	36	R65	128	128.067	67
L610	300	R610	111	111.018	18	R106	189	189.1	100
L78	200	R78	57	56.997	3	R87	143	143.083	83
L89	200	R89	91	91.072	72	R98	109	108.911	89
L1112	200	R1112	55	54.937	63	R1211	145	145.027	27
L1213	100	R1213	76	76.002	2	R1312	24	24.019	19
L1314	100	R1314	27	26.93	70	R1413	73	73.056	56
L1415	200	R1314	10	10.054	54	R1413	190	189.999	1

6.5 Conclusion

This chapter proposed a method to effectively detect and locate PP, PPG, and NPG faults in HVDC grids. Unlike the existing TW-based protection methods, the proposed scheme is independent of the arrival times of TWs, and focuses on the frequency spectrum of only the first TW initiated by a fault. The direction of the TW is identified based on the pattern of the current TW waveform. The FSR of the current TW is used to identify the fault zone and fault location with high accuracy. Both the primary and backup elements of the proposed relay fulfill the speed requirement for the protection of dc systems. Unlike existing two-terminal TW-based protection methods, the proposed scheme operates entirely based on local measurements, hence avoiding the delay of the communication system and the vulnerability to its failure. This method is also superior to existing single-terminal TW-based protection methods since it is faster and also eliminates the complexities of detecting the second TW after the fault inception, e.g., the small magnitude of the second TW for high-resistance faults. The proposed relay is sufficiently sensitive to detect and locate high-resistance faults with R_f of up to 200 Ω.

Chapter 7

Conclusion

7.1 Summary

The effect of DC faults on five different DC systems has been investigated. The studies were based on time-domain simulation of the DC systems models using PSCAD/EMTDC program. The objective of the studies was twofold: Identify unique fault properties in each DC system that can be used to devise a new relaying algorithm, and designing an adequate protection scheme for each DC system that is fast, sensitive, selective, accurate, reliable, independent, and based on local measurements. The studies were divided into five main parts.

1. *Protection of utility-scale PV arrays*: A variety of fault and partial shading conditions at different locations of the PV array underwent scrutiny. It was shown that the voltage of PV modules at different locations experienced a change in magnitude that lead to violation of the string KVL. Moreover, it was proved that the waveshape of the PV module voltage is different during fault and partial shading conditions. Once the fault and partial shading voltage properties have been pinpointed, simple yet effective scheme was proposed to detect, classify, and locate faults and partial shading disturbances.

2. *Protection of LVDC microgrids*: It was proved that low-resistance faults in LVDC microgrids result in very low fault current that cannot be detected by conventional protection schemes. The problem arises from the relatively low-voltage of such microgrids. However, the available literature on LVDC microgrid protection did not take into account fault resistance. An effective method that injects a fault signature signal has been proposed to detect low- and high-resistance faults in a timely manner.

3. *Protection of MVDC microgrids*: The multi-terminal nature and short lines of MVDC microgrids pose a protection challenge due to the very high fault current magnitudes attained within a couple of milliseconds. The shape of the current TWs at different relay locations across the microgrid was analyzed. A unique relation between the current TW waveshape and fault location has been identified. For the first time, the aforementioned relation, which is regarded as a drawback in many applications, was exploited to develop a time-domain protection scheme that detects, classifies, and locates DC faults within the required time.

4. *Protection of hybrid AC/DC microgrids*: In addition to the protection challenges posed by the DC-side, the AC-side of hybrid AC/DC microgrids experience very low fault current magnitudes due to the current control capability of inverter-based DGs and islanded mode of operation. Current and Voltage TWs at different relay locations across the AC/DC microgrid was analyzed. The unique relation between the voltage/current TW waveshapes and fault location was exploited to develop a time-domain protection scheme that detects, classifies, and locates both AC and DC faults within the required time.

5. *Protection of HVDC grids*: Selective protection system is required to isolate the faulty section of the HVDC grid within the couple of milliseconds after the onset of a fault to avoid loss of controllability over the MMCs in the neighbourhood of the fault, and jeopardizing the integrity of the entire DC grid. The frequency spectra of current TWs under various DC fault conditions has been examined. It was proved that there exists a relationship between the propagation distance of a TW through a conductor and the frequency attenuation rate of that TW. For the first time, the above-mentioned relation was utilized to develop a frequency-domain protection

scheme that detects, classifies, and locates DC faults within the required time.

7.2 Contributions

The contributions fall into two categories: the identification of unique fault properties in each system and the proposal of schemes that exploit these features to address DC systems' protection challenges.

7.2.1 Unique Fault Properties

The following are among the properties of faults in DC systems that this dissertation has identified.

1. The voltage across individual PV modules violate a string's KVL during faults and partial shading conditions. SG and SS faults split the fault strings into two regions. There exists an intra-string voltage relationship between the top and bottom PV module voltages and the array voltage. Moreover, an additional inter-string relationship exists during an SS fault. On the other hand, an OC fault causes all the PV modules in the faulted string to operate at open-circuit voltage. Meanwhile, all of the aforementioned fault types result in an exponential voltage waveform, whereas partial shading results in a sigmoidal waveform. For the first time, the transients caused by partial shading conditions were examined.

2. Faults in DC grids create a second order RLC fault circuit. Addition of passive elements, an inductor in parallel with a capacitor, on the line terminals of an LVDC microgrid result in a fourth and seventh order RLC, PPG and PP fault circuits, respectively. Once the fault circuit is active, the passive elements resonate at the designed frequency.

3. Exponential current TW waveshape is measured at different relay locations in an MVDC microgrid. The longer the TW propagates, the more significant the waveshape changes. This change is attributed to (i) the frequency-dependent attenuation,

and (ii) the dispersion of the TW. As a result, propagation through a conductor diminishes the high-frequency share of a TW spectrum, which changes the shape of the TW. Moreover, the pattern of a TW shape can be rising or falling depending on (i) the convention of the current measurement unit, (ii) the faulted pole type, i.e., positive or negative pole, and (iii) the location of the fault with respect to the relay, i.e., fault is in front or behind the relay.

4. Analysis of current TWs measured at relay locations of an HVDC grid revealed that the TW attenuation parameters due to skin-effect loss and dielectric loss are directly related to the frequency of a given TW component. Therefore, higher frequency components undergo more severe attenuation. In addition, since the TW attenuation parameters are related to the per-unit length quantities of the line/cable, the total TW attenuation of each frequency component increases with the increase in the distance traveled by the TW.

7.2.2 Proposal of Protection Schemes

This dissertation has presented the following schemes by exploiting the aforementioned properties. The proposed schemes can be categorized into time-domain and frequency-domain schemes.

- Time-domain protection schemes:

    1. For utility-scale PV arrays, a new time-domain voltage-based scheme was proposed. The scheme relies on a central IED located at the inverter, in addition to two voltage transducers on each string. The violation of the string KVL is used as a disturbance indicator. After that, the second derivative of the voltage across the top and bottom PV modules in the affect string is used to distinguish between faults and partial shading conditions. Faults have an exponential second derivative voltage, whereas partial shading second derivative voltage waveform switch from a positive to a negative value, indicating the presence of an inflection point, which is a sigmoid curve signature. Finally, the previously-discussed

intra-string, inter-string, and open-circuit voltage relationships are utilized to classify and locate SG, SS, and OC faults. In the case studies conducted on small and large utility-scale PV arrays under various meteorological and fault conditions, the proposed protection scheme was shown to be fast, sensitive, selective, scalable, accurate and capable of distinguishing between fault and partial shading conditions. Experimental results further validate the performance of the proposed method.

2. For MVDC microgrids, a novel time-domain TW-based scheme was proposed. The direction of the TW is identified based on the wave pattern of the current TW. The estimated time constant for the first locally-measured current TW initiated by a fault is used to identify the fault zone and fault location with high accuracy. The independence from the TW arrival time makes the proposed method applicable to short distribution lines. The results highlighted the speed, sensitivity, selectivity, accuracy, reliability, and grid configuration independence of the proposed method.

3. For hybrid AC/DC microgrids, another time-domain TW-based scheme was proposed. The direction of the fault is identified based on a discriminant function that utilizes both the voltage and current TWs. The area under the high-pass filtered discriminant function signal is used to identify the fault zone and fault location with high accuracy. The independence from the TW arrival time makes the proposed method applicable to short distribution lines. The results highlighted the speed, sensitivity, selectivity, accuracy, reliability, and grid configuration independence of the proposed method.

- Frequency-domain protection schemes:

1. A hybrid passive-overcurrent relay was proposed to effectively detect low and high-resistance faults in LVDC microgrids. The relay is equipped with two passive elements that generate a specific damped frequency during fault conditions. DWT is utilized to capture that frequency, and hence detect and identify the DC faults. For faster detection of bolted and low-resistance faults, an overcurrent function is used. The proposed relay operates based on local-bus measure-

ments and requires a moderate sampling frequency. Analytical modelling has confirmed that the proposed method is system independent. Furthermore, the proposed relay was shown to be fast, sensitive, and selective for both types of DC faults, with different resistances that can occur at various locations.

2. The frequency spectrum of locally-measured first current TW initiated by a fault was utilized to propose a novel frequency-domain TW-based scheme for HVDC grids. The frequency spectrum of a captured TW is obtained using FFT. The direction of the TW is identified based on the pattern of the current TW waveform. The FSR of the current TW is used to identify the fault zone and fault location with high accuracy. Both the primary and backup elements of the proposed relay fulfill the speed requirement for the protection of DC systems. The results highlighted the speed, sensitivity, selectivity, accuracy, reliability, and grid configuration independence of the proposed method.

7.3 Future Work

Further research on the protection of DC systems may include the topics listed below.

1. Protection of utility-scale PV arrays using travelling-wave-based techniques,
2. Effect of DC circuit breakers transients on the operation of relays,
3. Design of self-healing fault resilient DC grids.

References

[1] S. Amin, "For the good of the grid," *IEEE Power Energy Mag.*, vol. 6, no. 6, pp. 48–59, 2008.

[2] P. Pourbeik, P. Kundur, and C. Taylor, "The anatomy of a power grid blackout - Root causes and dynamics of recent major blackouts," *IEEE Power Energy Mag.*, vol. 4, no. 5, pp. 22–29, sep 2006.

[3] E. Lightner and S. Widergren, "An Orderly Transition to a Transformed Electricity System," *IEEE Trans. Smart Grid*, vol. 1, no. 1, pp. 3–10, jun 2010.

[4] M. Guarnieri, "The Beginning of Electric Energy Transmission: Part One," *IEEE Ind. Electron. Mag.*, vol. 7, no. 1, pp. 50–52, mar 2013.

[5] B. T. Patterson, "DC, Come Home: DC Microgrids and the Birth of the "Enernet"," *IEEE Power Energy Mag.*, vol. 10, no. 6, pp. 60–69, nov 2012.

[6] D. Nilsson and A. Sannino, "Efficiency analysis of low- and medium-voltage dc distribution systems," in *IEEE Power Engineering Society General Meeting, 2004.*, vol. 2. IEEE, 2010, pp. 2316–2322.

[7] IRENA, "Rethinking Energy 2017: Accelerating the global energy transformation," International Renewable Energy Agency, Abu Dhabi, Tech. Rep., 2017.

[8] A. a. S. Emhemed and G. M. Burt, "An Advanced Protection Scheme for Enabling an LVDC Last Mile Distribution Network," *IEEE Trans. Smart Grid*, vol. 5, no. 5, pp. 2602–2609, sep 2014.

[9] I. Std, "1653.4-2011 IEEE Standard for DC Traction Power Testing and Accept Criteria for System Applications up to 1500V DC Nominal," Tech. Rep., 2011.

[10] G. AlLee and W. Tschudi, "Edison Redux: 380 Vdc Brings Reliability and Efficiency to Sustainable Data Centers," *IEEE Power Energy Mag.*, vol. 10, no. 6, pp. 50–59, nov 2012.

[11] G. F. Reed, B. M. Grainger, A. R. Sparacino, and Z.-H. Mao, "Ship to grid: Medium-voltage DC concepts in theory and practice," *IEEE Power Energy Mag.*, vol. 10, no. 6, pp. 70–79, 2012.

[12] H. Li, W. Li, M. Luo, A. Monti, and F. Ponci, "Design of smart MVDC power grid protection," *IEEE Trans. Instrum. Meas.*, vol. 60, no. 9, pp. 3035–3046, 2011.

[13] C. Yuan, M. a. Haj-ahmed, and M. Illindala, "Protection Strategies for Medium Voltage Direct Current Microgrid at a Remote Area Mine Site," *IEEE Trans. Ind. Appl.*, vol. 9994, no. c, pp. 1–1, 2015.

[14] N. Chaudhuri, B. Chaudhuri, R. Majumder, and A. Yazdani, *Multi-terminal direct-current grids: Modeling, analysis, and control.* John Wiley & Sons, 2014, ch. 6.

[15] V. C. Billon, J. P. Taisne, V. Arcidiacono, and F. Mazzoldi, "The Corsican tapping: from design to commissioning tests of the third terminal of the Sardinia-Corsica-Italy HVDC," *IEEE Trans. Power Del.*, vol. 4, no. 1, pp. 794–799, 1989.

[16] ABB, "Québec - New England The first large scale multiterminal HVDC transmission in the world to be upgraded ." pp. 9–10, 2014. [Online]. Available: http://new.abb.com/systems/hvdc/references/quebec-new-england

[17] EirGrid Projects, "East-west interconnector project," p. 2014, 2014. [Online]. Available: http://www.eirgridprojects.com/projects/east-westinterconnector/

[18] "Zhoushan MTDC project," pp. 11–12, 2014. [Online]. Available: http://www.epri.sgcc.com.cn

[19] M. Alam, F. Khan, J. Johnson, and J. Flicker, "A comprehensive review of catastrophic faults in pv arrays: Types, detection, and mitigation techniques," *IEEE J. Photovolt.*, vol. 5, no. 3, pp. 982–997, May 2015.

[20] J. D. Flicker and J. Johnson, "Photovoltaic ground fault and blind spot electrical simulations." Sandia National Laboratories (SNL-NM), Albuquerque, NM (United States), Tech. Rep., 2013.

[21] B. Brooks, "The ground-fault protection blind spot: Safety concern for larger PV systems in the US," *Solar ABCs Report*, 2012.

[22] G. Ball and E. al., "Inverter ground-fault detection "blind spot" and mitigation methods," *Solar ABC*, 2013.

[23] J. Flicker and J. Johnson, "Analysis of fuses for blind spot ground fault detection in photovoltaic power systems," *Solar ABCs Report*, 2013.

[24] Y. Zhao and Etal, "Lineline fault analysis and protection challenges in solar photovoltaic arrays," *IEEE Trans. Ind. Electron.*, vol. 60, no. 9, pp. 3784–3795, 2013.

[25] Y. Zhao. and Etal, "Fault evolution in photovoltaic array during night-to-day transition," in *2010 IEEE 12th COMPEL Workshop*, 2010, pp. 1–6.

[26] B. Brooks., "The Bakersfield fire: A lesson in ground-fault protection," *SolarPro*, no. 4.2, 2011.

[27] R. Platon, J. Martel, N. Woodruff, and T. Chau, "Online fault detection in pv systems," *IEEE Trans. Sustain. Energy*, vol. 6, no. 4, pp. 1200–1207, Oct 2015.

[28] Y. Zhao, B. Lehman, R. Ball, J. Mosesian, and J.-F. de Palma, "Outlier detection rules for fault detection in solar photovoltaic arrays," in *Applied Power Electronics Conference and Exposition (APEC), 2013 Twenty-Eighth Annual IEEE*, March 2013, pp. 2913–2920.

[29] Z. Yi and A. Etemadi, "Fault detection for photovoltaic systems based on multiresolution signal decomposition and fuzzy inference systems," *IEEE Trans. Smart Grid*, vol. PP, no. 99, pp. 1–1, 2016.

[30] Y. Zhao.., L. Yang, B. Lehman, J.-F. de Palma, J. Mosesian, and R. Lyons, "Decision tree-based fault detection and classification in solar photovoltaic arrays," in *Applied Power Electronics Conference and Exposition (APEC), 2012 Twenty-Seventh Annual IEEE*, Feb 2012, pp. 93–99.

[31] Y. Zhao, R. Ball, J. Mosesian, J.-F. de Palma, and B. Lehman, "Graph-based semi-supervised learning for fault detection and classification in solar photovoltaic arrays," *IEEE Trans. Power Electron.*, vol. 30, no. 5, pp. 2848–2858, May 2015.

[32] Y. Hu, J. Zhang, W. Cao, J. Wu, G. Y. Tian, S. Finney, and J. Kirtley, "Online two-section pv array fault diagnosis with optimized voltage sensor locations," *IEEE Trans. Ind. Electron.*, vol. 62, no. 11, pp. 7237–7246, Nov 2015.

[33] N. Gokmen, E. Karatepe, S. Silvestre, B. Celik, and P. Ortega, "An efficient fault diagnosis method for pv systems based on operating voltage-window," *Energy conversion and management*, vol. 73, pp. 350–360, 2013.

[34] H. Al-Sheikh and N. Moubayed, "Fault detection and diagnosis of renewable energy systems: An overview," in *Renewable Energies for Developing Countries (REDEC), 2012 International Conference on*, Nov 2012, pp. 1–7.

[35] M. Akram and S. Lotfifard, "Modeling and health monitoring of dc side of photovoltaic array," *IEEE Trans. Sustain. Energy*, vol. 6, no. 4, pp. 1245–1253, Oct 2015.

[36] J. Yang, J. E. Fletcher, and J. O'Reilly, "Short-Circuit and Ground Fault Analyses and Location in VSC-based DC Network Cables," *IEEE Trans. Ind. Electron.*, vol. 59, no. 10, pp. 3827–3837, 2012.

[37] S. D. a. Fletcher, P. J. Norman, S. J. Galloway, P. Crolla, and G. M. Burt, "Optimizing the Roles of Unit and Non-unit Protection Methods Within DC Microgrids," *IEEE Trans. Smart Grid*, vol. 3, no. 4, pp. 2079–2087, Dec. 2012.

[38] S. D. A. Fletcher, P. J. Norman, K. Fong, S. J. Galloway, and G. M. Burt, "High-Speed Differential Protection for Smart DC Distribution Systems," *IEEE Trans. Smart Grid*, vol. 5, no. 5, pp. 2610–2617, Sep. 2014.

[39] W. Li, A. Monti, and F. Ponci, "Fault Detection and Classification in Medium Voltage DC Shipboard Power Systems With Wavelets and Artificial Neural Networks," *IEEE Trans. Instrum. Meas.*, vol. 63, no. 11, pp. 2651–2665, Nov. 2014.

[40] W. Leterme, P. Tielens, S. De Boeck, and D. Van Hertem, "Overview of Grounding and Configuration Options for Meshed HVDC Grids," *IEEE Trans. Power Del.*, pp. 1–1, 2014.

[41] J.-d. Park and J. Candelaria, "Fault Detection and Isolation in Low-Voltage DC-Bus Microgrid System," *IEEE Trans. Power Del.*, vol. 28, no. 2, pp. 779–787, Apr. 2013.

[42] J.-d. Park, J. Candelaria, L. Ma, and K. Dunn, "DC Ring-Bus Microgrid Fault Protection and Identification of Fault Location," *IEEE Trans. Power Del.*, vol. 28, no. 4, pp. 2574–2584, Oct. 2013.

[43] D. Salomonsson, L. Soder, and A. Sannino, "Protection of Low-Voltage DC Microgrids," *IEEE Trans. Power Del.*, vol. 24, no. 3, pp. 1045–1053, Jul. 2009.

[44] A. Hooshyar and R. Iravani, "Microgrid protection," *Proceedings of the IEEE*, vol. 105, no. 7, pp. 1332–1353, July 2017.

[45] M. E. Baran and N. R. Mahajan, "Overcurrent protection on voltage-source-converter-based multiterminal dc distribution systems," *IEEE Trans. Power Del.*, vol. 22, no. 1, pp. 406–412, Jan 2007.

[46] M. Monadi, C. Gavriluta, A. Luna, I. Candela, and P. Rodriguez, "Centralized protection strategy for medium voltage dc microgrids," *IEEE Trans. Power Del.*, vol. PP, no. 99, pp. 1–1, 2016.

[47] A. A. S. Emhemed, K. Fong, S. Fletcher, and G. Burt, "Validation of fast and selective protection scheme for an LVDC distribution network," *IEEE Trans. Power Del.*, vol. PP, no. 99, pp. 1–1, 2016.

[48] A. Hooshyar and R. Iravani, "A new directional element for microgrid protection," *IEEE Trans. Smart Grid*, vol. PP, no. 99, pp. 1–1, 2017.

[49] J. Liu, N. Tai, and C. Fan, "Transient-voltage-based protection scheme for dc line faults in the multiterminal vsc-hvdc system," *IEEE Trans. Power Del.*, vol. 32, no. 3, pp. 1483–1494, June 2017.

[50] L. Tang and B. T. Ooi, "Locating and isolating dc faults in multi-terminal dc systems," *IEEE Trans. Power Del.*, vol. 22, no. 3, pp. 1877–1884, July 2007.

[51] J. Liu, N. Tai, C. Fan, and S. Chen, "A hybrid current-limiting circuit for dc line fault in multi-terminal vsc-hvdc system," *IEEE Trans. Ind. Electron.*, vol. PP, no. 99, pp. 1–1, 2017.

[52] J. Sneath and A. D. Rajapakse, "Fault detection and interruption in an earthed hvdc grid using rocov and hybrid dc breakers," *IEEE Trans. Power Del.*, vol. 31, no. 3, pp. 973–981, June 2016.

[53] J. Hafner and B. Jacobson, "Proactive hybrid hvdc breakers-a key innovation for reliable hvdc grids," *CIGRE paper*, vol. 264, pp. 0093–9994, 2011.

[54] M. K. Bucher and C. M. Franck, "Contribution of fault current sources in multiterminal hvdc cable networks," *IEEE Trans. Power Del.*, vol. 28, no. 3, pp. 1796–1803, July 2013.

[55] S. p. Gao, Q. Liu, and G. b. Song, "Current differential protection principle of hvdc transmission system," *IET Generation, Transmission Distribution*, vol. 11, no. 5, pp. 1286–1292, 2016.

[56] X. Zheng, N. Tai, Z. Wu, and J. Thorp, "Harmonic current protection scheme for voltage source converter-based high-voltage direct current transmission system," *IET Generation, Transmission Distribution*, vol. 8, no. 9, pp. 1509–1515, Sept 2014.

[57] W. Leterme, J. Beerten, and D. V. Hertem, "Nonunit protection of hvdc grids with inductive dc cable termination," *IEEE Trans. Power Del.*, vol. 31, no. 2, pp. 820–828, April 2016.

[58] M. Chamia and S. Liberman, "Ultra high speed relay for EHV/UHV transmission lines – development, design and application," *IEEE Trans. Power App. Syst.*, vol. PAS-97, no. 6, pp. 2104–2116, Nov 1978.

[59] M. M. Mansour and G. W. Swift, "Design and testing of a multi-microprocessor travelling wave relay," *IEEE Trans. Power Del.*, vol. 1, no. 4, pp. 74–82, Oct 1986.

[60] M. Vitins, "A fundamental concept for high speed relaying," *IEEE Trans. Power App. Syst.*, vol. PAS-100, no. 1, pp. 163–173, Jan 1981.

[61] A. T. Johns, M. A. Martin, A. Barker, E. P. Walker, and P. A. Crossley, "A new approach to E.H.V. direction comparison protection using digital signal processing techniqles," *IEEE Trans. Power Del.*, vol. 1, no. 2, pp. 24–34, April 1986.

[62] J. Wu, H. Li, G. Wang, and Y. Liang, "An improved travelling wave protection scheme for LCC-HVDC transmission lines," *IEEE Trans. Power Del.*, vol. 32, no. 1, pp. 106–116, Feb. 2017.

[63] O. Nanayakkara, A. D. Rajapakse, and R. Wachal, "Traveling-wave-based line fault location in star-connected multiterminal HVDC systems," *IEEE Trans. Power Del.*, vol. 27, no. 4, pp. 2286–2294, Oct 2012.

[64] S. Azizi, M. Sanaye-Pasand, M. Abedini, and A. Hasani, "A traveling-wave-based methodology for wide-area fault location in multiterminal dc systems," *IEEE Trans. Power Del.*, vol. 29, no. 6, pp. 2552–2560, Dec 2014.

[65] W. Li, A. Monti, and F. Ponci, "Fault detection and classification in medium voltage dc shipboard power systems with wavelets and artificial neural networks," *IEEE Trans. Instrum. Meas.*, vol. 63, no. 11, pp. 2651–2665, Nov 2014.

[66] S. Sefidpour, J. Wang, and K. Srivastava, "Factors affecting traveling wave protection," in *Advanced Power System Automation and Protection (APAP), 2011 International Conference on*, vol. 2, Oct 2011, pp. 1359–1365.

[67] BP Solar, "BP 3 series: 215, 220, 225, 230 and 235W photovoltaic modules datasheet," 2011.

[68] C. Deline, J. Meydbray, and M. Donovan, *Photovoltaic shading testbed for module-level power electronics: 2014 update*. NREL, 2014.

[69] R. Mayfield, P. Gibbs, and P. Grana, "Reassessing DC voltage drop conventions," *SolarPro*, no. 8.3, 2015.

[70] A. Ahmed, L. Ran, S. Moon, and J.-H. Park, "A fast pv power tracking control algorithm with reduced power mode," *IEEE Trans. Energy Convers.*, vol. 28, no. 3, pp. 565–575, Sept 2013.

[71] J. Ahmed and Z. Salam, "A modified p&o maximum power point tracking method with reduced steady-state oscillation and improved tracking efficiency," *IEEE Trans. Sustain. Energy*, vol. 7, no. 4, pp. 1506–1515, Oct 2016.

[72] L. Qin, S. Xie, C. Yang, and J. Cao, "Dynamic model and dynamic characteristics of solar cell," in *ECCE Asia Downunder (ECCE Asia), 2013 IEEE*, June 2013, pp. 659–663.

[73] M. C. Di Piazza and G. Vitale, *Photovoltaic Sources: Modeling and Emulation*. Springer Science & Business Media, 2012.

[74] C. Cai and D. Aliprantis, "Cumulus cloud shadow model for analysis of power systems with photovoltaics," *IEEE Trans. Power Syst.*, vol. 28, no. 4, pp. 4496–4506, Nov 2013.

[75] M. Rashid, *Electric Renewable Energy Systems*, 1st ed. Academic Press, 2015.

[76] V. Fung, J. Bosch, S. Roberts, and J. Kleissl, "Cloud shadow speed sensor," *Atmospheric Measurement Techniques*, vol. 7, no. 6, pp. 1693–1700, 2014.

[77] M. J. Thompson, "Percentage restrained differential, percentage of what?" in *2011 64th Annual Conference for Protective Relay Engineers*, April 2011, pp. 278–289.

[78] Solar Radiation Laboratory, "Data Files From a multifilter rotating shadowband radiometer (MFR-7) for Eugene," 2015. [Online]. Available: http://solardat.uoregon.edu/SelectMFR.html

[79] National Electrical Code, "Article 690-solar photovoltaic systems," *NFPA 70*, 2014.

[80] S. Liu and R. A. Dougal, "Dynamic multiphysics model for solar array," *IEEE Trans. Energy Convers.*, vol. 17, no. 2, pp. 285–294, 2002.

[81] A. D. Rajapakse and D. Muthumuni, "Simulation tools for photovoltaic system grid integration studies," in *Electrical Power & Energy Conference (EPEC), 2009 IEEE*. IEEE, 2009, pp. 1–5.

[82] University of Washington, "Power Systems Test Case Archive." [Online]. Available: http://www.ee.washington.edu/research/pstca/

[83] Universal Cable, "XLPE Insulated Power Cables." [Online]. Available: http://www.ucable.com.my

[84] B. Jover, "Choosing the Right Earthing System," *Schneider Electric: Energy Regulations*, pp. 1–5, 2014. [Online]. Available: http://blog.schneider-electric.com/energy-regulations/2014/01/03/choosing-right-earthing-system/

[85] A. Yazdani and R. Iravani, "Voltage-Sourced Converters in Power Systems," pp. 73–78, Jan. 2010.

[86] S. R. Pulikanti, G. Konstantinou, and V. G. Agelidis, "DC-Link Voltage Ripple Compensation for Multilevel Active-Neutral-Point-Clamped Converters Operated with SHE-PWM," *IEEE Trans. Power Del.*, vol. 27, no. 4, pp. 2176–2184, 2012.

[87] H. Sira-Ramírez and R. Silva-Ortigoza, *Control Design Techniques in Power Electronics Devices*. Springer Science & Business Media, 2006.

[88] SEL, "SEL-411L Data Sheet Line Current Differential Protection Automation and Control System Major Features and Benefits," *Schweitzer Engineering Laboratories, Inc*, 2014.

[89] H. a. Darwish, M. H. Farouk, A. M. I. Taalab, and N. M. Mansour, "Investigation of Real-Time Implementation of DSP-based DWT for Power System Protection," in *Proceedings of the IEEE Power Engineering Society Transmission and Distribution Conference*, 2006, pp. 1258–1263.

[90] D. Hinrichsen and A. J. Pritchard, *Mathematical Systems Theory I: Modelling, State Space Analysis, Stability and Robustness*. Springer Science & Business Media, 2005, vol. 1.

[91] U. Alvarado, G. Bistué, and I. n. Adin, *Low Power RF Circuit Design in Standard CMOS Technology*. Springer Science & Business Media, 2011, vol. 104.

[92] E. Smith, "Dispersion in commonly used cables," CEBAF TN-91-022, April, Tech. Rep., 1991.

[93] K. Hashemi, "Transmission Line Analysis," *Brandeis University High Energy Physics Electronics Shop*, 2016. [Online]. Available: http://alignment.hep.brandeis.edu/Lab/XLine/XLine.html

[94] D. Hess and J. Goldies, "Application Note 916: A practical guide to cable selection," *National Semiconductor Corporation*, pp. 1–12, Oct 1993. [Online]. Available: http://www.ti.com/lit/an/snla164/snla164.pdf

[95] J. C. Jacob, R. K. Mishra, and K. Appaiah, "Quantization and feedback of principal modes for dispersion mitigation and multiplexing in multimode fibers," *IEEE Trans. Commun.*, vol. 64, no. 12, pp. 5149–5161, Dec 2016.

[96] A. Greenwood, *Electrical transients in power systems, 2nd edition*. New York, NY (USA); John Wiley and Sons Inc., Jan 1991, ch. 9.

[97] H. Blinchikoff and H. Krause, *Filtering in the time and frequency domains*. The Institution of Engineering and Technology, 2001, ch. 3.

[98] J. Duenas, "Isolated, shunt-based current sensing reference design," *Texas Instruments*, pp. 1–48, Dec 2014. [Online]. Available: http://www.ti.com/lit/ug/tidu384a/tidu384a.pdf

[99] W. Gander and J. Hrebicek, *Solving problems in scientific computing using Maple and Matlab®*. Springer Science & Business Media, 2011.

[100] P. Wessel and D. Bercovici, "Interpolation with splines in tension: a green's function approach," *Mathematical Geology*, vol. 30, no. 1, pp. 77–93, 1998.

[101] N. Eghtedarpour and E. Farjah, "Power control and management in a hybrid ac/dc microgrid," *IEEE Trans. Smart Grid*, vol. 5, no. 3, pp. 1494–1505, May 2014.

[102] D. E. Hedman, "Propagation on overhead transmission lines i-theory of modal analysis," *IEEE Transactions on Power Apparatus and Systems*, vol. 84, no. 3, pp. 200–205, March 1965.

[103] E. Clarke, *Circuit analysis of AC power systems*. Wiley, 1943, vol. 1.

[104] T. K. Vrana, Y. Yang, D. Jovcic, S. Dennetière, J. Jardini, and H. Saad, "The cigre b4 dc grid test system," *Electra*, vol. 270, no. 1, pp. 10–19, 2013.

[105] N. R. Council, *Microwave Processing of Materials*. The National Academies Press, 1994. [Online]. Available: https://www.nap.edu/catalog/2266/microwave-processing-of-materials

[106] B. Hyland, "Application node 5141: An improved and simple cable simulation model," *Maxim integrated*, pp. 1–12, Oct 2012. [Online]. Available: https://www.maximintegrated.com/en/app-notes/index.mvp/id/5141

[107] H. Lugschitz, *Overhead Lines and Underground Cables*. Springer International Publishing, 2017, pp. 1299–1318.

[108] O. M. Nanayakkara, A. D. Rajapakse, and R. Wachal, "Location of dc line faults in conventional HVDC systems with segments of cables and overhead lines using terminal measurements," *IEEE Trans. Power Del.*, vol. 27, no. 1, pp. 279–288, Jan 2012.

[109] D. T. Larose and C. D. Larose, *Data Preprocessing*. John Wiley & Sons, Inc., 2014, ch. 2, pp. 16–50.

[110] J. O. Smith, *Mathematics of the discrete Fourier transform (DFT): with audio applications*. Julius Smith, 2007, ch. 7.

[111] Environment Canada, "Wind speed over the last 25 years (annual data) for Toronto," 2015. [Online]. Available: https://toronto.weatherstats.ca/metrics/wind_speed.html

APPENDICES

Appendix A

Maximum Cloud Speed Calculation in Chapter 2

The most significant variation in the irradiance level and subsequently on a PV module voltage is caused by low-altitude cumulus clouds with a common height of H=1500 m [74]. It is assumed that v_c is equal to the wind speed at cloud height. The highest wind speed recorded in Toronto, ON, Canada—where this study was conducted—in the last 10 years has been $v_{w,meas}$=23.6 m/s, at a height of H_{meas}=10 m [111]. Using the power law equation (A.1) with λ being a constant equal to 0.155 [74], the fastest v_c is 51.3 m/s.

$$v_c(t, H) = v_{w,meas}(t) \left(\frac{H}{H_{meas}} \right)^{\lambda} \tag{A.1}$$

Appendix B

List of Publications

The following is a list of publications by the author during doctoral studies.

B.1 Peer-Reviewed Journal Articles

[1] K. A. Saleh, Ali Hooshyar, and E. El-Saadany, "Ultra-High-Speed Travelling- Wave-Based Protection Scheme for Medium-Voltage DC Microgrids", In Press, Oct. 2017.

[2] K. A. Saleh, Ali Hooshyar, E. El-Saadany, and H. H. Zeineldin, "Voltage-Based Protection Scheme for Faults Within Utility-Scale Photovoltaic Arrays", *IEEE Trans. Smart Grid*, In Press, Jan. 2017.

[3] K. A. Saleh, Ali Hooshyar, and E. El-Saadany, "Hybrid Passive-Overcurrent Relay for Detection of Fault in Low-Voltage DC Grids", *IEEE Trans. Smart Grid*, vol. 8, no. 3, pp. 1129 - 1138, Sept. 2015.

B.2 Submitted Journal Articles

[1] K. A. Saleh, Ali Hooshyar, E. El-Saadany, and H. H. Zeineldin, "Frequency- Domain Traveling-Wave-Based Protection for High-Voltage DC Grids", submitted to *IEEE Trans. Industrial Informatics*, (TII-17-1473), 07 Jul. 2017.

B.3 Conference Proceedings

[1] K. A. Saleh, Ali Hooshyar, and E. El-Saadany, "Passive Oscillator Based Protection Scheme for Faults Within Utility-Scale Photovoltaic Arrays", *2017 IEEE PES General Meeting*, Chicago, IL, USA, July 16 - 20, 2017.

B.4 Patents

[1] K. A. Saleh, Ali Hooshyar, and E. El-Saadany, 'Ultra-High-Speed Travelling-Wave Based Protection Scheme", U.S Provisional patent, serial #62/602,706, May 4, 2017.